Progress in Materials Science 76 (2016) 59–153

Contents lists available at ScienceDirect

Progress in Materials Science

journal homepage: www.elsevier.com/locate/pmatsci

Perspectives on oblique angle deposition of thin films: From fundamentals to devices

Angel Barranco, Ana Borras, Agustin R. Gonzalez-Elipe *, Alberto Palmero

Instituto de Ciencia de Materiales de Sevilla (CSIC-US), c/ Americo Vespucio 49, 41092 Seville, Spain

ARTICLE INFO

Article history:
Received 9 October 2014
Received in revised form 19 May 2015
Accepted 12 June 2015
Available online 28 August 2015

Keywords:
Oblique angle deposition
Glancing angle deposition
Magnetron sputtering
Electron beam evaporation
Nanostructured films
Growth modeling
Monte Carlo
Thin film devices
Transparent conductive oxide
Energy harvesting
Sensors
Optical devices
Wetting
Biomaterials
Biosensing
GLAD
Photovoltaic cells

ABSTRACT

The oblique angle configuration has emerged as an invaluable tool for the deposition of nanostructured thin films. This review develops an up to date description of its principles, including the atomistic mechanisms governing film growth and nanostructuration possibilities, as well as a comprehensive description of the applications benefiting from its incorporation in actual devices. In contrast with other reviews on the subject, the electron beam assisted evaporation technique is analyzed along with other methods operating at oblique angles, including, among others, magnetron sputtering and pulsed laser or ion beam-assisted deposition techniques. To account for the existing differences between deposition in vacuum or in the presence of a plasma, mechanistic simulations are critically revised, discussing well-established paradigms such as the tangent or cosine rules, and proposing new models that explain the growth of tilted porous nanostructures. In the second part, we present an extensive description of applications wherein oblique-angle-deposited thin films are of relevance. From there, we proceed by considering the requirements of a large number of functional devices in which these films are currently being utilized (e.g., solar cells, Li batteries, electrochromic glasses, biomaterials, sensors, etc.), and subsequently describe how and why these nanostructured materials meet with these needs.

© 2015 The Authors. Published by Elsevier Ltd. This is an open access article under the CC BY license (http://creativecommons.org/licenses/by/4.0/).

* Corresponding author.
E-mail address: arge@icmse.csic.es (A.R. Gonzalez-Elipe).

http://dx.doi.org/10.1016/j.pmatsci.2015.06.003
0079-6425/© 2015 The Authors. Published by Elsevier Ltd.
This is an open access article under the CC BY license (http://creativecommons.org/licenses/by/4.0/).

Contents

1. Oblique angle deposition of thin films

1.1. Introduction

Surface engineering is a technological area of high scientific and industrial interest thanks to the wide set of applications benefitting from its contributions. In addition to classical areas such as optics, tribology and corrosion/wear protection, where high compactness and a low porosity are important microstructural requirements, the advent of emerging technologies requiring porous or highly structured layers has fostered the development of thin film deposition procedures aimed at enhancing these morphological characteristics. A typical experimental approach in this regard is the use of an oblique angle geometrical configuration during deposition. Evidence of highly porous, optically anisotropic thin films grown using this technique were first reported more than a hundred years ago [1,2], but it was not until the 1950s–1970s that focus was given to the tilted columnar microstructure of these films and the factors controlling its development [3–9]. Following these initial steps, the last 20–25 years have witnessed the systematic application of oblique angle deposition (OAD) procedures for the development of a large variety of devices in fields such as sensor technology, photovoltaic cells, magnetism, optical devices, electrochemistry and catalysis; all of which require strict control over porosity, anisotropy and/or crystallographic texture of the film. A substantial number of papers, excellent reviews and books [10–20] have been published during this period, providing a well-documented background into both, the principles and the scientific/technological impacts of this synthesis method as well as the films it can produce. The recent publication of a book on this exciting topic [21] clearly demonstrates the ample, ongoing interest that the scientific community has in this subject, and readers are addressed to these aforementioned reviews and books to acquire an initial insight into the main features and possibilities of the OAD of thin films.

In general, the term OAD or other widely used alternatives such as "glancing angle deposition" (GLAD), and "ballistic deposition", are all associated in the literature with the physical vapor deposition (PVD) of thin films prepared by evaporation, which usually entails electron beam (e-beam) bombardment. Since the OAD concept can be more broadly applied whenever the source of deposition particles and the substrate surface are obliquely aligned, it is used in this review to describe a particular geometry in the deposition reactor rather than a particular technique. The intent here is to critically discuss the OAD of thin films from a perspective that is not restricted to evaporation, but also considers plasma- and laser-assisted deposition methods such as the magnetron sputtering (MS) technique, in which the presence of gas molecules may induce the scattering of particles and alter their otherwise rectilinear trajectory. Ion beam-assisted deposition procedures, in which a significant amount of energy is released onto the film surface by obliquely impinging particles, are also briefly discussed. A second scope in this review is to provide an atomistic insight into the mechanisms controlling the morphological development of OAD thin films, particularly its porosity, the tilt orientation of the nanostructures and any preferential texture. Although different geometrical models and empirical rules have been proposed in the last few decades to roughly account for these features in films prepared by e-beam evaporation, and to a lesser extent by MS, we believe that the time is ripe to discuss with better accuracy the atomic mechanistic effects controlling the development of morphology and crystallography of OAD thin films.

Overall, the increasing interest shown by the scientific community in these films has been a direct consequence of their unique morphology, which has fostered the development of new applications

and devices with specific functionalities. As such, the third and final scope of this review is the description of some of the more outstanding applications and new devices that incorporate OAD thin films.

1.2. Structure, organization and review content

This review is organized into five sections in addition to this introduction. Targeting readers with no previous knowledge on this subject, Section 2 presents a phenomenological description of OAD thin films and their unique morphology, which is formed from tilted nanocolumns promoted from the so-called "surface shadowing" effects. The outline of this section is similar to that in other published reviews and books [10–21], thus readers may complete their understanding of the basic principles by consulting the relevant literature on the subject.

Generally speaking, the OAD term refers to a configuration in which the material flux arrives at the surface of a substrate at an oblique angle. The most widely used approach to achieve this is the evaporation of material from a crucible through the impingement of electrons, although OAD thin films prepared by resistive evaporation under vacuum have also been reported [22–26]. Starting with this concept, Section 3 describes the different thin film processing techniques in which restrictions imposed by the deposition method or the presence of a gas in the chamber may alter the directionality of the particles being deposited. Here, MS [27], plasma enhanced chemical vapor deposition (PECVD) [28], pulsed laser deposition (PLD) [29] and vacuum liquid solid deposition (VLS) [30] are all considered and subjected to specific analysis. We also briefly discuss in Section 3 the effect of interaction momentum and energy exchange between the substrate and obliquely impinging energetic particles. High-power impulse magnetron sputtering (HIPIMS) [31] and ion-beam-assisted deposition (IBAD) [32] are two typical examples of these latter procedures. For the presentation of the majority of the results, we have assumed that readers are already familiar with common material characterization techniques such as electron microscopy and X-ray diffraction. However, some mention has been made on less conventional methods such as grazing incidence small-angle X-ray scattering (GISAXS) [33] and reflection high-energy electron diffraction (RHEED) [34] that have been used recently in the study of OAD thin films, and which have contributed to deepening the understanding of their properties. Contrary to the organization typically adopted by other reviews into OAD thin films, where basic properties such as their porosity, nanocolumnar shape or bundling association are correlated to their tilted nanocolumnar microstructure, we have opted to include a discussion on these features in Section 3. The main reason for this is that mechanistic factors other than the "surface shadowing effect" are strongly affected, not only by the preferential oblique directionality of vapor atoms, but also by additional specific energetic interactions that are discussed for the first time in this review. The discussion on methods other than evaporation, along with the analysis of bundling effects, adsorption properties and texturing effects in particular are all novel aspects that have not been systematically addressed in previous reviews on this subject.

Section 4 accounts for the main OAD features described in Sections 2 and 3 from a mechanistic perspective, aiming to explain the atomic-scale evolution of a thin film's microstructure during growth by e-beam evaporation and MS at oblique angles. Here, new fundamental ideas developed in the last years by our group are introduced, with these concepts allowing our understanding of the OAD phenomena to move beyond classical paradigms such as the tangent rule [9], as well as consider the film growth by methods other than evaporation. Particularly relevant in this regard is a systematic assessment of the mechanistic aspects involved in MS depositions that are not present in conventional e-beam evaporation.

Section 5 describes a wide set of applications in which OAD thin films are incorporated into devices. Unlike previous reviews and books [10–21], where a systematic and thorough description of thin film properties constitutes the backbone of the analysis, we have elected in this review to go directly to the end use so as to critically assess the many successful cases of OAD films being employed. This exercise has resulted in an astonishing and overwhelming number of papers (approximately 300) being identified from the last seven-to-eight years in which a new applications or devices where OAD thin films have been introduced. To cope with such a volume of results and to get a comprehensive description, we have relied on just a brief analysis of the expected

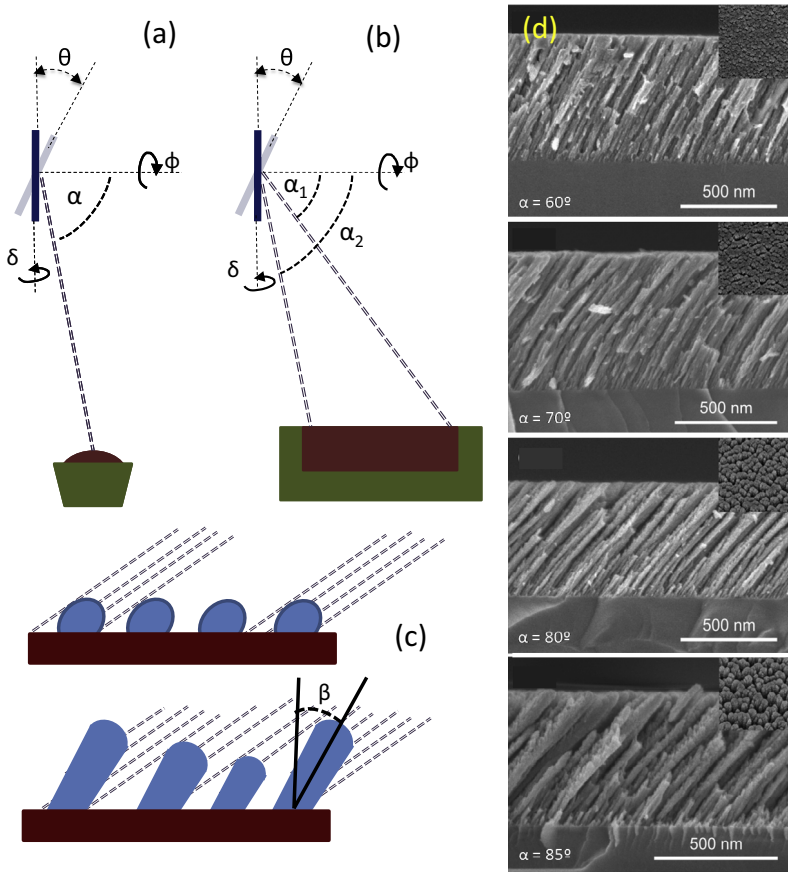

Fig. 2.1. OAD processes and SEM image of a typical OAD thin film microstructure: (a and b) definition of deposition angles from a punctual and large area source, respectively; (c) illustration showing the effect of shadowing during the initial and subsequent stages of deposition and the control mechanism of the tilting angle of the nanocolumns; (d) cross sectional and normal (inset) SEM micrographs of a series of TiO_2 thin films e-beam deposited at zenithal angles varying from 60° (top) to 85° (bottom). Note the change in the tilting angle of the nanocolumns when varying the deposition angle [48].

performance of such films, providing a summary of the contributions made by different authors active in the field.

Finally, Section 6 presents a short critical evaluation of the potentiality of up-scaling the OAD technology for industrial production. It will become apparent throughout this review that a critical shortcoming of OAD methods is their limited capability to be homogeneously applied over large surface areas, or to coat a large number of thin-film samples in a reproducible and efficient manner. This final section therefore discusses some of the more recent proposals and considerations to overcome these limitations and make the OAD methodology commercially competitive.

Although the literature selected for this review encompasses the previously mentioned papers extending from the beginning of the twentieth century to the present, we have focussed on only those published in the last 10–15 years; or in the case of the applications and devices discussed in Section 5, on the literature that followed the comprehensive review of Hawkeye and Brett in 2007 [16]. We expect that this systematization of the most recent literature on the subject, its critical analysis, and the proposal of new paradigms in thin film growth and description of emerging applications will

be of particular interest to researchers already active in the field and, most importantly, attract new scientists from other areas that may be able to contribute to the development of this exciting topic.

2. Shadowing effects and film morphology

2.1. Introduction

In this section, we address the basic concepts involved in the deposition and processing of thin films in an oblique angle configuration by developing a comprehensive survey of the already well-established knowledge on the topic. Though we describe the fundamentals of OAD by referring to the available literature, this knowledge can be complemented by reading some of the cited reviews on evaporated OADs [10–21]. This description is framed within the context of classical concepts in thin-film growth such as the Thorthon's structure zone model (SZM) and other related approaches [35–37]. The core concept of this section is the so-called "shadowing mechanism", which is the main governing process responsible for the appearance of singular nanostructures within the OAD of thin films.

2.2. Thin film deposition at oblique angles

The deposition of thin films at low temperatures (i.e., when thermally activated mobility processes are rather limited), while keeping the substrate in a normal geometry with respect to the evaporated flux of material, gives rise to compact thin films. Within the classical SZM [35,36], the resulting microstructure is recognized as being Type I, which is characterized by very thin, vertically aligned structures and a high compactness.

When the deposition flux arrives at an oblique angle at the substrate surface, an additional variable is introduced into the growth process that has a significant influence on the development of the film's microstructure and compactness. It is generally accepted that the mechanistic factor controlling the nanostructural evolution of the films is a "shadowing effect", which prevents the deposition of particles in regions situated behind initially formed nuclei (i.e., shadowed regions) [9,11]. Under these conditions, the absence of any diffusion of ad-particles means that vapor particles are incorporated at their point of impact, a process that is usually recognized as ballistic deposition giving rise to tilted columnar and highly porous microstructures. Different descriptions and geometrical models accounting for these shadowing effects can be found in previous publications on the subject [38–41]. Although most recent mechanistic models for the formation of nanocolumns will be described in detail in Section 4, we will recall here some of the basic concepts that intuitively account for the importance of shadowing in controlling the microstructure of an OAD thin film.

2.2.1. Geometry of the deposition processes and shadowing effects

Fig. 2.1(a) and (b) presents two ideal OAD geometrical schemes for the deposition of atoms from a small source or from a large area, respectively. The first scenario is typical of e-beam assisted evaporation, which is the most common experimental arrangement for the OAD of thin films. With the exception of a few thermal evaporation experiments [22–26], the second situation applies exclusively to MS and other deposition techniques that are performed in the presence of a certain gas pressure, a situation that is of relevance to the techniques and results reviewed in Section 3. These schemes highlight the geometrical parameters relevant to the OAD of thin films, namely the zenithal angle of alignment between the source and the film (α), the azimuthal angle (ϕ) and the polar angles (δ) and (θ). The zenithal and azimuthal angles are well defined in e-beam assisted evaporation experiments, as the target source can be considered located at a fixed point. In contrast, the direction from which deposition particles can arrive from a large source can vary significantly, and so, for the sake of convenience, the value of α is in this case defined as the angle between the direction normal to the substrate and the center of the target.

According to Fig. 2.1(c), which illustrates the most basic notions of OAD of thin films [9–12], the first nuclei formed during the earliest stages of deposition project a shadow behind them that

prevents the deposition of any further evaporated material within these "shadowed" regions. As deposition progresses, these nuclei induce the formation of tilted and separated nanocolumns which, as discussed in detail later in this section and in Section 3, is a feature that creates useable properties such as porosity, birefringence and magnetic anisotropy. This relation has been recognized in early works dealing with OAD thin films, and since then, several attempts have been made to correlate the tilt angle of the nanocolumns (β) with the zenithal evaporation angle, α (see Fig. 2.1(b)). The so-called *tangent rule* (Eq. (2.1)) [6,9] and *cosine rule* (Eq. (2.2)) [38] have to date been the two most popular heuristic expressions correlating the oblique angle of evaporation and the tilt angle of the nanocolumns:

$$\tan\alpha = 2\tan\beta, \tag{2.1}$$

$$\beta = \alpha - \arcsin(1-\cos\alpha)/2. \tag{2.2}$$

Although other, more complicated, empirical descriptions have also been proposed [42–44], understanding the fundamental factors controlling the tilt angle of the nanocolumns is still an open question that requires additional considerations, as explained in Section 4. Indeed, none of the proposed semi-empirical expressions have completely succeeded in accounting for the tilt angle of nanocolumns, particularly in the case of depositions with high zenithal angles (i.e., when $\alpha > 60°$). Systematic studies of a large variety of metals recently carried out by Zhao et al. [40,45] have clearly demonstrated that the tilt angle of the columns is a material-dependent property, and therefore cannot be solely attributed to simple geometrical relationships. Based on atomistic considerations, we propose in Section 4.2 a model to explain why the tilt angle of the nanocolumns depends on the chemical nature of the deposited material, as well as the characteristics of the deposition reactor itself.

From a geometrical point of view, it is obvious that the shadowing effects associated with the directionality of the incoming particles will be relaxed when they are produced from a large area source (Fig. 2.1(b)) and/or when their directionality is randomized through scattering processes by gas molecules [46,47], as it is typically the case in MS, PECVD and PLD techniques. Yet, even under these conditions, a preferential direction of arrival can be preserved to some extent, thereby inducing the growth of OAD thin films with tilted nanocolumnar structures.

The simple geometrical considerations regarding shadowing that are shown schematically in Fig. 2.1(b) have direct experimental implications with regard to the microstructural development in the e-beam assisted OAD of thin films (i.e., when evaporation occurs from a well-defined punctual source). The first issue is the critical sample size at which deposition is homogeneous. For instance, in an experimental configuration such as that depicted in Fig. 2.1(a), the zenithal deposition angle is at a maximum on the uppermost side of the substrate, and at a minimum on its lower side. Consequently, the sample size needs to be constrained to within few square centimeters to maintain a well-defined geometrical configuration (i.e., a well-defined angle of incidence, α). The up-scaling of this OAD methodology has therefore been a significant impediment to its industrial implementation, and recent proposals in this regard will be discussed in Section 6. Vapor collimation is another important experimental factor, which as discussed in Section 4, may significantly affect the microstructure of the thin film. Therefore, adjusting the target to substrate distance, or using slits and other alternatives, favours the effective control over the nanostructuration mechanisms of OAD thin films.

2.3. Effects of temperature and deposition rate on the morphology of OAD thin films

A basic assumption made in the previous considerations on the evolution of OAD thin film morphologies is that growth proceeds at low temperatures, and thus thermally activated diffusive processes on the film surface make little contribution to the nanostructuration of the film. Within the framework of SZM [35–37], this implies a transition from Zone I to Zone T; the latter occurring when $T_s/T_f > 0.3$ (where T_s is the temperature of the substrate and T_f the melting temperature of the deposited material). In Zone T, thin films deposited with a normal configuration possess a microstructure formed by perpendicular and compacted columnar grains that are thicker than those produced in Zone I. Similarly, heating the substrate during OAD produces a change in microstructure

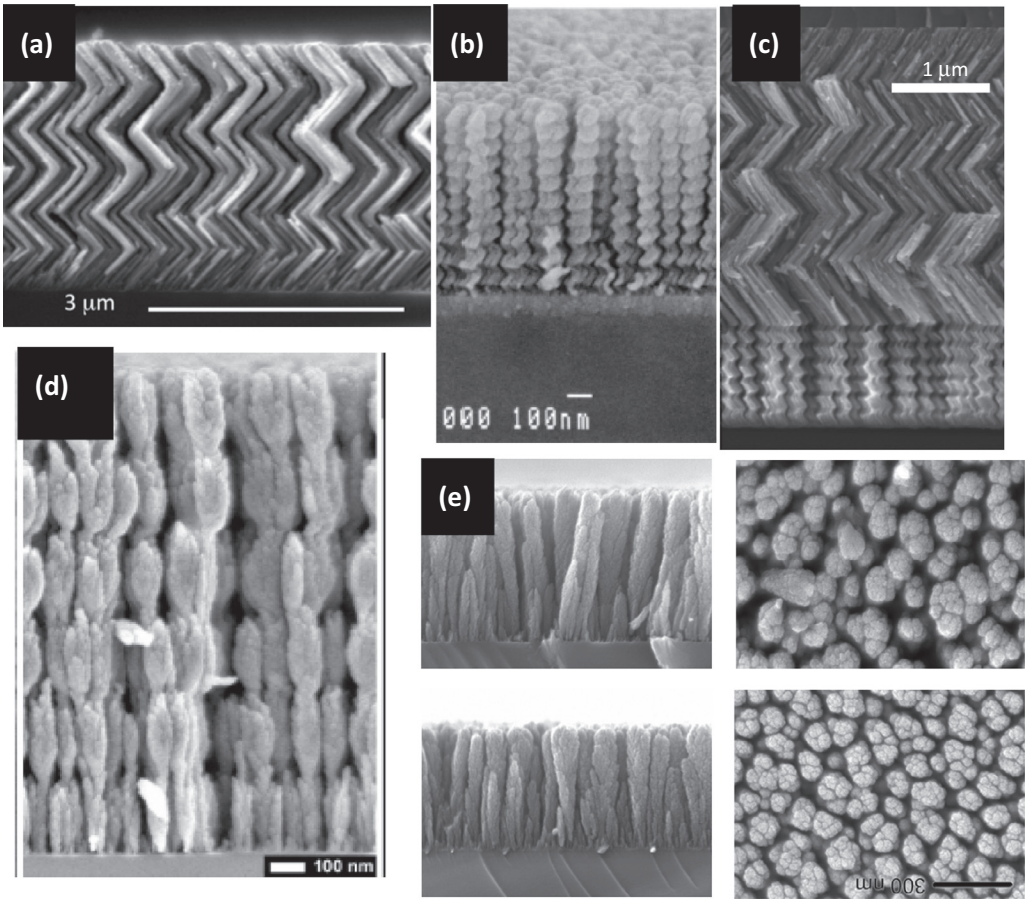

Fig. 2.2. Selected SEM micrographs of OAD sculptured TiO_2 thin films obtained by moving the substrate during deposition. Cross sectional SEM images of (a) zig-zag nanocolumns obtained by back and forth azimuthal turning of the substrate [63], (b) spiral nanocolumns obtained by continuous azimuthal rotation (i.e., dynamic OAD) [87], (c) zig-zag plus spiral nanocolumns (author's unpublished results), (d) nanocolumns with width modulation obtained by azimuthal rotation and back and forth polar angle tilting [87], and (e) vertical nanocolumns obtained by rapid azimuthal rotation at two different rates [65].

due to an increase in the mobility of ad-particles [49]. One way of rationalizing these nanostructural changes is to assume that dominance of shadowing in controlling the film growth is partially reduced by the diffusion of ad-particles from their point of impact to otherwise inaccessible "shadowed" regions. Deposition rate also plays an important role in controlling surface diffusion and atom relocation, as the rapid arrival of new particles could bury and/or interfere with particles diffussing onto the substrate or thin film surface. It stands to reason that high temperatures and low deposition rates would allow ad-particles to diffuse over greater lengths, with the opposite tendency being expected at low temperatures and high deposition rates. This should be accompanied respectively by either a decrease or increase in the nanocolumn tilt angle (β), which was confirmed by Nakhodkin and Shaldervan [50] for a large variety of materials. Nevertheless, in a systematic investigation of the OAD of magnetic metals and alloys (Co, Ni, Fe), Hara et al. [51–56] showed that although the aforementioned relation between temperature and deposition rate was generally maintained, other effects besides diffusion must be involved to explain unexpected deviations in the growth tendencies and the appearance of more complex morphological patterns. For a large variety of metals and oxides deposited by DC magnetron sputtering, Deniz et al. [49] determined the nanostructuration

Table 2.1
Select *sculptured thin films* prepared by changing the geometry of deposition.

Microstructure	Movements involved	Material	Application/properties	Ref
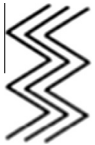 *zig-zag*	Azimuthally turned by 180° 	TiO_2	Dye sensitized solar cells Enhanced birefringence	[63,64]
		Cr	Mechanical properties	[68,69]
		Alq_3	Polarization effects (also spiral)	[71]
		Mn	Electrochemical capacitors	[72]
		$Eu:Y_2O_3$	Selective polarization transmission of fluoresced light (also spiral)	[73,74]
 *Helical, spiral*	Continuous, slow azimuthal rotation 	Cu	Highly textured	[26]
		SiOx	nanostructures	[75]
		Fe	Optical circular dichroism	[76]
		TiO_2	Chiral and magnetic films	[77]
		Au, Ni,	Circular polarizers	
		Polystyrene	Helical structures as a template for perforated helical thin films	[78]
		TiO_2	Selective reflection of polarized light	[79]
 *Vertical and s-shaped nanocolumns*	Fast azimuthal rotation 	SiO_2	Vertical templates for Si nanotubes	[80]
		TiO_2	Mechanical properties	[65]
		TiO_2/Si	Scaffold for ALD*. Humidity sensors	[81]
		TiO_2/Mg F_2	Optical anisotropy	[82]
	Azimuthal tilting plus fast rotation	TiO_2 (s-shape)	Selective transmission of linearly polarized light	[83]
 *Thickness variation with depth*	 Polar and azimuthal movements	TiO_2	Narrow band pass optical filters	[84]
		TiO_2	Bragg reflector	[85]
		Si	Rugate filter oxidation of Si	[86]
		Si	Rugote filters	[87]
		ITO[1]	Conductive Bragg microcavity	[88]
No defined shape	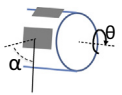	YSZ[2]	Thermal barrier coatings	[89–91]
		Mo	Development of in-plane texture	[92]
	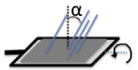			

temperature threshold $\theta_T = T_s/T_f$, above which ad-atom surface diffusion becomes dominant over surface shadowing, thereby preventing the formation of a typical OAD nanocolumnar morphology. For metals, this temperature threshold has been tentatively established at around $0.33T_f$, while for oxides the value is approximately $0.5T_f$.

Variation in the morphology of OAD thin films with deposition conditions was thoroughly explored by Abelmann and Lodder [11] by considering that changes in temperature, deposition rate and the extent of surface contamination by adsorbed impurities may have a significant influence on the tilt angle of nanocolumns, as well as on other morphological characteristics such as their *bundling* association. According to these authors, the diffusion of ad-particles in either a random manner, or with specific directionality resulting from momentum exchange between the deposition particles and the thin film surface, can be affected by all these factors. In Section 4, we will come back to the importance of momentum exchange and other mechanisms in determining the morphology of OAD thin films. Similarly, the *bundling* association of nanocolumns, a morphological feature generally overlooked in the most recent literature on the subject, will be treated specifically in Sections 3.6.2 and 4.2.2.

In addition to the tilt angle, the shape and size of the OAD thin film nanocolumns can be altered by changing the temperature and deposition rate. Although a quantitative evaluation of these changes is not yet available, various works have addressed this problem and studied the morphological changes and other nanostructures [57–59] induced as a function of temperature. For example, using a simple nucleation model, Zhou et al [41] proposed that the evolution of the nanocolumn growth depends on the diameter of the nuclei formed during the initial stages of deposition. That is, if larger nuclei are formed at high temperatures and/or they possess a low melting point, then thicker nanocolumns will develop during OAD. A thickening of nanocolumns and a decrease in their tilt angle has been clearly observed in different materials by Vick et al. [60] and Tait et al. [38], who attributed these effects to an enhanced diffusion of ad-particles during growth. However, in light of other results [11,53], it is evident that the general use of these diffusion arguments to predict OAD thin film morphologies needs to be critically discussed.

2.4. Sculptured thin films

A quick overview of the literature on OAD thin films reveals that the concept *sculptured films* is used for both, the simple, tilted OAD morphologies hitherto discussed, as well as other more complex thin film microstructures in which the orientation and/or width of the nanocolumns adopt a singular form (e.g., oblique matchsticks, chevrons, multiple zigzags, S's, C's, helices and even superhelices) in response to moving the substrate during deposition [61]. Interest in these sculptured thin films is driven not only by scientific curiosity, but also because of the many potential applications that such nanostructures might have [16–18]. Different *sculptured thin films* can be obtained by changing either alternatively or simultaneously the zenithal (α), azimuthal (ϕ) and/or polar (θ) angle (c.f., Fig. 2.1 (a) and (b)) to alter the incoming direction of the deposition flux during growth. As demonstrated by Monte Carlo simulation analyses [62], shadowing effects can be regarded as the main factor in determining the large variety of nanocolumnar morphologies that can be achieved by moving the substrate around its different axes along a predefined pattern. For illustrative purposes, Fig. 2.2 provides some selected SEM micrographs of TiO_2 thin films that depict some of the different morphologies that can be obtained by tilting and/or rotating the substrate during the deposition. Much work in this area has been carried out by Brett et al. [16,17], who along with other authors [63–92], have systematically employed different substrate movements to tailor the morphology of *sculptured thin films*.

To illustrate the possibilities that can be offered by such films, Table 2.1 gathers together a selection of *sculptured thin films* and schematically describes their morphology, the substrate motion responsible for their formation, the type of material, and any related properties and/or target applications. Note that rotating the substrate around the azimuthal axis (ϕ) in Fig. 2.1(a)) while maintaining a constant zenithal angle (α) provides a single degree of freedom to control the film nanostructure in what is sometimes referred to as "*dynamic*" OAD. In this way, singular shapes such as zig-zags, helixes or spirals, or vertical nanocolumns can be obtained by controlling the rate, direction, etc. of the

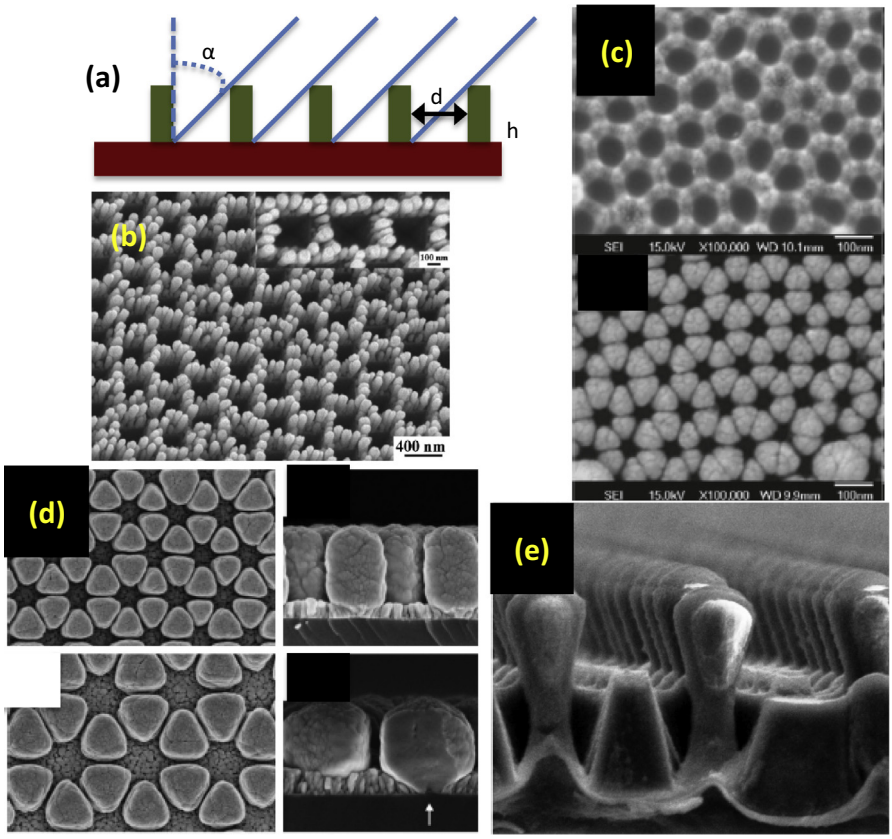

Fig. 2.3. OAD of thin films on patterned substrates. (a) Schematic showing the effect of patterned features on shadowing effects. Depending on the height, **h**, the distance between the patterned features, **d**, and their geometrical arrangement on the substrate, different zones are selectively covered by the deposited material while others remain inaccessible to the particle flux. SEM micrographs of different OAD layers on different patterned substrates, (b) Ta deposited on a substrate covered with packed nanospheres (nanosphere lithography deposition) [112], (c) hexagonal arrays of W deposited over two time periods on an Al lattice template produced by anodization [102], (d) hexagonal arrays of Ge deposited over increasing periods of time on a patterned gold substrate [105], and (e) Si nanostructures OAD deposited on a nanoimprinted substrate with periodic stepped and flat surfaces [106].

movement. For example, a zig-zag microstructure is obtained by tilting the substrate back and forth by 180° over set periods of time, while helical or spiral structures are obtained by slowly and continuously rotating the substrate around the azimuthal angle. If the speed of rotation around ϕ is sufficiently high, then a vertical nanocolumn is obtained due to an averaging of the incoming flux angle during growth; the areal density and width of the nanocolumn being determined in this case by the rotation rate. The control of this morphological quantity, therefore, represents a very simple method of tuning the density and other macroscopic properties of thin films. In addition, S-type microstructures can be obtained by combining a tilt movement with a rapid azimuthal rotation during deposition. Similarly, tilting around the polar angle θ (Fig. 2.1(a)) for a given period of time, while simultaneously rotating the substrate around the azimuthal angle ϕ, has been used to fine tune the density and refraction index of thin films.

Besides azimuthal rotation at a constant zenithal (α) angle commonly used to average the growth process and obtain perpendicular nanocolumns, *tangential or flipping* rotation of the sample substrate

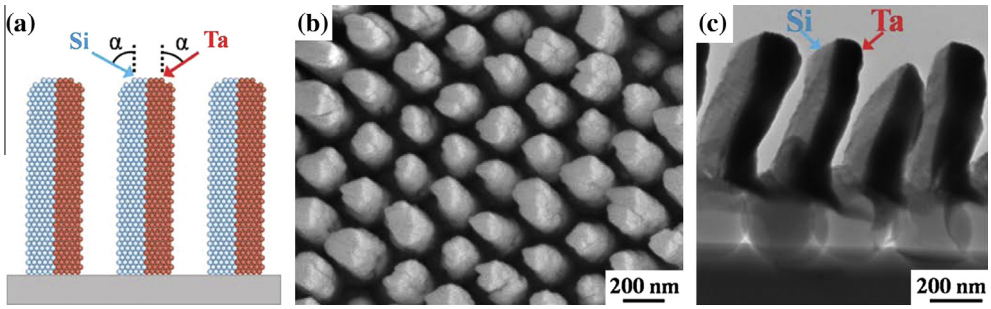

Fig. 2.4. Simultaneous OA co-deposition of Si and Ta from two sources onto a patterned substrate. (a) Schematic of the deposition process. (b and c) Normal and cross sectional micrographs of the nanostructures obtained. The resulting features appear well separated because the substrate is not flat, but instead presents a patterned structure to maximize the shadowing effect [111].

(see the last rows in Table 2.1) has been proposed by some authors as a way to fabricate low density films [89–92]. Even if such movements do not produce "sculptured microstructures" in the strict sense of a well-defined and shaped nanostructure, we consider them here because they may represent an interesting approach to up-scaling the OAD process (see Section 6).

Other sample rotations and/or movements include the so-called *PhiSweep*, wherein the substrate is rotated back and forth around ϕ, and left for controlled periods of time at each of these angular positions [93]. Meanwhile, with *swing tilting* rotation, the substrate is smoothly rotated back-and-forth along its azimuth within an angular range of $\Delta\phi$, which is called the swing angle. These methods have also been used to obtain 3D nanostructures on substrates with previously deposited seed patterns [94,95] (see Section 2.5).

2.5. OAD on nanostructured substrates

Another way to control the surface shadowing effect so as to achieve specific morphologies and layer properties is to carry out deposition using substrates with a well-controlled surface topography. The idea of modifying the nanostructure of a film using a pre-deposited template is quite simple: it exploits the shadow effect by utilizing features already present on the surface. This artificially generated shadowing mechanism is illustrated schematically in Fig. 2.3(a), where it is considered that no deposition may take place behind an obstacle. The key point, therefore, is to control the shadow cast by a series of patterned hillocks, protrusions or other well-defined features on the surface. Some model calculations have been proposed to determine the dimensions of these features in ordered arrays, their relative arrangement in the plane and the distances between them so as to effectively control the shadowing effect and ultimately obtain new artificially designed nanostructures [96].

The simplest version of OAD on a template uses a rough substrate surface; the elongated mounds or facets promoting the accumulation of deposited material onto the most prominent features, while at the same time preventing the arrival of vapor flux at the shadowed regions [97]. Expanding on this simple approach, the use of substrates with a well-defined lithographic pattern opens up a range of new and unexpected possibilities for the nano-structuring of OAD thin films. To this end, patterned substrates consisting of well-ordered nano-structured array patterns or seed layers have been prepared through a variety of lithographic methods, laser writing, embossing or other top-down fabrication methods [24,87,98–109]. Among these, the use of colloidal lithography (i.e., OAD on a substrate pre-coated with packed nanospheres of different materials) has gained much popularity over the last few years thanks largely to its simplicity [110–113]. With the aid of selected examples, Fig. 2.3 illustrates the possibilities that these approaches provide for the tailored growth of all-new supported nanostructures.

Other options for controlling the thin film morphology arise when the deposition onto a template pattern is combined with the controlled movement of the substrate. For example, S-shaped 3D photonic structures used as polarizers (c.f. Table 2.1) have been fabricated by *Phisweep* or

swing rotation of substrates with a pre-deposited template structure [93,94]. At present, this use of templates in the OAD of thin films has transcended pure scientific interest, and is now developed for advanced technological applications. For example, mass-produced metal wire grid polarizers are being fabricated via the OAD deposition of antireflection FeSi and SiO_2 layers on previously deposited aluminum columnar arrays [87,114,115]. Other emerging applications in biomedical areas [107,116,110,117], or for controlling the wetting properties of substrates [102,118], also rely on the use of patterned surfaces rather than the direct OAD of thin films (see Section 5.5).

2.6. Evaporation from two sources

In most of the deposition techniques discussed thus far the evaporated material originates from a single target source, and thus the chemical composition of the film produced is homogeneous. An alternative methodology for the OAD of thin films relies on the use of two sources positioned at oblique polar (δ) angles to the substrate at an equal or different zenithal (α) angle (Fig. 2.1(a)) in what has been named glancing angle co-deposition (GLADCO) by some authors [119]. Typically, such a configuration of evaporation sources produces nanocolumns with an inhomogeneous composition when operated at constant evaporation rates. This inhomogeneous growth was critically evaluated by Van Kranenburg et al. [10], who also studied the development of *bundling* associations between nanocolumns in a direction perpendicular to the flux. This type of inhomogeneous growth process was also studied theoretically by means of MC models [120], and more recently by statistical models [45].

In the search for new functionalities and properties, different authors have used these two aforementioned approaches to tailor the composition and distribution of components in a growing nanostructure. Simultaneous or alternant evaporations have been used along with control over the relative evaporation rate of each source to tailor the morphology and composition of OAD thin films. A survey of the different possibilities offered by this technique was recently undertaken by He et al. [19], who described new options such as controlling the nanocolumn composition along its length or diameter, or incorporating nanoparticles into either single or more complex nanostructures by simply moving the substrate. These principles have been applied by various authors to prepare laterally inhomogeneous nanocolumns [111,113,121,122], or to fabricate alloy or multicomponent nanocolumnar films [123–129].

The combination of the template approach discussed in the previous section and evaporation from two sources opens the possibility of simultaneously controlling both, the microstructure (i.e. thickness, orientation, etc.) and the lateral composition of the nanocolumns. Fig. 2.4 gives an example where OAD has been carried out using two sources on a substrate with packed nanospheres to produce thick nanocolumns with a laterally inhomogeneous chemical composition. Yet despite these advances, the possibilities offered by this method to further control the nanocolumnar morphology and other properties of the films remain largely unexplored. This was made clear in a recent work by He et al. [125], which demonstrated the possibility of enhancing the porosity of Si–Cu and SiO_2–Cu nanocolumnar arrays through the selective removal of copper with a scavenger chemical solution.

3. Alternative processes, and the microstructure and crystallographic structure of OAD thin films

It is likely considered that e-beam, and to a lesser extent thermal evaporation, have been the most widely utilized methods for the OAD of thin films. This has certainly been true regarding the effective control of the geometry of the nanofeatures through shadowing effects (e.g., the growth of *sculptured thin films*); however, there are other alternatives that make use of the OAD geometrical configuration to develop new microstructures, textures and general properties in films. In these other methods, several physical mechanisms, including the thermal diffusion of ad-particles discussed in the previous section, can affect the deposition process and the efficiency of shadowing mechanisms.

An interesting effect is the relocation of deposited particles through liquid–solid preferential agglomeration at sufficiently high temperatures, which constitutes the basis of the so-called vacuum liquid solid (VLS) method [30]. Another possibility is to alter the direction of the deposition particles

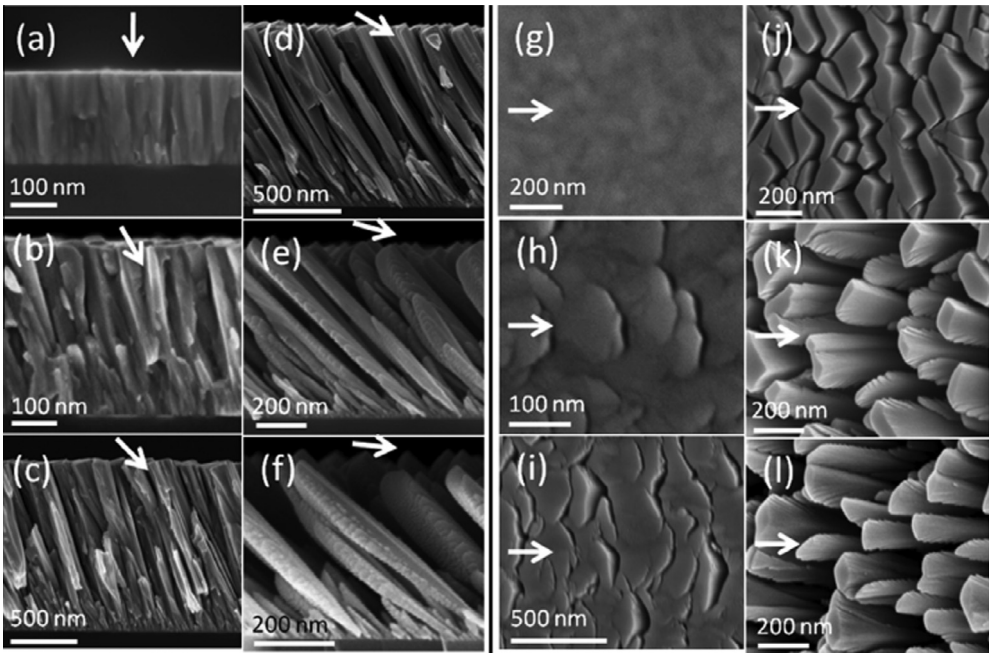

Fig. 3.1. Side (left two panels) and top (right two panels) SEM images of Mo nanorods grown by OAD on a stationary substrate at incidence angles of: (a and g) 0°, (b and h) 30°, (c and i) 45°, (d and j) 60°, (e and k) 75° and (f and l) 85°. The white arrow in each image shows the incident flux direction. Note that the scale bars in the figures vary due to the difference in thickness [151].

by introducing a gas to scatter them during their flight from the source to the substrate, thereby inducing a certain randomization in their trajectories [46,130]. Such a situation is encountered when deposition is carried out by MS, PLD and PECVD, among others. Total or partial randomization of the particle trajectory leads to a softening of the geometrical constraints imposed by a pure "line of sight" configuration, and in doing so causes the microstructure of the films to deviate from the hitherto discussed typical morphological patterns. In the presence of a gas, not only is the geometry of the deposition process critical to controlling the film microstructure, but also the mean free path of the deposition particles. Consequently, in order to retain at least some of the features typical of OAD growth, particularly the tilt orientation of the nanocolumns and a high porosity, it is essential that the deposition particles arrive at the film surface along a preferential direction, thereby allowing shadowing mechanisms to take over the nanostructural development of the films.

3.1. Vapor–liquid–solid deposition

The vapor–liquid–solid (VLS) technique was first proposed by Wagner and Ellis [131] as a suitable method for the fabrication of supported nanowires. It is a high temperature procedure, in which liquid droplets of a deposited material act as a catalyst to dissolve material from the vapor phase, which then diffuses up to the liquid solid interface and precipitates as a nanowire or nanowhisker. Typical VLS growth therefore proceeds through two transition steps, vapor-to-liquid and liquid-to-solid, making it vital to maintain the substrate temperature at a critical value capable of enabling these diffusion processes. The combination of VLS with OAD has proven very useful in tailoring nanostructures with very different shapes (nanowires, nanotrees, other branched structures, etc.). For example, by keeping the substrate at typical VLS growth temperatures, crystalline Ge nanowhiskers with a nanostructure determined by the angle of material flux have been obtained [132]. Fancy ITO (indium tin oxide)

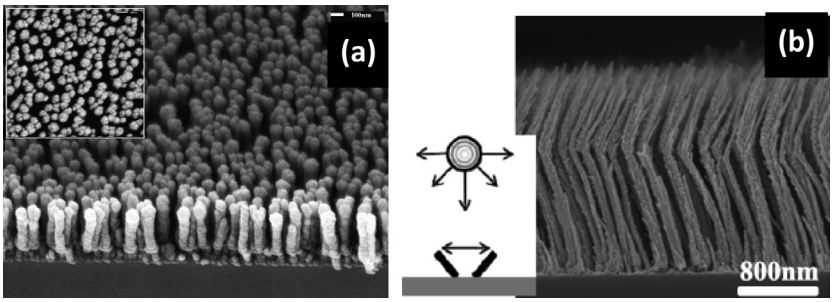

Fig. 3.2. SEM images of nanostructured columnar thin films fabricated by plasma and laser methods. (a) Carbon nanorods obtained by PLD with the plum in a glancing configuration with respect to the substrate [173]. (b) Zig-zag Ag@ZnO nanowires prepared by PECVD using a glancing configuration for the precursor flow relative to the substrate, as shown schematically in the center of the figure [187].

2D-branched nanostructures have also been fabricated by combining VLS and OAD while azimuthally rotating the substrate [133–137]. In this case, liquid indium–tin alloy droplets act as both the catalyst and the initial nuclei for branch formation. This means that the final branched structure can be controlled by rotating the substrate or varying the zenithal angle according to a predefined pattern to adjust the shadowing effect created during the arrival of vapor flux (see Section 5.1) [134,135].

3.2. Magnetron sputtering

In the MS technique, a flux of sputtered atoms or molecules is produced by the bombardment of plasma ions onto an electrically biased target. The sputtered atoms are then deposited onto a substrate, which is usually placed in a normal configuration with respect to the flux direction and therefore parallel to the target [27]. Owing to its high efficiency, reliability and scalability, this technique is widely used industrially [138].

The MS technique has been also used in OAD configurations by placing the substrate at an oblique angle with respect to the direction normal to the target (see Fig. 2.1(b)). Despite the complexity of the mechanisms involved (see Section 4), no systematic correlations have yet been established between the deposition parameters (e.g., gas pressure, electromagnetic power of the magnetron, pulse regime, target–substrate distance, deposition angle, etc.) and the resulting thin film microstructure. Besides the existence of particle scattering events, another significant difference with respect to the e-beam evaporation is the large size of the material source (see Fig. 2.1(b)). In Section 4, we will discuss some of the mechanistic effects that may induce changes in the microstructure of MS-OAD films.

While e-beam evaporation has been used for the deposition of a large variety of materials, including amorphous and crystalline semiconductors [80,86,106,139,140], metals [29,141–146], oxides [48,79,89,147–149] and even molecular materials [71,103,150], MS has been the most widely used method for the deposition of metals and oxides when control over the crystalline structure and/or surface roughness is an issue.

Within the scheme of SZMs [35–37], MS deposition results in films that grow in Zone T over an ample range of pressures and temperatures. Moreover, new physical effects that can affect the microstructure and crystallographic structure of the films can occur under OAD conditions. Nevertheless, the growth of separate nanocolumnar structures tilted usually in the direction defined by "shadowing" mechanisms can be considered a characteristic feature of MS-OAD films. Fig. 3.1 shows a series of nanostructured Mo thin films deposited by MS at oblique angles, wherein the tilt angle of the nanocolumns and their separation clearly increases with the zenithal angle of deposition, α [151]. There are numerous examples of nanostructured thin films (mainly oxides, nitrides and metals) in the literature on MS-OAD [68,69,151–172]; but in general, the quantification of the nanocolumn tilt angle and film porosity is not as straightforward with MS as it is with e-beam deposition. To approach conditions existing during vacuum evaporation and promote tilted

nanocolumnar growth, MS deposition at low pressures and/or at short target–substrate distances [60] has been proposed as a way of reducing gas-particle scattering effects. In a recent work on gold deposition by MS, we studied the influence of gas pressure and substrate inclination on the nanocolumnar development and porosity of films [172]. Through this, we identified a continuous microstructural variation with pressure and tilt angle of the substrate from compact to porous films, the latter being formed by tilted nanocolumns or continuous layers with elongated pores extending along the deposition direction. The mechanistic factors controlling this evolution have been rationalized within an extended structure zone model scheme that will be discussed in detail in Section 4 (see Section 4.3.4).

Additional movement of the substrate, typically in the form of azimuthal rotation (i.e., dynamic OAD), has also been used during MS-OAD to create modified thin-film microstructures. In general, the effects obtained by incorporating this additional degree of freedom are similar to those reported for the evaporation technique, except the microstructure may now progressively evolve from separated nanocolumnar nanostructures to homogeneous porous layers by increasing the gas pressure or target–substrate distance [68,151,170–172].

MS in OAD geometries has emerged as a powerful tool to tailor the crystallographic texture of films along both out- and in-plane directions; i.e., it makes it possible to obtain layers in which individual crystallites are aligned along preferential crystallographic directions perpendicular to the substrate and/or parallel to the substrate plane. Crystallization is very common in metals, even when deposition takes place at room temperature, and can occur in oxides if the substrate temperature is high enough. Thus, crystallization can be promoted by increasing the energy and momentum given to the surface via ion bombardment [11,157]. A more detailed description of the texturization effects in OAD thin films will be presented in Section 3.7.

3.3. Pulsed laser deposition

In the PLD technique, a laser beam impinging onto a target ablates its uppermost layers that form a plasma plume with numerous energetic particles. This plume is directed toward a substrate, where the ablated material is deposited in the form of a thin film [29]. Remarkably, a key feature in this technique is the conservation of the target stoichiometry when employing multicomponent targets. Moreover, in general conditions, the highly energetic character of the species in the plume promotes that thin films usually grow compact, although nanocolumnar and porous thin films can be grown by intentionally introducing typical OAD geometries [173–178]. Much like the OAD of thin films prepared by evaporation or MS, the main purpose in most cases is the effective control of texture alignment so as to obtain a columnar microstructure and/or porous layers. For example, in cobalt ferrite oxide thin films, preferential orientation along the [1 1 1] crystal direction and compressive strain tunable as a function of film thickness can be obtained by PL-OAD, whereas almost strain-free and random polycrystalline layers are produced when using normal-incidence PLD under the same conditions [177]. Nanocolumnar mixed oxide thin films, including $YBa_2Cu_3O_x$ [179] and $La_{0.7}Sr_{0.3}MnO_3$ [180], have been prepared by PL-OAD to take advantage of the preservation of the target stoichiometry. Thin films with simple composition, enhanced porosity and controlled microstructure have also been deposited by PL-OAD, for instance to grow porous nanocolumnar ZnO thin films [175,176] by controlling both, the zenithal and azimuthal angles of deposition. Similarly, porous carbon thin films consisting of perpendicular nanocolumns [173] (see Fig. 3.2(a)) or more complex zig-zag morphologies [174] were obtained through azimuthal rotation of the substrate to an oblique angle configuration. In all these cases, even though the plasma plume was full of highly energetic neutral and charged species, shadowing effects are still of relevance during deposition, promoting the formation of an open film microstructure. This means that parameters such as the temperature of the plume species (related to the power and other characteristics of the laser pulses), the distance between the target and substrate, the pressure in the deposition chamber and the effective width/length of the plume need to be carefully controlled to effectively tailor the final morphology of a film.

3.4. Plasma-assisted deposition

Plasma-assisted deposition, usually called *plasma enhanced chemical vapor deposition* (PECVD), is a typical thin film fabrication technique employed to homogeneously coat large-area substrates that is only rarely used for the preparation of layers with singular nanostructures [27,181]. In this process, a volatile-metal precursor is dosed in a reactive plasma chamber, where it decomposes to deposit a thin film, releasing volatile compounds (e.g., CO_2, H_2O, etc.) that are evacuated together with the gaseous reaction medium. Depending on the plasma characteristics, thin films of metal, oxide, nitride, oxinitride or other compounds can be obtained. By definition, this procedure requires a certain plasma gas pressure to operate, a feature that seems to preclude the intervention of shadowing effects associated with the preferential arrival of deposition particles travelling in a particular direction. It should be noted, however, that this does not exclude nanostructuration due to shadowing effects of randomly directed species [46]. However, mechanisms inducing certain preferential directionality of deposition species have been incorporated in plasma-assisted deposition by making use of particular effects. The best known example of this is the preparation at elevated temperatures of supported carbon nanotubes (CNTs) and other related nanostructures (e.g., graphene) [182–185]. The growth of CNTs is catalytically driven by the effect of metal nanoparticles that are initially deposited on the substrate, and which remain on the CNT tips during growth. During this process, it is assumed that the electric field lines within the plasma sheath are perpendicular to the surface (a common feature of plasma-conductive wall interactions), which is a decisive factor in the vertical alignment of the CNTs [182,183]. As previously reported [185], tilted CNT orientations can be achieved by applying an intense external electric field at an oblique angle to the substrate and introducing a precursor gas parallel to it, which is believed to induce the preferential arrival of charged species along the externally imposed electric field.

In the so-called remote PECVD processes, where the plasma source is outside the deposition zone, the preferential direction of arrival of precursor species moving from the dispenser toward the vacuum outlet has been used to fabricate metal-oxide composite layers consisting of well-separated vertical and tilted nanocolumns, as well as other types of branched nanostructures [186–188]. An example of such a nanostructure is depicted in Fig. 3.2(b), which shows a series of zig-zag Ag@ZnO nanorods created by the plasma deposition of ZnO on substrates with deposited silver nanoparticles. Note that in this experiment, the substrates were tilted to impose a preferential direction of arrival to the precursor molecules. In addition to this geometrical OAD arrangement, plasma sheath effects and the high mobility and reactivity of silver under the action of an oxygen plasma seem critical factors in forming a nanocolumnar microstructure while inhibiting the growth of a compact film that would be expected with conventional PECVD [189].

The possibilities offered by the combination of different plasma types and OAD to tailor the microstructure of thin films and supported nanostructures are practically unexplored, and therefore very much open to new methodological possibilities. A good example of work in this direction is that of Choukourov et al. [190], in which tilted nanocolumnar structures of Ti–C nanocomposites were fabricated by adding hexane to the plasma during the MS-OAD deposition of Ti, altering the composition of the film and its microstructure. A significant number of other interesting examples of the newly coined term "plasma nanotechnology" can be also be found in recent literature on the subject [191].

3.5. OAD of thin films under the impingement of energetic species

In the previous section, it was indicated that in addition to deposition species, other neutral or ionized particles generated in the plasma may interact with the film during its growth, particularly in the case of PECVD, MS and PLD. That is, both the deposition particles and plasma species tend to exchange their energy and momentum with the substrate surface. In early models dealing with the analysis of OAD thin films prepared by evaporation, the influence of particle momentum on the evolution of the film's microstructure was explicitly considered [11], but its effectiveness in controlling the microstructure was not always clear due to the small amount of momentum exchanged in most OAD processes. For instance, in thermal or electron beam evaporation processes, the energy of

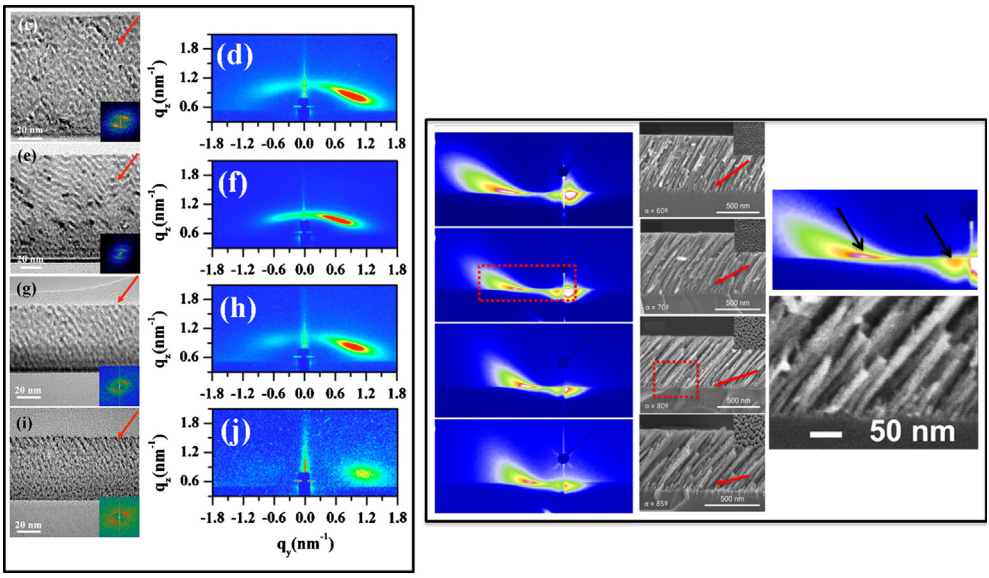

Fig. 3.3. GISAXS and SEM analysis of tilted nanostructures prepared by OAD. (Left) Ni–C composite films prepared by fully ionized vacuum arc and OAD under different conditions, from top to bottom, with a decreasing proportion of Ni and changing from 15 to 30 V of bias voltage during deposition [206]. (Right) OAD TiO_2 thin films prepared by evaporation at zenithal angles ranging from 60° to 85° from top to bottom [48]. For the two families of films, the GISAXS spectra are asymmetric and display well-defined maxima associated with the correlation distances existing in the system. In the OAD evaporated thin films, the GISAXS patterns present two maxima (see the amplified pattern at the right for an example) that have been tentatively associated with two correlation distances, one in the buffer layer (see the magnified SEM image at the right) and another between the well-developed nanocolumns. The red arrows in the SEM micrographs indicate the flux direction. Note that the tilting orientation of the nanostructures with respect to the flow direction is opposite for the evaporated and vacuum arc OAD thin films.

the deposition particles is only in the order of 0.2–0.3 eV, and so its influence on the development of a specific thin-film microstructure and/or crystalline structure can usually be neglected. Yet, in conventional PECVD or MS, the kinetic energy of some species can reach much higher values in the order of a few tens of eV due to ions impinging onto the growing surface, although the overall amount of energy exchanged per deposited species usually stays low enough to not induce any appreciable change in the film nanostructure. This situation changes, however, when the energetic interactions are increased beyond a certain level [36]. In this section, we will address situations in which the arrival of deposition material at the substrate is accompanied by a massive transfer of energy and momentum carried by either the deposition particles themselves, or by rare gas ions and other molecules present in the system. The pronounced transfer of energy and momentum to a surface along an oblique orientation creates significant changes in the microstructure and other characteristics of thin films. Thus, even if the supplied energy contributes to a higher compactness by increasing the mobility of ad-particles [31,184], the film nanostructure may still keep some of the typical characteristics of an OAD film such as morphological asymmetry (i.e., the appearance of a tilted pattern) or a preferentially oriented crystallographic texture. Although a detailed description of the mechanisms involved is far beyond the scope of the present review (readers are instead referred to more specific books or reviews on this subject [32,192,193]), we will provide here some clues for the OAD of thin films prepared by high-power impulse magnetron sputtering (HIPIMS) [31] and ion-assisted deposition (IAD) [32].

3.5.1. High-power impulse magnetron sputtering

This deposition method operates under extremely high power densities in the order of some kW cm^{-2}, with short pulses (impulses) of tens of microseconds and a low duty cycle (on/off time ratio

<10%). Under these conditions, there is a high degree of ionization of sputtered material and a high rate of molecular gas dissociation. The impingement of these charged species and their incorporation onto the growing film also likely contribute to its densification [31], which is the most valuable feature of HIPIMS from an application point of view. Another advantage of this technique is the fact that it offers less line-of-sight restrictions than conventional MS, thus ensuring that small surface features, holes and inhomogeneities are well coated. The combination of high densification, homogenization and conformity are linked to the high energy and momentum of obliquely directed neutral particles and the perpendicular incidence of plasma ions produced in the HIPIMS discharge.[1] This peculiar transport behavior results in a variation in the flux, energy and composition of the species impinging on the substrate as the deposition angle is changed. Specifically, the ion to neutral ratio is generally higher and the average ion energy lower when substrates are placed perpendicular (i.e., in a OAD configuration) to the target than instead of classic parallel configuration [194]. The composition of the deposited films is also modified at oblique angles due to the angular distribution of the neutral species, the ejection of which tends to be favored along the target normal direction. This combination of effects has been utilized in controlling the composition and microstructure of ternary Ti–Si–C films [195], an example of the so-called MAX phases [196] that are characterized by their attractive combination of metallic and ceramic properties.

Although the influence of the deposition angle in combination with other deposition parameters on the microstructure and texture of HIPIMS-deposited thin films has not been systematically investigated, differences between conventional MS and HIPIMS have been observed in the deposition of Cu and Cr films [197,198]. That is, with these two metals, it has been found that the tilt angle of the nanocolumns is lower in HIPIMS-OAD than in conventional MS-OAD. For copper films grown at room temperature, the tilt angle is independent of the vapor flux's degree of ionization, whereas with Cr at elevated temperatures it is affected by ionization. These differences, as well as the changes induced in the crystallographic texture of the films, have been accounted for by a phenomenological model that incorporates atomic shadowing effects during the early nucleation steps [197,198].

3.5.2. Ion-assisted deposition

Ion-beam-assisted deposition is a classic method for producing highly compact thin films through the simultaneous impingement of deposition particles and energetic ions [32]. This term encompasses a large variety of procedures, which vary depending on how the deposition species and ions are produced or the ion energy range. Herein, we will comment only on the effect of low energy ions; i.e., with typical energies in the order of some hundreds of eV or lower. In the first possible scenario under these conditions, thin film growth initially occurs through the aggregation of neutral species, being assisted by ions stemming from an independent source. For the sake of convenience, we shall refer to this as ion-assisted OAD (IA-OAD) [199–204]. In the second case, a thin film is formed by the impingement of a highly or completely ionized flux of deposition species arriving at the substrate along an oblique direction. We will refer to this experimental arrangement ion-beam OAD (IB-OAD) [205,206].

A straightforward application of the IA-OAD method concerns the control of the crystalline texture of the deposited films [199,204]; i.e., the variation of the crystallographic planes of the crystallites with respect to the substrate by changing the impingement angle of the ions. Moreover, as neutral species are produced in IA-OAD by e-beam evaporation, this has been proposed as a method capable of also controlling the film morphology (i.e., the tilt angle of the nanocolumns, areal density, etc.), and possibly also the birefringence of the films [201,202,207–209]. Indeed, it has been demonstrated that the tilt angle of the nanocolumnar structures can be increased in a large set of oxides and fluoride materials [201], and their areal density generally decreased, when the growing films are bombarded with neutralized ions with a kinetic energy of 390 eV. An enhanced surface diffusion of ad-particles due to heating and/or momentum transfer from the accelerated species and/or sputtered particles have been suggested as possible reasons for these morphological variations. However, the large number of parameters involved in these experiments and the factors affecting the physical processes

[1] Plasma ions generally follow the lines of electric field in a plasma.

involved (e.g., the effects of sputtering efficiency [203] and relocation phenomena on the angle of incidence and energy of the impinging ions [210]) have so far prevented any predictive description of tendencies.

The IB-OAD processes, wherein the majority of deposition species are ionized and impinge along a well-defined off-normal angle with respect to the substrate, has not yet been extensively studied. A nice example of the nanostructuration that can be achieved in the vacuum arc deposition of Ni and C, given in Fig. 3.3(a) [206], shows a selection of cross-sectional electron micrographs and GISAXS (glancing incidence small angle X-ray scattering) patterns of this type of thin films. The red arrow indicates the impingement direction of the ionized atoms which, in this experiment, had energies ranging between 20 and 40 eV. These micrographs show that the films are compact and formed from tilted layers or lamellas containing C and Ni. They also show that a decrease in the tilt angle of the layers and a widening of their periodic structure occur when the Ni content and ion energy are increased. These results suggest that, on average, the ion-induced atomic mobilization in the growing film is not random, but instead proceeds preferentially along the direction of momentum of the impinging ions. The importance of momentum and energy transfer is further highlighted by the opposite tilting orientation of the Ni and C lamellas with respect to that of the nanocolumns whenever they grow as a result of surface shadowing mechanisms; e.g., by e-beam or MS OAD. This figure also shows other GISAXS characteristics [211] for tilted nanocolumnar films prepared by e-beam OAD. Although this characterization technique has not yet been extensively used to study OAD thin films, it has been used recently to obtain information regarding the tilting orientation of the nanostructures and the correlation distances from the asymmetry and position of maxima in the GISAXS patterns [33,171,206].

3.6. Microstructure of OAD thin films

In the previous section, we implicitly assumed that the development of tilted and/or sculptured nanostructures is the most typical morphological characteristic of OAD thin films. In this section though, we develop a more detailed discussion of other relevant microstructural features such as roughness, porosity or preferential association of the nanocolumns (a phenomenon usually referred to as *bundling*); features that grant OAD films some of the unique properties required for a large variety of applications. A discussion on the development of specific crystallographic textures will also be presented later in this section. Although most of these characteristics stem from shadowing mechanisms, the contribution of energetic interactions or other random deposition processes outlined previously will also be taken into account as part of this analysis.

3.6.1. Surface roughness and nanocolumn width

The termination of the nanocolumnar features at the surface of a film generates a peculiar topography that is characterized by a high surface roughness. Surface analysis of OAD evaporated thin films by atomic force microscopy (AFM) reveals that the RMS surface roughness increases with the deposition angle (α) and thickness of the films [70,212,213]. This tendency stems from the general finding that the diameter of the nanocolumns increases with their length in a competitive process, wherein the growth of some nanocolumns prevails against that of others; a situation that is shown schematically in Fig. 2.1(c). Depending on film thickness and deposition angle, typical RMS roughness values ranging from 2–3 to 15 nm have been reported for OAD thin films prepared by e-beam evaporation [70,212,213].

The progressive widening of individual nanocolumns with film thickness has been systematically analyzed within the context of the dynamic scaling theory of surface growth [214,215]. This conceptual framework analyzes the evolution of surface patterns and roughness with deposition time (i.e., with thin-film thickness) to give a scaling law of: $w_s \sim t^p$, where w_s is the RMS roughness and p the so-called growth exponent, a parameter whose value depends on the dominant mechanisms governing the film growth. This association between surface roughness and the width of column terminations has prompted many authors to check for the existence of a similar power law correlating nanocolumn width and height; i.e., $w \sim d^{p'}$, where w is the width of the nanocolumn at a certain length, d, with respect to the substrate, and p' is the growth/scaling exponent [22,23,109,216–221].

The validity of this relation has been proven for many metals and oxides, which paved the way for different mechanistic studies of OAD thin film growth. Interesting morphological features, such as a correlation in lengths between nanocolumns or an increase in nanocolumnar diameter, have been related to the scaling parameter [219]. Furthermore, the influence of temperature on the power law has also been recently examined along with the relations between the exponent values and the growth process [220].

A simple power law description of nanocolumn width evolution with film thickness cannot hold true when shadowing is not the prevalent mechanistic factor of growth, as is the case in MS-OAD and other deposition processes discussed in Section 3.5. Thus, crystallization and growth in Zones II or T of SZM clearly preclude any description of the growth mechanism according to simple rational schemes based on dynamic scaling concepts [161]. For example, thin film crystallinity may significantly alter the dependence of roughness on thickness when facetted growth of nanocrystals suddenly occurs. An example of such a sudden modification in surface roughness in relation to crystallinity was reported by Deniz et al. [171] in AlN MS-OAD thin films, where a sharp increase in RMS roughness was found when a given nitrogen concentration was added in the plasma gas.

3.6.2. Correlation distance and bundling association

An initial assessment of the nanocolumnar arrangement in OAD thin films might suggest the absence of any clear organization and a random distribution of nanocolumns within the film. However, some experimental evidence by AFM and SEM analysis of the surface and morphology of thin films directly contradict this simple view [48,219–222]. For example, in the case of evaporated OAD thin films, it has been found that well-defined correlation lengths and intercolumnar distances emerge depending on the deposition conditions. What is more important, these can be formally described with a power law scaling approach [219]. Similarly, through SEM analysis of the surface of a series of OAD thin films, Krause et al. [222] identified repetitive correlation distances between surface voids separating the nanocolumns that were dependent on the deposition parameters. Using AFM, Mukherjee et al. [220] were also able to determine the period of surface roughness features in different OAD thin film materials, and correlated the values obtained with specific growth exponents.

To confirm the existence of correlations between nanocolumns in the interior of films, not just at their surface, we have previously used a bulk technique such as GISAXS [33]. With this method, it is possible to determine both the tilting orientation of the nanocolumns and the correlation distances among them. Fig. 3.3 shows a series of GISAXS patterns corresponding to TiO_2 thin films that were prepared by e-beam OAD at different zenithal angles. We see from this that while the asymmetric shape of the patterns clearly sustains a tilted orientation of the nanocolumns, the position of the maxima in each pattern provides a rather accurate indication of the correlation distances existing in the system [33,48]. It is also interesting that these patterns depict two well-defined maxima, suggesting the existence of a common correlation distance of about 14 nm in all the films, as well as a second much longer correlation distance parameter that progressively increases from 30 to 200 nm with increasing film thickness and deposition angle. We tentatively attributed the smaller of these correlation distances to the repetitive arrangement of small nanocolumns/nuclei in the initial buffer layer formed during the first stages of deposition, with the larger of the two being attributed to the large nanocolumns that develop during film growth. Owing to the bulk penetration of X-rays the values obtained were averaged along the whole thickness of the film, the progressive increase observed with thicker films confirming that the nanocolumn width extends from the interface to the film surface.

In early studies of evaporated OAD thin-film materials [10,11,54,56], it was soon recognized that nanocolumns can associate in the form of *bundles*; i.e., laterally connected groupings of nanocolumns arranged in a direction perpendicular to the vapor flux. This *bundling* association has since been reported in a large variety of OAD thin films prepared by either evaporation or MS [143–145,223–226], and though development of this microstructural arrangement has been mainly reported for metal thin films [10,11,54,56,144,145,223,224], it has also been utilized as a template structure with oxides to develop new composite thin films (see for example [225] and [226]). Surprisingly, aside from some detailed discussions in early reviews [10], this *bundling* phenomenon has not attracted much attention in recent investigations on OAD thin films. In the present review, we therefore

highlight its importance and refer the reader to Section 4, where we present a critical discussion of the growth mechanisms contributing to the development of this microstructural arrangement.

3.6.3. Porosity and adsorption properties

For many applications such as sensors, electrochemistry, catalysis, electrochromism, and antireflective layers, the porous character of an OAD thin film is a key feature in device fabrication (see Section 5). Here, two related concepts need to be taken into account: porosity and effective surface area. The former refers to the actual empty volume that exists within the films, whereas the latter represents the effective area created by the internal surface of these pores that makes possible the interaction with a medium through adsorption. Note that some pores might be occluded, in which case their internal area would not affect the adsorption properties of the films.

Porosity can be assessed in an indirect way by determining the optical constants of thin films, and then deriving the fraction of empty space by means of the effective medium theory [227]. However, as this approach requires relatively complex optical models based on "a-priori" assumptions regarding layer/pore structure and connectivity, its results can only be regarded as approximate at best.

A close relation seems to exist between porosity and the growth mechanisms and conditions. For example, the porosity of a Cu OAD thin film is qualitatively related to its deposition rate and the wetting ability of copper on a silicon substrate, in such a way that the initially formed nuclei control the posterior evolution of the thin film's microstructure and therefore also the final porosity of the film [143]. Modeling the OAD thin film microstructure and growth by Monte Carlo (MC) simulation and other numerical methods has been carried out to better understand the evolution of porosity as a function of the deposition angle [93,228], with Suzuki et al. [62] deducing that evaporated OAD thin films should present a maximum surface area at an evaporation angle of 70°. Interestingly, experiments exploring different adsorptions from the liquid phase have confirmed a maximum surface adsorption capacity at this "magic deposition angle" [63,229–231].

As these past approaches have relied on indirect measurements, calculations or qualitative assessments of porosity or surface area, they have obvious limitations concerning the determination of the true value of pore volume, internal surface area or pore size distribution. The traditional method of analyzing porosity in a powder involves determining the specific surface area through the so-called BET (Brunauer, Emmett and Teller) [232] method, in which the amount of N_2 or other gas/vapor that is adsorbed at its condensation temperature onto the internal surface of open pores is quantified [233]. By assuming a certain effective area for each molecule in the first adsorbed monolayer, it is possible to determine from the amount of adsorbed gas both, the porosity and effective surface area. The extrapolation of this procedure, however, is not straightforward in the case of OAD thin films because of the relatively small amount of material available in the micron-thick or less layers, which hampers the application of conventional BET instruments. To circumvent this limitation, modified adsorption techniques based on the classical BET method have been developed. One of these is a modified volumetric method based on Kr adsorption and a special set up, which was used by Krause et al. [222] to determine the pore volume and pore size distribution of TiO_2 and SiO_2 thin films. In this particular case, the pore volume ratios were found to vary from 20% to 50% depending on the type of material and the deposition geometry. This same method was also used to characterize the porosity of IA-OAD thin films [202], showing that porosity and surface area decrease due to the ion-induced mobilization of ad-particles. We have also developed a volumetric method using a quartz crystal monitor to measure the adsorption of water by the pores in a film [234,235], with which we assessed the porosity of TiO_2 and SiO_2 OAD thin films [48,63]. Analysis of the measured water adsorption isotherms revealed that the overall OAD film porosity is made up of both meso- and micro-pores (according to IUPAC, these terms are applied to pores with throats bigger and smaller than 2 nm, respectively [233]), giving a total porosity of 50–60% relative to the total film volume depending on the thickness and evaporation angle. The partition between micro and mesopores also changed with film thickness and evaporation angle, with approximate volume percentages of 30–50% meso pores to 15–20% micro pores. Thus, as an initial approximation, the meso-pore volume can be related to the intercolumnar space. This is clearly evident in SEM micrographs of OAD thin films, such as those given Figs. 2.1 and 2.2. Assessment of micro-pores is less straightforward, as these must be distributed within the interior of the nanocolumns. Nevertheless, the pore size distribution and surface area of

Table 3.1
Crystalline properties of OAD thin films of different elements and compounds.

Material	Deposition technique	Crystallinity features	Ref.
Al	Evaporation	Highly textured (111) films	[250]
Si	Evaporation	Crystallization suppressed for $\alpha > 40°$	[106]
Co	Evaporation	No preferential orientation	[25,141]
Cu	MS	Tilted (111) orientation for relatively thick films	[251]
	Evaporation	No preferential orientation	[26,144]
	Evaporation	Evolution from a (111) to (200) texture upon azimuthal rotation	[26,144]
	HIPIMS	Highly textured (111) films	[197]
Cr	HIPIMS	Highly textured (110) films, tendency to biaxial orientation	[197]
	MS	(110) to (200) texture change depending on process conditions	[252]
	MS	Highly textured (110) films. Zig-zag films	[67–70,164]
Fe (Fe/Pd bilayers)	Evaporation	Highly textured (110) layers	[253]
Fe	Evaporation	Texture highly dependent on substrate temperature	[53–56]
	Evaporation	(111) textured films. Development of biaxial films with substrate controlled movement	[146]
	Evaporation	Change in preferential texturing from (100) to (111) with pressure. Correlation between (100) and (111) textures with bundling association	[53–56,224]
Co	Evaporation	{0001} crystal habits correlated with bundling association	[223]
Ni	MS	Evolution of preferential texture with temperature from (110) to (111) in the growing direction	[254]
Hf	IBAD	(110), (002) or (100) preferred orientations depending on impingement angle and ion to atom ratio	[204]
Ag	IBAD	(111) and (200) preferred orientations depending on the ion impingement angle	[200]
W	MS	(100) texture by controlled substrate rotation and some biaxial orientation	[152]
	MS	Phase evolution with deposition angle	[218]
Ru	MS	$\{1\,0\,\bar{1}\,0\}$ preferential texturing by OAD and substrate rotation	[156,221,255]
	MS	Different textures developed depending on tilt angle and substrate rotation	[256]
Co–Cu	IBAD	Change of crystalline structure from hcp to fcc by ion beam irradiation	[199]
Co–Cr	Evaporation and MS	*c*-axis oriented along the nanocolumn axis	[257]
Cd–Te	Evaporation	Change from cubic to hexagonal structure depending on zenithal angle	[139]
AlN	MS	Sudden development of a preferential (0002) orientation along the nanocolumn axis with the concentration of N_2 in the plasma gas	[171]
	MS	Variation of *c*-axis (0002) orientation with geometry and other parameters	[165]
CrN	MS	Preferential formation of (001) films on single crystal MgO (001)	[258]
Fe_2O_3	Evaporation	Textured (110) films, effect of temperature	[149]
RuO_2	MS	Crystalline films upon heating	[49]
SnO_2	MS	Crystalline films upon heating	[49]
ITO	VLS	Nanotrees made of single crystals. Biaxial orientation	[136]
ZnO	MS	Highly textured (002) films. Partial loss of preferential texturing with the deposition angle and oxygen in the plasma gas	[169]
ZnO (M)	MS	Loss of (002) preferential texturing with pressure and magnetron power	[168]
	MS	(002) texturing with substrate rotation	[148]
Co-ferrite	PLD	Highly textured (111) films	[177]
YSZ[a]	MS	(100) textured films. Change of zenithal angle by rotation	[89]
	Evaporation	Change from (111) to other textures upon substrate rotation to modify the zenithal angle	[90,91]

[a] Yttria stabilized zirconia thin films obtained by rotating the substrate to change the zenithal angle, as reported in the last row of Table 2.1.

different oxides has been determined by Flaherty et al. [231] using a similar adsorption system consisting of a quartz crystal monitor and different vapors condensed at room temperature. This confirmed that the maximum internal surface area per unit volume occurs when $\alpha = 75^{\circ}$.

An important consequence of the high porosity of OAD thin films of an oxide or other transparent dielectric material is that depending on the environment [227], their optical constants vary in response to the condensation of water in their pores. Thus, unless they are encapsulated, this effect precludes their straightforward incorporation into real-world optical devices [48]. Surprisingly, this effect has been generally overlooked in many works regarding the use of OAD thin films as an antireflective coating or multilayer in solar cells or other related environmental applications [236–238]. On the other hand, the development of humidity sensors takes advantage of this very change in the optical constants of OAD films and multilayers due to the adsorption of water vapor from the atmosphere [78].

Porosity, surface area and chemical adsorption capacity are not homologous concepts. This idea, which is inherent to the field of adsorbents and catalysts, is not common when dealing with OAD thin film devices as only very few works have specifically addressed this issue. Some time ago, Dohnálek et al. [239] made use of a temperature programmed desorption (TPD) technique, very well known in catalysis [240] to study adsorption processes on flat surfaces [241], to examine the adsorption capacity of OAD MgO thin films. They experimentally determined that the fraction of active adsorption sites in these thin films was higher than that of films prepared at normal geometry, and that the distribution of sites with different adsorption binding energies changed with deposition temperature. Unfortunately, no systematic studies involving adsorption processes from the gas phase, together with the subsequent desorption mechanism, have been pursued thereafter.

In the liquid phase of a photonic sensor incorporating dye molecules in transparent OAD thin films (see Section 5.4), we have observed that the pH of the medium greatly modifies the adsorption capacity of cationic or anionic organic molecules from the rhodamine and porphirine families [229,230,242–248]. To account for this pH dependent behavior, we have used the classical zero point of charge concept (*zpc*), which is widely used in colloidal chemistry [249]. According to this, the surface of colloidal oxides becomes either positively or negatively charged depending on whether the surrounding liquid has a pH that is lower or higher than the *zpc* of the investigated material. Thus, by simply adjusting the pH of the solution and the concentration of dissolved molecules, it is possible to control the amount of molecules adsorbed in the OAD thin film or selectively favor the adsorption of one type of molecule over another. Pre-irradiation of the films with UV light to modify their surface properties has been also utilized to control the type and amount of molecules adsorbed from a liquid medium [242]. In the course of these studies, it was also demonstrated that the adsorption equilibrium of tetravalent porphyrin cations in a OAD TiO_2 thin film follows a Langmuir-type isotherm, while the adsorption kinetics adjust to an Elovich model [244]. Undoubtedly, these preliminary studies are insufficient to reach a sound general conclusion, but a tight collaboration between thin film material scientists and colloidal chemists should help to deepen our understanding of the adsorption properties of OAD thin films.

3.7. Texture and crystalline structure of OAD thin films

Crystalline and porous OAD thin films prepared by evaporation are needed for many different applications (e.g., catalysis, photo-catalysis, sensors, etc.) in which a combination of porosity and a well-controlled crystalline structure is essential. Most oxides deposited by e-beam evaporation at room temperature are usually amorphous, but both metals and ceramics become crystalline when their deposition is carried out at sufficiently high temperatures. Furthermore, the crystallization of metals, oxides and other dielectrics deposited in OAD geometries is promoted when using MS, PLD or other techniques that involve the exchange of energy and momentum with the growing film. In most cases, in addition to being crystalline, these thin films present a well-defined texture; i.e., a preferential orientation of the crystallographic planes of their individual crystallites. Both out- and in-plane (i.e. biaxial) preferential orientation may occur in these thin films depending on the deposition conditions. In the case of the former, the crystallites exhibit a preferential orientation with a given crystallographic axis perpendicular to the surface, whereas the other unit cell axes are randomly

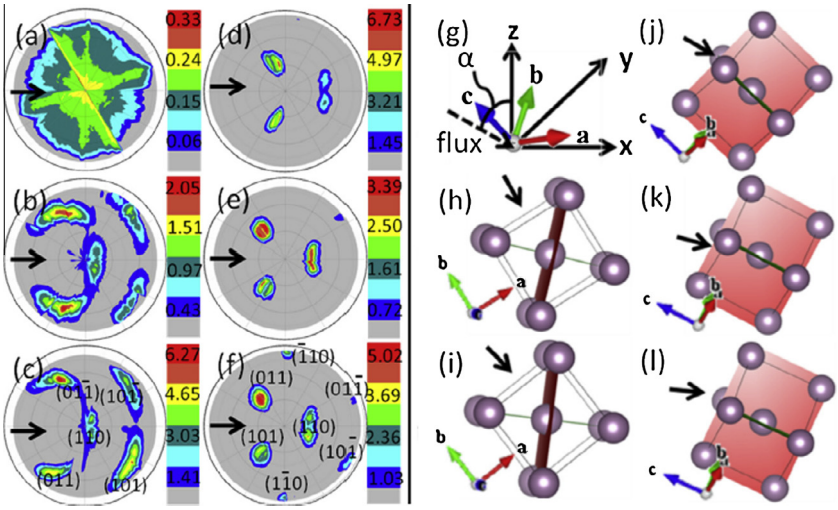

Fig. 3.4. (Right) RHEED surface pole figures of MS-OAD Mo thin films deposited using different zenithal angles: (a) 0°, (b) 45°, (c) 60°, (e) 75°, (f) 85°. The indices for the diffraction poles are labeled in (c) and (f). (Left) Schematic representation of the crystal coordinate (vectors **a**, **b** and **c**) and substrate coordinate (vectors **x**, **y** and **z**) systems. Dashed arrows show the flux direction. Panels (h) to (l) represent the different preferential orientations of the BCC crystallites for the previous polar plots. At 60°, 75°, and 85° the intensity of the poles becomes displaced and more localized, indicating a change from a $(1\,1\,0)[1\,\bar{1}\,0]$ to a well-defined $(1\,1\,1)[1\,1\,\bar{2}]$ biaxial texture. This implies that the orientation of the cubic crystallites experiences a clockwise rotation of 90° when going from (i) to (j) (i.e., vector **c** is rotated toward the plane of the page [151]).

Table 3.2
Summary of biaxially aligned OAD thin films.

Material	Deposition technique	Crystallinity features	Biaxial texture[a]	Ref.
Mg	Evaporation	[0001] direction moves toward the vapor flux when varying the deposition angle	$(1\,0\,\bar{1}\,0)[0\,0\,0\,\bar{1}]$	[23,24,34]
Ge	Evaporation (230–400 °C)	Evolution with temperature from polycrystalline to biaxially oriented. Epitaxial effects	$(001)[1\,1\,0]$	[140]
Cr	MS	Texturing increases with film thickness	$(1\,0\,0)[1\,1\,0]$	[161,166]
Mo	MS	Change of biaxial orientation with deposition angle	$(1\,1\,0)[1\,\bar{1}\,0]$ $\alpha = 45°$ $(1\,1\,1)[1\,1\,\bar{2}\,0]$ $\alpha = 60°$	[151]
Mo	MS flipping rotation of substrate	Different morphologies possible. Continuous variation of α during deposition	$(1\,1\,0)[1\,\bar{1}\,0]$	[92]
W	MS flipping rotation of substrate	Different morphologies possible. Continuous variation of α	$(1\,0\,0)[1\,\bar{1}\,0]$	[152,153]
MgO	MS	Bundling association of crystallites	$(1\,1\,1)[1\,0\,0]$	[166,167]
TiN	MS	Dependence of biaxial orientation on experimental parameters	$(1\,1\,1)[1\,0\,0]$	[159,161]
YSZ	MS	Dependence of biaxial orientation on experimental parameters. Out of plane orientation changes to $(1\,1\,1)$ when increasing the oxygen amount in the system	$(0\,0\,1)[1\,1\,1]$	[159–161]
TiAlN	MS	Biaxial alignment by tilting the substrate. Texturing decreases with temperature	$(2\,0\,0)[1\,1\,1]$	[154,155]

[a] Texturing is represented according to the following convention: parenthesis indicate the family of planes growing parallel to the substrate (out-of-plane direction) and brackets the direction of facets defining the crystallite habits (which generally grow toward the incoming flux of material).

oriented. With the latter, however, individual crystals possess a similar orientation along the direction perpendicular to the plane and parallel to the surface plane. This second situation is similar to that of a single crystal, with the difference being that OAD polycrystalline thin films instead consist of small crystallites with similar orientation. The development of preferential orientations during the OAD of thin films has been the subject of an excellent discussion by Mahieu et al. [160,161], who studied the out-of-plane texturing mechanisms of MS deposited thin films within the context of the extended SZM. According to their description, preferential out-of-plane oriented films are obtained in Zones T and II of SZM when sufficiently high ad-particle mobility leads to a preferential faceting of crystallites along either planes with the lowest growing rate (Zone T) or highest thermodynamic stability (Zone II). As a result, the films become textured with the fastest growth direction perpendicular to the surface. In addition to this out-of-plane orientation mechanism, the growth of biaxial thin films by OAD is favored by the preferential biased diffusion [11] of ad-particles when they arrive at the film surface according to their direction. Obviously, this situation can be controlled by adjusting the orientation of the substrate with respect to the target, in which case this preferential diffusion can be used to ensure grain growth in the direction of the most favorable faceted crystal habit facing the incoming flux of material. From a mechanistic point of view, both the mobility of ad-particles during growth and the angular distribution of the incoming material flux are critical for the effective growth of biaxially aligned thin films; the particles mobility favoring biaxial alignment and their angular spread contributing to its randomization. Consequently, parameters such as pressure, target–substrate distance, deposition angle, film thickness, bias potential of the substrate, temperature and the presence of impurities may play an important role in determining the degree of biaxial orientation.

This strong dependence that the crystalline structure of OAD thin films has on the experimental parameters means that although some trends in texture can be predicted [11,161], significant deviations associated with the use of different deposition conditions and/or techniques (e.g., conventional MS, pulsed MS, HIPIMS, temperature of substrate, bias, etc.) should be expected. A selection of crystalline OAD thin films is presented in Table 3.1 to highlight the specific features of their crystallographic structure. This gathered data broadly confirms that crystallization occurs when thin films are grown within Zone T and II of the SZM; i.e., in evaporated films prepared at high temperatures, or by using MS or other techniques that involve ion bombardment during deposition (e.g., IA-OAD).

Biaxially oriented thin films are of the utmost interest for many applications, for example the synthesis of oriented high-temperature thin-film superconductors [259], magnetic-oriented systems [260], coatings for mechanical applications [261], or controlling the heat transport properties of a surface [262]. To determine the texture of such films, particularly their biaxial orientation, polar X-ray diffraction analyses and, more recently, reflection high-energy electron diffraction electron diffraction (RHEED) techniques [34,263] are typically employed. With the first of these methods the retrieved information that stems from the bulk of the film, whereas in the second, it comes from the outermost surface layers. As an example of the possibilities of this latter technique, Fig. 3.4 shows selected RHEED pole diagrams illustrating the evolution of biaxial texturing during the MS-OAD of Mo (the morphology of the same film is shown in Fig. 3.1) [151]. It is apparent from this figure that the pole diagrams change with deposition angle, revealing the development of a $(1\,1\,0)[1\,\bar{1}\,0]$ biaxial texture when $\alpha > 30^{\circ}$ (note that Mo has a cubic structure), in which the [1 1 0] axis is oriented along the out-of-plane perpendicular direction and the $[1\,\bar{1}\,0]$ axis is along an in-plane direction. The sharpening of the pole patterns for $\alpha = 45^{\circ}$, and the appearance of new poles for $\alpha > 60^{\circ}$, sustain the development of a new texture when the deposition angle increases. The representation on the right-hand side of this figure describes the nature of these textural changes, while additional explanations are provided in the figure caption.

Table 3.2 summarizes some select examples of biaxial thin films prepared by OAD. Most of these were prepared by MS, though the two metals prepared by evaporation have either a low melting point (e.g., Mg) or are the product of thermally activated synthesis. This confirms the need to identify experimental conditions that favor the controlled diffusion of ad-particles during film growth to ensure effective control over the texture of the thin film. Another point worth noting from this table is the possibility of changing the facet termination of the individual crystallites by changing the deposition angle (e.g., Mg, Mo), and the fact that the selection of specific OAD conditions is generally

critical to the development of a given biaxial orientation. In some cases, the clear prevalence of a given orientation confirms the importance of the energetic factors related to the development of a given crystallite facet for the control of texture. Thus, epitaxial effects (e.g., Ge) and the influence of substrate roughness or film thickness in effectively controlling the texture confirm that mechanistic conditions mediating ad-particle diffusion are quite important to controlling the biaxial orientation. The *bundling* association of crystallites (e.g., MgO) is another interesting feature present in some biaxially OAD thin films.

4. New concepts for process-control in oblique angle depositions: simulations and experiments

In this section we deal with the fundamentals of OAD by discussing them from an atomistic point of view. Rather than a critical enumeration of previously reported models, we have focused this discussion on a set of new concepts that provide an updated conceptual framework for understanding the growth process by e-beam evaporation and MS at oblique angles. For a better assessment, these concepts have been explained using classical models which, using mainly geometrical considerations, have been previously proposed to describe the basic growth mechanisms of this type of films. In this regard, numerous works and review papers have already dealt with both, the phenomenology and key theoretical issues involved in the OAD of thin films by different deposition techniques [10,11,14,264]. The terms 'simulations' and 'experiments', which were intentionally included in the title of this section, underline the importance of a combined approach when dealing with complex atomistic phenomena such as those involved in the OAD of thin films. From a fundamental perspective, a key model in this section is the SZM that was already mentioned in Sections 2 and 3 [35–37,142]. Despite its phenomenological basis, it provides valuable information on the competition between surface shadowing mechanisms and thermally activated diffusion, which is useful for introducing simplified assumptions in growth models under various conditions [265].

This section is organized into two well differentiated parts. In the first of these we address the problem of e-beam evaporation and consider the deposition of particles through a purely ballistic model; i.e., we assume that there is no significant scattering of particles in the gaseous phase during their flight from the source to substrate, and that the shadowing mechanism is the predominant nanostructuration process. In the second we explicitly address MS deposition, in which scattering interactions in the gaseous/plasma phase are considered so as to understand how they may affect the microstructure of the film.

4.1. Methods to model the shadowing-dominated growth of thin films

When dominated by surface shadowing mechanisms, the aggregation of vapor particles onto a surface is a complex, non-local phenomenon. In the literature, there have been many attempts to analyze the growth mechanism by means of pure geometrical considerations; i.e., by assuming that vapor particles arrive at the film surface along a single angular direction [38,41]. Continuum approaches, which are based on the fact that the geometrical features of the film (i.e., the nanocolumns) are much larger than the typical size of an atom [42,266,267], have been also explored. For instance, Poxson et al. [228] developed an analytic model that takes into account geometrical factors as well as surface diffusion. This model accurately predicted the porosity and deposition rate of thin films using a single input parameter related to the cross-sectional area of the nanocolumns, the volume of material and the thickness of the film. Moreover, in Ref. [39], an analytical semi-empirical model was presented to quantitatively describe the aggregation of columnar structures by means of a single parameter dubbed the fan angle. This material-dependent quantity can be experimentally obtained by performing deposition at normal incidence on an imprinted groove seeded substrate, and then measuring the increase in column diameter with film thickness. This model was tested under various conditions [40], which returned good results and an accurate prediction of the relation between the incident angle of the deposition flux and the tilt angle of the columns for several materials.

Semi-empirical or analytical approaches have provided relevant information regarding film nanostructuration mechanisms; however, molecular dynamics (MD) [14] and MC [62,120,268]

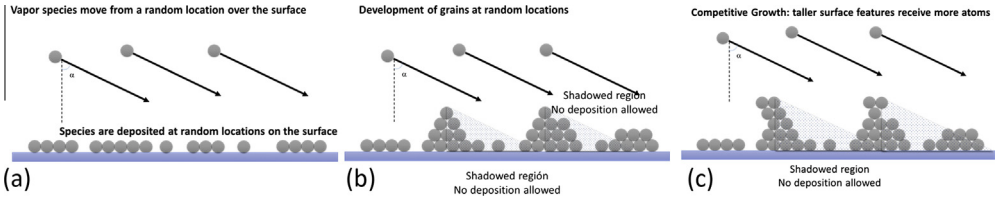

Fig. 4.1. First stages of growth during the OAD of thin films. (a) Individual vapor species arrive at random locations on the surface with a given tilt angle. (b) Deposited particles accumulate within certain regions in the form of grains of material that then cast shadows over other surface zones where vapor species cannot be deposited. (c) Taller surface features are more likely to grow, initiating a competitive growth process in which the taller a feature is the larger its shadow, thus forming tilted columnar structures.

methods have provided further insights into the growth dynamics from atomistic and fundamental points of view. The MD approach considers the incorporation of single species onto a film one by one, describing in detail the trajectory of each particle by means of effective particle–surface interaction potentials. Unfortunately, given the computational power presently available, this procedure only allows simulations over time scales in the order of microseconds, even with hyperdynamic techniques [269]. Since real experiments usually involve periods of minutes or even longer, this constraint represents a clear disadvantage when comparing simulations to experimental data. In this way, two-dimensional MD simulations carried out [270] with the intent of investigating the role of substrate temperature, the kinetic energy of deposition particles and the angle of incidence on the film morphology predicts that increasing substrate temperature and incident kinetic energy should inhibit the formation of voids within the film and promote the formation of a smooth and dense surface. Moreover, it was also found that increasing angles of incidence promote the appearance of tilted, aligned voids that ultimately result in the development of columnar nanostructures. In contrast to MD techniques, MC models approach the problem from a different perspective by allowing the analysis over longer time and space scales. In this case, MD simulations are employed to describe the efficiency of different single-atom processes using probabilities, which are then subsequently put together. Although this strategy accelerates by some orders of magnitude the simulation time, except in the case of athermal processes [212]), ad-atom diffusion must be excluded from the calculations to obtain a realistic simulation of the growth of a thick thin film. This means that MC simulations of the deposition process are suitable to conditions within Zone I of the SZM, which is where the preparation of the majority of evaporated OAD thin films takes place. Nevertheless, since thermal activation may also be involved in thin film growth [11,60,271], and may have certain influence on the nanostructural evolution of the films, this activation has been explicitly considered in some MC simulations of up to a few hundred monolayers of material. For example, a three-dimensional atomistic simulation of film deposition [272], which included the relevant thermally activated processes, was developed to explain the growth of an aluminum thin film onto trenches. In another work, Yang et al. [273] employed a two-step simulation wherein arriving species are first placed at the landing location point, with a kinetic MC then describing their subsequent diffusion. Want and Clancy [274] included the dependence of atom sticking probabilities on temperature to describe the deposition process, whereas Karabacak et al. [22] considered the ad-atom thermally activated mobility by introducing a fixed number of ad-atom diffusion jumps onto the surface following deposition.

When only surface shadowing is considered in the simulations, a classical MC model with cubic geometry proceeds in the following way: punctual deposition species are thrown onto a two-dimensional substrate that defines the x–y coordinate plane, with the z-axis being defined by the direction perpendicular to it. The three-dimensional space is then divided into a $N_L \times N_L \times N_H$ grid, in which cells are assigned a value of 1 if they contain a deposited species, or are otherwise given a value of 0. A cell with a typical size in the order of the distance between atoms in the material represents a species in the network. From an initial random position above the film, each deposition particle is thrown toward the substrate following a direction defined by the spherical angles θ' and φ', where

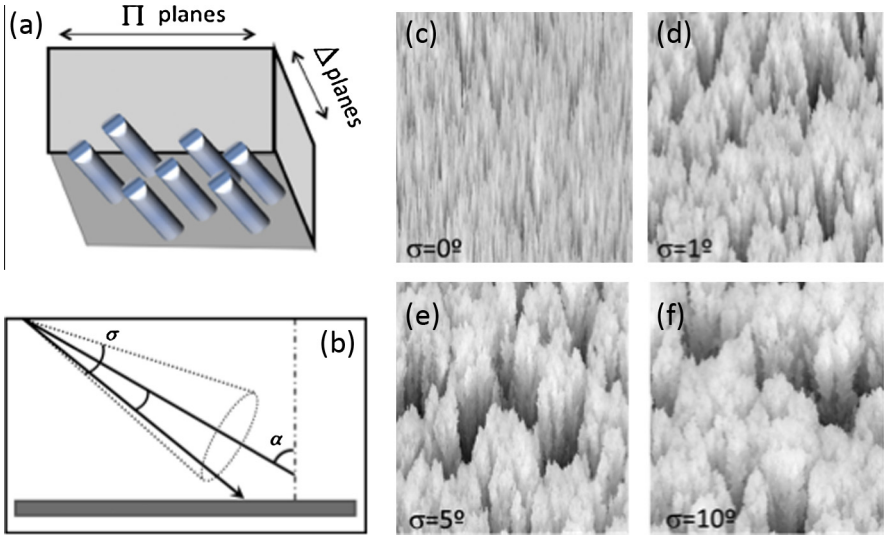

Fig. 4.2. (a) Definition of the **Δ** and **Π** planes. (b) Angular broadening of the deposition flux indicating that vapor species arrive at the surface following a Gaussian incident angle distribution function with a mean value of α and a dispersion angle of σ. (c) Top view of a simulated thin film, in which it is assumed that vapor species start moving from a random location and approach the surface along a single direction defined by $\alpha = 80°$. This simulated surface shows no trace of 3D nanocolumns, even though the cross-sectional view indicates the presence of 2D tilted features. The formation of 3D nanocolumns is inhibited because each slice of material in the **Π** plane is independent. (d–f) Same as (c), but with σ set to (d) 1°, (e) 5° or (f) 10°.

$\theta' \in [0,\ \pi/2)$ is the polar angle of incidence ($\theta' = 0$ is the direction normal to the substrate) and $\varphi' \in [0,\ 2\pi)$ is the azimuthal angle. By assuming periodic boundary conditions for the system, particle movement proceeds along a straight line until it hits the surface at a given location, where it then sticks (ballistic approach). For each deposition particle, the angles θ' and φ' are randomly calculated by defining an incident angle distribution function per unit time and unit surface, $I(\Omega)$, where $d\Omega = \sin\theta'\, d\theta' d\varphi'$ and represents a differential solid angle.

The procedure hitherto described represents a very simple approach to simulating thin film growth under general conditions, a quite complex process in which other mechanisms may be also present. A brief summary of these additional issues are:

- Incoming vapor species may interact with the surface and not follow a straight trajectory, thus other processes resulting from the proximity of the vapor species to the surface should be introduced. As will be described later in this section (Section 4.2.1), this is straightforwardly connected to so-called surface trapping mechanisms.
- Although most OAD films analyzed had been synthesized under conditions pertaining to Zone I of the SZM model, thermally activated processes may also influence the film nanostructure to some extent [11].
- Vapor species arriving at a landing location may carry enough energy to move or induce additional displacements in the material's network. As we will see later, this is relevant in MS depositions where the vapor species may possess hyperthermal energies.
- When the plasma interacts with the film, there are numerous energetic species that may affect the film nanostructuration; e.g., plasma ions or neutral species in excited states [275,276].
- High growth temperatures may promote the crystallization of the film and the appearance of surface potentials that favor atomic displacements along preferential directions/planes of the network.

The full analysis of these processes is an active research area, and the study of their combined effect on the film nanostructuration is an open field of investigation. In the following sections we discuss

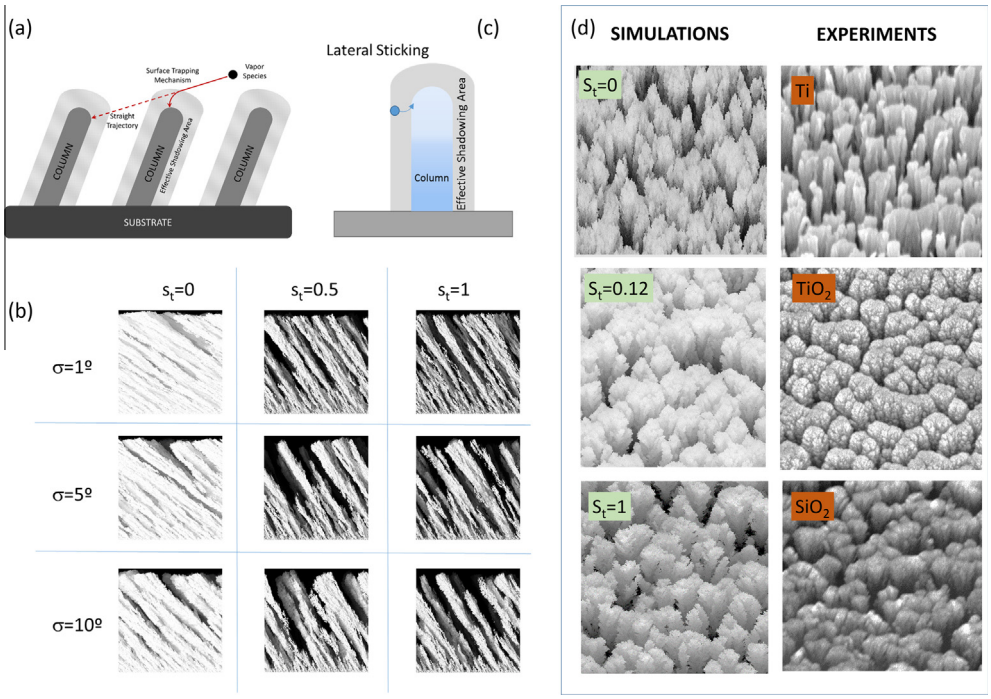

Fig. 4.3. (a) Illustration of the surface trapping mechanism, which unlike typical ballistic models where vapor species follow straight trajectories, introduces the possibility that trajectories may bend within an effective shadowing region. (b) Cross sectional views of simulated films for different values of σ and s_t [282]. (c) Representation of the lateral sticking process implicit in the trapping mechanism. (d) Simulated and SEM top views of different thin films. Simulations were made with the software package STRONG [281].

some of the previous mechanisms by considering the results of some fundamental experiments carried out under simplified conditions to highlight the influence of a particular process.

4.2. Evaporation at oblique angles under ballistic conditions

From a conceptual point of view, the sublimation of a given material in a vacuum reactor, and the subsequent condensation of gaseous species on a solid surface, is a simpler problem than those encountered in PECVD or reactive MS techniques, where a strong interaction between deposition and plasma species may occur during the travel of the former from the material source to the substrate (some specific interactions involved during the MS-OAD of thin films will be addressed in Section 4.3). As mentioned in previous sections, a general picture of the OAD growth at low temperatures only considers a purely ballistic approach; i.e., vapor species arrive at the film surface along straight, oblique trajectories and remain at the landing location, giving rise to a tilted columnar nanostructure [277]. Fig. 4.1(a)–(c) schematically describes the first stages of growth that are believed to occur during the oblique arrival of ad-atoms. In the first stage (Fig. 4.1(a)), individual vapor species arrive at random locations on the surface along a tilted direction, which is defined by the angle α. In the second stage (Fig. 4.1(b)), the deposited particles accumulate within certain regions in the form of grains, which then cast "shadows" behind them, preventing other particles from depositing. Through this shadowing effect, taller surface features are more likely to grow through the incorporation of new particles, whereas regions lower in height will scarcely develop due to the "shadow" cast by the former (see Fig. 4.1(c)). This selective growth of taller surface features introduces a competitive process whereby the taller a feature, the larger its shadow, which ultimately results in the formation

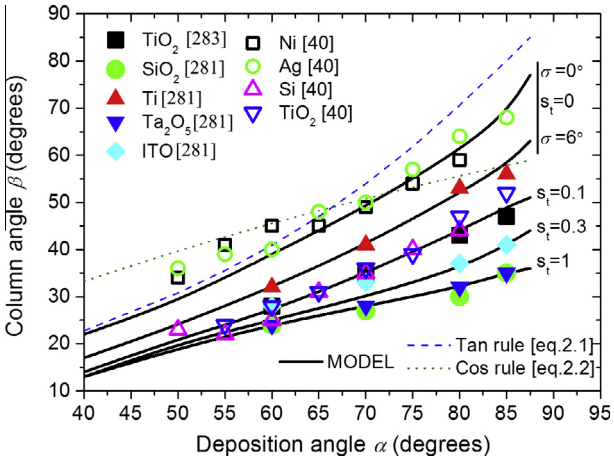

Fig. 4.4. Results of the surface trapping model for different values of s_t and σ, together with experimental data for different materials. Trends predicted by the tangent rule (Eq. (2.1)) and cosine rule (Eq. (2.2)) are also depicted [280].

of tilted columnar structures [43,278,279]. Karabacak et al. [217] introduced the so-called *shadowing length* to describe nanocolumnar growth: a parameter that plays a similar role as the diffusion length during the conventional development of island growth morphologies. As we will see later in this section, the shadowing length concept has been extended to three-dimensional growth by introducing a *shadowing region* and, more recently, an *effective shadowing region*.

In general, the low kinetic energy of a vapor species that lands on the surface (the energy of evaporated atoms is around 0.2 eV) ensures that no kinetic energy-induced processes are likely to take place when using the evaporation technique. Furthermore, the competitive growth that gives rise to a tilted columnar nanostructure is directly dependent on the angle at which the vapor species arrives [228]. The connection between the value of α and the tilt angle of the columns, β, is of outmost importance to controlling the film's properties [39,41,44], and has been roughly described by means of the heuristic tangent rule [11] (Eq. (2.1)). In most cases, this rule accurately describes the relation between both angles when $\alpha \leqslant 60^\circ$ [270]. More recently, Tait et al. [38] proposed the so-called cosine rule (Eq. (2.2)), which succeeds in describing the relation between both angles for some materials, but fails with others. Indeed, one of the main problems posed by these two equations is the implicit assumption that the relation between both angles is purely geometric, and therefore leaves aside any material- or experimental reactor-dependent influence. Based on recently published results [280–282], we describe in the next section how these factors influence the nanocolumnar evolution of OAD thin films prepared by evaporation

4.2.1. Nanocolumn tilt angle and the surface trapping mechanism

One of the most common misconceptions when considering the OAD growth of evaporated thin films lies in the idea that particles arriving at the substrate *along a single angular direction*, α, give rise to three-dimensional columnar structures. In Fig. 4.2(c) we see a top view of a film surface that was simulated by assuming a unique angle of incidence for the vapor species, $\alpha = 80^\circ$, from which it is clear that this condition would never give rise to volumetric three-dimensional columnar structures. This is attributed to a lack of correlation among Π planes (see Fig. 4.2(a) for its definition), meaning that each slice of material parallel to the Π plane is independent of the one that follows, which precludes the formation of columnar, cylindrical structures. This implies that the classical description presented in Fig. 4.1(a)–(c) corresponds to a two-dimensional model, in which the tilted structures do not develop in three dimensions. Actually, in real experiments, it is most likely that the evaporation source is non-punctual and that some unlikely collisions may take place among vapor species. These, and other experimental effects, may slightly broaden the angular distribution of evaporated particles

along the nominal direction defined by the α angle. In Refs. [280,282], the effect of this broadening on the microstructure of a thin film was studied by assuming that the distribution of momentum amongst species in the gaseous phase was Gaussian (see Fig. 4.2(b)), with a mean value of α and a variance of σ. As it is seen in Fig. 2.4(d), a slight broadening of the momentum flux when $\sigma = 1^\circ$ is enough to induce the formation of a tilted three-dimensional columnar volumetric structure. The influence of σ on the film microstructure is also evident in Fig. 4.2(d)–(f), where higher values of σ can be seen to produce an increase in the diameter of individual nanocolumns. However, this experimental parameter alone cannot explain the different tilt angle of the nanocolumnar structures found with different deposited materials.

According to Refs. [280,282], an atomistic process called the *surface trapping mechanism* can account for the existence of short-range interactions between vapor species and the growing film surface, which is a classical phenomenon that has been discussed in the literature for decades [120]. In contrast with typical ballistic models of thin film growth, where evaporated species in the gaseous phase are assumed to follow straight trajectories [215], the *surface trapping mechanism* considers that vapor species passing within a few angstroms from the surface may deviate in their trajectory and deposit at a nearby location (see Fig. 4.3(a)). A way of accounting for the interaction potential between vapor species and the film surface is by defining the *surface trapping probability*, s_t, according to the following rules:

(i) when a vapor species impinges head-on onto the surface, its probability of sticking at that location is 1, and
(ii) when a vapor species moves over the surface at a distance of less than 4–5 Å, its probability of sticking at that position is s_t.[2]

The trapping probability concept should not be confused with the sticking probability, which accounts for the overall probability of a particle to be deposited onto a surface regardless of its particular location. Furthermore, most studies into particle sticking on surfaces have only considered a perpendicular incidence and therefore only accounted for head-on sticking processes [215].

From a physical point of view, the trajectories of species in the vapor phase near the surface should depend on the interaction potential between them (chemical nature, distance, etc.), as well as their relative velocity. Typical van der Waals and electrostatic attractive forces mostly operate within distances of a few angstroms, which is in line with the assumptions of the *surface trapping mechanism*. Thus, the low kinetic energy of vapor species under typical evaporation conditions and the oblique incidence geometry should favor trapping, as under these conditions, particles would move longer distances in the vicinity of the surface before landing. The value of s_t would therefore depend on the chemical nature of both, the interacting species and the surface; i.e., on the chemical nature of the sublimated material.

Simulations of the influence of σ and s_t on the columnar microstructure of a thin film are presented in Fig. 4.3(b), while the effect of σ and s_t on the tilt angle of the nanocolumns as a function of α is shown in Fig. 4.4, along with the trends derived by applying the tangent and cosine rules. Since the simulation results for $s_t \geqslant 0.1$ are weakly dependent on the particular value of σ, results for $\sigma = 6^\circ$ are presented. Meanwhile, for $s_t = 0$, calculation results are presented for both $\sigma = 0^\circ$ and $\sigma = 6^\circ$. Overall, it is found that the higher the value of s_t, the less tilted the columns are. This tendency supports the notion that surface trapping effectively modifies the geometrical shadowing mechanism, which must now be described through an *effective shadowing area* (see Fig. 4.3(a)). This concept describes the actual region around the surface features of the film that are able to trap flying vapor species, and in doing so, cast a shadow over the surface. It is worth noting in Fig. 4.3(b) that the model results seem to follow the tangent rule when $\alpha \leqslant 60^\circ$, a coincidence which indicates that the *surface trapping mechanism* is not relevant at low incident angles, but rather only introduces important deviations with respect to a pure geometrical model at high incident angles.

[2] Note that the trapping probability, s_t, is introduced per next neighbor. That is, if the vapor atoms encounter N next neighbors at a given position, the trapping probability is $1 - (1 - s_t)^N$.

Further confirmation of the existence of an *effective shadowing area* is provided by the results presented in Fig. 4.4. This plot shows a series of experimental and simulated values of β as a function of α for TiO_2, SiO_2, Ta_2O_5, ITO and Ti (all grown using the same experimental setup at low temperature), and for Ni, Al, Si and TiO_2 (also grown at low temperature, but in a different reactor) [40]. The good concordance evident between the experimental values of β for any given material and the simulations for a given value of s_t indicates that this parameter only depends on the chemical nature of the sublimated material and the composition of the film. The results for the TiO_2 and Ti thin films are well described by the pairs of values $s_t = 0.1$ and $\sigma = 6^\circ$, and $s_t = 0$ and $\sigma = 6^\circ$, respectively, with the common value of $\sigma = 6^\circ$ suggesting that the angular broadening of the deposition flux only depends on the characteristics of the deposition setup (geometry of the reactor, operating pressure, size of the source, etc.). Further discussion regarding the effect of these two parameters on the tilt angle of the nanocolumns for thin films of other materials has been published previously in Refs. [280–282].

4.2.2. Surface area, roughness and bundling association of nanocolumns in OAD films

In Section 3, we mentioned that the actual surface area of the films, their roughness and accessible pore volume are all relevant microstructural quantities for the use of OAD films in different applications. Substantial simulation work has therefore been devoted to predicting the most appropriate experimental conditions required to maximize the actual surface area of OAD thin films [283]. With this in mind, Suzuki et al. [62] used a three-dimensional MC model to show that films grown at $\alpha \sim 70^\circ$ have the maximum surface area. This prediction agrees with the efficiency results of dye-sensitized solar cells and the performance of other devices [48,63,284,285], wherein it was found that the maximum yield of films deposited with $\alpha \sim 70^\circ$ was justified by their maximum adsorption capability [222].

The surface roughness of OAD thin films is another relevant microstructural feature that is associated with the termination profile of nanocolumns at the film surface. The evolution of both the nanocolumn width and surface roughness as a function of the thin film thickness has been theoretically analyzed within the premise of the Dynamic Scaling Theory (see Section 3.6.1) [215]. This framework has been widely utilized to model the growth of a large variety of thin films, and has made it possible to correlate some empirically determined critical exponents with the mechanisms involved. For example, the width of nanocolumns, w, as a function of column length, d, has been found to follow a power law dependence $w \sim d^{p'}$, where p' is the so-called growth exponent [22]. In the same paper, a MC model was used to prove that if surface shadowing dominates the growth, then the value of this exponent is $p' = 0.5$, while it drops to a lower value when surface diffusion plays a relevant role [220]. The tight correlation between the growth exponent and the shadowing mechanism was further demonstrated by Buzea [219] for Si thin films prepared by dynamic OAD. This author showed that the value of p' strongly depends on the tilt angle of the vapor flux, and that it directly controls the distance between nanocolumns.

The evolution of the surface roughness, w_s, of OAD thin films has also been analyzed under similar premises, and found to generally follow the power law [215]:

$$w_s(L) \sim \begin{cases} w_{sat}, & \text{if } L \gg L_{crossover} \\ L^{\gamma}, & \text{if } L \ll L_{crossover} \end{cases}, \tag{4.1}$$

where L is the linear size of the substrate on which the film grows, $L_{crossover}$ is the length at which saturation of the roughness, w_{sat}, occurs and γ is the roughness exponent used to describes surface roughness evolution at small scales of length. In addition, w_{sat} fulfills the law $w_{sat} - w_{sat}(0) \sim \alpha^{\kappa}$, where $w_{sat}(0)$ is the surface roughness of a reference film grown with $\alpha = 0^\circ$ and κ is the saturated roughness exponent. In Ref. [286], it was found that the roughness of OAD thin films of Ti grown by evaporation can be described by the exponent $\kappa = 7.1 \pm 0.2$, which agrees well with the value of $\kappa = 6.7 \pm 0.4$ that was determined by three-dimensional MD calculation [216].

In Section 3.6.2, we presented the relevant effects encountered during the OAD of thin films in relation with the anisotropic coalescence of nanocolumns into bundles. However, despite the relevance of this to numerous applications, no systematic analysis of the meso-scale development of this bundle association has yet been carried out [82,287]. Herein, we would like to address how

the trapping mechanism already presented in Section 4.2.1 in connection with the tilt angle of the nanocolumns may also account for the formation of bundles. Fig. 4.3(c) illustrates how the trapping process also occurs with vapor species passing laterally near a growing nanocolumn. A consequence of this preferential trapping would be a faster lateral growth of nanostructures in the direction perpendicular to the vapor flux, ultimately provoking columnar coalescence along this same direction. To prove this hypothesis, Fig. 4.3(d) shows three simulations of equally-thick thin films grown under the assumption of an angular broadening of 6° and trapping probabilities, s_t, of 0, 0.12 and 1. When $s_t = 0$, the columns are small in diameter and grow separately, creating a homogeneous distribution over the substrate. With higher trapping probabilities, the column diameter increases and the nanocolumns merge in the direction perpendicular to that of the vapor flux, leaving elongated gaps among these 'columnar fronts'. These simulations are compared with selected scanning electron microscopy images of Ti, TiO_2 and SiO_2 thin films created under the conditions defined in Fig. 4.4.[3] The concordance between the experimental data and simulations demonstrates that at least in the case of the three materials investigated, the trapping mechanism is a reasonable hypothesis to explain the different tendency for bundle formation exhibited by the thin films of this series. Furthermore, even though this analysis is restricted to a limited set of materials, it is believed that this semi-quantitative justification of bundling formation provides an indication of its general character, and will be further validated by additional studies. The challenges that clearly need to be faced here, however, are to perform first principles calculation of the trapping probability for a given evaporated material, or achieve experimental control of the angular broadening of the evaporated material. There is also a clear need for new paradigms in relation to the quantitative analysis of other processes, such as thermally activated diffusion during growth at high temperatures [288], as well as the existence of anisotropic surface potentials associated with crystallization rearrangements.

4.3. Magnetron sputtering deposition at oblique angles

Numerous works in the literature have dealt with the fundamentals of MS deposition at normal incidence [289–295]. From this, it is known that classical MS depositions, in which the growth surface is parallel to the target, usually yield dense and compact films, thanks mostly to the high energy of the deposition particles and the impingement of plasma ions during growth [296,297]. In contrast, when deposition is carried out in an OAD configuration, other processes may play important roles in the development of columnar and porous nanostructures [212].

The main challenges facing the MS deposition of thin films center around the control over the chemical composition of the layers, the deposition rate and the film nanostructure. There are many excellent reviews dealing with the first two issues when working under a normal configuration [298,299], but the third has only been scarcely addressed, even under simplified conditions. In this section, we will focus on some of the mechanistic aspects that are important to account for the MS-OAD of thin films in connection with the development of a columnar nanostructure. For this analysis, we have avoided the use of complex models for the transport of sputtered particles inside the plasma, and have instead employed a simplified approach based on effective thermalizing collision (ETC) theory [47,130,300,301]. This has already provided numerous results and straightforwardly applicable mathematical formulae pertaining to the deposition rate and final microstructure of MS thin films.

In the following subsection, we analyze the main differences between evaporation and MS in terms of atomistic processes. Following this, we briefly describe the mechanism of sputtering and explain the transport of sputtered particles by means of ETC theory. This theory will then be employed to deduce a formula that describes the deposition rate at oblique angles. Finally, the influence of deposition conditions on the films' morphology is described.

4.3.1. MS-OAD of thin films versus evaporation

When comparing evaporation and MS techniques, the following key differences become apparent:

[3] Note that the values of s_t agree with those reproducing the tilt angle of the nanocolumns in Fig. 4.4 for Ti, TiO_2 and SiO_2.

- *Plasma-generated species in contact with the film during growth*: In MS-OAD deposition, the plasma contains numerous energetic species such as positive or negative ions, or highly reactive species that may impinge on the film during growth and affect its nanostructure and chemical composition [293,302].
- *Size of the material source:* Under typical e-beam evaporation conditions, the material is sublimated from pellets situated very far away from the film (1 m or more). In MS deposition, the size of the source (target) is within the same order of magnitude as the target/film distance. Thus, the deposition particles stem from a wide area racetrack, meaning that the deposition angle is not fixed but rather varies over a relatively large interval (see Fig. 2.2(b)).
- *Kinetic energy of vapor atoms*: In MS, the mean kinetic energy of sputtered particles is in the order of 5–10 eV, whereas under typical evaporation conditions it is in the order of 0.2–0.3 eV. Since the typical energy threshold required to mobilize atoms deposited on the surface is $\sim$5 eV, the impingement of vapor atoms onto the film may cause the rearrangement of already deposited species [212,303–305].
- *Collisional processes in the vapor phase*: The working pressures in MS are much higher than in typical e-beam evaporations, where the mean free path of evaporated species is typically greater than the source/substrate distance. In contrast, the pressure in MS can be varied within a relatively broad interval, meaning that sputtered particles can experience a large number of collisions before their deposition [162]. These collisions have a direct impact on the kinetic energy and momentum distribution (including the direction of arrival) of the sputtered particles when they eventually reach the film surface [302,306–308].

All these differences are of great relevance for the control of fundamental atomistic processes involved in the growth of a thin film, and make the previously introduced *surface trapping* probability and angular broadening concept insufficient to describe the nanostructural development of MS-OAD thin films.

4.3.2. Sputtering and transport of sputtered particles in plasma

The sputtering of atoms in MS is caused by positive ions of the plasma, which are accelerated toward the target within the plasma sheath [289]. These ion–solid interactions are complex, and as such have been the subject of study over many decades [32]. For the purposes of this review on OAD, the quantities of interest have been limited to the so-called *sputtering yield* and the *energy distribution of sputtered particles*. The former takes into account the number of ions ejected from the target surface per ion arriving, whereas the latter function determines the energy and angular distribution of ejection. Based on standard binary collision approaches [309], the sputtered particle distribution at the target can be calculated to be proportional to $E(E+U)^{-3}\cos\xi$, where E is the kinetic energy, U the solid target binding energy and ξ the ejection angle. Thus, sputtered atoms preferentially leave the target along a direction perpendicular to the surface with an average energy of around $U/2$; i.e., an energy much higher than the thermal energy of gaseous species inside the reactor.

Even if the sputtered atoms leave the target with energies in the order of 5–10 eV and a high preferential directionality, collisional processes with (predominantly) neutral species of the plasma gas may drastically alter both the energy distribution function and the directionality of the particles when they reach the substrate. Sputtered particles arriving at the film surface can be broadly separated into three categories depending upon their collisional transport: (i) particles that have not collided with any gas atoms and arrive at the film surface with their original kinetic energy and direction, (ii) those that have experienced a large number of collisions with background plasma/gas atoms and therefore possess low (thermal) energy and an isotropic momentum distribution, and finally, (iii) those that have undergone several collisions, but still possess significant kinetic energy and some preferential directionality. This transport has been thoroughly studied in the literature by means of MC models of gas phase dynamics using different elastic scattering cross-sections to determine the energy and momentum transfer in each collision [162]. However, the complexity of the mechanisms involved makes it difficult to find analytical relations between quantities of interest and experimentally controllable parameters. With the aim of simplifying the description and deducting general analytic

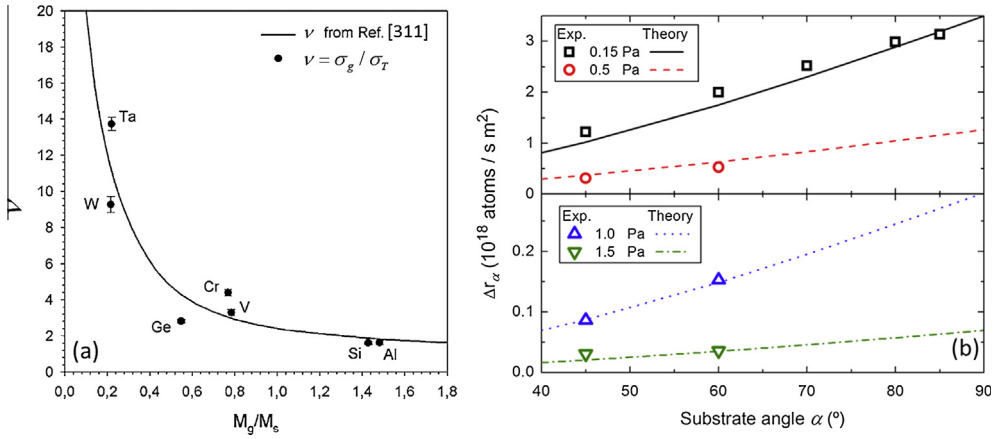

Fig. 4.5. (a) Number of collisions required to thermalize a sputtered particle in plasma as a function of the ratio between the mass of the plasma gas and sputtered atoms. The solid line is a calculation of Westwood [310], which was made by assuming an initial kinetic energy of 5 eV and Ar as the sputter gas, while the dots are the results of a numerical fitting of the Keller–Simmons formula obtained by ETC formulation [292]. (b) Deposition rate of Ti thin films as a function of the experimentally obtained substrate tilt angle and background pressure, and the expected trend based on ETC theory and Eq. (4.6) [130].

relations, the effective thermalizing collision (ETC) approximation has been successfully applied to describe the collisional transport of sputtered particles in a plasma [47,300,301]. This theory introduces the concept of effective thermalizing collision: an effective scattering event between a sputtered atom and gaseous species that results in the former losing its original kinetic energy and initiating a random thermal motion in the gas. As we will see next, this enables the deduction of simple analytical equations that relate the main fundamental quantities, though the connection between actual collisional quantities in the plasma/gas and this effective mechanism remains the main issue for the practical application of these ideas. A summary of the main concepts and approximations utilized within this theory to assess the division between ballistic and thermalized species is presented next, but interested readers may get a more detailed description in Refs. [47,300,301].

One of the most relevant quantities describing the collisional transport of particles in a gas is the mean free path, $\lambda = 1/N\sigma_g$, which represents the typical distance covered by a sputtered particle between two consecutive collisions in the plasma/gas. Here, σ_g, is defined by the cross-section of an elastic scattering event, while N is the density of gas atoms. The ETC theory also introduces what is known as the thermalization mean free path, λ_T, to account for the typical average distance covered by a sputtered atom in the plasma/gas before becoming thermalized. Likewise, a so-called thermalization cross-section, σ_T, is introduced through the relation $\lambda_T = 1/N\sigma_T$. In this way, the flux of ballistic (non-thermalized) sputtered atoms at a distance of L from the target can be expressed as $\Phi_0 \exp(-L/\lambda_T)$, where Φ_0 is the flux of sputtered particles at the source (target). The amount of thermalized sputtered atoms per unit of time in the plasma/gas is also given as: $\Phi_0[1 - \exp(-L/\lambda_T)]$. Using these formulae, it is possible to account for the Keller–Simmons (K–S) formula, which is a well-known empirical equation in classical MS deposition (i.e., in non-oblique configurations) with a single sputter gas [301]. This formula describes the dependence between the deposition rate and relevant experimental parameters such as the plasma gas pressure, p_g, and the distance between the cathode and the film, L, as:

$$r_{KS} = \frac{p_0 L_0}{p_g L}\left[1 - \exp\left(-\frac{p_g L}{p_0 L_0}\right)\right], \tag{4.2}$$

where r_{KS} is the deposition rate and $p_0 L_0$ is an adjustable parameter dubbed the characteristic pressure–distance product. This empirical equation was deduced in Ref. [301] from fundamental principles within the ETC framework, which found the relation $p_g L/p_0 L_0 = L/\lambda_T$. To simplify the calculations, the quantity $\Xi = L/\lambda_T$ was defined in Ref. [307] as the thermalization degree of the sputtered particles.

Thus, when Ξ is much less than one, the distance between the target and the film is much smaller than the typical thermalization mean free path; i.e., most deposition particles arrive with a high energy and along a preferential direction. However, when Ξ is much greater than one, the thermalization mean free path is much smaller than the target/film distance and most species should be thermalized when they arrive at the film surface (with low energy, and following an isotropic momentum distribution function). By means of this quantity, the K–S formula now reads:

$$r_{KS} = \Phi_0 \frac{1 - \exp(-\Xi)}{\Xi}. \tag{4.3}$$

To determine σ_T, we show in Fig. 4.5(a) the fitting of this theory to experimental data. The good fitting demonstrates that this parameter is connected with the geometrical cross-section of an elastic scattering event between a sputtered atom and a plasma atom through the relation: $\sigma_T = \sigma_g/\nu$, where ν is the average number of subsequent elastic collisions required for the thermalization of the sputtered particles, as calculated by Westwood [310]. Likewise,

$$\lambda_T = \nu\lambda. \tag{4.4}$$

This Eq. (4.4) allows σ_T to be calculated for any given sputtered atom or sputter gas, which implies that the complex dynamics of hyperthermal atoms sputtered from the cathode within a plasma can be simplified by means of an effective thermalization cross-section that describes the progressive loss of kinetic energy and directionality (i.e., the momentum distribution) of the sputtered particles.

In regard to the OAD of thin films, the previous assessment of the partition that exists between ballistic and thermalized sputtered atoms is of the utmost importance, as the former contributes to the film's nanostructuration through *shadowing effects* and other hyperthermal phenomena responsible for, among other things, the development of nanocolumns or specific textures. Moreover, in the OAD configuration, basic deposition magnitudes such as the deposition rate or the final composition and microstructure of complex thin film materials will be drastically affected by the thermalization degree of sputtered particles. Given its importance to any MS-OAD process, we specifically analyze the relation between the thermalization degree and deposition rate in the next section. An example showing the importance of the thermalization degree of sputtered particles on the control of composition and microstructure in complex MS-OAD thin films can be found in the recent work by Gil-Rostra et al. [311] on the MS-OAD of $W_xSi_yO_z$ electrochromic thin films, in which a net W enrichment of the deposited film with respect to the target and continuous variation in the tilt angle of the nanocolumns were attributed to more effective scattering of Si than W by Ar atoms in the plasma gas. That is, W has a much higher atomic mass than Si, and so its energy and momentum is less affected by binary collisions with much lighter Ar atoms. Silicon, on the other hand, has an atomic mass similar to Ar, and so is more effectively scattered to become distributed in all directions within the deposition chamber. Consequently, the films become enriched in tungsten and exhibit a microstructure in which, for any given deposition geometry, the tilt angle of the nanocolumns increases with W content.

4.3.3. Deposition rate at oblique incidence

Despite its importance to thin film processing, evaluation of the deposition rate in MS-OAD has only been recently addressed [130]. From the ETC concept, the total deposition rate on a tilted substrate can be written as the sum of a highly directed contribution of energetic ballistic particles and a thermalized contribution. The ballistic contribution can be estimated as a function of the average angle of arrival, α, as per:

$$r_B = \Phi_0 \exp(-\Xi)\cos\alpha. \tag{4.5}$$

Meanwhile, due to their non-preferential directionality, it is reasonable to assume that the deposition rate of thermalized atoms, r_D, is not dependent on the particular value of α. On the basis of this, it can be easily calculated for $\alpha = 0$ as: $r_D = r_{\alpha=0} - (r_B)_{\alpha=0} = r_{\alpha=0} - \Phi_0 \exp(-\Xi)$, where $r_{\alpha=0}$ is the deposition rate at normal geometry. Thus, by introducing the deposition rate at oblique incidence, $r_\alpha = r_B + r_D$, and the quantity $\Delta r_\alpha = r_{\alpha=0} - r_\alpha$, we arrive at the formula:

$$\Delta r_\alpha/\Phi_0 = \exp(-\Xi)(1 - \cos\alpha). \tag{4.6}$$

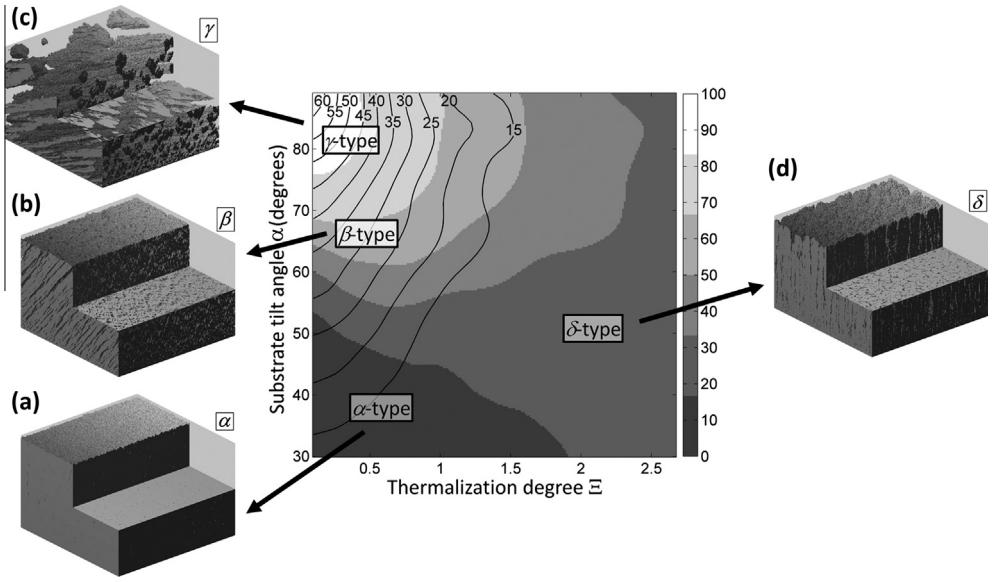

Fig. 4.6. Microstructure phase map of gold nanostructures grown by magnetron sputtering deposition at oblique angles. Evident in this map is the formation of four different microstructures α, β, γ and δ as a function of the thermalization degree and substrate tilt angle. The particular characteristics of these four microstructure types are illustrated by the four MC simulations (a–d) included in the figure. The intensity of color in the map indicates the percolation depth of mesopores from the surface of the film, whereas the lines indicate the tilt angle of the columnar/porous structures in the films [172].

Eq. (4.6) relates the deposition rate to relevant process parameters such as the tilt angle of the substrate and the thermalization degree. In this way, when Ξ is significantly low, the deposition rate is found to have a strong dependence on the deposition angle, $\Delta r_\alpha \sim \Phi_0(1-\cos\alpha)$. This dependence stems from a highly directional arrival of deposition particles that makes the deposition rate highly dependent on the relative orientation of the film with respect to the target. When Ξ is much above 1, it is found that $\Delta r_\alpha \sim 0$; i.e., the deposition rate is little affected by the substrate orientation angle. Indeed, under these conditions most deposition particles are thermalized, and so the deposition rate should be independent of α, a concept that is in good agreement with the original hypothesis of the ETC theory.

Overall, whenever the KS formula is applicable, a general formula for the growth of magnetron-sputtered thin films at oblique angles can be derived from Eqs. (4.4) and (4.5):

$$\frac{r_{\alpha=0}-r_\alpha}{r_{\alpha=0}}=\frac{\Xi}{\exp(\Xi)-1}(1-\cos\alpha). \tag{4.7}$$

This formula establishes a relation between the deposition rate at oblique angles and at normal incidence with the thermalization degree and zenithal angle of the substrate. The predictions of this model are of general characteristics, but have been successfully applied to describing the growth of Ti thin films at different tilt angles and background pressures, as shown in Fig. 4.5(b).

4.3.4. Microstructure phase map for OAD-MS thin films

At the present point in the discussion of the influence of basic atomic interactions on the characteristics of MS-OAD thin films, it is evident that experimental parameters and magnitudes such as geometry, gas pressure, temperature and energy/momentum distribution of the sputtered particles, will have a decisive influence on the thin film properties. However, no systematic works have yet been carried out in which their combined influences have been considered. For thin films grown using a normal configuration, the SZM model [35–37] has proven to be quite an important contribution to

qualitatively describing the morphological features of thin films deposited under different temperatures and pressures. Clearly then, a similar approach is needed for dealing with MS-OAD thin films. An attempt along these lines can be found in a recent work by our group [172], which provided a thorough experimental and theoretical analysis of the microstructural evolution of Au thin films deposited by MS-OAD as a function of Ξ and α. In this, we compared the different microstructures obtained by systematically varying these two parameters in MC simulations where only the surface shadowing mechanism and collisional processes in the plasma gas were considered. The different microstructures obtained were then rationalized in the form of a phase map along the schemes of the SZM. Fig. 4.6 illustrates the four different generic microstructures obtained, which are characterized by the following features:

- *α-type microstructure*: the film is compact and has no well-defined geometrical patterns in the bulk. It is formed at low thermalization degrees with small deposition angles (typically when $\Xi < 1.5$ and $\alpha < 50^\circ$).
- *β-type microstructure*: the film possesses a highly coalescent, tilted columnar structure (i.e., columns are not isolated from each other, but are always touching), with large elongated mesopores percolating from the surface to the bottom of the film. It is obtained at low thermalization degrees and higher deposition angles (typically when $\Xi < 1$ and $50^\circ < \alpha < 75^\circ$).
- *γ-type microstructure*: the film is defined by isolated and well-defined tilted nanocolumns. It is formed at even lower thermalization degrees and much higher deposition angles (typically when $\Xi < 0.5$ and $75^\circ < \alpha < 90^\circ$).
- *δ-type microstructure*: the film is characterized by vertical, coalescent column-like structures, with a high density of micro and mesopores occluded in the material. It is formed at high thermalization degrees and a wide range of deposition angles (typically when $\Xi > 2$), similar to those reported in Ref. [312] when low-energy deposition particles arrive at the film surface following an isotropic angular distribution function.

Fig. 4.6 shows the formation of these different microstructures on a phase diagram, as well as through a series of MC simulations to visualize their main columnar and pore features. A very good concordance in shape was revealed between these simulated structures and the experimental films. In addition, the MC simulation provided clues to understand the formation of the different thin film microstructures by assuming a different thermalization degree for the sputtered gold atoms. This quantity identified different surface shadowing processes during the early stages of thin film formation and subsequent growth. A detailed description of the mechanistic effects under each working condition is reported in Ref. [172].

The aforementioned study was carried out in order to account for the growth of gold nanostructures as a function of substrate tilt angle and working pressure during MS-OAD. The generalization of this kind of analysis to other materials and conditions is still very much an open issue and will be addressed in the next few years. It is worth noting here that gold represents a very simple case, which can be properly simulated by taking into account very simple phenomena such as atomic scattering in the plasma phase and shadowing effects. To fully explain the nanostructures created in the MS-OAD of other materials, additional complex phenomena associated with the high energy of sputtered particles would need to be included. Thus, processes such as the kinetic energy-assisted mobility of surface atoms, biased diffusion, and upwards or downwards funneling mechanisms, among others, cannot be disregarded, and very likely will need to be incorporated into the analysis (see Refs. [303–305]). For example, Dalla Torre et al. [212] developed a MC model that considers a set of different interactions and mechanisms, including binary collisions between incoming gaseous atoms and those deposited on the film surface, and thermally activated processes or different hyperthermal relaxation processes that are dependent on the kinetic energy and momentum transfer such as the reflection of incoming particles, biased-diffusion, kinetic energy-assisted diffusion or re-sputtering. Overall, they found good qualitative agreement between simulations and experimental data with the growth of Ta thin films by DC sputtering at oblique angles, and demonstrated the relevance of these processes to the nanostructural development of these films. Moreover, in Ref. [49], a detailed experimental study of several materials was carried out to determine the temperature threshold at which thermally acti-

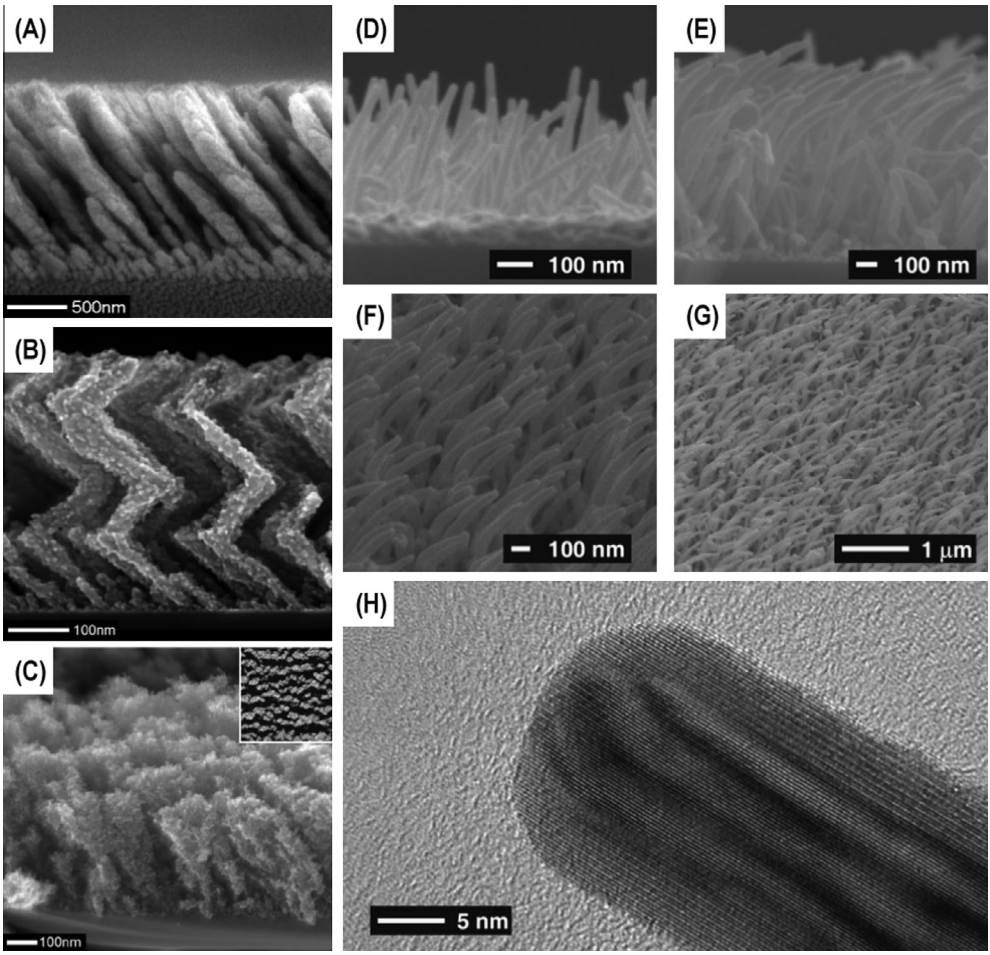

Fig. 5.1. ITO microstructures prepared by OAD under (A–C) high vacuum conditions or (D–H) nitrogen flux. (A) Tilted nanocolumns deposited at $\alpha = 85°$, (B) chevron films deposited at $\alpha = 85°$ while rotating the substrate azimuthally three times by $\varphi = 180°$, and (C) a vertical biaxial film formed by fixing $\alpha = 85°$ using dynamic OAD. Samples prepared under nitrogen flux were deposited with $\alpha = 70°$ at a pressure of 1.33×10^{-2} Pa: (D) cross-sectional view of the initial stages of column formation, showing a fairly random growth direction, (E) cross-sectional view of oriented columns at the end of deposition (total length ca. 1, 2 μm), (F and G) tilted top view of the columns showing their tapered profile and uniform distribution, (H) TEM image of an ITO nanocolumn with a core/shell inner structure. Reproduced with permission from (A–C) [317] and (D–H) [329].

vated processes on the film surface compete with surface shadowing mechanisms for control over the formation of the film nanostructure. In agreement with the SZM, they found that for elemental metal thin films with a melting point above that of Al (933 K) the value of T/T_f was $T/T_f > 0.33$, whereas for oxide thin films it was $T/T_f > 0.5$ (see Section 3). Thus, the influence of thermally activated processes must be considered to account in a generalized way for the evolution of different microstructures during MS-OAD [49].

In addition to the concepts already discussed in this section, a systematic analysis of how the impingement of plasma ions affects the nanostructuration of a film at oblique angles is still notably absent. Nevertheless, plasma ions have been widely used for numerous purposes, such as the removal of defects, the densification of materials, improving mechanical properties, smoothing surface, and the crystallization of materials. When dealing with porous materials, however, their energy must be kept low enough to influence the film nanostructuration without producing full densification. Yet it is only

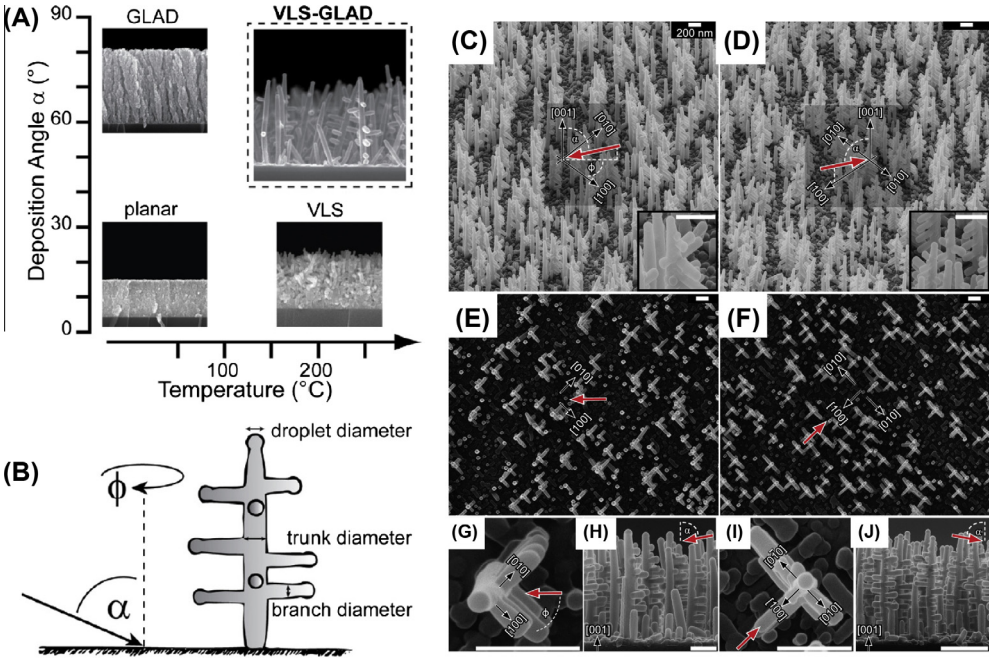

Fig. 5.2. Comparison of VLS-OAD nanostructures. (A) Unique morphologies created by a high substrate temperature and high deposition angle. (B) Schematic defining the deposition angle (α) and angle of rotation around the substrate normal (Φ). Typical nanowhiskers are characterized by a trunk, droplet and numerous branches. The vapor flux arrives at an oblique angle (α) to the substrate normal and is offset by an angle (ϕ) from the [100] direction of the single cubic crystal YSZ substrate. (A–D) SHIM images of ITO nanotrees grown on YSZ with $\alpha = 85°$ and $\phi = 45°$ (resulting in L-shaped nanotrees) and (E–H) $\phi = 0°$ (resulting in T-shaped nanotrees). (C and D) are oblique images, (E–G) and (I) are plan view images, (H and J) are cross-sectional images. Red arrows depict vapor flux orientation, whereas black arrows indicate crystal directions of the YSZ substrate. All scale bars represent 200 nm. (A and B) were taken from [133], while (C–J) were taken from [137].

recently that this effect has been analyzed by altering the ion energy using different electromagnetic waveforms so as to change the plasma potential. In Ref. [313], it is demonstrated that the introduction of a shallow low-energy ion impingement on the film surface during growth affects the tilt angle of the columns and the overall film porosity. Even though this effect has only been reported for TiO_2 thin films, this result suggests that the modulation of low-range ion energies is necessary to tune the morphological features of the columnar structures in plasma-assisted depositions.

5. Applications and devices

The incorporation of OAD thin films in a large variety of advanced devices is a clear indication of their maturity and excellent prospects for a successful implementation in a large range of technological fields. Although it is impossible in the space of this review to cover all of the advanced applications and devices that rely on OAD thin films, the following sections present a review on a select number of works published in the last seven-to-ten years that, in our opinion, best illustrate the possibilities of this material type and technology. We have grouped this selection into the following broad subjects: transparent and conductive oxides (TCOs), energy harvesting, sensors and actuators, optic and photonic devices, wetting and microfluidics, and biomaterials and biosensors.

5.1. Transparent conductive oxides

Of the thin film materials used for the fabrication of photonic or electronic devices, transparent conducting oxides (TCOs) occupy a central position, being indispensable for the fabrication of solar

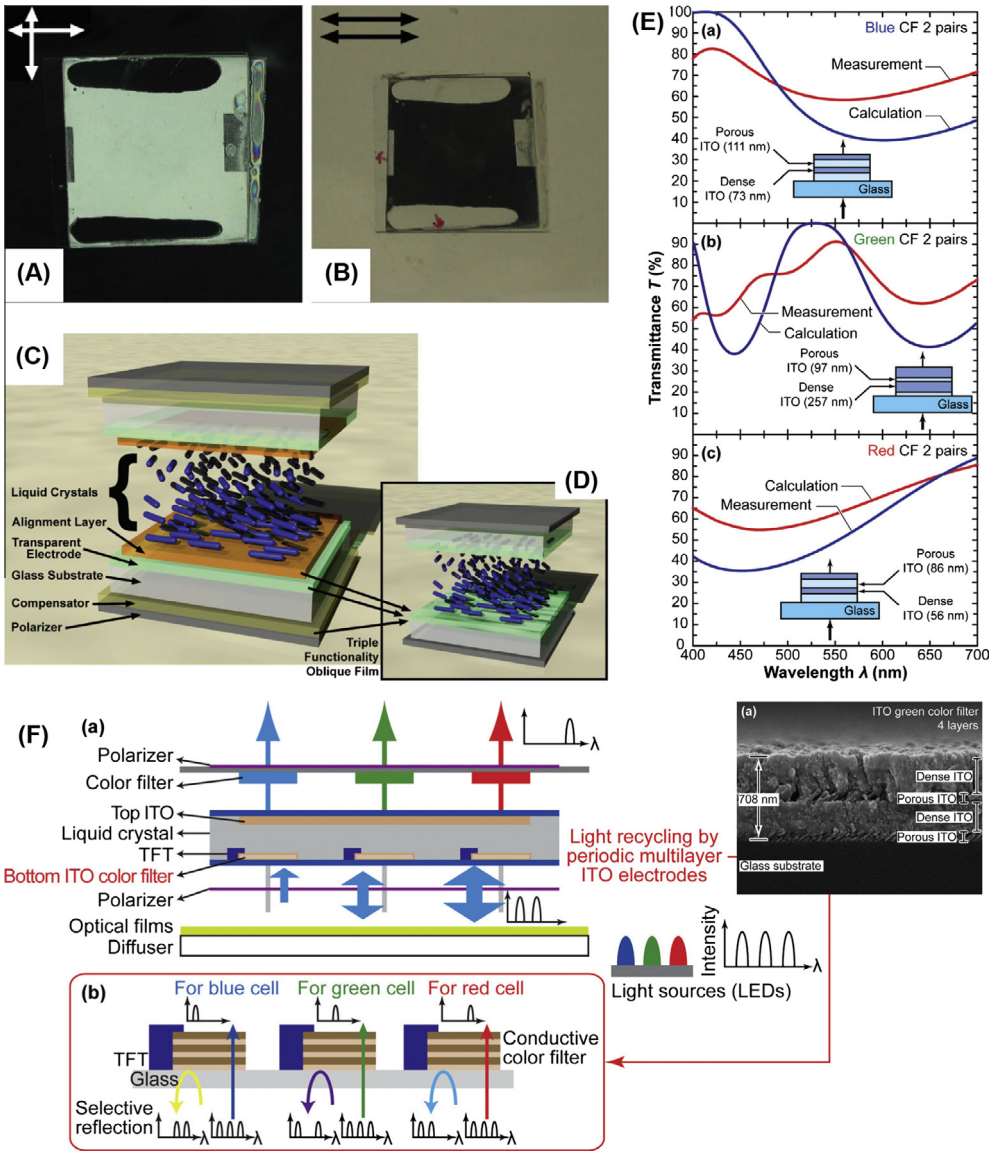

Fig. 5.3. Schematic and performance of devices using OAD ITO films for (A–D) the alignment of liquid crystals and (E and F) as color filters. The liquid crystal E7 is aligned in a twisted nematic configuration by two ITO films deposited at $\alpha = 65°$. The cell is shown between crossed polarizers in (A), and between parallel polarizers in (B). The polarizer absorption axes are indicated as arrows. (C) Schematic of a typical LCD system incorporating separate layers acting as transparent electrodes, LC alignment layers and birefringent compensators. (D) Unification of the functions of these three components within an ITO nanopillar layer. (E) Measured and simulated transmittance of multilayer coatings acting as color filters by stacking porous/dense ITO layers. (F) Graded refractive index, single-material multilayer functioning as an electrode and interference color filter in a LCD. The bottom part of the panel shows enlarged cross-sectional views of the ITO color filters and their expected functions. The inset presents a cross sectional SEM micrograph of the four porous/dense stacked layers acting as green color filter. (A–D) taken from [317], (E and F) taken from [88].

cells, electroluminescent and electrochromic systems or electrochemical devices [314]. Thanks to its low resistivity ($\sim 10^{-4}\,\Omega\,\mathrm{cm}$), high transmittance in the visible range (80–90%) and low-deposition temperature, tin-doped indium oxide (ITO) is the most popular TCO used by industry [314,315].

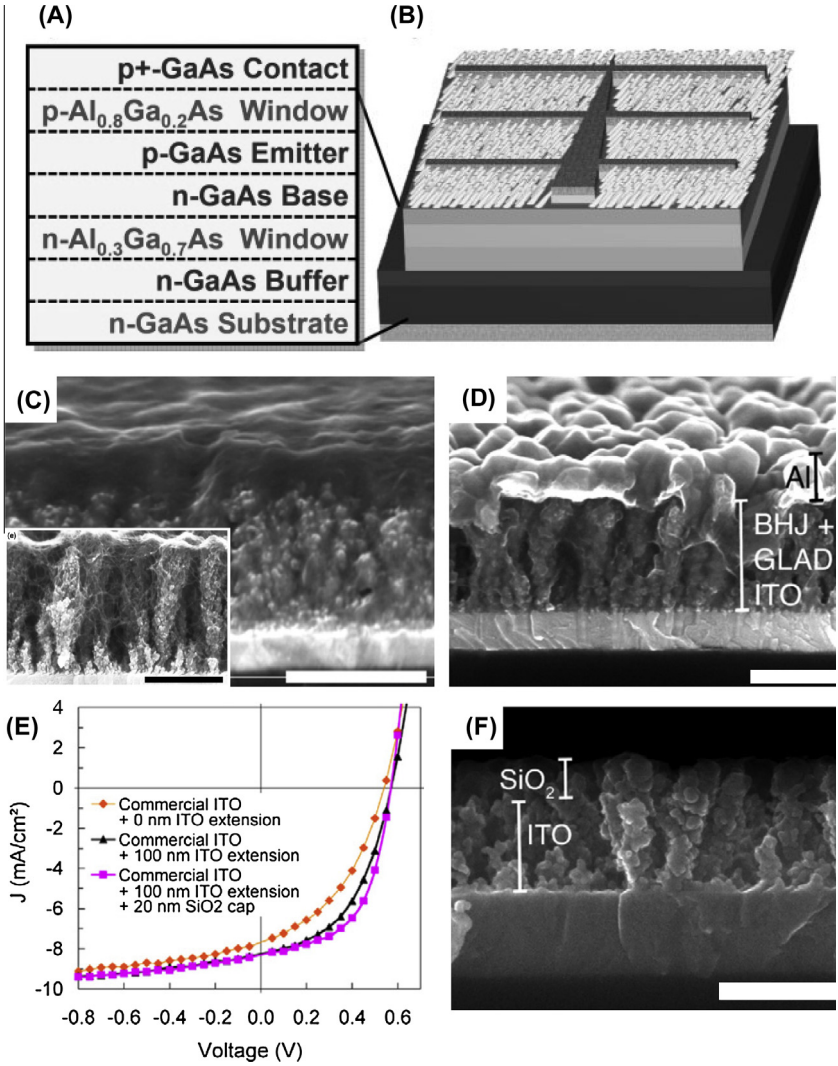

Fig. 5.4. Nanosculptured OAD-ITO films used as antireflecting and conducting layers in solar cells. (A and B) Schematic of tapered ITO nanocolumns used in AsGa solar cells. (C–F) Highly porous ITO nanocolumns implemented in Si solar cells. (A) Detailed epitaxial structure of a single-junction GaAs solar cell in which ITO nanocolumns act as a conductive AR coating (B). (C) SEM micrograph showing the infiltration of P3HT/PCBM BHJ into a cobweb-like PEDOT:PSS and OAD nanoelectrode array. The inset shows the as-grown ITO nanostructure after electrodeposition of PEDOT:PSS. (D) SEM micrograph of the entire BHJ OPV structure, including an Al top contact. (E) *J–V* plots obtained under illumination of a BHJ organic cell device fabricated with commercial ITO (orange diamonds), OAD ITO (black triangles) and silica-capped OAD ITO (magenta squares) anodes. (F) SEM image of 150 nm OAD ITO capped with 50 nm silica. Scale bars in (C and D) = 500 nm, and in (F) = 200 nm. (A and B) are from [329], (C–F) from [319].

Indeed, it is only the need to replace the expensive indium component that has prompted the search for alternative TCO formulations, which are briefly summarized at the end of this section. The fabrication of highly porous and/or sculptured ITO thin films has been attempted by e-beam OAD from ITO pellets, both under high vacuum conditions [316–327] and in a carrier gas flux (usually nitrogen) [320,328–330]. Fig. 5.1 shows some examples of the thin films and various microstructures that can be obtained by controlling the deposition conditions. This rich variety of potential morphologies is made

possible by strict control of deposition parameters (e.g., working pressure, residual or carrier gas, substrate geometry and temperature) that are known to have a direct impact on the growth mechanism (see Sections 2 and 3). The morphologies obtained can be divided into three groups: (i) standard tilted nanocolumnar layers fabricated by OAD at low pressure (Fig. 5.1(A)–(C)), (ii) nanostructures with a tapered nanocolumn profile over a critical length obtained by deposition with a carrier nitrogen flux (Fig. 5.1(D)–(H)), and (iii) nanowhiskers and hierarchical, multi-branched tree-shaped nanostructures obtained by sequential application of VLS-OAD [133,134,137,331] (see Section 3.1 and Fig. 5.2 for a more detailed description of the singular branched nanostructures created using this method). Selected applications relying on these nanostructured TCO films will be discussed in the sections that follow.

5.1.1. Electronic and photonic applications

Owing to their open microstructure, controlling the electrical properties of ITO-OAD films has required the development of specific methodologies and the use of relatively sophisticated techniques. These have included axial resistivity measurements by a cross-bridge Kelvin system [321], terahertz time-domain spectroscopy (THz-TDS) [325], or combinations of experimental and theoretical studies [324]. These, and other investigations, relating the OAD microstructure of ITO nanopillars to the deposition parameters [317] (Fig. 5.1(A)–(C)) have proved that it is possible to achieve optical transmittances and electrical conductivities comparable to those of compact ITO thin films.

The good electrical performance, high porosity and nanocolumnar structure of ITO-OAD films has fostered their incorporation as active components into liquid crystal displays (LCDs) for the alignment of calamitic liquid crystals (Fig. 5.3(A) and (B)). Typically, an LCD display integrates different layers of transparent electrodes, LC alignment layers and birefringent compensators (Fig. 5.3(C)), functions that can be provided by just one OAD-ITO nano-columnar film (Fig. 5.3(D)). Meanwhile, coatings with a graded refractive created by combining dense ($\mathbf{n}(500\,\text{nm}) = 2.10$) and porous ($\mathbf{n}(500\,\text{nm}) = 1.33$) stacked layers of ITO through changing the zenithal angle of deposition [88] have been used for photonic and combined photonic–electronic applications. For example, different color filters designed and fabricated using this approach have been utilized as the bottom electrode of a LCD system (Fig. 5.3 (E) and (F)). Other photonic components such as Bragg reflectors [316,332], broadband antireflective and conductive materials [331], and transparent electrodes and antireflection contacts in organic light emitting devices [330,333] have also incorporated similar photonic and conductive layers.

5.1.2. Solar cell components

OAD ITO layers have been used as transparent conducting and antireflective coatings in: organic photovoltaic solar cells [319,334], Si-based solar cells [322,323,327] and GaAs photovoltaic devices [329]. The photon absorption capacity of a solar cell is one of the main factors contributing to its global efficiency. Thus, in order to reduce the light reflection coefficient and increase the amount of transmitted light, antireflection coatings (AR) are usually incorporated on the front side of these devices. Because of their high porosity (see Section 3.6), OAD thin films and multilayer structures have an inherently low refraction index, making them suitable for AR-layer applications [331,332,335]. An added benefit of ITO OAD films used for this purpose resides in their high electrical conductivity. From the point of view of cell manufacturing, another advantage is the possibility of using a single material as an AR coating rather than the multilayer structure of alternating layers of different refractive index that are typically used (see Section 5.4). Going beyond the use of conventional ITO OAD films, Yu et al. [329] have proposed a new AR concept based on the peculiar ITO nanocolumns presented in Fig. 5.1 (D)–(H). The characteristic tapered and bent microstructure of these nanocolumns works as a collective graded-index layer offering outstanding omnidirectional and broad-band antireflection properties for both *s*- and *p*-polarizations. The benefit to a GaAs solar device integrating one of these ITO films (Fig. 5.4(A) and (B)) over not using an AR layer is as much as 28%, with nearly 42% of the enhancement in the photocurrent generated through the transparent gap of the window layer.

Nanocolumnar ITO films have also been used as high surface area 3D nanoelectrodes in organic solar cells [319]. Fig. 5.4(C)–(F) depicts a device consisting of an OAD-ITO electrode electrochemically modified with nanofibrous PEDOT:PSS (poly(3,4-ethylenedioxythiophene):poly(p-styrenesulfonate)) to produce a cobweb-like structure (inset in Fig. 5.4(C)), which is then infiltrated by spin-coating with

a P3HT:PCBM photoactive layer (Fig. 5.4(C)). The cross-sectional view given in this figure provides evidence that the ITO layer is effectively infiltrated by the photoactive material, a requisite for good performance with this type of solar cell device. The cell is electrically contacted with an evaporated aluminum layer on top (Fig. 5.4(D)), which integrates the insulating electrode formed by OAD-ITO nanopillars covered with OAD-SiO_2 caps (Fig. 5.4(E) and (F)). This solar cell configuration exhibits better performance than equivalent devices based on compact ITO films.

In a very recent collaborative work between the Pohang University and the Ressenlaer Polytechnick Institute [336], ITO nanohelix arrays were used as three-dimensional porous electrodes, antireflection coatings and light-scattering layers in bulk heterojunction solar cells. These ITO arrays provided an enhancement in both the total light absorption and the charge transported from the photoactive layer to the electrode; the combination of these effects resulting in a 10% increase in short-circuit current density and a substantial increase in the power-conversion efficiency.

5.1.3. Sensors and biosensors

As a result of their high surface area and outstanding optical/electrical properties, ITO nanopillar layers have been extensively used as biosensors to detect immobilized biomolecules within their pores by means of different spectro-electrochemical methods. One example of this is the rapid absorption of microperoxidase within the meso- and micro-pores of OAD ITO layers, which has been used for the detection of a series of adsorbed redox biomolecules that were electrochemically monitored by derivative cyclic volt-absorptiometry [320,337]. Using another sensing approach, Byu et al. [338] demonstrated that the performance of surface plasmon resonance (SPR) gold biosensors can be enhanced by adding an OAD-ITO layer to increase the surface area available for the target molecules. These decorated substrates present a much higher sensitivity than bare gold films in the analysis of ethanol–water mixtures. The high surface area of ITO-OAD films has also proven decisive in the development of resistive gas sensors for NO_2 [339], in that a maximum sensitivity of 50 ppb and short response time have been achieved with highly porous films prepared using high zenithal angles of deposition (see Section 3.6). Further improvements were obtained by incorporating a bottom layer of Fe_2O_3 or SiO_2 as seeds to favor the growth of interconnected ITO nanorods, with their inner channels being highly accessible to the surrounding medium.

5.1.4. Alternative TCO films prepared under OAD conditions

The high cost and increasing demand of indium over the last few years have prompted the development of TCO films with other compositions; this also being true of TCO thin films prepared under OAD conditions. Al-doped zinc oxide (AZO) thin films prepared by either e-beam or MS OAD [323,340–344] have been successfully used in solar cells and LED devices. The synthesis of Sb-doped tin oxide (STO) and Nb-doped titanium oxide (TNO) films with a strictly controlled composition, microstructure and porosity has also been recently reported to achieve outstanding optical transparency and electrical conductivity [323,345,346]. In most of these preparations, MS has been the technique of choice for the simple reason that it is better suited for depositions over large areas. Some examples in the literature include the MS-OAD of Ga-doped ZnO [168,347,348] and the development of a co-sputtering method for the fabrication of high and low refractive index layers of TNO and AZO, respectively, for use in the preparation of a transparent and conductive distributed Bragg reflector [340,349]. In this structure, the eight-period stack of AZO/TNO layers produces a reflectivity of ~90% along a spectral region centered at 550 nm, and a resistivity of less than $2 \times 10^{-3}\ \Omega$ cm. Because of this outstanding performance, this system has been proposed as a mirror and charge injection layer to substitute the existing dielectric Bragg reflectors in vertical cavity surface emitting lasers.

5.2. Energy harvesting and storage

The last few years have borne witness to a tremendous expansion in the development of efficient renewable energy sources and/or the implementation of new, advanced energy storage and saving methods. Among the solutions proposed for the development of these new methods, we have seen that OAD thin films play a special role due to their unique properties. In this section we review some of the recent advances in the development of OAD thin films for renewable energy applications, with a

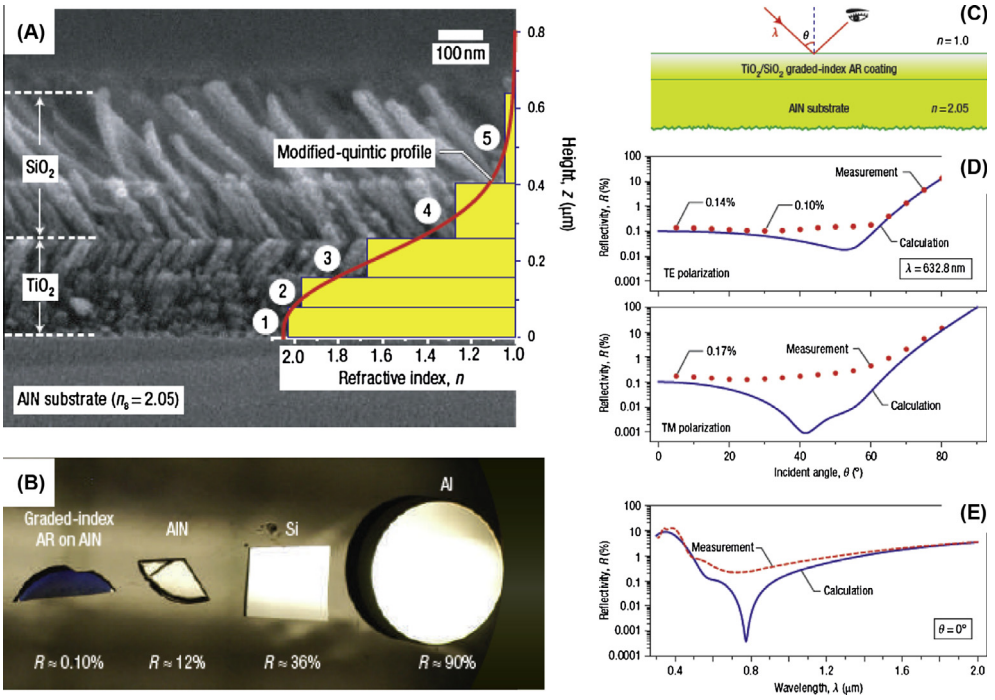

Fig. 5.5. Development of AR coatings through a combination of graded refractive index materials. (A) Cross-sectional SEM micrograph of a graded-index coating consisting of three TiO_2 nanorod layers on the bottom and two upper SiO_2 nanorod layers. Interfaces between all layers appear clearly defined. The feature size of individual nanorods (ca. 50 nm) is much smaller than the wavelength of visible light, giving transparency and an absence of light scattering in this wavelength range. The low-n films are found to be stable, with no evidence of degradation due to the adsorption of moisture. The inset bar diagram indicates the refractive index of each layer. (B) Photograph of a graded-index antireflection coating deposited on AlN and specular surfaces of AlN, Si and Al. (C) Schematic of the reflectivity measurements. (D) Theoretical (solid line) and measured (dotted line) reflectivity of a graded-index coating versus incident angle for a wavelength λ = 632.8 nm. (E) Wavelength dependence of theoretical (solid line) and measured (dashed line) reflectivities of the graded-index coating at normal incidence [237].

special emphasis on electricity generation by photovoltaic solar cells, solar-driven photocatalytic hydrogen production, fuel cells, electric energy storage with lithium ion rechargeable batteries and electrochromic coatings. The emerging topic of piezoelectric generators based on OAD thin films will also be introduced.

5.2.1. Photovoltaic applications

OAD nanostructures represent versatile candidates to fabricate the many diverse elements of a photovoltaic solar cell device. Following a simplified description, OAD thin films have been used as: (i) transparent conducting layers, (ii) active semiconductor materials for electron–hole production upon absorption of photons, (iii) electron or hole conducting/blocking layers, (iv) sculptured counter electrodes, and (v) antireflection coatings. In Section 5.1 we reviewed the latest developments regarding the OAD of ITO and other TCOs used as transparent conducting materials and AR coatings in different solar cells architectures. In this section, we summarize the advances that have been made in the fabrication, design and optimization of other OAD nanocolumnar thin films utilized in this type of device/component.

5.2.1.1. AR coatings. Layers of OAD nanocolumnar materials other than TCOs have been used as AR coatings to optimize the efficiency of various types of solar cell device. Their use is motivated by expected improvements in photon harvesting, carrier separation or carrier collection efficiencies.

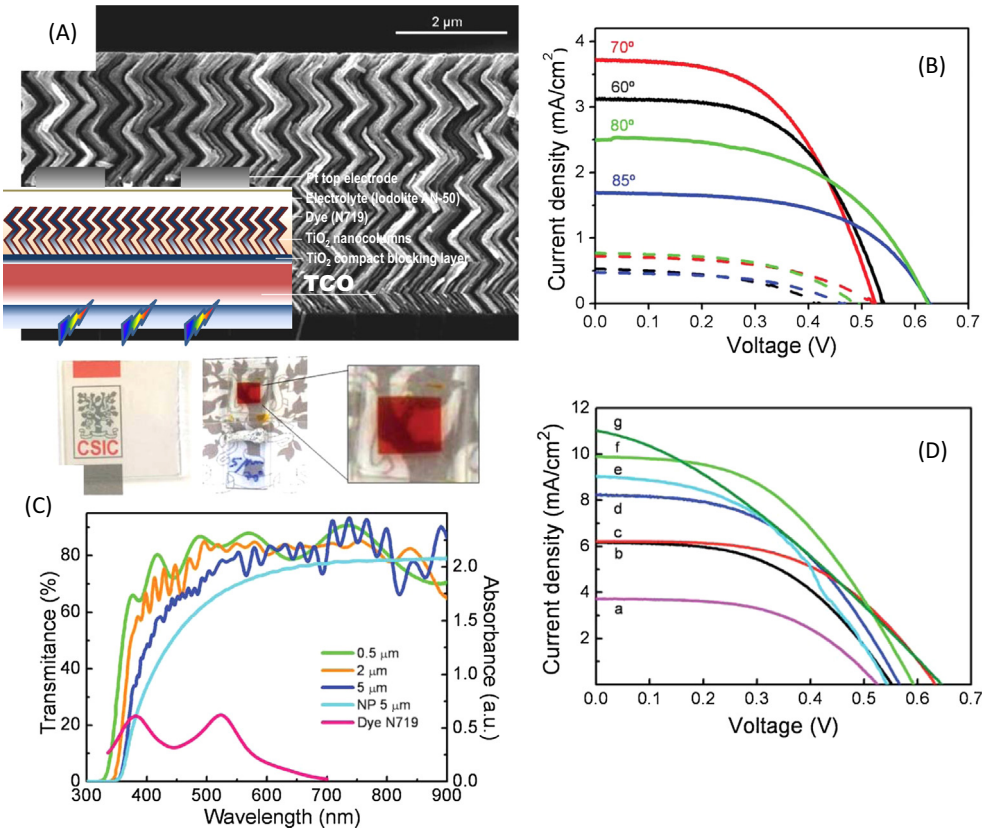

Fig. 5.6. TiO_2 as DSSC photoanode. (A) Cross-sectional SEM micrograph of a zigzag thin film consisting of ten stacked 500 nm TiO_2 layers (5 μm total thickness) prepared by successive azimuthal rotation of the substrate by 180°. The inset shows a schematic of the DSSC device. (B) *I–V* curves for TiO_2 photoanodes deposited at different angles and used either as prepared (dashed lines) or after crystallization by annealing at 400 °C (full lines). (C) UV–vis transmission spectra for a series of OAD TiO_2 films with different thicknesses consisting of single and stacked 500 nm-thick layers prepared in a zigzag configuration. The transmission spectrum of a nanoparticle thin film and the absorption spectrum of the N719 dye solution are included for comparison. The photographs presented in the top of the panel correspond to a 5 μm-thick zigzag film infiltrated with dye to show the high transparency of the final cells. (D) *I–V* curves obtained from DSSCs utilizing zigzag TiO_2 thin films grown at $\alpha \approx 70°$ to thicknesses of: (a) 500 nm, (b) 1 μm, (c) 1.5 μm, (d) 2 μm, (e) 2.5 μm, (f) 3 μm and (g) 5 μm [63].

Photon harvesting in photoactive solar cell components substantially increases if light is scattered or confined within the system, and so the implementation of an AR coating at the front side of a solar cell is a well-known method of confinement that enhances light absorption by the active material. Since sunlight has a broad spectrum and its angle of incidence changes throughout the day, high-performance AR coatings must be efficient over the entire solar spectrum and a wide range of incident angles [335]. A good approach to avoid Fresnel reflections (i.e. optical reflections at the interface between two materials with different refractive indexes) is to insert an interface with a graded refractive index between the two media. Schubert et al. [350,351] have shown that the interference coatings formed by stacking OAD films with different refractive indexes may provide the desired broadband and omnidirectional AR characteristics needed for photovoltaic cell applications. There have been two general approaches adopted for the fabrication of AR OAD structures for solar cell applications: the multilayer stacking of low and high refractive index materials, and the combination of layers of the same material but with different densities (i.e. porosities, see Sections 2.4 and 3.6). In the case

of the former, Schubert et al. [237] have reported the lowest refractive index material known to date, with a n value ~1.05 for SiO_2. They also succeeded in fabricating a graded-index broadband and omni-directional AR coating consisting of alternant layers of TiO_2 and SiO_2 with refractive indexes ranging from 2.7 to 1.3 and 1.45 to 1.05, respectively. As reported in Fig. 5.5, such a coating effectively reduces the Fresnel reflections when deposited on an AlN substrate (n is ~2.03).

A typical example of an AR OAD coating used to enhance photon harvesting is one formed by stacked TiO_2 and SiO_2 layers [228,351–353], which in some cases are prepared through successive sputtering of the two materials [354,355]. The extension of this procedure to large area substrates, including deposition on conformable polymers, has also been reported [356,357]. Other reported attempts include the fabrication of single-material AR coatings by stacking different refractive index layers of ITO (see Section 5.1), MgF_2 [358], SiO_2 [358–361], TiO_2 [362], alumina [363], ZnS [364] or ZnO [365].

Composite and compositionally complex thin film materials have also been used to increase the scattering of light in solar cell devices. Some examples of this approach include: (i) antireflection and self-cleaning coatings for III–V multi-junction solar cells made of OAD layers of gold grown on nanocone arrays fabricated by plasma etching borosilicate glass [366], (ii) magnetron sputtered $Ti_xSn_{1-x}O_2$ films prepared on top of a seed layer of polystyrene spheres [367,368], (iii) HfO_2 films [369] combined with amorphous porous silicon with closed porosity [370], and (iv) sculptured TiO_2 films [371].

5.2.1.2. Photon absorption components. The implementation of OAD thin films and nanostructures as active photon absorption components in solar cells is another relevant field of interest for these materials. One approach in this context consists of exploiting the high surface area of columnar OAD films to increase the interface area between p- and n-type semiconductors or, depending on the type of solar cell, between a semiconductor and an electrolyte. In order to reduce the electron–hole recombination probability, OAD nanostructures are also used to diminish the transport distance of the minority carriers from the absorbing semiconductor to the charge collection electrode. Furthermore, the unique architecture of OAD films at the nanometer scale provides different ways to increase both the interface area and carrier lifetime in solar cells. Various cases will be presented next to illustrate the possibilities in dye and quantum dot (QD) sensitized solar cells, organic and hybrid photovoltaic solar cells and Si-based solar cells.

5.2.1.3. Dye sensitized solar cells (DSSCs). Titanium dioxide nanomaterials have been extensively used as a wide-band-gap semiconductor in DSSCs [372]. In typical cells of this type, anatase thin films are made from agglomerated nanoparticles, nanotubes or nanorods, while light-absorbing dye molecules are adsorbed onto the oxide surface [372–374].

Studies into one-dimensional TiO_2 nanomaterials for DSSCs have been motivated by the idea that the transport of charge carriers along tubes or nanowires may be more efficient than through a nanoparticle film, where electrons must cross many boundaries before reaching the collection electrode. According to this, one-dimensional nanostructures should have a lower diffusion resistance than nanocrystalline films, thereby facilitating the collection of photogenerated charge carriers [375]. With this in mind, several authors have used OAD TiO_2 nanocolumnar films as photo-anodes in DSSCs [48,63,64,284,376,377], achieving performances similar to that of cells based on conventional TiO_2 nanoparticle films. A schematic showing the typical structure of a DSSC incorporating an OAD TiO_2 photoanode is given in Fig. 5.6(A). In most cases, a compact TiO_2 layer is first deposited between the porous OAD TiO_2 and TCO substrate to prevent the direct contact between the electrolyte and electrode [63,64,284]. Ruthenium 535-bisTBA, also known as N719, is the most common dye in this type of solar cell. In the example shown in Fig. 5.6, the electrolyte chosen was Iodolite AN-50. Other combinations of dye and electrolyte have also been used with OAD TiO_2 films, including viscous and fast-recombining ionic-liquid electrodes [284]. Most research into OAD TiO_2 photoanodes has correlated photo-efficiency improvement with geometry, porosity, microstructure and the dimensions of the TiO_2 nanostructure. Indeed, much work has been devoted to determine the effect of these morphological characteristics on physical phenomena such as the amount of dye incorporated, electrolyte diffusion, light absorption and scattering or charge transport efficiency. To this end, several

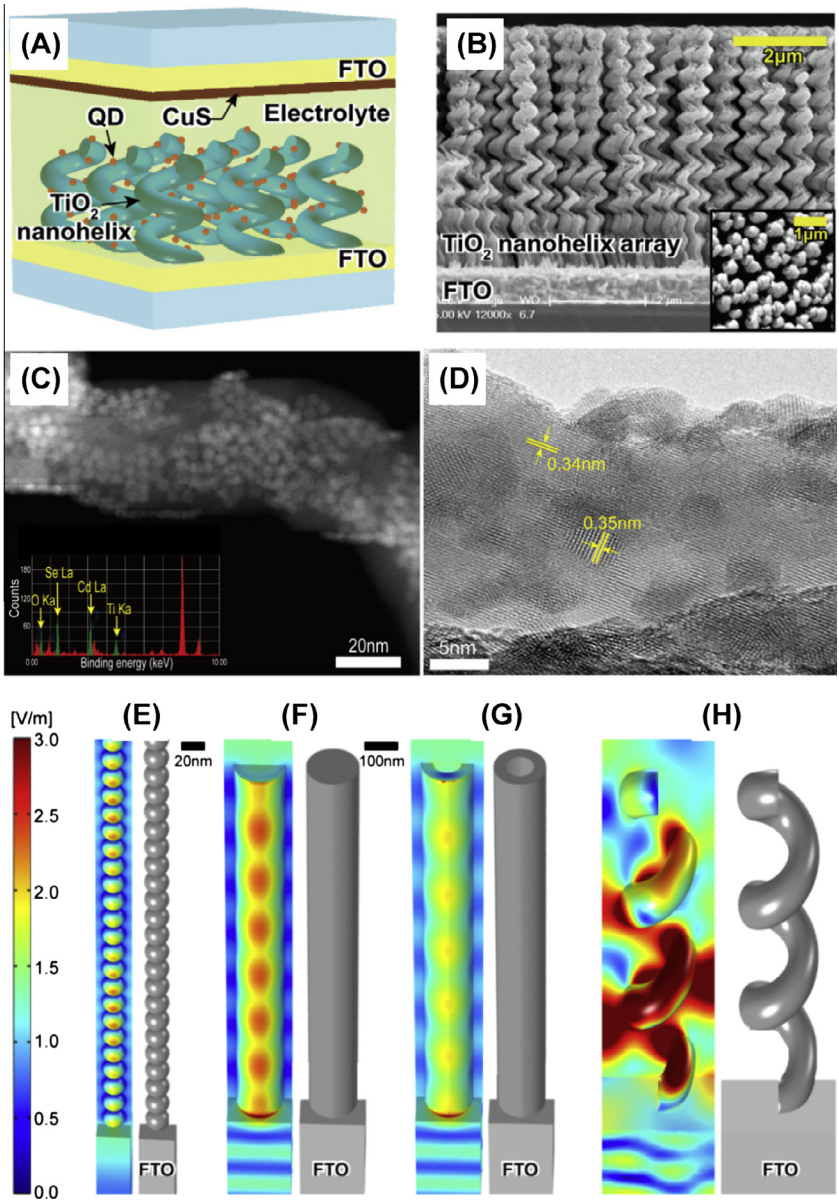

Fig. 5.7. Three-dimensional TiO_2 nanohelices as a QDSSC photoanode. (A) Schematic diagram of a QD-sensitized solar cell based on TiO_2 nanohelix arrays. (B) Cross sectional and (inset) top view SEM images of a TiO_2 nanohelix array deposited on an FTO-coated glass substrate. The highly porous structure facilitates the penetration of QDs and electrolyte into the pores. (C) Low magnification STEM-HAADF image of a TiO_2 nanohelix loaded with CdSe QDs (bright spots). The difference in average atomic number between CdSe and TiO_2 causes different HAADF intensities. The presence of CdSe QDs in close contact with TiO_2 was further confirmed by EDS measurements, as shown in the inset. (D) HRTEM image of CdSe QDs loaded on a TiO_2 nanohelix with indication of the measured lattice spacing of TiO_2 (0.34 nm) and CdSe (0.35 nm). Representation of the geometry (right) and simulated electric field distribution at the surface (left) in (E) for a series of stacked TiO_2 nanoparticles (10 nm radius, 30 nm period), (F) a TiO_2 nanorod (75 nm radius, 200 nm period), (G) a TiO_2 nanotube (70 nm inner, 75 nm outer radius, 200 nm period), and (H) a TiO_2 nanohelix (125 nm helix radius, 75 nm wire radius, 600 nm period) when a X-polarized electromagnetic wave is incident on these nanostructures. A periodic boundary condition is imposed along the in-plane direction of the FTO substrate in each simulation. An identical scale bar (shown on left side) for the electric field strength is applied to (F, G and H) [382].

OAD geometries have been studied ranging from vertical [64] to tilted [63,64,284,376] nanocolumns, and from zig-zag [63] to nanohelix nanostructures [64,284,377]. Our group has recently utilized OAD TiO_2 nanocolumnar films in the fabrication of transparent DSSCs (see Fig. 5.6) [63], wherein the effects of crystallinity and deposition angle on cell efficiency were evaluated for values of α of between 70° and 85° (Fig. 5.6(B)). After annealing the samples to acquire an anatase phase [63,64,377,378], the highest cell efficiency was found with a 70° OAD TiO_2 film. This result was attributed to the relatively high dye loading capacity of these layers (see Sections 3.6 and 4.2.2). In the quest for a highly transparent DSSC, it was also found that zig-zag geometries produce less light scattering than straight tilted nanocolumns or nanohelixes (see Refs. [64,377]) and impart the cell with a higher mechanical stability. The photograph in Fig. 5.6(C) of a 5 μm-thick dye-infiltrated film with a zig-zag geometry demonstrates the high transparency of the cell (90% at certain wavelengths). Overall, a conversion efficiency of ~2.78% was reached with 3 μm thick electrodes, which is comparable with a particle electrode of similar thickness. This was achieved together with a high cell transparency, thus supporting the implementation of these devices for glass coloring and related applications in the field of fenestration.

A modified OAD methodology named GLADOX has been reported by Kondo et al. [369]. It combines the sputtering of Ti at oblique angles with a posterior anodization to produce highly porous TiO_2 hierarchical nanostructures (nanobrushes). Following annealing to induce crystallization to anatase, these nanoporous photoanodes were incorporated in a DSSC where they yielded an overall performance (conversion efficiency of ~1.27% for 1.5 μm thickness) that is comparable with a nanoparticulate reference cell of the same thickness. Improved charge transport and the potential to increase photoelectrode thickness without any significant detriment to the conduction capacity of photogenerated electrons are just some of the advantages cited for this type of nanobrush system.

5.2.1.4. Quantum dot (QD) solar cells. Generally speaking, the semiconductors used in photovoltaic devices possess a small bandgap and can potentially absorb all photons with energies above this minimum threshold. Unfortunately, owing to the small energy difference between photo-generated electrons and holes in these systems, small bandgap semiconductors produce lower potentials than wider bandgap semiconductors. Various approaches have been tried to combine the benefits of both large and small bandgap semiconductors in order to expand the range of absorbed wavelengths and use each absorbed photon to its full potential. One such attempt consisted of combining semiconductors and QDs of progressively decreasing bandgap energies to promote the absorption of radiation across the entire visible spectrum [379–381]. These QDs were made from materials such as CdS, CdSe and CdTe that strongly absorb in the visible region [379,380], and which can inject photoexcited electrons into wide bandgap materials such as TiO_2 and ZnO. Moreover, these QDs display a high extinction coefficient (the capability to generate multiple excitons) and the capability of tuning their energy absorption band through the control of their size. Utilizing these ideas, Zhang et al. [381] proposed the OAD co-evaporation (see Section 2.6) of TiO_2 and CdSe at $\alpha \approx 86°$ to deposit composite nanorods on ITO. Femtosecond transient absorption spectroscopy analysis of the charge transfer processes in this system revealed efficient electron transfer from the conduction band of CdSe QDs to the conduction band of TiO_2. This result was attributed to the high interfacial area and a strong electronic coupling between the two materials, and represents a nice example of the possibilities that OAD and co-deposition can bring to engineering compositions and nanostructures at interfaces with a strict control over chemical states.

Very recently, Schubert et al. [382] reported QDs solar cells based on the decoration of three-dimensional TiO_2 nanohelixes with CdSe QDs, as illustrated in Fig. 5.7(A). The SEM micrograph in Fig. 5.7(B) shows a characteristic cross section of the TiO_2 nanohelixes grown on FTO, clearly showing how their large and open pores can accommodate both QDs and electrolyte. As demonstrated by HAADF-STEM (see glossary), the distribution of QDs along the TiO_2 nanohelixes is quite homogeneous and densely packed (Fig. 5.7(C)). The enhanced electron transport properties reported for this system have been related to the high crystallinity of the nanohelixes (Fig. 5.7(D)), while their three-dimensional geometry seems to enhance light scattering effects and therefore the cell absorption capability and efficiency (Fig. 5.7(E)–(H)). The results of this work also suggest that one-dimensional nanorods and nanotubes with diameters in the order of a determined light

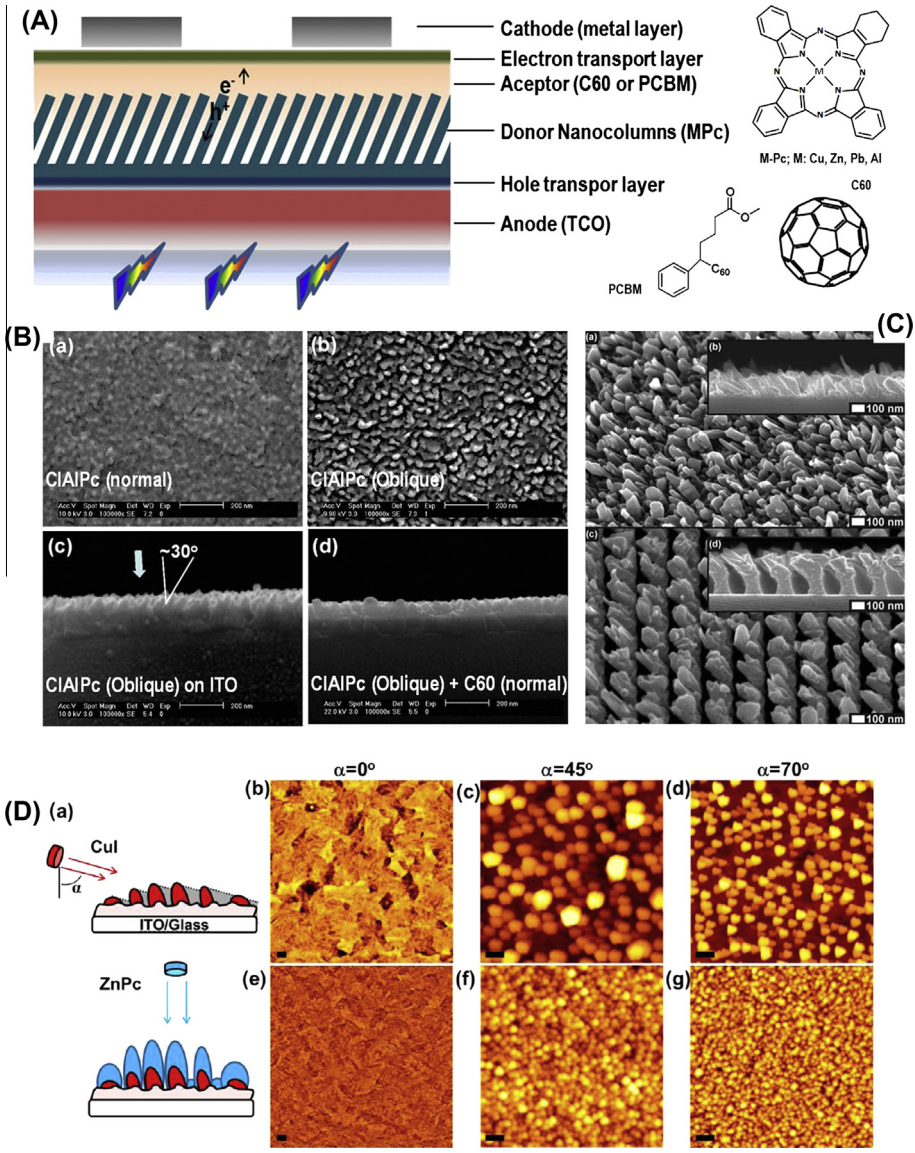

Fig. 5.8. Organic solar cells by OAD. (A) Schematic diagram of a nanostructured organic solar cell. In a typical small-molecule PV cell, nanocolumns are formed by donor-like metal phthalocyanines grown by OAD, and the acceptors by C_{60} (deposited by evaporation) or PCBM (often dissolved in chlorobenzene (CB) or 1,2-dichlorobenzene (DCB) for film casting). The molecular structures of some organic compounds used in small-molecules PV cells are shown besides the schematic. (B) Small-molecule PV cell based on the OAD of ClAlPc (donor) and subsequent perpendicular deposition of C_{60} (acceptor). Comparison between normal (a) and oblique (b) deposition of phthalocyanine shows the open porosity achieved by OAD, even with these low-thickness layers. (C and D) Examples illustrating MPc deposition by evaporation at oblique angles onto a pre-seeded substrate. (C) Normal and (inset) cross sectional SEM images of OAD CuPc deposited on bare silicon (top) and on pre-seeded Pt/Si substrates (bottom). (D) (Left) Schematic illustration of the growth of ZnPc nanostructures on CuI seeds deposited at an oblique angle. (Right) AFM micrographs of seeds grown on ITO at different angles, and (b–d) similar images after deposition of 40 nm of ZnPc. Scale bar = 200 nm. (B) is from [394], (C) from [100] and (D) from [397].

wavelength may act as guides for this wavelength rather than as scattering centers, as it is the case with nanoparticles in conventional electrodes. This solar cell based on TiO_2 nanohelix arrays exhibits a two-fold improvement in solar energy conversion efficiency (1.34%) with respect to QD solar cells based on a nanoparticle layer electrode (0.66%).

5.2.1.5. Hybrid solar cells. So far, TiO_2 has been the most common material used in the fabrication of hybrid solar cells consisting of an inorganic (e.g., TiO_2) and an organic component. Here, the TiO_2 acts as a good electron conductor, and is combined with conjugated polymeric poly(3-hexylthiophene) (P3HT, the most widely used compound for this function) or small-molecule p-channel materials that act as hole conductors. OAD TiO_2 thin films have been extensively used for the fabrication of different types of hybrid solar cells [383–385]. The intended function of the OAD oxide is to provide a well-defined intercolumnar space in which the small size of the P3HT infiltrated domains can limit the distance travelled by photo-generated e^--h^+ pairs (i.e., excitons) until the electrons are captured by the TiO_2. Relying on the same principle of confinement, various works have reported the use of other OAD thin film materials in the fabrication of hybrid polymer and small molecule solar cells. Examples of this include hybrid solar cells incorporating the semiconductor InN and Pb-phthalocyanine [386], or Si/P3HT solar cells in which Si nanowires are fabricated at low temperatures by hot-wire chemical vapor deposition at oblique angles [387] or typical OAD procedures [106,388,389].

5.2.1.6. Organic solar cells. The principle of operation for a fully organic photovoltaic (OPV) solar cell is similar to that of a hybrid solar cell in that solar light is absorbed by a photoactive material, thereby creating electron–hole pairs (i.e., "excitons") with a given binding energy that must be overcome for their effective separation. However, the short exciton diffusion lengths characteristic of organic semiconductors (e.g., up to 50 nm for some metal phthalocyanines and 10 nm for many polymers) tends to limit the thickness of the device, and consequently, the light absorption capacity of the cell [390]. Moreover, for an efficient exciton separation and carrier collection at the semiconductor's heterojunction, the two materials must possess the right offset between the highest occupied molecular orbital (HOMO) and the lowest unoccupied molecular orbital (LUMO). The microstructure needed to successfully tackle these operating restrictions is one in which electron and hole conductor materials are distributed in the form of small, interpenetrating nano-domains with a size smaller than the exciton diffusion length [390–392]. The OAD method is well suited to these morphological requirements and has been widely used to grow organic nanomaterials for OPV devices. The majority of these OAD-OPV devices incorporate nanostructures formed by the sublimation of small-molecule materials [103,393–400], although some works have also reported the use of conjugated polymers or composites formed by small molecules and a conjugated polymer [401,402]. Fig. 5.8(A) shows a simplified view of a nanocolumnar OPV device and the molecular structure of some of its components. The most common donor materials in small molecule OAD-OPVs are metal phthalocyanines (MPc) such as CuPc [103,150,395–397,399], PbPc [398] and ClAlPc [394]. The most common acceptor in these devices is fullerene, either in its sublimable (C_{60}) or soluble form as [6,6]-phenyl-C61 butyric acid methyl ester. In the latter case, the solvent choice and solution concentration critically affect the OPV performance because of difficulties in controlling the domain size and fragility of the donor/acceptor interface [396]. One of the first examples of an OPV formed through the evaporation of both donor MPc and acceptor C_{60} is presented in Fig. 5.8(B), wherein the device structure was developed by growing a ClAlPc film at oblique angles ($\alpha \approx 60°$) on ITO, followed by evaporation at a normal incidence of C_{60} [394]. The authors demonstrated that the increase in contact area at the ClAlPc/C_{60} heterojunction interface leads to an increase in efficiency comprised between 2.0% and 2.8% relative to planar heterojunctions. Equivalent experiments with OAD-CuPc/C_{60} OPV cells also resulted in efficiency improvements ranging between 1.3% and 1.7%.

To better control the shape and size of the organic photoactive nanocolumns, Brett et al. [103,395,403] thoroughly investigated the evolution of the morphology and porosity of a OAD-CuPc thin film using a pre-seeded ITO substrate (Fig. 5.8(C)) [103]. Similarly, Taima et al. [397] recently investigated the use of CuI OAD seeds to pattern the growth of ZnPc nanocolumnar arrays (Fig. 5.8 (D)). Optimized ZnPc/C_{60} bilayer cells fabricated following this approach presented a three-fold higher

efficiency (4.0%) than an equivalent planar cell. Additional results from nanopatterning with organic seeds can be found elsewhere [150,399].

The OAD of C_{60} as an electron acceptor material has also been tried in C_{60}/P3HT cells [402] and, in combination with another hole collecting material (i.e., P3CBT), for the manufacture of inverted solar cells. Although the efficiencies achieved in this case were rather low (i.e. less than 1%), the values obtained were still two-to-four times greater than those for an equivalent planar cell fabricated by solution processes.

5.2.2. Water splitting, fuel cells and hydrogen storage

The use of hydrogen as an energy vector in transportation or for the production of electricity has been proposed as a clean alternative to hydrocarbon fuels. At present, it is extensively used in chemical synthetic applications (e.g., ammonia production, or in the petrochemical, food and metal industries); however, its wider use as an energy vector faces serious scientific, technological and economic challenges regarding its production, storage and final combustion. In the sections that follow we summarize some of the recent advances in the use of OAD thin film materials for applications covering the whole chain of hydrogen technology. Considering the most commonly recurring themes addressed in recent publications on the subject, this review will be divided into three main parts: the solar generation of hydrogen, fuel cells and hydrogen storage.

5.2.2.1. Solar generation of hydrogen through photocatalytic water splitting. In the four decades since the seminal work of Fuyishima and Honda [404], in which TiO_2 was used as photo-active UV semiconductor, the energetically efficient photocatalytic splitting of water has remained a dream. Yet since then, TiO_2 has been extensively used in UV-driven photo-catalytic applications, with much effort being devoted to moving its spectral response to the visible part of the solar spectrum (e.g., by doping) or to develop alternative semiconductor compounds active in the visible spectrum and stable in aqueous media. The solar driven generation of hydrogen generally requires a semiconductor (a metal oxide or sulfide), as well as a metal acting as an electron trapper, electrode or co-catalyst. According to a simplified description of the process, the absorption of a photon by the semiconductor creates an electron–hole pair. The hole then migrates to the surface of the oxide, where it becomes trapped by OH^- groups adsorbed at the surface and yields oxygen. Meanwhile, the electron reaches the active metal and forms hydrogen by reducing protons. There are two main approaches to achieving solar-light induced water splitting: (i) the use of a photo-electrochemical cell (PEC), wherein the semiconductor and metal are connected through an external circuit, and (ii) loading a powder-based semiconductor oxide with metal catalytic particles, usually Pt, decorating its surface [405]. To efficiently convert water into molecular hydrogen and oxygen, any practical system must also fulfill the following requirements: (i) the semiconductor must possess a narrow band gap (i.e. active in the visible) to absorb a significant amount of solar light, (ii) it should promote both proton reduction and water oxidation, and (iii) it must remain stable in the electrolyte during long irradiation periods [231]. Owing to the difficulties in meeting all these requirements, recent approaches have relied on the simultaneous use of two semiconductor materials that independently promote the oxidation and reduction processes of the water splitting reaction [406]. In this way, n-type semiconductor photoanodes for oxygen evolution and p-type semiconductor photocathodes for hydrogen evolution are combined within the same system.

Aside from some intrinsic properties of semiconductors required for the intended application (i.e. a high light-absorption coefficient, low recombination probability, etc.), nanostructured materials with a high surface area are always desirable for water photo-catalytic splitting [405]. Since OAD semiconductor thin films and nanostructures comply with these requirements, they result ideal candidates for PEC devices and applications. Mullins et al. have extensively investigated the manufacturing of OAD materials for PECs and Li-ion batteries electrodes, with a concise review from 2012 provided in Ref. [231]. An outstanding result of these works has been the preparation by OAD of photo-active alpha-Fe_2O_3 photoanodes capable of collecting light in both the UV and visible regions of the solar spectrum. These authors have also reported the controlled doping of these nanostructures with Ti, Sn or Si by co-evaporation at oblique angles (see Section 2.6) [406–408] or by LPD-OAD [409]. The same co-evaporation method has also been used for the synthesis of $BiVO_4$ and Co-doped $BiVO_4$,

two active semiconductor materials capable of water photo-splitting using visible light [126]. More recently, the same group has explored the OAD deposition of tungsten semicarbide (W_2C) which, when deposited on p-Si substrates, proved to be an efficient photo-active support for Pt nanoparticles [410].

The combination of two n-type semiconductors with comparable band gaps in a single photo-anode has been proposed as a means of optimizing both the lifetime of the electron–hole pair and the charge-separation efficiency at the surface. To this end, Ludwig et al. [411] prepared by MS a layered system consisting of WO_3/TiO_2 nanostructures. For this, they followed a combinatorial approach, whereby a WO_3 layer in the form of wedges was first deposited by controlling the sputtering pressure, and then was followed by TiO_2 nanocolumnar layers deposited by MS-OAD. Similarly, Zhao et al. [412] prepared core/shell TiO_2/WO_3 and WO_3/TiO_2 nanorods through dynamic electron beam OAD by varying the zenithal angle, α, from 86° for the core to 11° for the shell. Their results suggest that the use of core/shell nanorods as photo-anodes preserves the optical properties and water splitting performance of the core, while the shell composition determines the flat band potential at the surface [413,414]. These authors have also developed a plasmonic-driven PEC cell consisting of heterostructured Ag/TiO_2 nanoarrays with silver nanoparticles embedded in the outer surface layers of TiO_2 nanocolumns [149]. The metal nanoparticles in this structure induce an enhanced photocatalytic activity under both visible- and UV–visible illumination through a plasmon-promoted electron transfer in the case of the former, and by facilitating electron–hole separation in the latter. The same authors have also pioneered the application of OAD ZnO as an n-type semiconductor for PEC cells [415]. In the course of these investigations, they compared the performance of materials deposited by PLD at both normal (PLD ZnO) and glancing at $\alpha = 86°$ (PLD-OAD ZnO) incidences with electron beam evaporation at the same incident angle (named GLAD ZnO in the authoŕs work). These deposition methods yielded different ZnO microstructures: a compact thin film (PLD), and nanoplatelet (PLD-OAD) and nanoparticulated (GLAD) thin films. From the point of view of PEC performance, GLAD ZnO generated the highest initial photocurrent, most likely thanks to a fast charge transport kinetics resulting from a small defect concentration in this material.

5.2.2.2. Hydrogen storage. Among the proposed hydrogen storage methods, the trapping of hydrogen by chemical or physical bonding into suitable materials has provided some of the highest volumetric densities reported to date [405]. The conditions required for suitable hydrogen storage applications are a high storage capacity, fast kinetics and a high reversibility of both hydrogenation and dehydrogenation processes. Additional requirements are a low-reaction temperature and operating pressure, easy activation, minimal deterioration of the material and an affordable cost [416]. Solid-state hydrogen storage involves either chemisorption or physisorption; the latter mechanism usually involving van der Waals interactions that require cryogenic temperatures. Chemisorption involves the dissociation of hydrogen molecules and formation of metal hydrides (e.g., AlH_3, MgH_2, TiH_2 and LiH), which usually requires high temperatures and a catalyst. The main problem usually encountered with these hydride compounds, however, is their high sensitivity to oxygen.

In principle, OAD nanostructures are good candidates as hydrogen storage materials because their intercolumnar space allows for a reversible volume expansion during the transformation from metal to hydride and vice-versa. Moreover, thanks to their high surface area, nanocolumns enable faster hydrogen adsorption/desorption rates than compact materials. A pioneering work related to this possibility using OAD nanostructures of $LaNi_5$ was published by Jain et al. in 2001 [417]. Following this idea, Zhao et al. investigated the synthesis and performance of Mg nanoblades both with and without vanadium decoration [418–420]. Wang et al. also applied the OAD method to fabricate Mg nanoblades decorated with Pd [416,421]. To increase the chemical stability of the system, the Pd/Mg nanoblades were protected with a conformal layer of parylene: a polymeric material that is highly permeable to hydrogen, but prevents the passing of other gases [422]. Meanwhile, the resistance of Mg nanorods to oxidation under conditions ranging from room temperature to 350 °C was also demonstrated for MS-OAD magnesium prepared under controlled conditions [423].

5.2.2.3. Fuel cells. Fuel cells convert chemical energy into electrical current through the chemical reaction of a fuel (H_2, hydrocarbons or methanol) with oxygen or other oxidizing agents. The main

components of the cell are anode, electrolyte and cathode. The type of electrolyte, fuel, working temperature and start-up time are the criteria utilized for the classification of fuel cells [424]. In this section, we summarize some of the recent applications of OAD thin films as components in proton exchange membranes or polymer electrolyte fuel cells (PEMFCs and PEFCs) at low temperatures, solid oxide fuel cells operated at high or intermediate temperature (SOFCs and IT-SOFCs) and direct-methanol fuel cells (DMFCs).

5.2.2.4. PEMFC fuel cell components. These cells operate at low temperatures and a key issue to improve their performance is to increase the catalytic efficiency of the cathode for the oxidation of hydrogen under these mild operating conditions. Gall et al. [425–428] and Karabacak et al. [127,429–431] have extensively applied OAD methodology to the fabrication of Pt-based cathodes for PEMFCs and develop Pt/C cathodes through the dynamic MS-OAD of carbon nanorods ($\alpha \sim 85^\circ$) onto flat, pre-patterned substrates, followed by posterior decoration of their tips with Pt deposited by MS in the classic (non-oblique) configuration [426]. The use of these pre-patterned surfaces yielded C layers that were highly porous in the vicinity of the substrate, but became rather compact and similar to thin films obtained by conventional MS at their ends. This topology ensures that the Pt layers deposited on top of these OAD carbon films present similar microstructures as those deposited on conventional carbon substrates. The performance of these two types of Pt/C cathode was similar at high potentials, whereas at lower potentials the performance of Pt deposited on a pre-patterned substrate was significantly higher. This difference in behavior was attributed to a more effective mass-transport of oxygen to the Pt reaction sites through the porous structure of the pre-patterned cathodes. To increase the available open porosity of the system, these authors applied an additional in-situ etching treatment once the Pt/C-OAD cathodes were inserted into the cell [427]. Meanwhile, to assess the importance of thin film porosity, they also compared the performance of compact Pt layers deposited using a conventional (non-oblique) configuration, and porous MS-OAD layers of Pt. The columnar porous electrodes were found to exhibit a higher (lower) mass-specific performance than the compact electrodes with a high (low) current density, a result that was attributed to the higher porosity of the latter and lower electrochemically active surface area of the former [425].

Karabacak et al. [429–431] focused their investigations on the MS deposition of well-crystallized Pt nanorods to improve their efficiency in oxygen reduction reactions without carbon support. To achieve this, they studied the formation of well-isolated, single-crystalline and vertically aligned Pt nanorods formed by dynamic OAD at an oblique angle of 85°, finding that the Pt OAD films exhibit a higher specific activity, higher electron-transfer rate and comparable activation energy when compared to conventional Pt/C electrodes. This enhanced performance was attributed to the single-crystalline character, larger crystallite size and dominance of Pt(1 1 0) facets in these OAD thin films.

Minimizing the Pt loading in the cathode is a common strategy to reduce the cost of PEMCS. One possibility in this regard that has been widely explored in the case of OAD films is the search for chemically stable substrates other than carbon where substrate oxidation and the resulting loss of Pt nanoparticles can be avoided or minimized. With this in mind, the use of Pt/Ti-OAD nanocolumnar systems [432], Pt/CrN cathodes [426] or Pt decorated Cr nanorods [431] have all been proposed. In the case of the latter two examples, nanostructured CrN and Cr layers prepared by MS-OAD act as supporting layers. Meanwhile, in Ref. [431], a conformal Pt layer was deposited on top of the Cr nanorods using a small angle deposition (SAD) ($\alpha < 45^\circ$) approach that yields a core/shell nanostructure in which self-shadowing effects are absent at normal incidence. This Pt(SAD)/Cr(OAD) layer configuration provides a higher oxygen reduction reaction activity and superior catalyst performance than a Pt layer deposited in a normal configuration. With the same purpose, this group recently reported the MS-OAD of Pt–Ni alloy nanorods by dynamic co-deposition at $\alpha \sim 90^\circ$ relative to two independent Pt and Ni sputter sources [127]. In this way, they demonstrated that the alloy composition and microstructure can be fine-tuned by controlling the OAD conditions, and that upon electrochemical cycling these Pt–Ni nanorods remain more stable than Pt nanorods or conventional high-surface-area Pt/C electrodes. The fabrication by OAD of niobium oxides (for PEMFCs) and Ni (for alkaline direct alcohol fuel cells, or ADAFCs) as supports for Pt cathodes has also been recently reported by Brett et al. [433,434].

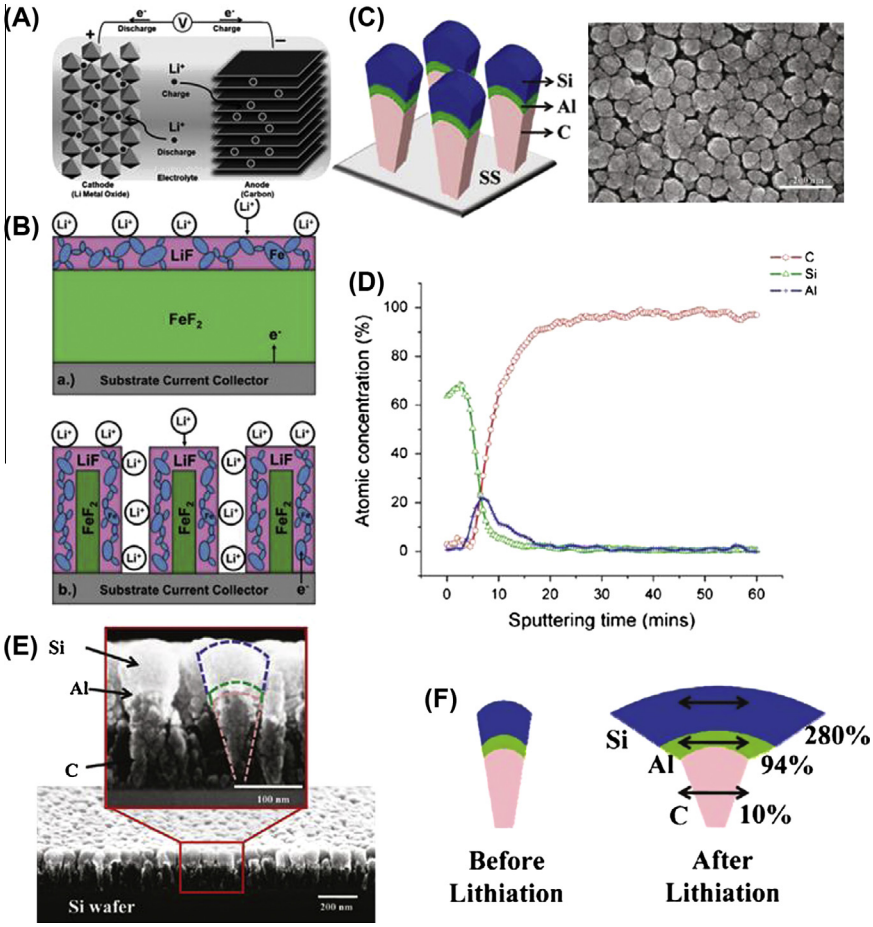

Fig. 5.9. (A) Schematic diagram of a conventional Li ion battery showing the anode, cathode and electrolyte. Li ions are extracted from the cathode and inserted into the anode during charging. This process is reversed during discharging, when Li ions are extracted from the anode and inserted into the cathode. (B) Application of an OAD microstructure to a Li-ion microbattery with FeF_2 as a cathode. (C) (Left) Schematic showing a C–Al–Si nanoscoop structure deposited on stainless steel (SS) and (right) top view SEM image of the as-fabricated C–Al–Si nanoscoop structure. (D) X-ray photoelectron spectroscopy depth profile of a C–Al–Si nanoscoop structure deposited on SS. (E) Cross-sectional SEM view of C–Al–Si nanoscoop structures deposited on a Si wafer. A magnified cross-section is also shown to highlight the C, Al, and Si regions. (F) Illustration of the principle of strain-graded multilayer nanostructures. (A) is from [440], (B) from [442] and (C–F) from [445].

Though less common, MS-OAD has been applied for the fabrication of Pt-doped CeO_2 anodes for PEMFCs [435]. In this work, carbon nanotubes (CNTs) were used as both support and template to obtain a specific three-dimensional anode morphology. Oxide layers doped with Pt were then deposited onto the tips of the CNTs by co-sputtering the two components, with the resulting configuration exhibiting satisfactory catalytic activity.

5.2.2.5. DMFC fuel cell components. One of the challenges in this type of cell, which operates at moderate temperatures, is preventing the poisoning of the Pt catalyst by carbon monoxide (CO) formed during the methanol oxidation reaction. Alternate layers of Pt and Ru nanorods deposited by sputtering in a OAD configuration have been proposed as a catalyst for this type of DMFC cell [436]. The aim of this Pt–Ru configuration is that the CO-poisoned platinum is regenerated through

its reaction with oxygen species formed on the ruthenium (i.e., $CO + O_{surf} \rightarrow CO_2$). As a result, when used in an acidic medium, the Pt/Ru OAD multilayers exhibit an electrocatalytic activity with respect to methanol electro-oxidation reaction that is higher than that of equivalent monometallic Pt nanorods.

5.2.2.6. SOFC fuel cell components. OAD has also been used for the fabrication of electrolyte layers in SOFCs working at intermediate temperatures. One of the first published examples in this research topic dealt with the OAD of porous yttria-stabilized zirconia (YSZ) thin films, wherein CeO_2 was infiltrated by spin-coating [437]. This configuration takes advantage of the excellent oxygen ion transport of doped ceria at intermediate temperatures to reduce the operational temperature of YSZ (about 1000 °C) electrolyte without affecting the power density of the device. Indeed, the resulting composite CeO_2/YSZ(OAD) system displayed a high conductivity in the 300–550 °C temperature range, with values higher than those attained with a compact CeO_2 layer. For high-temperature SOFCs, Lii et al. [438] explored the OAD of YSZ and strontia-doped lanthanum manganite (LSMO) for use as an electrolyte and oxygen reducing cathode, respectively. The comparable thermal expansion coefficient of these two ceramic materials contributes to an "in operando" stability of the system, while the triple phase boundary formed between the cathode acting as a catalyst, the reacting gas and the solid electrolyte favors exchange reactions involving oxygen gas molecules and ions in the electrolyte. This bilayer system was fabricated by dynamic e-beam OAD at $\alpha = 80°$ and 200 °C, and was subsequently annealed at 900 °C to produce a well-crystallized material with a microstructure consisting of vertically aligned YSZ nanorods and oblique LSMO nanocolumns. At 600 °C it exhibited a resistance that was ten-times lower than that of a single porous LSMO catalyst layer. Very recently, the same authors have pushed the OAD technology a step forward with the fabrication of both the anode (Ni/YST) and cathode (Samaria-doped ceria (SDC)/$La_{1x}Sr_xCo_{1y}Fe_yO_{3d}$ (LSCF)) of a SOFC [439].

5.2.3. Li-ion batteries

Owing to their flexible design and high energy density, Li-ion batteries have become one of the most popular storage systems used in portable electronics. The basic components of these batteries are cathode, anode and electrolyte. As shown schematically in Fig. 5.9(A), they operate by extracting Li ions from the cathode and inserting them into the anode during charging [440,441]. This process is reversed during discharging, when Li ions are extracted from the anode and inserted into the cathode. Typical cathode materials are laminar oxides ($LiCoO_2$ and TiO_2), spinels ($LiMn_2O_4$) and transition metal phosphates ($LiFePO_4$), while common anode materials include Si, graphite, carbon and Sn. A standard electrolyte consists of solid lithium salt in an organic solvent. The nature of the insertion and extraction mechanisms varies from the electrochemical intercalation of layered oxides and graphite, to alloy formation with Sn or Si. The electrode's performance is typically quantified in terms of its charge capacity per unit weight, a functional parameter that is directly linked to the electrode's porosity [440]. The superior performance of porous materials stems from the fact that a high electrode/electrolyte interfacial area favors a rapid ion-coupled electron transfer rate and provides direct access to the bulk and surface atomic layers (Fig. 5.9(B)) [442]. Furthermore, nanosized and structurally disordered materials can better accommodate volume changes and lattice stresses caused by structural and phase transformations during lithiation/delithiation [231]. Films deposited by OAD comply with most of these requirements, and so the technique has been applied to the fabrication of both anodes [125,231,443,80,444–447] and cathodes [231,442,448–450].

Silicon is a material very well suited to Li-ion battery anodes because its nominal charge capacity can exceed ten-times that of graphite. However, Si anodes must also face the problem of the huge volume change (about 400%) that occurs during the insertion/extraction of Li ions. The stress associated with this can cause cracking and pulverization of the Si anodes, eventually leading to a loss of electrical contact and fading of electrical capacity [440]. Brett et al. [443] have demonstrated the advantages of OAD Si films used as three-dimensional Li-ion battery anodes by showing that vertical Si nanorods (porosity ca. 80%) have twice the expected capacity of a compact film, and can therefore sustain more than 70 insertion/removal cycles without any significant capacity fade [80]. Koratkar et al. extended the OAD method to the growth of Si nanorods on a Cu foil for their direct implementation in the cell [440]. Other groups had previously demonstrated that OAD Si nanosprings display a high compliance

and offer enhanced stress resilience during Li ion exchange [451]. In recent publications, different authors have also proposed advanced designs for a battery anode that combines several materials (carbon, aluminum and silicon) in each nanocolumn with a so-called strain-graded nanoscoop microstructure (Fig. 5.9(C)–(F)) [445,452]. This system can undergo rapid volume changes without interfacial cracking or delamination because its stacked microstructure provides a gradual variation of strain due to the different volumetric expansion of the three materials when alloyed with lithium. The manufactured anodes were deposited by DC-MS and consisted of an array of C nanorods with an intermediate layer of Al capped by a scoop of Si. The carbon nanorods were prepared by dynamic OAD with $\alpha = 85^{\circ}$, whereas the subsequent Al and Si flux incidence was normal to the carbon nanocolumns. Fig. 5.9(C)–(E) shows a schematic representation of the nanoscoops, together with their characteristic normal and cross-sectional views and corresponding XPS depth-profile. Fig. 5.9(F) presents the estimated variation in volume following lithiation, showing that a large volume expansion of Si is possible without provoking device failure thanks to the introduction of an intermediate layer of aluminum. This provides a gradual transition of strain from carbon to silicon and permits stable operation of the electrode under numerous high-rate charge/discharge processes. Another type of composition-graded Si-based nanorods with controlled amounts of copper, which was prepared by OA co-deposition, has also shown significant improvements in conductivity and an enhanced adhesion to substrates [125,444]. In another example, pure OAD Al anodes grown on titanium/glass substrates demonstrated a specific capacity close to the theoretical maximum, as well as an average columbic efficiency of $\sim 91\%$ [80].

Mullins et al. proposed an alternative procedure to increase the stability of Si anodes, which consisted of dosing small amounts of oxygen during the growth (partial bulk oxidation) of Si OAD films, followed by posterior annealing at low temperature in air (surface oxidation). The formation of these bulk and surface oxides provides a high capacity (2200 mA h/g) with virtually no capacity loss during the first 120 cycles, and only a slight capacity fade ($\sim$0.15% per cycle) between 150 and 300 cycles. As a result, the anodes retained up to $\sim$80% of their original capacity after 300 cycles [453]. These authors have also explored the use of silicon–germanium alloys [446] and pure germanium [454] as anode materials. Germanium is expected to be a suitable material for battery anodes as its high electronic and ionic conductivity should allow for a very high charge/discharge rate. Thus, by systematically changing the composition of $Si_{(1-x)}Ge_x$ alloy, it was found that the anode's specific capacity decreased and its electronic conductivity and high-rate performance increased with germanium content. Meanwhile, an outstanding result found when using pure germanium OAD thin films in sodium-ion batteries was a high rate of operation at room temperature with this anode material [454]. For an overall view of this work on ion batteries, readers are redirected to a recent review of this group [231], where in addition to summarizing their advances in the fabrication of anodes, they also comment on the use of amorphous OAD TiO_2 films as cathodes (see Ref. [126]).

Various OAD nanostructures have been used recently as lithium battery cathodes. For example, needle-like $LiFePO_4$ films deposited by off-axis pulsed laser deposition have been used for this purpose [448,449], as well as FeF_2 cathodes prepared by dynamic OAD with tailored periodic vertical porosity [442] (Fig. 5.9(B)). Unlike the behavior of dense thin films, the ion and electron transport properties of these nanostructured cathodes are independent of their vertical thickness. As shown in the bottom part of Fig. 5.9(B), this is because the vertically aligned porous microstructures of these films assures a high accessibility of Li^+ ions along the whole electrode, as well as a substantial increase in area of the substrate–electrolyte-film triple point interface. Moreover, with this particular morphology, it is possible to achieve high conductivities with cathode thicknesses up to 850 nm, which is about six-times the maximum thickness attainable with FeF_2 dense films due to their relatively insulating nature.

5.2.4. Electrochromic applications

During recent years, electrochromic coatings have evolved into a practical solution for indoors energetic control, displays and other esthetic applications [455]. Although different oxides and organic compounds are also utilized, the most popular system for fenestration and house-light control is based on tungsten oxide as an active electrochromic layer that is tunable from a deep blue to a transparent state, and a nickel oxide layer as a contra-electrode. Electrochromic film devices based on tungsten oxide consist of a reducible WO_3 layer, a second thin-film electrode and an electrolyte containing a

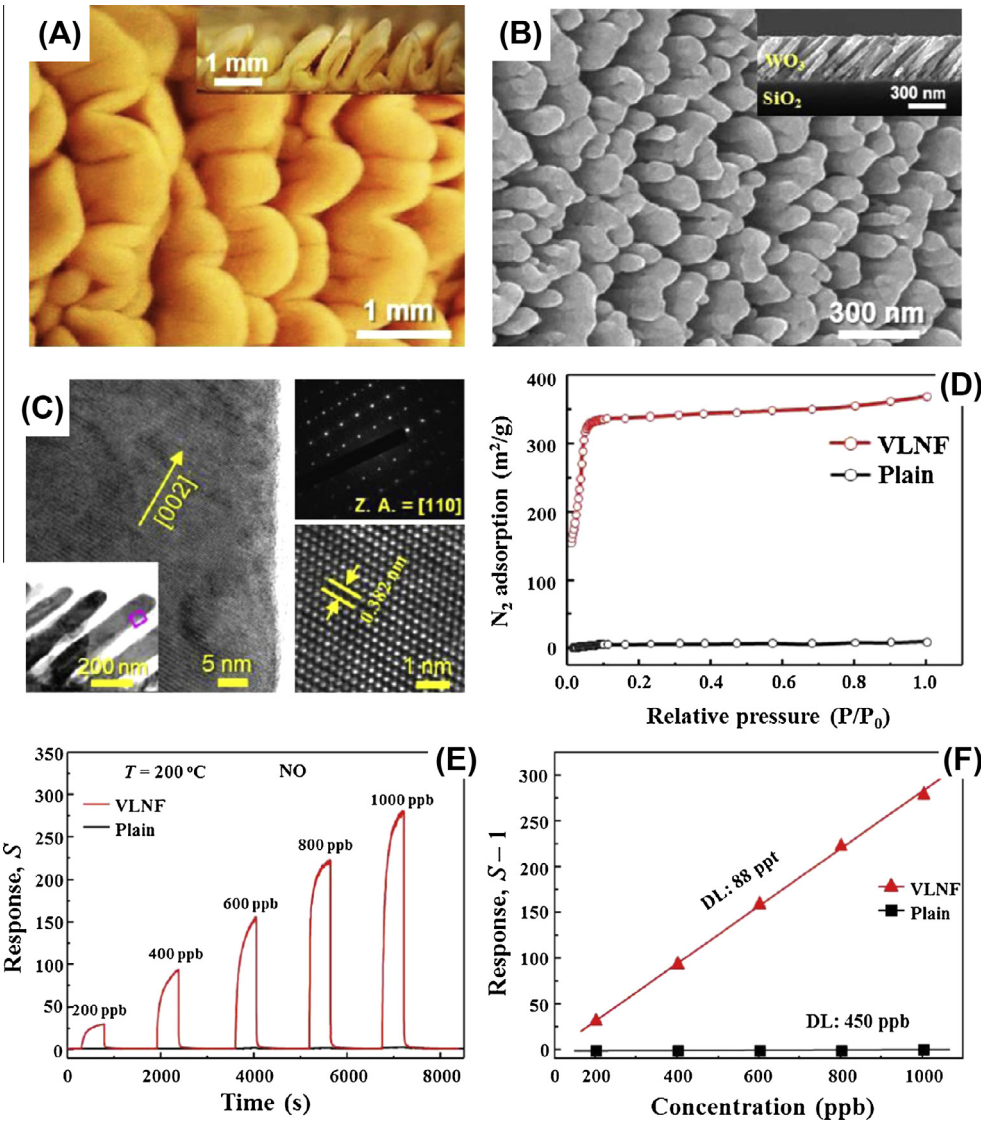

Fig. 5.10. (A) Normal and cross sectional (inset) photographs of chicken intestine villi. (B) Normal and cross-sectional (inset) SEM images of MS-OAD WO_3. (C) High resolution TEM and electron diffraction analysis showing the highly crystalized state of the nanorods. (D) N_2 adsorption isotherms of a 380 nm-thick WO_3 OAD thin film compared with that of a 380 nm-thick flat film. (E) Dynamic sensing transients of an OAD sensor and a sensor based on a dense WO_3 film (plain sensor) to 0.2–1 ppm NO at 200 °C in a 80% relative humidity atmosphere. (F) Response of OAD and plain sensors as a function of NO concentration at 200 °C. Theoretical detection limits (DL) of both sensors are also presented [471].

M^+ cation (typically H^+ or Li^+) that is incorporated into the film during the reduction cycle. Optimal device performance therefore requires rapid incorporation of M^+ ions into the film and their reversible release to the electrolyte during reduction and oxidation cycles, respectively (i.e., $WO_x + e^- + M^+ \rightarrow WO_x$ (M) for the reduction cycle). Optimizing the electrochromic behavior involves increasing the incorporation capacity and maximizing the diffusion rate of M^+ cations within the film structure. These two requirements are fulfilled if the thin film of the cathode has high porosity, making OAD thin

films prepared by either thermal evaporation or MS ideal candidates for this purpose. Accordingly, Granqvist et al. [456] reported in 1995 the preparation of WO_3 electrochromic thin films by MS-OAD; however, even if the open and highly porous character of these films is very promising for their implementation as fast switchable electrochromic layers, only more recent attempts have incorporated OAD oxide thin films for this purpose [311,457,458]. These recent studies report the MS-OAD of $W_xO_zSi_y$ [311,457] and $Co_xO_zSi_y$ [458] solid-solution thin films and their implementation as electrochromic cathodes. The high porosity of such films makes them very suitable for this application, with the integrated devices presenting fast response times and a high coloration capacity. In addition, these mixed oxide solid solutions add the possibility of controlling the optical properties (e.g., refraction index, absorption coefficient, etc.) in the bleached state by varying the relative amount of silicon with respect to either W or Co.

5.2.5. Piezoelectric nanogenerators and piezotronic effect

One of the most promising options for the development of generators directly implementable in wireless nanosystems is to apply the piezoelectric effect to convert mechanical energy (such as body movement or muscle stretching), vibrational energy (such as acoustic or ultrasonic waves) or hydraulic energy (such as body fluid flow) into electricity. This topic has experienced ceaseless development in recent years thanks largely to the works of Wang et al. [459,460]. The piezoelectric effect relies on the generation of electrical voltage by imposing a mechanical stress/strain on a piezoelectric material and vice-versa. Typical examples of piezoelectric nanogenerators are based on 1D ZnO nanostructures, although other materials such as ZnS, CdS, GaN and InN are expected to show an improved performance because of their relatively higher piezoelectric coefficient. Although still in the very early stages, promising results pertaining to the exploitation of OAD piezoelectric materials have recently appeared in the literature [460–463]. The MS-OAD of ZnO and orientational control of obliquely aligned epitaxial InN nanorod arrays by OAD using a plasma-assisted molecular beam epitaxy system have been descried in Refs. [462,463]. In some of these works, the piezoelectric output voltage was determined by scanning the Pt(Si) tip of an atomic force microscope along four different directions with respect to the tilt angle of the ZnO NWs. These studies revealed an anisotropic generation of electricity as a function of the characteristic geometry of the OAD films [462]. Meanwhile, other authors have reported an increase in the output power generated by growing InN nanorods tilted along the direction of the piezoelectric field, while also applying mechanical deformation with a force normal to the surface [461].

5.3. Sensors

Nanosensors is another area of application that has greatly profited from the inherent high surface area and controlled nanoporosity of OAD nanostructures when utilized as transducers for the determination of different chemical analytes. The use of OAD thin films for biosensor applications will be reviewed in Section 5.6 and the use of photonic detection methods in Section 5.5. Most cases discussed here refer to electrical gas sensors, although a couple of examples using acoustic and optofluidic devices for liquid monitoring are also critically described. A short subsection devoted to particular applications in the field of pressure sensors and actuators complete this analysis of sensors.

5.3.1. Gas and vapor sensors

Typical gas and vapor sensor devices that use OAD thin films as transducer elements rely on changes in resistivity or electrical capacitance upon exposure to a corresponding analyte. Capacitance humidity sensors consisting of OAD TiO_2 nanostructures deposited on interdigitated electrodes were developed some time ago by Brett et al. [202,464–466]. Although other OAD materials respond to humidity variations (e.g., SiO_2 and Al_2O_3), sensors utilizing TiO_2 exhibit the greatest change and show an exponential increase from $\sim$1 nF to $\sim$1 μF when the humidity changes from 2% to 92% [467]. The same group developed room temperature SiO_2 OAD sensors to selectively detect methanol, ethanol, 1-propanol, 2-propanol and 1-butanol by monitoring both the frequency dependent capacitance and impedance changes in the system [468]. In this work, it was also determined that for ethanol and 1-butanol sensor aging is reduced by UV illumination, a treatment that had no effect when

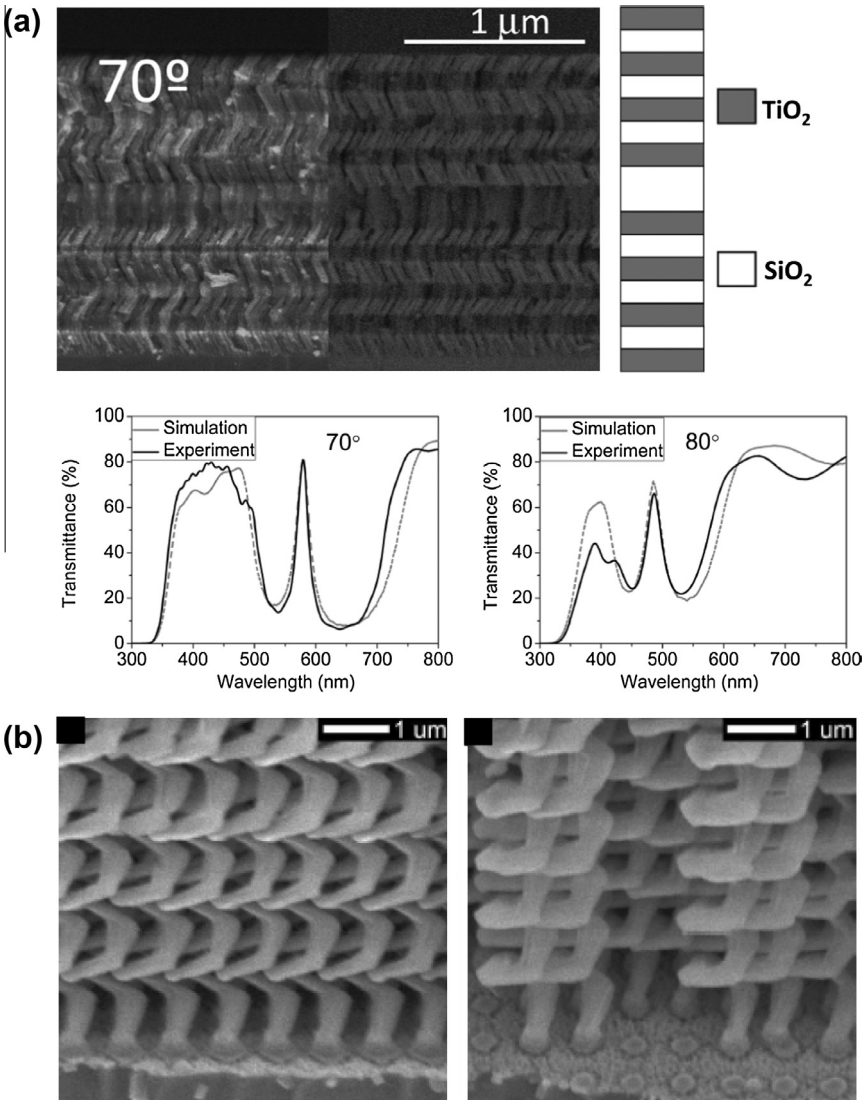

Fig. 5.11. (a) SEM micrographs of a 1D Bragg microcavity fabricated with a central defect layer within the periodic distribution of high index (TiO_2) and low index (SiO_2) layers deposited by OAD at 70°. The accompanying schematic shows the stacking order of the component layers. UV–vis transmission spectra (experimental and simulated) are shown in the bottom for microcavities deposited at 70° and 80°. The defect layer in the center of this stacking gives rise to a narrow resonant peak in the center of the photonic band-gap [285]. (b) SEM micrographs of square-spiral Si structures arranged in a tetragonal lattice to form a 3D photonic crystal. This arrangement is obtained by deposition on a substrate with a periodic topography of small seeds, as shown in the right micrograph [506].

detecting other alcohols. Capacitive humidity sensors based on OAD polyimide have also been reported [469].

Different conductometric oxide sensors based on the variation in resistance of a transducer material upon exposure to the analyte (mainly oxidative or reducing gases and volatile organic compounds (VOCs)) have been prepared by OAD. For example, ZnO nanorods prepared by MS-OAD present a high reproducibility and sensitivity, fast response and short recovery times in the detection of hydrogen

and methane at mild temperatures (150 °C) [470]. Similarly, tungsten oxide (WO_3) nanocolumns have been used as conductometric sensors of NO, NO_2 and ethanol [471–473]. To illustrate the possibilities and lay-out of a typical OAD conductimetry sensor device, Fig. 5.10 summarizes some of the results obtained with one of these WO_3 sensors [471] in the detection of NO. This particular system consists of MS-OAD WO_3 films grown on interdigitated Pt electrodes. A key feature of the WO_3 nanorods (Fig. 5.10(B)) is their resemblance to intestinal villi (Fig. 5.10(A)), even after crystallization by annealing at 500 °C (Fig. 5.10(C)). Nitrogen isotherms and BET analysis revealed that the surface area of the nanostructured film was about 30-times greater than that of a flat, compact reference layer (Fig. 5.10 (C)). This resistive sensor was tested with different analytes, including NO, as a function of temperature at a relative humidity of 80% (Fig. 5.10(E) and (F)). The results obtained confirmed a NO detection limit of as low as 88 ppt and an extremely high selectivity to NO under humid conditions approximating human breath even in the presence of ethanol, acetone, NH_3 or CO. These results support the possibility of fabricating high quality sensor elements for breath analyzers to diagnose asthma, or for the detection of NO in aqueous media.

The magneto-optical detection of minority components is a new and sophisticated method of detection based on the coupling between a plasmonic signal and a ferromagnetic layer under the influence of a magnetic field. In a recent work, we proved that the sensitivity of such a device could be enhanced by depositing a thin OAD TiO_2 layer onto the magneto-optical layer structure [474]. This transparent layer ensured a significant increase in the surface area available for adsorption, without affecting the optical signal coming from the device.

One way of avoiding interference problems during the detection of multicomponent analyte mixtures is the incorporation of various sensing elements in the same device, and the use of a mathematical factor or multicomponent analysis procedure. Electronic noses (e-noses) are a typical example of this type of devices. Recently, Kim et al. [475] developed a multi-sensor e-nose chip incorporating six different nanostructured gas-sensing layers prepared by OAD: TiO_2 thin films, TiO_2 nanohelices, ITO slanted nanorods (see Ref. [339]), SnO_2 thin films, SnO_2 nanohelices and WO_3 zig-zag nanostructures. These films were monolithically integrated onto a sapphire wafer through a combination of conventional micro-electronics processes and OAD. The thin film resistivity was measured through interdigitated electrodes, while the OAD nanostructures were tested in a top–bottom electrode configuration. The prototype e-nose showed specific sensitivity for various gases such as H_2, CO and NO_2.

5.3.2. Liquid sensors

Detection in liquid media has also benefitted from the use of OAD thin films incorporated into ultrasonic devices or complex photonic structures produced by stacking thin film layers with different refractive indices. Sit et al. [476,477] studied the use of nanostructured OAD SiO_2 thin films to enhance the sensitivity of surface acoustic wave (SAW) sensors for liquid monitoring. Here, SiO_2 films were deposited on top of SAW devices operating at 120 MHz and were then implemented in an oscillator circuit. The evolution of the frequency signal was monitored as a function of the relative humidity, as well as for different viscous mixtures of glycerol and deionized water. In an early work [478], a similar approach was used for the in-situ evaluation of the elastic properties of SiO_2 nanocolumns deposited on a SAW circuit.

Our group has developed a very simple but effective photonic device for the optofluidic determination of the concentration of liquid solutions. This method utilizes a Bragg microcavity consisting of periodic and alternant SiO_2 and TiO_2 thin films of equivalent thickness, plus a thicker SiO_2 layer acting as a defect; all of which are prepared by e-beam OAD (see Section 5.4 and Fig. 5.11(a)) [285]. The resonant absorption peak characteristic of this type of photonic structure shifts when the system is infiltrated with a liquid, and the magnitude of this shift can be directly correlated with the concentration of the solution. This system has proven to be very useful in monitoring low and high concentrations of glucose or NaCl in aqueous solutions, or the proportion of components in a glycerol/water mixture.

5.3.3. Pressure sensors and actuators

Study into the mechanical properties of OAD thin films and three-dimensional nanostructures such as nanohelixes and nanosprings has received continuous attention in reviews [16] and numerous

works on the subject [66,479–486]. These studies have provided very useful information regarding the elastic and mechanical properties of this type of thin films and nanostructures; knowledge that has been applied to the development of different sensor devices for the monitoring of mechanical forces and pressure. For example, Gall et al. [487] have reported the fabrication of a nanospring pressure sensor based on zigzag and slanted Cr OAD nanostructures. These nanocolumnar arrays exhibited a reversible change in electrical resistivity upon loading and unloading that amounted to 50% for zigzag or nanospring structures, but only to 5% for tilted nanorods. An accompanying change in the resistivity of these sculptured films was attributed to the formation of direct pathways for electric current when the nanosprings are compressed. Individual metal microsprings have also been used as fluidic sensors and chemical-stimulated actuators by virtue of their reliable superelasticity; their flow rate being calibrated by determining the elongation of Ti or Cr-decorated polymeric microsprings [488]. Meanwhile, a very sensitive pressure sensor based on the piezoelectric properties of embossed, hollow asymmetric ZnO hemispheres prepared by OAD has been recently reported [489].

5.4. Optical applications and devices

The analysis and modeling of the optical properties of OAD thin films has been one of the most important areas of their study. Indeed, the optical properties represent one of the most valuable tools for assessment over microstructure and composition distribution in this type of films, as they are controlled by the deposition geometry and other experimental conditions. Ongoing advances made in this area have been extensively reviewed in excellent reports dealing with OAD thin films [16,17], while a specific up-to-date analysis of their optical properties, including aspects such as their design, fabrication, theoretical analysis and practical examples, can be found in Ref. [21]. A comprehensive evaluation of theoretical calculations and simulations of the optical properties of OAD films, multilayers and other less complex devices can be found in the monograph of Lakhtakia and Messier [20]. Taking into account the extensive available knowledge regarding the optical properties of OAD thin films and multilayers, and considering that a clear distinction between the optical properties and potential applications is somewhat artificial, the present review has been limited to an analysis of aspects closer to specific operating devices and their final applications. Readers more interested in the fundamentals of optical properties are referred to the previous publications already mentioned.

5.4.1. Passive optical applications

As a result of their tilted nanocolumnar structure, OAD thin films are optically anisotropic; as such, transparent dielectric films deposited by OAD are intrinsically birefringent, whereas metallic absorbing films are dichroic. The anisotropic character of OAD thin films is a precise feature that was first investigated during the earliest stages of research into these materials [1,2].

Preceding sections have provided ample evidence of the fact that the OAD technique is a straightforward method for the fabrication of transparent dielectric optical films. This procedure has been successfully utilized for the synthesis of single-layers, multilayers and graded refractive index films, all of which have been utilized as antireflective coatings, rugate filters, Bragg reflectors, waveguides, etc. Examples of some of the dielectric materials prepared by OAD include SiO_2, TiO_2, Ta_2O_5, MgF_2, ZnO, Si, Y_2O_3, Eu-doped Y_2O_3, ZrO_2, Al_2O_3, Nb_2O_5 and ITO [17,20,21]. Other transparent conducting oxides (TCO) have also been prepared by OAD for integration into a large variety of optoelectronic devices (see Section 5.1). In addition, a considerable number of organic materials have been deposited in the form of OAD optical coatings [71,103,394,400]. Such a wide range of OAD coatings has allowed them to cover the entire spectral range required for their use as interference filters.

A characteristic feature of the OAD technique is the potential to change the nanocolumnar direction by modifying the deposition geometry. This can give rise to two- and three-dimensional structures constructed from multisections of oriented nanocolumns, zig-zags, helices or S/C-shapes (see Section 2.4). According to Lakhtakia and Messier [20,490], there are two canonical classes of OAD structures. The first type, sculptured nematic thin films, includes slanted columns, zig-zag, and S- and C-shaped columns. These materials have been extensively used for the fabrication of optical components such as polarizers, retarders or filters [66,491,492]. The second class encompasses helicoidal columns and chiral-sculptured thin films, which are able to reproduce the behavior of

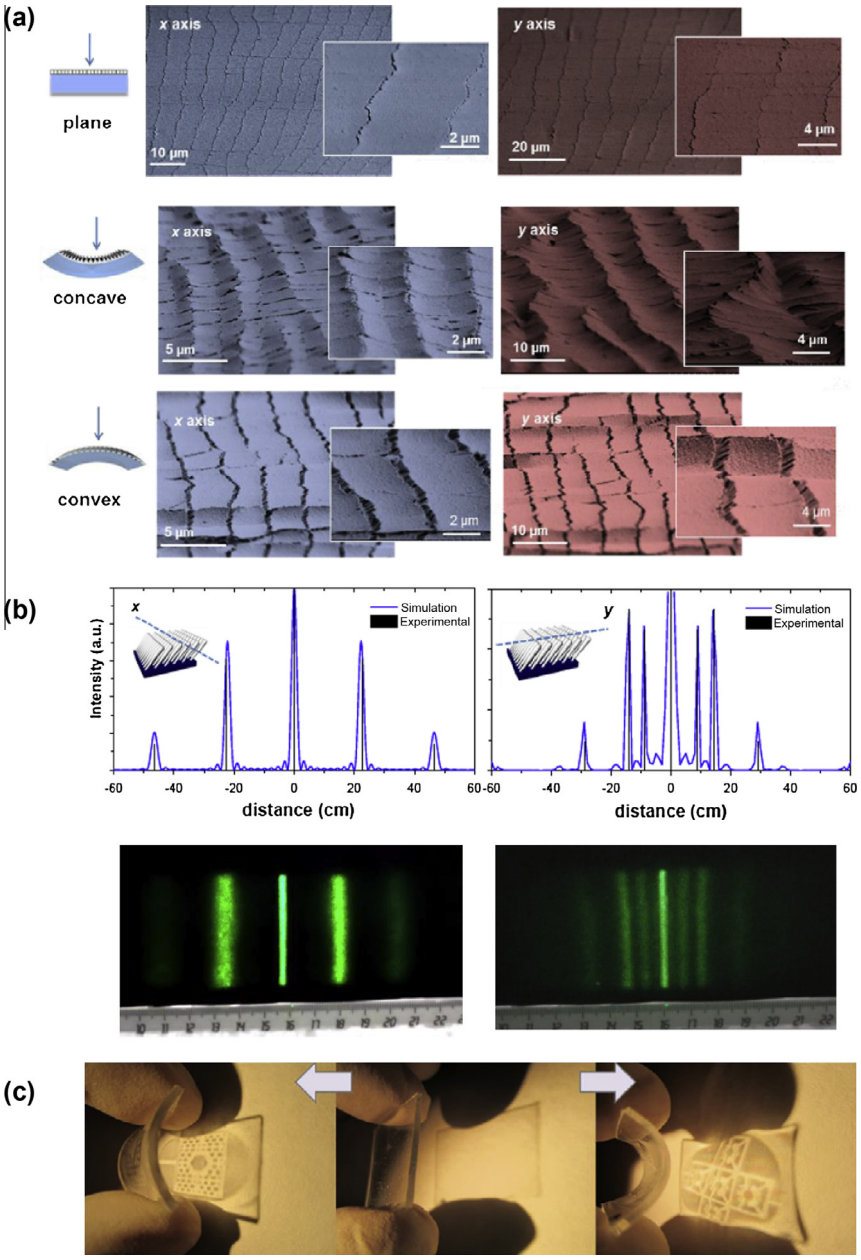

Fig. 5.12. (a) SEM micrographs of two PDMS foils coated with nanocolumnar SiO_2 films deposited by OAD. The images correspond to a flat foil (top) and to the same foil bent to form a concave (middle) or convex (bottom) surface, as indicated. The foils were bent along the film's bundling *x*-axis (left panel in blue) and along its growth *y*-axis (right panel in red). (b) Fraunhoffer diffraction patterns obtained by illuminating a concave surface bent along the bundling *x*- (right) and growth *y*- (right) axes with a 532 nm laser beam. The experimental diffraction patterns can be simulated by assuming a Fraunhoffer diffraction by the periodic undulation observed in the concave surfaces shown in (a). (c) Examples of invisible labels fabricated by depositing a nanocolumnar SiO_2 thin film on each side of a PDMS foil using two different shadow masks. The flat double-sided coated foil is transparent (central picture). The projected light reveals the pattern printed on the concave surface, whereas the pattern on the opposite convex surface remains invisible (left and right pictures) [507].

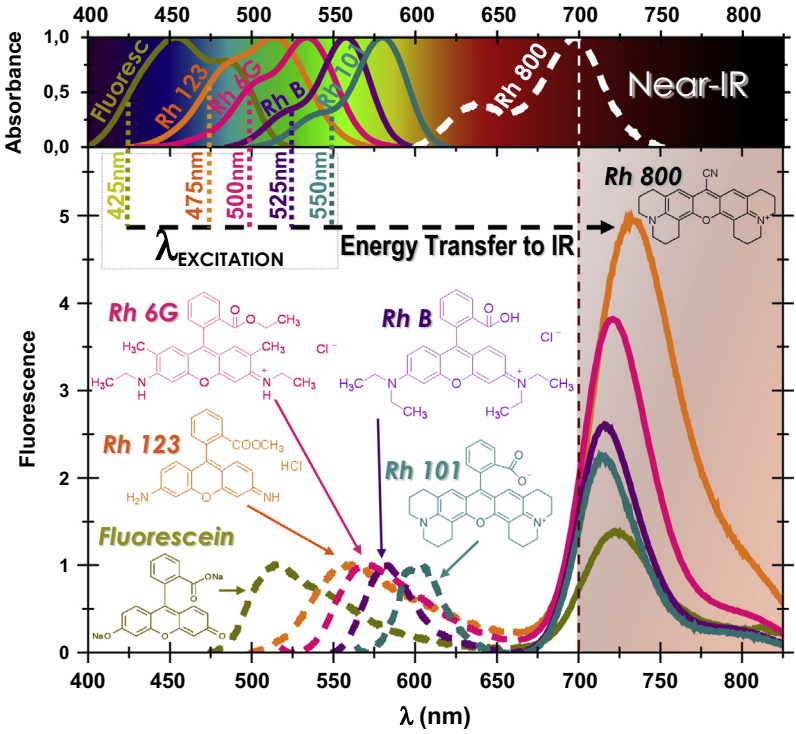

Fig. 5.13. Normalized absorption (top) and fluorescence (bottom) spectra corresponding to one of the five dye couples of Rhodamine X–Rhodamine 800 (Rhodamine X: Fluorescein, Rhodamine 123, Rhodamine 6G, Rhodamine B and Rhodamine 101) anchored in SiO_2 OAD thin films. Dashed and full lines correspond to bands attributable to the emission from Rhodamine X and Rh800 molecules, respectively. The Rhodamine 800 emission is induced by an energy transfer processes from the other rhodamines when excited by absorption at the wavelengths indicated in the upper panel [513].

cholesteric liquid crystals by preferentially reflecting circularly polarized light of the same handedness as the film's microstructure (circular Bragg phenomenon). Chiral filters based on this principle and presenting different degrees of complexity have been successfully designed and fabricated by OAD [77,79,493–495].

As explained in Section 2.2, changing the deposition geometry or using more than one deposition source (Section 2.6) permits a gradual in-depth change in composition, density and microstructure of films. In terms of their optical properties, this means that either by alternating the type of deposited material and/or changing the densification, the refractive index profile along the film thickness can be effectively tuned. This possibility has been used to fabricate antireflection coatings [236,496,497] and rugate filters that are characterized by a sinusoidal index profile [90,92,498,499]. One-dimensional photonic crystals (also designated as Bragg stacks) and Bragg microcavities have also been fabricated by successively stacking oxides of different refractive indices (e.g., low index SiO_2 and high index TiO_2) [285,500–502] or with porous-graded Si posteriorly oxidized by high temperature annealing [503]. An example of a Bragg microcavity fabricated by stacking different layers of SiO_2 and TiO_2 prepared by OAD is presented in Fig. 5.11(a). Such optical structures depict a narrow resonant peak that is affected by the infiltration of liquids in their pores, a feature that has been utilized for the development of responsive systems to determine the concentration of solutions (see Section 5.3). More complex 3D square-spiral photonic crystals with a tetragonal arrangement of elements that exhibits well-defined band gaps in the visible, NIR or IR spectrum have also been fabricated by OAD (see Fig. 5.11 (b)) on lithographically pre-patterned substrates [504–506].

An emerging topic in the field of electronics and photonics is the development of flexible devices. A flexible optical component combining the intrinsic nanometric order of OAD thin films with an additional micron-level arrangement has been recently developed by our group through the OAD of an oxide thin film on elastomeric PDMS foils [498]. Manually bending this device gives rise to a switchable grating formed by parallel crack micropatterns (Fig. 5.12(a)). An outstanding feature of this type of foldable optical component is that the crack spacing is directly determined by the nanocolumnar structure and material composition of the OAD film (the former controlled by the zenithal angle of deposition), but it is independent on either the film thickness or foil bending curvature. We have attributed this microstructuration effect to the *bundling* association of the film's nanocolumns (see Sections 3.6.2 and 4.2.2). These self-organized patterned foils are transparent in their planar state, yet can work as a customized reversible grating when they are bent forming the concave surface shown in Fig. 5.12(b). The labeling possibilities of this type of optical component are illustrated in Fig. 5.12(c).

5.4.2. Active optical applications and devices

Within this category we consider OAD thin films and more complex device structures capable of actively responding to excitation from the medium. Luminescent films, optical sensors and plasmonic effects will be commented briefly to illustrate the potential applications in this domain.

5.4.2.1. Luminescent films. A standard approach to the manufacturing of luminescent films is the OAD of intrinsically luminescent materials. Here, the nanocolumnar-tilted orientation of conventional OAD films ensures that the luminescent emission of the material is linearly polarized [73]. Similarly, helical structures of luminescent materials produce a circular polarized emission [71]. In all cases, the polarization of light seems related to a widely studied filtering effect produced by the particular nanostructure of each thin film or structure [73].

Another possibility in the synthesis of luminescent OAD-based materials relies on the anchoring of luminescent molecules on the internal surface of thin films; the basic principles of which were discussed in Section 3.6.2. The incorporation into the nanocolumnar film of a luminescent or alternative guest molecule with specific functionality [246] presents some similarities with conventional synthesis routes utilized for the sol–gel method [508–510] and wet-chemistry processes [511] used in the fabrication of hybrid luminescent materials. In these hybrid OAD films, however, functional molecules are anchored to the chemical functionalities of oxide surfaces (e.g., the –OH groups in TiO_2 or SiO_2 nanoporous films) either electrostatically [243,246,512] or by forming covalent bonds [244]. The luminescence of the resulting hybrid nanocomposite depends on the dye distribution (i.e., the aggregation state of dye molecules or simply the distance between them) within the porous nanocolumnar structure of the films. Different activation processes such as thermal treatment [243] or the UV-illumination of semiconducting host films [242] have been used to enhance or modify the luminescence properties of the films. An interesting example of the possibilities offered by this anchoring approach is the energy transfer process made possible from the visible to near-IR spectrum exhibited by rhodamine laser dye pairs adsorbed in nanocolumnar SiO_2 OAD thin films [513]. Fig. 5.13 shows that when different rhodamine pairs (all of which include Rhodamine 800 as a near-IR emitting dye) are adsorbed in the host films, excitation of the visible-spectrum absorbing rhodamine produces a very intense luminescence in the infrared. This luminescence cannot be induced by the direct excitation of Rhodamine 800, and has been attributed to an energy transfer induced by the formation of luminescent J-heteroaggregates between the two classes of dye molecules; a phenomenon observed for the first time in these hybrid OAD films [513]. Although this is still largely unexplored, the possibilities for this type of process for wavelength-selective wireless optical communications (e.g. inside satellites) are quite promising, as most optical detectors function in the near-IR spectrum.

5.4.2.2. Optical sensors. OAD photonic architectures are ideal for the development of photonic sensors. In these systems, the large pores separating the nanocolumns in the films enable the rapid access and interaction of analyte molecules either directly with their internal surface or with active molecules anchored on it. Generally, analyte adsorption is the main limiting step of the sensing response in an OAD structure, which is in stark contrast to the diffusion-limited sensing typical of bulk sensors

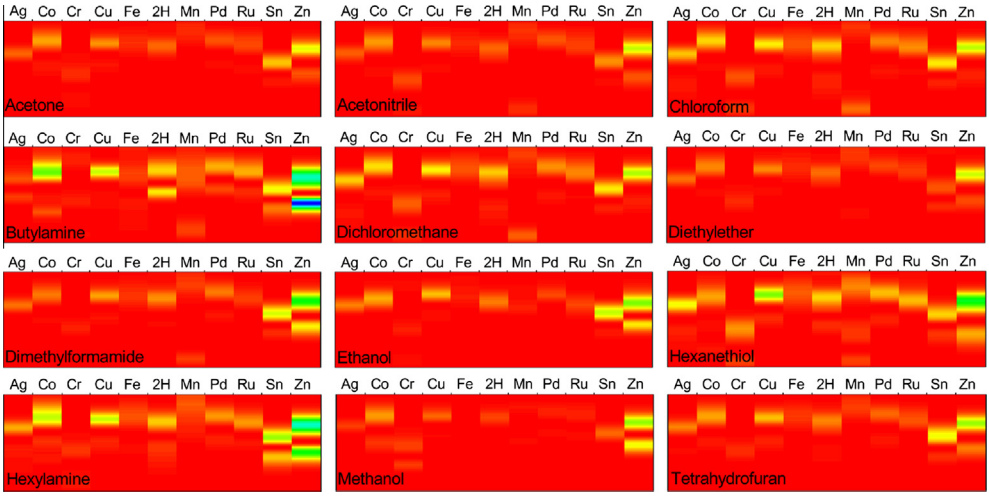

Fig. 5.14. Identification patterns obtained for the indicated volatile organic analytes adsorbed on nanocolumnar OAD TiO_2 thin films functionalized with metallic porphyrins. Porphyrins are 5,10,15,20-tetrakis(4-carboxyphenyl)-21H,23H-porphyrin and ten metal derivatives. In the metal derivatives, two hydrogen atoms in the center of the molecule are replaced with Ag(II), Co (III), Cr(II), Cu(III), Fe(III), Mn(III), Pd(II), Ru(II), Sn(IV) or Zn(II). Color scale goes from red to blue, where red indicates no change between exposed and non-exposed spectra and blue is the highest detected change [247].

[17]. Filing the pores of the OAD films in the final stage of massive infiltration or adsorption can be directly monitored by (for example) measuring gas adsorption isotherms (see Section 3.6.3). The optical properties of OAD films and multilayer structures also respond to the environment, be that a gas or liquid that condense and/or fill the pores occupying the inner volume of the films. The dependence of the film's refractive index and the overall optical response of these systems on the conditions of the medium have been one of the main motivations for using nanocolumnar films or nanostructures as optical sensors. Some examples of optical sensors based on changes in the optical properties of OAD structures are the use of helical nanocolumns [490] and Bragg stacks [285,502] for infiltrated liquid sensing, or the use of photonic crystals for high-speed water vapor detection [514,515] and colorimetric detection of humidity [516] (see Section 5.4 for a more complete review of humidity sensors).

One drawback of direct sensing strategies that are based on changes in refractive index is the lack of selectivity. That is, selective detection can only be achieved when, by a specific reaction, the analyte modifies the light absorption properties (i.e. the color) of the nanocolumnar film. Examples of this approach are the optical detection of H_2 with Pd/WO_3 OAD films that change from transparent to blue when exposed to this gas [517], and the color change of cobalt oxide nanocolumnar films when exposed to CO [518]. Another possibility to improve selectivity involves modifying the surface chemistry of nanocolumns by derivatization with functional molecules. For example, the silane derivatization of porous TiO_2 OAD films makes them insensitive to changes in ambient humidity [519].

In hybrid thin films, one way of directly enhancing sensitivity is to incorporate within the OAD films a dye molecule whose light absorption and/or luminescence changes reversibly through a specific reaction with a given analyte. Our group has widely investigated this procedure and developed different composite sensor systems based on this principle. For instance, acid vapors can be detected from the change in optical absorption and fluorescence of OAD TiO_2 films with tetracationic metal-free porphyrin incorporated in their pores [229,244]. Typically, the selectivity of these hybrid systems is mainly determined by the chemical reactivity of the anchored molecules. Thus, by combining a free base porphyrin with ten of its metal derivatives anchored in columnar OAD films, it has proven possible to selectively detect more than ten volatile organic compounds through spectral imaging, as illustrated in Fig. 5.14 [247]. This confirms that the selectivity and performance of these hybrid systems are determined by how the sensing molecules are bonded to the porous OAD matrix [248].

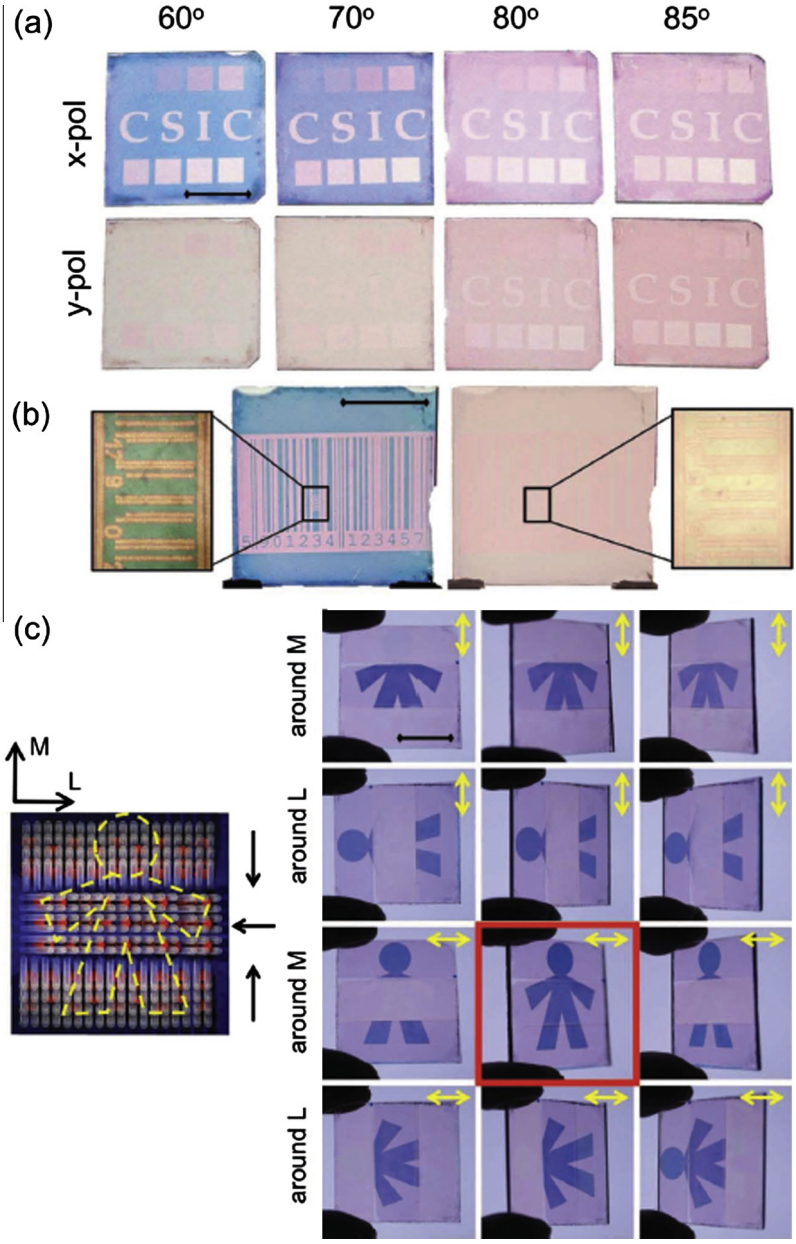

Fig. 5.15. (a) Pictures taken with *x*- and *y*-polarized light sources for a series of dichroic Au/SiO_2 samples deposited at $\alpha = 60°$, 70°, 80° and 85°. Selected zones of these samples were laser treated at different powers. (b) Standard bar code written with a laser onto an Au/SiO_2-60° sample and monitored with *x*- and *y*-polarized light. The magnified images show the presence of a secondary micrometric bar code engraved in one of the bars. (c) Optically encrypted figure drawn by laser and observed with polarized light illumination of an Au/SiO_2-60° sample with three different orientations of SiO_2 nanocolumns, as shown in the scheme at the left side of this panel. The complete shape of the figure can only be retrieved if the orientation of the columns in every zone is known in advance, and the appropriate sample orientation and light polarization are selected (red square) [226].

5.4.2.3. Plasmonics and plasmonic-related applications. Plasmonics is a rapidly evolving area that explores the interaction between an externally applied electromagnetic field and the free electrons in a metal. These free electrons can be excited in the form of collective oscillations, named plasmons, by the electric component of light. At certain incident conditions, namely when the incident light frequency matches the intrinsic frequency of the free electrons, a resonant absorption occurs. This phenomenon is called surface plasmon resonance (SPR), or in the case of nanometric metallic structures, localized surface plasmon resonance (LSPR). OAD has been utilized by many authors for the controlled fabrication of metallic structures intended for plasmonics applications; a topic that has recently been reviewed by He et al. [520] and Abdulhalim [521]. The OAD technique presents some competitive advantages with respect to many other fabrication techniques for metallic supported nanostructures (e.g., self-assembly, electron beam lithography, nanosphere lithography, etc.), the most significant of these being direct control over the composition and shape of the metallic nanocolumns and the scalability of the method to large areas. Plasmonic structures made by OAD have been successfully employed for the fabrication of dichroic systems and labels, sensor and biosensor applications through the analysis of LSPR changes, molecular detection by surface enhanced Raman scattering (SERS), metal-enhanced fluorescence (MEF), surface-enhanced infrared absorption (SEIRA), and the development of metamaterials. A brief discussion of the possibilities offered by OAD techniques in relation to selected applications is presented next.

5.4.2.4. Dichroism and plasmonic applications. In non-spherical silver or gold nanoparticles, plasmon absorption resonance is highly dependent on the polarization state of light. In practice, this polarization dependence manifests itself by the appearance of two plasmon resonance absorptions peaking at different wavelengths depending on the orientation of the electric component vector of light with respect to the largest axis of the nanostructure. Dichroic silver nanoparticles and aggregates can be formed during the earliest OAD stages on flat and transparent substrates [522], with the polarization dependence of their SPR being attributed to their in-plane anisotropy. This effect can be greatly enhanced by nanosecond laser treatments under ambient conditions at relatively low powers, but both anisotropy and dichroic behavior are completely lost at higher laser powers. Strongly dichroic structures have also been obtained by us through the OAD deposition of silver onto OAD nanocolumnar SiO_2 films acting as a substrate [225,523]. In this case, the in-plane anisotropy characteristic of the SiO_2 nanocolumns is used as a template to induce anisotropic growth of the silver film. The treatment of these composites with an unpolarized nanosecond IR laser induces selective melting of the silver and posterior solidification in the form of long nanostripes on the surface, which promote and enhance the dichroic response of the system. This dichroic laser-patterning process has been attributed to a successive metal percolation and dewetting mechanism along the lines defined at the surface by the SiO_2 nanocolumnar *bundles* (see Section 4.2.2). Depending on the laser power, zones with a localized increase in dichroism and/or totally deactivated regions can be written on the composite film surface. The use of this writing procedure has been suggested for the optical encryption of information at a micron level [225]. Nano-columnar silver films directly prepared by OAD have been tested for SERS (see below) and for surface-enhanced Raman [524–526].

Recently, a host–guest strategy based on the formation of anisotropic Au nanodiscs inside the intercolumnar space of *bundled* OAD SiO_2 nanocolumns has been reported by our group [226]. The method relies on that the size, shape and orientation of gold nanoparticles are defined by the tilt angle of the nanocolumns and the intercolumnar space distance, which are experimentally determined by the zenithal angle of evaporation. These composite materials have been applied to the development of optical encryption strategies in combination with local laser patterning. The distinct colors of the untreated zones seen in Fig. 5.15(a) are due to the different anisotropies of the gold nanoparticles depending on the characteristics of the SiO_2 host layer. The effect of this laser treatment is to locally remove the dichroic character of the composite film by inducing melting and resolidification of the anisotropic gold nanoparticles. This treatment can be applied to selected zones with a micron-scale level of control (Fig. 5.15(b)). In addition, this selective writing can be applied to complex dichroic thin film arrangements in which gold nanodiscs present different orientations as a result of being prepared on SiO_2 film zones with nanocolumn bundles that have grown after azimuthally turning the substrate 180°. In this system, retrieving the original information (in this example, the complete shape of the

figure drawn by the laser) requires interrogation of the system using an appropriate polarization of light and a given planar orientation of the plate (Fig. 5.15(c)). A deeper discussion regarding the possibilities of this type of system for optical encryption and the fabrication of anti-counterfeiting labels can be found in Ref. [226].

5.4.2.5. Sensing applications based on plasmons. The characteristics of the LSPR are not only dependent on the size and shape of metal nanoparticles, but also on their dielectric environment. Typically, most OAD metal nanoparticle films are made of either Ag or Au. Fu et al. [527] studied the deposition of Au/TiO_2 and Au/Ti structures by OAD, with the first case producing a red shift of 30 nm in the plasmon resonance when the nanostructure was covered by a TiO_2 layer with a nominal thickness of 5 nm, a change that was attributed to a modification in the refractive index of the medium immediately surrounding the Au nanoparticles. In the latter case, the observed red shift was a function of both the coating thickness and coverage. These results indicate that the OAD technique is very versatile in allowing for the deposition and fine-tuning of LSPR structures, as well as the development of sensors [521,528]. Using uniform films with tuned, narrow particle size distributions, a linear relationship between the plasmon resonance wavelength and refractive index of the surrounding media was identified in OAD Ag and Au nanocolumns immersed in liquids with different refractive indexes [529]. Similarly, a number of biosensors for the highly selective detection of different small molecules have also been developed. Selectivity in this case is mediated by anchoring different receptor molecules on the surface of Au or Ag, which is made possible thanks to the rich surface chemistry of these metals. Examples or this approach are the detection of anti-rabies immunoglobulin G [529], neutravidin [530] and streptavidin [531].

5.4.2.6. Surface enhanced Raman spectroscopy applications. Surface enhanced Raman spectroscopy (SERS) is very sensitive in the detection of minute amounts of molecules in solution upon their adsorption on noble metal substrates, even in the sub-micromolar range. A variety of noble metal nanocolumnar films, most of which have been made of Ag and fabricated by OAD [532–535], have all demonstrated excellent properties as substrates for SERS chemical and biological sensing. Indeed, the SERS enhancement factor and reproducibility of results obtained with OAD Ag nanocolumns was similar, or even superior to that reported for other Ag nanoparticle systems [536,537]. Investigations in this field have generally concluded that the efficiency of OAD structures as SERS transducers is tightly linked to their structural and microstructural characteristics, which in turn can be tailored by controlling the experimental conditions of deposition such as the angle and thickness of the nanocolumns [538,539] or the deposition temperature [540]. Another possibility offered by OAD to enhance SERS performance is the manufacturing of complex architectures that incorporate intentional "hot-spots"; i.e., areas where an enhanced electromagnetic field amplifies the Raman scattering signals. OAD Ag films with L-shape [541], zig-zag [542] and square helical nanostructures [543] have all been reported to promote the formation of such "hot-spots" to increase the sensitivity of SERS analyses.

5.4.2.7. Metal enhanced fluorescence. Metal enhanced fluorescence (MEF) refers to the enhancement in emission intensity of a fluorophore molecule in the proximity of a metal nanostructure due to a localized increase in the electromagnetic field associated with the SPR. Dipole–dipole interactions also play a major role in this enhancement mechanism [544]. While MEF enhancement factors of up to 70 relative to dense metal films have been reported for OAD films made of Ag and Al, equivalent films made of Au and Cu have proven to be far less effective [545,546]. In these studies, the influence of nanocolumn tilt angle, film porosity, the nature of the substrate, and the distance between the fluorophores and metallic structures were all systematically investigated. Various applications of this MEF effect using OAD metallic structures have been reported for biosensing in water and bioimaging [544], whereby a specific detection can be enhanced through the immobilization of the fluorescent receptor onto a metal nanostructure [545–547].

5.5. Wetting and microfluidics

Mimicking nature to obtain superhydrophobic/superhydrophilic, adhesive/anti-adhesive and, more recently, omniphobic and wetting anisotropic surfaces and coatings has been a topic of ongoing interest in the field of nanotechnology over the last two decades; a period that has witnessed the convergence of efforts from academia and industry in the search for new surface functionalities [548–550]. The wetting angle of a liquid drop on a flat surface is determined by Young's Law, and it is the result of a balance between the cohesive forces acting on the line of contact between the drop, the solid surface and the air/gas environment. It is therefore dependent on the interfacial energies between the solid–liquid, solid–vapor and liquid–vapor phases. Put simply, when the solid–vapor interface presents a low surface tension, the water contact angle (WCA) increases. Surfaces with WCAs higher (smaller) than 90° are usually referred to as being hydrophobic (hydrophilic), while those with WCAs higher than 150° (smaller than 10°) are considered superhydrophobic (superhydrophilic). The terms oleophobic and oleophilic designate surfaces with contact angles above and below 90°, respectively, with low surface tension liquids such as non-polar alkanes, oils and non-polar solvents. One of the most long-awaited successes in this field has been the development of reliable, simple and low-cost techniques for the fabrication of superomniphobic surfaces; i.e., coatings capable of repelling both water and low surface tension liquids [551].

The main factors controlling the contact angle of liquid droplets on a solid are the chemistry and the roughness of the surface, the latter being intimately related to the microstructure of the material [552]. Two classic models named after Wenzel (applicable to rough surfaces) [553] and Cassie–Baxter [554] (applicable to heterostructured materials with porous nanostructures) relate the contact angle on actual surfaces, characterized by a specific roughness and microstructure, to the nominal angle on an ideally flat surface of the same material.

5.5.1. Surface-controlled wettability

Oblique angle deposition techniques have been extensively used to control the wettability of materials, as they permit a fine control over both the surface chemistry and roughness. The high versatility of this technique in obtaining different nanostructures (metals, organic compounds, oxides, hybrids and other complex heterostructures) is an additional feature that supports its use for wetting applications. Important achievements have been made in the last few years through the OAD fabrication of surfaces possessing singular adhesive properties [555], hydrophobicity [556–559], superhydrophobicity [186–188,557,560–563], superhydrophilicity [366] or superolephobicity [564,565]. Initial approaches to the development of highly hydrophobic surfaces by OAD combined the surface nanostructuration capability of this technique with the chemical modification of the surface composition by different methods. For example, the RF sputtering deposition at oblique and normal incidence of polytetrafluoroethylene (PTFE), a hydrophobic material commonly known as Teflon, has been reported to increase the water contact angle of OAD Pt [556] and W nanorods [558,559]. In this way, superhydrophobic WCAs as high as 138° and 160°, respectively, were achieved by controlling the deposition angle, substrate rotation and reactor pressure. Veinot et al. [560,566] were responsible for some of the earliest works showing the formation of superhydrophobic surfaces consisting of OAD SiO_2 nanocolumns and 3D nanostructures modified by the chemical grafting of siloxane molecules. More recently, a similar approach involving the molecular vapor deposition of silane onto metal OAD nanocolumns has been proposed as a way of fabricating anti-icing surfaces [558]. Moving a step forward, Choi et al. [561,562] have produced superhydrophobic surfaces with a dual-scale roughness that mimics lotus petal effects (i.e., the ability to pin water droplets while maintaining a large contact angle) [567]. This was achieved through the fluorosilanization of Si nanowires arranged at a micron-level via OAD onto a pre-patterned substrate decorated with gold nanoparticles. Other pre-patterned metal OAD nanorods have been combined with Teflon deposition to control the roughness, morphology and chemistry of the surface, thereby rendering it superhydrophobic [558]. Habazaki et al. [564,565] have expanded this hierarchical roughness concept by using aluminum sputtered OAD nanorods as a starting material, followed by their anodization and surface decoration with fluorinated alkyl phosphate. These surfaces showed an interesting omniphobic behavior characterized by a high repellency of water, oils and hexadecane.

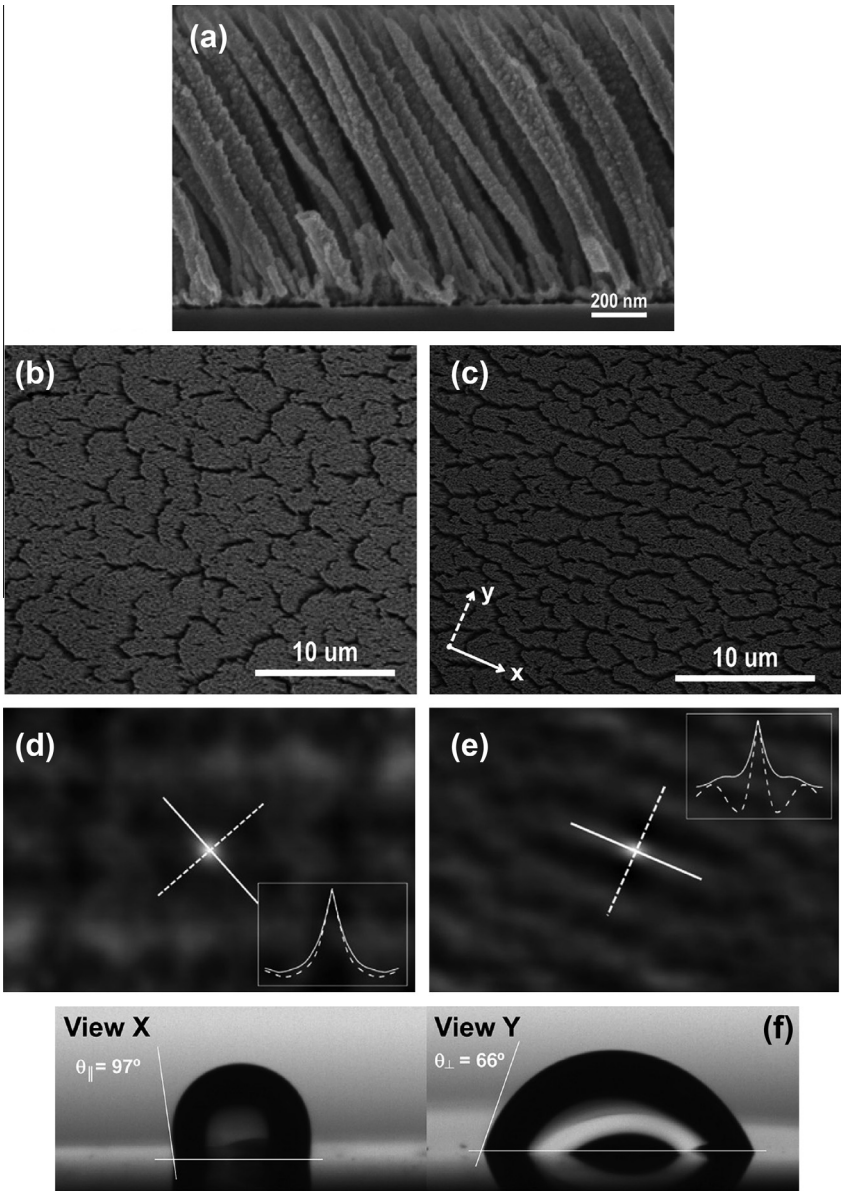

Fig. 5.16. Nanocarpet effect on tilted ZnO nanorods. (a) Cross-sectional SEM micrograph of tilted nanorods fabricated by PECVD at 130 °C. Low-magnification normal-view SEM micrographs of a nanocarpet formed by dripping water onto a surface with a WCA of ~120° on (b) vertical and (c) tilted ZnO nanorods; the latter shows the formation of stripe-like nanocarpets. (d and e) Two-dimensional autocorrelation of the surfaces in (b and c) and corresponding line profiles for the marked directions. (f) Image of a sessile water drop taken for the directions parallel and perpendicular to the aligned nanocarpets in (d) [563].

5.5.2. Light-controlled surface wettability

Active surfaces, in which the contact angle can be changed by external stimuli, are an emerging topic of interest in the field of surface wetting. To this end, our group has developed different plasma approaches for the deposition of nanofibers, nanorods and nanowires made of inorganic semiconductors (TiO_2 and ZnO) [568], small-molecules [569] and hybrid and heterostructured nanostructures

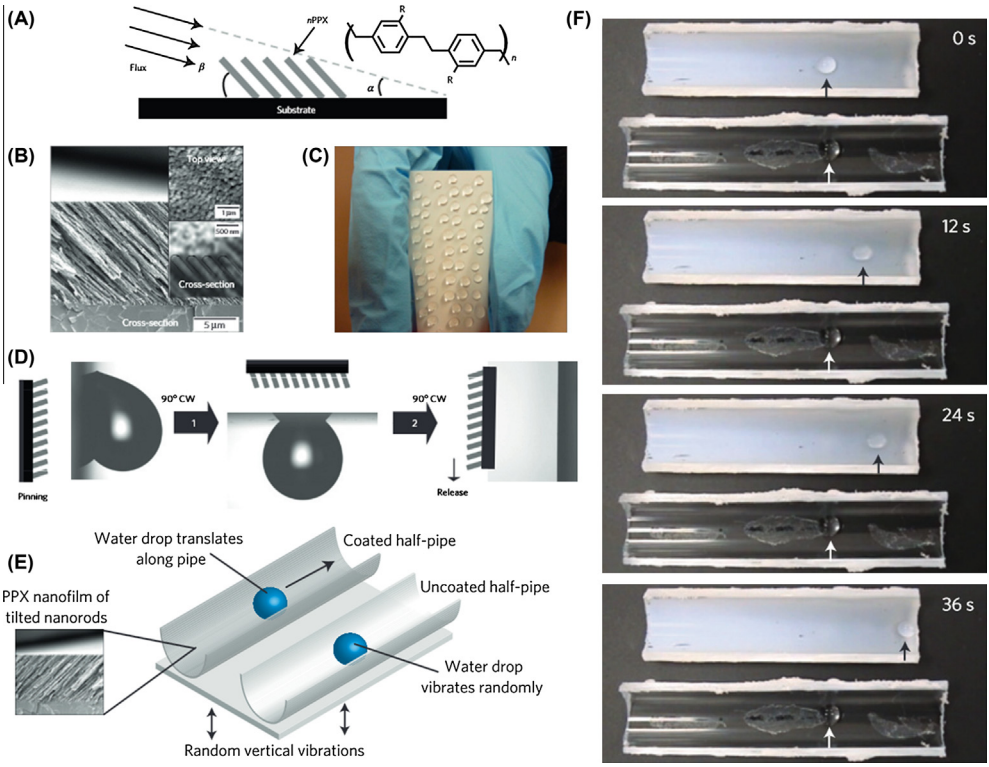

Fig. 5.17. Overview of the preparation of a PPX nanofilm and its anisotropic wetting properties. (A) PPX nanofilm deposition by OAP. (B) Cross-sectional SEM image of a PPX nanofilm (insets show a top view and high-resolution cross-section). (C) Picture of an anisotropic adhesive surface with water drops sticking on its surface. (D) Water adhesion and release with three configurations of the nanofilm. Schematics illustrate the nanorod inclination for each surface orientation, while the photographs show the anisotropic wetting behavior and release of the water droplet. (E) Drop motion on a PPX nanofilm coated half-pipe. Two half-pipes, one coated with PPX nanofilm and the other uncoated, were glued to a base. Low-amplitude 85 Hz random vibration of the base caused translational droplet motion on the coated half-pipe, but not on the uncoated pipe. (F) Time-lapse of droplet motion in the coated and uncoated half-pipes. Water drops moved axially on the half-pipe coated with PPX nanofilm, whereas those on the uncoated half-pipe merely vibrated randomly. Glue is visible beneath the uncoated pipe, but the surface is smooth and clean. Arrows indicate the droplet position [580].

(metal@metal-oxide [186–188,563] and organic@inorganic core@shell nanowires [570]) that can be activated by light illumination. Furthermore, by tailoring the density, morphology and chemical characteristics of these 1D nanostructures, we have been able to fabricate ultrahydrophobic surfaces; i.e., surfaces with an apparent WCA of 180° [242,569]. In addition, by working with Ag@metal-oxide nanorods and nanowires prepared by PECVD in an oblique configuration, we have taken advantage of the well-known photoactivity of TiO_2 and ZnO to reversibly modify the WCA of their surfaces from superhydrophobic to superhydrophilic [188,242,563] by irradiating them with UV light, and in some cases, with visible light [186,187,563]. This illumination does not alter the nanostructure of the films, but rather only their surface properties, thus enabling fine control over the final WCA of the system. To gain deeper insight into the surface state of these photoactive ZnO nanorods grown at oblique angles after water dripping (Fig. 5.16(a)), we have also carried out a thorough study of the evolution of WCA due to the formation of surface nanocarpets [563].

5.5.3. Nanocarpet effect

The nanocarpet effect refers to the association of aligned and supported nanorods or nanowires after their immersion in a liquid, and relates to their deformation by capillary forces. This

phenomenon has attracted considerable interest since the pioneering works of Nguyen et al. [571], where they demonstrated the self-assembly transformation of supported CNTs into cellular foams upon immersion in a liquid and subsequent drying off. Although it is still a subject of controversy, it seems that a critical factor controlling nanocarpet formation is the penetration of the liquid into the inter-rod space of the 1D nanostructured surfaces. Although the literature on this subject has mainly focused on CNT arrays, its expected impact in biomedical research, superhydrophobicity and microfluidics has fostered the investigation of other systems such as OAD nanorods of Si [572–574], functionalized Si [575], SiO_2 [576,577], carbon [485], metal [578] and ZnO [563]. Indeed, the nanocarpet effect has already served to increase the WCA on 1D surfaces [563,573] through the formation of a double or hierarchical roughness. From a fundamental point of view, it has also been used to provide a fingerprint of liquid droplets deposited on vertically aligned, tilted, zigzag and squared spring conformations of hydrophilic or hydrophobic materials [573,579]. In Ref. [563] we studied the evolution of the nanocarpet morphology in UV pre-illuminated OAD ZnO surfaces and their transformation from a superhydrophobic (Cassie–Baxter) state to a superhydrophilic (Wenzel) state, passing through a modified Cassie–Baxter state. In addition, as summarized in Fig. 5.16, we have shown the possibility of controlling the nanocarpet microstructure by pre-illuminating the surface for given periods of time (Fig. 5.16(b) and (c)), or by using samples consisting of partially hydrophobic tilted nanorods, to induce asymmetric wetting after contact with water (Fig. 5.16(d) and (e)).

5.5.4. Anisotropic wetting

Anisotropic wetting and the development of droplets with asymmetric contact angles has emerged as an appealing area of research due to the industrial interest in materials capable of inducing a preferentially oriented spreading of liquid or with an asymmetrical adhesive surface [549,580–583]. Parylene (PPX) films deposited by oblique angle polymerization (OAP) are a particularly outstanding example of this singular wetting behavior [583–587]. Fig. 5.17 provides a summary of results from the fabrication of anisotropic films with unidirectional adhesive and wetting properties [580], which clearly demonstrates the possibilities of the OAP technique for the fabrication of PPX nanorods with a pin-release droplet ratchet mechanism derived from their singular microstructure. These nanofilms exhibited a difference of 80 μN in droplet retention force between the pin and release directions, the latter being characterized by a micro-scale smooth surface on which microliter droplets are preferentially transported. These OAP nanostructures and their unique unidirectional properties have been recently used to control the adhesion and deployment of fibroblast cells [581,588].

5.5.5. Microfluidics

Liquids moving not in the form of droplets, but rather as a continuous flow (microfluidics), have also benefited from the application of OAD thin films. Although the number of papers published on this topic is quite limited, there are a few that clearly illustrate the potential of these films to improve the handling of liquids in small channels and devices. For example, OAD has been used to fabricate nanostructures that were subsequently embedded in PDMS microchannels using a sacrificial resist process. These microchannels were filled with different kinds of sculptured SiO_2 OAD thin films, and the resulting three-dimensional structure was used as a DNA fractionator capable of a more effective micro-scale separation of these large molecules [589]. Microfluidic systems have also been provided with additional functionalities thanks to OAD films in order to develop various kinds of responsive systems. Fu et al. [590] recently reported the fabrication of a microfluidic-based MEF detection system in which tilted Ag nanorod films or SiO_2/Ag multilayers were integrated into a capillary electrophoresis microdevice, which was then utilized for the separation and detection of amino acids. This system demonstrated an enhanced detection by a factor of six at half times when used in a fluorescence device, thus opening the way for further improvements and functionalities.

5.6. Biomaterials and biosensing

The singular surface topography and microstructure of OAD thin films (see Section 3) provides unique possibilities for their utilization as biomaterial substrates, and for the development of biosensors.

5.6.1. Cell–surface interaction

In this case, the key investigated feature is the effect of surface topography on the proliferation of cells and/or the adsorption of proteins that mediate cell adherence and proliferation. In a series of works on the OAD of platinum films, either directly onto flat substrates or onto polymer-packed nanospheres to provide a second nanostructuring pattern to the layers (see Section 2.5), Dolatshahi-Pirouz et al. [110,116,117] showed that the particular surface topography of these latter layers promotes the growth and proliferation of osteoblast cells. For different *in-vivo* applications it is also critical that certain cells grow preferentially over others, a possibility that has been explored *in-vitro* by these same authors using OAD Pt films. In particular, they demonstrated that fibrinogen, an important blood protein, preferentially adheres to whisker-like nano-rough Pt substrates when compared to flat Pt surfaces, and that the proliferation of human fibroblasts is significantly reduced on these nanostructured surfaces [116]. Over the course of these studies, the growth of the film nanocolumns could be described by a power law relationship (see Sections 3.6 and 4.2) between the increments in their length and width [110]. The dependence found between the power law exponent and deposition angle was subsequently used to establish indicators that can be employed to predict cell growth on OAD thin films based on the characteristics of their surface topography determined by this deposition parameter.

Another critical issue affecting the practical implementation of biomaterials in different domains is their capacity to act as a biocide layer; i.e., to prevent the development of bacteria. In this regard, α-Fe_2O_3 nanocolumnar OAD thin films have demonstrated to be quite effective in both limiting bacterial growth on their surface and contributing to the inactivation of *Escherichia coli* O157:H7 when subjected to visible light irradiation [591]. This light response has been proposed for the development of improved visible-light antimicrobial materials for food products and their processing environments. A study into the viability of different bacteria on a nanocolumnar thin film of Ti prepared by MS-OAD has shown that unlike *Staphylococcus aureus*, the growth of *E. coli* is significantly reduced on the nanostructured film, and that this is accompanied by an irregular morphology and cell wall deformation [592]. In a very recent publication on nanostructured Ti surfaces prepared by MS-OAD, we have claimed that while the specific topography produced by the vertical nanorods of the layers are effective in stimulating the growth of osteoblasts on their surface, it simultaneously hinders the development of different types of bacteria. This behavior makes these substrates ideal for implants and other applications in which osteointegration must be accompanied by efficient biocide activity [593].

5.6.2. Biosensor applications

The high surface area of OAD thin films when compared to a compact film has been a key argument for their use in biosensor applications (as well as for their use as conventional gas and liquid sensors as discussed in Section 5.3). However, given that biosensing needs to be carried out at room temperature in a liquid media, yet still requiring a high sensitivity, alternative transduction methodologies are normally used. An overview of instances in which these procedures have been used in conjunction with OAD thin films is the focus of this subsection. One example is the use of electrochemical transduction with MS-OAD NiO thin films for the enzymatic detection of urea in biological fluids [594]. On the nanostructured surface of such films, the urease enzyme becomes easily grafted while the urease–NiO system promotes a high electro-catalytic activity. This provides detection limits as low as 48.0 μA/(mM) and a good linearity over a wide range of concentrations (0.83–16.65 mM). Monitoring H_2O_2 is of strategic importance in many applications, not just because it is a byproduct of a wide range of biological processes, but also because it is a mediator in food, pharmaceutical, clinical, industrial and environmental analysis. Consequently, TiN OAD nanocolumns have been recently proposed as an electrochemical sensor for H_2O_2, which was accompanied by a thorough study about the relation between sensitivity and catalytic activity on the one hand and the deposition angle on the other [595]. A double detection method using UV–visible absorption spectroscopy coupled with cyclic voltammetry was employed by Schaming et al. [596] with 3D nanostructured OAD ITO electrodes for the characterization of cytochrome C and neuroglobin, two proteins that act *in-vivo* to prevent apoptosis.

The photonic detection of analytes has also benefitted from OAD thin films, with Zhang et al. [597] reporting that the sensitivity of a photonic crystal consisting of linearly etched strips on silicon can be

enhanced by OAD of an 80 nm layer of TiO_2 on its surface. This system demonstrated an up to four-fold enhancement in sensitivity toward polymer films, large proteins and different small molecules.

Another transduction concept based on the plasmon detection of analytes was developed by Zhang et al. [598]. These authors proposed the use of gold nanoparticles with a controlled size and homogeneous distribution, which were prepared via OAD on a substrate previously covered with a close-packed layer of polystyrene spheres acting as a template (see Section 2.5). This template layer promotes the development of well-defined gold nanoparticles with a high plasmon resonance activity, which turned out to be very sensitive in detecting biotin–streptavidin molecules. A detection limit of 10 nM was achieved by following both the position of the plasmon resonance band and its variation in intensity upon adsorption.

A quite different approach to evaluate the concentration of H_2O_2 has been proposed by Zhao et al. [122,599], who developed an original protocol for the fabrication of catalytic nanomotors using dynamic OAD. These nanomotors consist of asymmetrically Pt-decorated TiO_2 nanoarms grown on silica microbeads, and have a sensing mechanism that relies on the fact that the asymmetric distribution of Pt in the nanoarms induces their rotation in the presence of H_2O_2 at a variable rate of 0.15 Hz per each percent of this compound in the medium. As with conventional gas sensors, multisensing is also a challenge in the field of biosensor devices. In this context, Sutherland et al. [600] have reported a new method that combines protein adsorption on the surface of a nanostructured quartz crystal microbalance (QCM-D) with optical (surface plasmon resonance SPR) and electrochemical detection (cyclic voltammetry CV). The procedure allows for the quantification of both the amount and activity of bound proteins.

6. Concluding remarks: up-scaling and industrial implementation of OAD processes

The previous sections have clearly shown that OAD procedures constitute a mature technology with a clear understanding of their physical basis and a wide range of potential applications in different domains. Yet despite this, the incorporation of OAD thin films in real industrial applications is still limited, with different factors seemingly hindering the successful transfer of this technology from research laboratories to industrial production. The following features have been identified as the major shortfalls when it comes to the successful up-scaling of OAD methodology [19]:

1. Fabrication process is too complicated when used at an industrial scale.
2. Low productivity because of the angular dependence of the deposition rate.
3. Difficult to develop a general methodology usable for the large-scale production of different nanostructures and materials in a unique experimental set-up.
4. For the most sophisticated nanostructures (e.g., sculptured thin films or complex multilayers), there are limitations associated with the sophisticated movements needed for a large number of substrates and/or large substrate areas at an industrial level.
5. Increased cost of OAD thin films when compared with other methods of nanostructuration that do not require vacuum conditions.

Both electron beam evaporation and magnetron sputtering are widely used at an industrial scale for the deposition of thin films at normal geometry, with a large variety of products manufactured by these methods, either on large area surfaces or for the production of high-tech commodities. Moving large substrates in front of large magnetron targets or using roll-to-roll methods are just some of the approaches that have made these techniques cost-effective and highly competitive at an industrial scale [601]. The limited industrial implementation of OAD procedures is therefore quite striking given that, as indicated by Suzuki [87], large dome-shaped substrate holders (approximately 2 m in diameter) are currently used in batch-type coaters for e-beam deposition of optical films, and these would require only slight modification to successfully mount substrates obliquely for up-scaled production. As pointed out by Zhao [19], a general concern when using an oblique geometric configuration is the inherent decrease in deposition rate; however, this limitation can be easily overcome by compensating with an increase in the evaporation power.

The large-scale industrial deployment of e-beam or MS methods in an OAD configuration would certainly be cost effective if innovative and reliable procedures to handle the substrates are implemented. Some proposals in this regard were made in 1980s by Motohiro et al. [602], who utilized the ion-beam sputtering technique with an ion gun in an OAD configuration and a roll-to-roll procedure for the preparation of CdTe thin films intended for photovoltaic applications. Other authors have made alternative proposals to use OAD methodology for large scale production. For example, Sugita et al. [603] suggested the use of a continuously varying incidence (CVI) method, which consists of a rolling system in front of an electron beam evaporator with a shadow shutter to ensure that only species arriving at a given oblique angle reach the rolling surface. This method was used for the fabrication of tape recording ribbons consisting of Co–Cr films [604]. As already reported in Section 2.4 (Table 2.1), other authors [89–91] have used a similar procedure for the fabrication of porous thin films for thermal isolation. In this, and other similar rotating configurations, the incoming angle of species relative to the rotating surface is systematically changed so that even if the growth of the film is dominated by shadowing processes that would produce porosity, it does not maintain a fixed and well defined microstructure due to the continuously varying zenithal deposition angle. Although the mass production based of OAD films is not extended to the large-scale production of final products, there are various niche applications that have already benefitted from this technology in recent years. For example, metal wire grid polarizers are already mass produced by the OAD deposition of antireflection FeSi and SiO_2 layers on previously deposited aluminum columnar arrays [87,114,115] (see Section 2.5). Magnetic recording/video tapes are another example where OAD techniques have been successfully employed in large scale production [604–607].

Very recently, Krause et al. [608] used a simplified roll-to-roll system to analyze the geometrical conditions and translate the deposition recipes of typical OAD films and architectures from flat moving substrate to a roll configuration. The representative structures obtained prove that a successful translation from the laboratory to mass production is possible, even for thin films with a complex shape. In summary, although the general principles for the successful implementation of OAD methodologies at an industrial scale are already available, and some successful attempts have been made to fabricate different serial products, the large scale engineering of the process and a reduction in cost is needed to make OAD thin films competitive with alternative technologies. We believe that the time is ripe to achieve this goal and that the near future should see new developments and applications in the market that are based on the outstanding properties and performance of thin films prepared by deposition at oblique angles.

Acknowledgements

This review has been carried out as part of the research activity of the "Nanotechnology on Surfaces" laboratory at the Instituto de Ciencia de Materiales de Sevilla, which is sponsored by different projects of the Junta de Andalucía (TEP8067, TEP5283 and P10-FQM-6900) and the Ministry of Economy and Competitiveness of Spain (CONSOLIDER CSD2008-00023 MAT2013-42900-P, MAT2013-40852-R). One of the authors (ARGE) also wishes to acknowledge the hospitality and support of Prof. Zschech and their colleagues at the "Dresden Center for Nanoanalysis" of the Technische Universität Dresden (Germany) during a sabbatical that permitted the realization of a considerable part of this work.

References

[1] Kaempf K. Grösse und ursache der doppelbrechung in kundtschenspiegeln und erzeugung von doppelbrechung in metallspiegelndurch zug. Ann Phys 1905;321:308–33.
[2] Bergholm C. Über doppelbrechung in kathoden zerstäubten metallsuchten. Ann Phys 1913;348:1–23.
[3] König H, Helwig G. Über die struktur schrägaufgedampfter schichten und ihr einfluß auf die entwicklung submikroskopischer oberflächen rauhigkeiten. Optik 1950;6:111–24.
[4] Young NO, Kowal J. Optically active fluorite films. Nature 1959;183:104–5.
[5] Smith DO, Cohen MS, Weiss GP. Oblique-incidence anisotropy in evaporated permalloy films. J Appl Phys 1960;31:1755–62.
[6] Nieuwenh JM, Haanstra HB. Microfractography of thin films. Philips Tech Rev 1966;27:87–91.
[7] Lewis B, Campbell DS. Nucleation and initial growth behaviour of thin films. J Vac Sci Technol 1967;4:209–18.

[8] Nakhodkin NG, Shaldervan AI. Effect of vapor incidence angles on profile and properties of condensed films. Thin Solid Films 1972;10:109–22.
[9] Dirks AG, Leany HJ. Columnar microstructure in vapor-deposited thin films. Thin Solid Films 1977;47:219–33.
[10] Van Kranenburg H, Lodder C. Tailoring growth and local composition by oblique-incidence deposition: a review and new experimental data. Mater Sci Eng R 1994;11:295–354.
[11] Abelmann L, Lodder C. Oblique evaporation and surface diffusion. Thin Solid Films 1997;305:1–21.
[12] Robbie K, Brett MJ. Sculptured thin films and glancing angle deposition: growth mechanics and applications. J Vac Sci Technol A 1997;15:1460–5.
[13] Messier R, Vijayakumar C, Venugopal VC, Sunal PD. Origin and evolution of sculptured thin films. J Vac Sci Technol A 2000;18:1538–45.
[14] Wadley HNG, Zhou X, Johnson RA, Neurock M. Mechanisms, models and methods of vapor deposition. Prog Mater Sci 2001;46:329–77.
[15] Zhao YP, Ye DX, Wang GC, Lu TM. Designing nanostructures by glancing angle deposition. Proc SPIE 2003;5219:59–73.
[16] Hawkeye MM, Brett MJ. Glancing angle deposition: fabrication, properties, and applications of micro-and nanostructured thin films. J Vac Sci Technol A 2007;25:1317–35.
[17] Taschuk MT, Hawkeye MM, Brett MJ. Glancing angle deposition. In: Martin PM, editor. Handbook of deposition technologies for films and coatings. Oxford, UK: Elsevier; 2010. p. 621–51.
[18] Tawfick S, Volder M, Copic D, Park SJ, Oliver CR, Polsen ES, et al. Engineering of micro- and nanostructured surfaces with anisotropic geometries and properties. Adv Mater 2012;24:1628–74.
[19] He Y, Zhao Y. Advanced multi-component nanostructures designed by dynamic shadowing Growth. Nanoscale 2011;3:2361–75.
[20] Lakhtakia A, Messier R. Sculptured thin films. Nanoengineered morphology and optics. Bellingham, Washington, USA: SPIE Press; 2005.
[21] Hawkeye MM, Taschuk MT, Brett MJ. Glancing angle deposition of thin films: engineering the nanoscale. Wiley Series in Materials for Electronic & Optoelectronic Applications; 2014 [September 29].
[22] Karabacak T, Singh JP, Zhao YP, Wang GC, Lu TM. Scaling during shadowing growth of isolated nanocolumns. Phys Rev B 2003;68:125408.
[23] Tang F, Parker T, Li HF, Wang GC, Lu TM. Unusual magnesium crystalline nanoblades grown by oblique angle vapor deposition. J Nanosci Nanotechnol 2007;7:3239–44.
[24] Tang F, Wang GC, Lu TM. In situ reflection high energy electron diffraction surface pole figure study of biaxial texture evolution in anisotropic Mg nanoblades during shadowing growth. J Appl Phys 2007;102:014306.
[25] Szmaja W, Kozłowski W, Balcerski J, Kowalczyk PJ, Grobelny J, Cichomski M. Study of obliquely deposited thin cobalt films. J Alloys Compd 2010;506:526–9.
[26] Chen L, Andrea L, Timalsina YP, Wang GC, Lu TM. Engineering epitaxial-nanospiral metal films using dynamic oblique angle deposition. Cryst Growth Des 2013;13:2075–80.
[27] Musil J, Baroch P, Vlcek J, Nam KH, Han JG. Reactive magnetron sputtering of thin films: present status and trends. Thin Solid Films 2005;475:208–18.
[28] Samukawa S, Hori M, Rauf SH, Tachibana K, Bruggeman P, Kroesen G, et al. The 2012 plasma roadmap. J Phys D: Appl Phys 2012;45:253001.
[29] Eason R, editor. Pulsed laser deposition of thin films. Hoboken, New Jersey: John Wiley & Sons; 2007.
[30] Ruda HE, Polanyi JC, Yang SY, Wu Z, Philipose U, Xu T, et al. Developing 1D nanostructure arrays for future nanophotonics. Nanoscale Res Lett 2006;1:99–119.
[31] Sarakinos K, Alami J, Konstantinidis S. High power pulsed magnetron sputtering: a review on scientific and engineering state of the art. Surf Coat Technol 2010;204:1661–84.
[32] Gonzalez-Elipe AR, Yubero F, Sanz JM. Low energy ion assisted film growth. Londres: Intern Coll Press; 2003. p. 1–288.
[33] Gonzalez-Garcia L, Barranco A, Muñoz-Paez A, Gonzalez-Elipe AR, Garcia-Gutierrez MC, Hernandez JJ, et al. Structure of glancing incidence deposited TiO_2 thin films as revealed by granzing incidence small-angle X-ray scattering. Chem Phys Chem 2010;11:1–5.
[34] Tang F, Parker T, Wang GC, Lu TM. Surface texture evolution of polycrystalline and nanostructured films: RHEED surface pole figure analysis. J Phys D: Appl Phys 2007;40:R427–39.
[35] Thornton JA. Influence of apparatus geometry and deposition conditions on structure and topography of thick sputtered coatings. J Vac Sci Technol 1974;11:666–70.
[36] Petrov I, Barna PB, Hultman L, Greene JE. Microstructural evolution during film growth. J Vac Sci Technol A 2003;21: S117–28.
[37] Movchan BA, Demchishin AV. Study of structure and properties of thick vacuum condensates of nickel, titanium, tungsten, aluminum oxide and zirconium dioxide. Phys Met Metallogr 1969;28:83–90.
[38] Tait RN, Smy T, Brett MJ. Modelling and characterization of columnar growth in evaporated films. Thin Solid Films 1993;226:196–201.
[39] Tanto B, Eyck T, Lu TM. A model for column angle evolution during oblique angle deposition. J Appl Phys 2010;108:026107.
[40] Zhu H, Cao W, Larsen GK, Toole R, Zhao Y. Tilting angle of nanocolumnar films fabricated by oblique angle deposition. J Vac Sci Technol B 2012;30:030606.
[41] Zhou Q, Li Z, Ni J, Zhang Z. A simple model to describe the rule of glancing angle deposition. Mater Trans 2011;52:469–73.
[42] Lichter S, Chen J. Model for columnar microstructure of thin Solid films. Phys Rev Lett 1986;56:1396–9.
[43] Meakin P. Ballistic deposition onto inclined surfaces. Phys Rev A 1988;38:994–1004.
[44] Hodgkinson I, Wi QH, Hazel J. Empirical equations for the principal refractive indices and column angle of obliquely deposited films of tantalum oxide, titanium oxide, and zirconium oxide. Appl Opt 1998;37:2653–9.
[45] Zhao Y, He Y, Brown C. Composition dependent nanocolumn tilting angle during oblique angle deposition. Appl Phys Lett 2012;100:033106.

[46] Yanguas-Gil A, Cotrino J, Barranco A, Gonzalez-Elipe AR. Influence of the angular distribution function of incident particles on the microstructure and anomalous scaling behavior of thin films. Phys Rev Lett 2006;96:236101.
[47] Palmero A, Rudolph AH, Habraken FHPM. One-dimensional analysis of the rate of plasma-assisted sputter deposition. J Appl Phys 2007;101:083307.
[48] Gonzalez-Garcia L, Parra-Barranco J, Sanchez-Valencia JR, Barranco A, Borras A, Gonzalez-Elipe AR, et al. Correlation lengths, porosity and water adsorption in TiO_2 thin films prepared by glancing angle deposition. Nanotechnology 2012;23:205701–11.
[49] Deniz D, Lad RJ. Temperature threshold for nanorod structuring of metal and oxide films grown by glancing angle deposition. J Vac Sci Technol A 2011;29:011020.
[50] Nakhodkin NG, Shaldervan AL. Effect of vapor incidence angles on profile and properties of condensed films. Thin Solid Films 1972;10:109–22.
[51] Hara K, Kamimori T, Fujiwara H. Texture and columnar structure of evaporated cobalt films. Thin Solid Films 1980;66:185–9.
[52] Fujiwara H, Hara K, Kamamori T, Takemoto K, Hashimoto T. Texture and columnar structure of evaporated cobalt films. Thin Solid Films 1980;66:177–83.
[53] Hashimoto T, Okamoto K, Hara K, Kamiya M, Fujiwara H. Columnar structure and texture of iron films evaporated at oblique incidence. Thin Solid Films 1982;91:145–54.
[54] Okamoto K, Hashimoto T, Hara K, Kamiya M, Fujiwara H. Columnar structure and texture of iron films prepared at various pressures. Thin Solid Films 1985;129:299–307.
[55] Hara K, Kamiya M, Hashimoto T, Okamoto K, Fujiwara H. Columnar structure of obliquely deposited iron films prepared at low substrate temperatures. Thin Solid Films 1988;158:239–44.
[56] Okamoto K, Hashimoto T, Hara K, Kamiya M, Fujiwara H. Columnar structure and texture of iron films prepared at various evaporation rates. Thin Solid Films 1987;147:299–311.
[57] Suzuki M, Nagai K, Kinoshita S, Nakajima K, Kimura K, Okano T, et al. Vapor phase growth of Al whiskers induced by glancing angle deposition at high temperature. Appl Phys Lett 2006;89:133103.
[58] Khare C, Patzig C, Gerlach JW, Rauschenbach B, Fuhrmann B. Influence of substrate temperature on glancing angle deposited Ag nanorods. J Vac Sci Technol A 2010;28:1002–9.
[59] Wang HH, Shi YJ, William C, Yigal B. Strong surface diffusion mediated glancing-angle deposition: growth, recrystallization and reorientation of tin nanorods. Chin Phys Lett 2008;25:234–7.
[60] Vick D, Friedrich LJ, Dew SK, Brett MJ, Robbie K, Seto M, et al. Self-shadowing and surface diffusion effects in obliquely deposited thin films. Thin Solid Films 1999;339:88–94.
[61] Messier R, Venugopal VC, Sunal PD. Origin and evolution of sculptured thin films. J Vac Sci Technol A 2000;18:1538–46.
[62] Suzuki M, Taga Y. Numerical study of the effective surface area of obliquely deposited thin films. J Appl Phys 2001;90:5599–607.
[63] Gonzalez-Garcia L, Gonzalez-Valls I, Lira-Cantu M, Barranco A, Gonzalez-Elipe AR. Aligned TiO_2 nanocolumnar layers prepared by PVD-GLAD for transparent dye sensitized solar cells. Energy Environ Sci 2011;4:3426–35.
[64] Wong MS, Lee MF, Chen CL, Huang CH. Vapor deposited sculptured nano-porous titania films by glancing angle deposition for efficiency enhancement in dye-sensitized solar cells. Thin Solid Films 2010;519:1717–22.
[65] Gaillard Y, Rico VJ, Jimenez-Pique E, Gonzalez-Elipe AR. Nanoindentation of TiO_2 thin films with different microstructures. J Phys D: Appl Phys 2009;42:145305.
[66] Van Popta AC, Cheng J, Sit JC, Brett MJ. Birefringence enhancement in annealed TiO_2 thin films. J Appl Phys 2007;102:013517.
[67] Lintymer J, Martin N, Chappe JM, Delobelle P, Takadoum J. Influence of zigzag microstructure on mechanical and electrical properties of chromium multilayered thin films. Surf Coat Technol 2004;180(181):26–32.
[68] Lintymer J, Martin N, Chappe JM, Delobelle P, Takadoum J. Nanoindentation of chromium zigzag thin films sputter deposited. Surf Coat Technol 2005;200:269–72.
[69] Lintymer J, Martin N, Chappe JM, Takadoum J, Delobelle P. Modeling of Young's modulus, hardness and stiffness of chromium zigzag multilayers sputter deposited. Thin Solid Films 2006;503:177–89.
[70] Lintymer J, Martin N, Chappe JM, Takadoum J. Glancing angle deposition to control microstructure and roughness of chromium thin films. Wear 2008;264:444–9.
[71] Hrudey PCP, Westra KL, Brett MJ. Highly ordered organic Alq3 chiral luminescent thin films fabricated by glancing-angle deposition. Adv Mater 2006;18:224–8.
[72] Broughton JN, Brett MJ. Electrochemical capacitance in manganese thin films with chevron microstructure. Electrochem Solid-State Lett 2002;5:A279–82.
[73] Hrudey PCP, Taschuk M, Tsui YY, Fedosejevs R, Brett MJ. Optical properties of porous nanostructured Y_2O_3:Eu thin films. J Vac Sci Technol A 2005;23:856–61.
[74] Hrudey PCP, Taschuk M, Tsui YY, Fedosejevs R, Brett MJ. Effects of film structure on photoluminescent emission properties of nanostructured Y_2O_3: Eu thin films. In: Andrews DL, Cao GZ, Gaburro Z, editors. SPIE proceedings nanophotonic materials, Bellingham, WA 5510; 2004. p. 78–87.
[75] Fan B, Vithana HKM, Kralik JC, Faris SM. Optical circular dichroism of vacuum-deposited film stacks. Opt Commun 1998;147:265–8.
[76] Liu F, Umlor MT, Shen L, Weston J, Eads W, Barnard JA, et al. The growth of nanoscale structured iron films by glancing angle deposition. J Appl Phys 1999;85:5486–8.
[77] Krause KM, Brett MJ. Spatially graded nanostructured chiral films as tunable circular polarizers. Adv Funct Mater 2008;18:3111–8.
[78] Elias AL, Harris KD, Brett MJ. Fabrication of helically perforated gold, nickel and polystyrene thin films. J Microelectromech Syst 2004;13:808–13.
[79] Van Popta AC, Brett MJ, Sit JC. Double-handed circular Bragg phenomena in polygonal helix thin films. J Appl Phys 2005;98:083517.
[80] Huang Z, Harris KD, Brett MJ. Morphology control of nanotube arrays. Adv Mater 2009;21:2983–7.

[81] Taschuk MT, Harris KD, Smetaniuk DP, Brett MJ. Decoupling sensor morphology and material: atomic layer deposition onto nanocolumn scaffolds. Sens Actuat B 2012;162:1–6.
[82] Woo SH, Hwangbo CK. Optical anisotropy of TiO_2 and MgF_2 thin films prepared by glancing angle deposition. J Kor Phys Soc 2006;49:2136–42.
[83] Leontyev V, Wakefield NG, Tabunshchy KK, Sit JC, Brett MJ, Kovalenko A. Selective transmittance of linearly polarized light in thin films rationally designed by FDTD and FDFD theories and fabricated by glancing angle deposition. J Appl Phys 2008;104:104302.
[84] Hawkeye MM, Brett MJ. Narrow band pass optical filters fabricated with one-dimensionally periodic inhomogeneous thin films. J Appl Phys 2006;100:044322.
[85] Leontyev V, Hawkeye M, Kovalenko A, Brett MJ. Omnidirectional reflection from nanocolumnar TiO_2 films. J Appl Phys 2012;112:084317.
[86] Robbie K, Yan Cui Y, Elliott C, Kaminska K. Oxidation of evaporated porous silicon rugate filters. Appl Opt 2006;45:8298–303.
[87] Suzuki M. Practical applications of thin films nanostructured by shadowing growth. J Nanophoton 2013;7:073598.
[88] Yan X, Mont FW, Poxson DJ, Cho J, Schubert EF, Kim MH, et al. Electrically conductive thin-film color filters made of single-material indium-tin-oxide. J Appl Phys 2011;109:103113.
[89] Schulz U, Terry SG, Levi CG. Microstructure and texture of electron beam physical vapor deposited TBCs grown under different rotation modes. Mater Sci Eng A 2003;360:319–29.
[90] Wada K, Yamaguchi N, Matsubara H. Effect of substrate rotation on texture evolution in ZrO_2–4 mol% Y_2O_3 layers fabricated by electron beam physical vapor deposition. Surf Coat Technol 2005;191:367–74.
[91] Wada K, Yoshiya M, Yamaguchi N, Matsubara H. Texture and microstructure of ZrO_2–4mol% Y_2O_3 layers obliquely deposited by electron beam physical vapor deposition. Surf Coat Technol 2006;200:2725–30.
[92] Chen L, Lu TM, Wang GC. Biaxially textured Mo films with diverse morphologies by substrate-flipping rotation. Nanotechnology 2011;22:505701–8.
[93] Jensen MO, Brett MJ. Porosity engineering in glancing angle deposition thin films. Appl Phys A: Mater Sci Process 2005;80:763–8.
[94] Ye DX, Karabacak T, Picu RC, Wang GC, Lu TM. Uniform Si nanostructures grown by oblique angle deposition with substrate swing rotation. Nanotechnology 2005;16:1717–23.
[95] Krabbe JD, Leontyev V, Taschuk MT, Kovalenko A, Brett MJ. Square spiral photonic crystal with visible band gap. J Appl Phys 2012;111:064314.
[96] Jensen MO, Brett MJ. Periodically structured glancing angle deposition thin films. IEEE Trans Nanotechnol 2005;4:269–77.
[97] Whitacre JF, Rek ZU, Bilello JC, Yalisove SM. Surface roughness and in-plane texturing in sputtered thin films. J Appl Phys 1998;84:1346–53.
[98] Horn MW, Pickett MD, Messier R, Lakhtakia A. Selective growth of sculptured nanowires on microlithographic lattices. J Vac Sci Technol A 2004;22:3426–30.
[99] Kesapragada SV, Gall D. Anisotropic broadening of Cu nanorods during glancing angle deposition. Appl Phys Lett 2006;89:203121.
[100] Zhuo CM, Gall D. The structure of Ta nanopillars grown by glancing angle deposition. Thin Solid Films 2006;515:1223–7.
[101] Liu YJ, Zhang ZY, Dluhy RA, Zhao YP. The SERS response of semiordered Ag nanorod arrays fabricated by template oblique angle deposition. J Raman Spectrosc 2010;41:1112–8.
[102] Kannarpady GK, Khedir KR, Ishihara H, Woo J, Oshin OD, Trigwell S, et al. Controlled growth of self-organized hexagonal arrays of metallic nanorods using template-assisted glancing angle deposition for superhydrophobic applications. ACS Appl Mater Interfaces 2011;3:2332–40.
[103] Van Dijken JG, Fleischauer MD, Brett MJ. Controlled nanostructuring of CuPc thin films via glancing angle deposition for idealized organic photovoltaic architectures. J Mater Chem 2011;21:1013–9.
[104] Patzig C, Khare C, Fuhrmann B, Rauschenbach B. Periodically arranged Si nanostructures by glancing angle deposition on patterned substrates. Phys Status Solidi B 2010;247:1322–34.
[105] Khare C, Fechner R, Bauer J, Weise M, Rauschenbach B. Glancing angle deposition of Ge nanorod arrays on Si patterned substrates. J Vac Sci Technol A 2011;29:041503.
[106] Merkel JJ, Sontheimer T, Rech B, Becker C. Directional growth and crystallization of silicon thin films prepared by electron-beam evaporation on oblique and textured surfaces. J Cryst Growth 2013;367:126–30.
[107] Tauseef Tanvir M, Aoki Y, Habazaki H. Formation of porous niobium films by oblique angle deposition: influence of substrate morphology. Thin Solid Films 2009;517:6711–6.
[108] Ye DX, Karabacak T, Lim BK, Wang GC, Lu TM. Growth of uniformly aligned nanorod arrays by oblique angle deposition with two-phase substrate rotation. Nanotechnology 2004;15:817–21.
[109] Zhou CM, Gall D. Development of two-level porosity during glancing angle deposition. J Appl Phys 2008;103:014307.
[110] Dolatshahi-Pirouz A, Pennisi CP, Skeldal S, Foss M, Chevallier J, Zachar V, et al. The influence of glancing angle deposited nano-rough platinum surfaces on the adsorption of fibrinogen and the proliferation of primary human fibroblasts. Nanotechnology 2009;20:095101.
[111] Zhou CM, Li HF, Gall D. Multi-component nanostructure design by atomic shadowing. Thin Solid Films 2008;517:1214–8.
[112] Zhou CM, Gall D. Surface patterning by nanosphere lithography for layer growth with ordered pores. Thin Solid Films 2007;516:433–7.
[113] Kesapragada SV, Gall D. Two-component nanopillar arrays grown by glancing angle deposition. Thin Solid Films 2006;494:234–9.
[114] Suzuki M, Takada A, Yamada T, Hayasaka T, Sasaki K, Takahashi E, et al. Antireflection coatings with $FeSi_2$ layer: application to low-reflectivity wire grid polarizers. Thin Solid Films 2011;519:8485–9.
[115] Suzuki M. Low-reflectivity wire-grid polarizers multilayered by the glancing-angle deposition technique. J Nanophoton 2011;5:01150.
[116] Dolatshahi-Pirouz A, Jensen T, Vorup-Jensen T, Bech R, Chevallier J, Besenbadier F, et al. Synthesis of functional nanomaterials via colloidal mask templating and glancing angle deposition (GLAD). Adv Eng Mater 2010;12:899–905.

[117] Pennisia CP, Dolatshahi-Pirouz A, Foss M, Chevallier J, Fink T, Zachar V, et al. Nanoscale topography reduces fibroblast growth, focal adhesion size and migration-related gene expression on platinum surfaces. Colloids Surf B: Biointerfaces 2011;85:189–97.
[118] Khedir KR, Kannarpady GK, Ishihara H, Woo J, Ryerson C, Biris AS. Design and fabrication of Teflon-coated Tungsten nanorods for tunable hydrophobicity. Langmuir 2011;27:4661–8.
[119] He Y, Brown C, He Y, Fan J, Lundgren CA, Zhao Y. Porous three-dimensional nanorod arrays through selective chemical etching of nanocomposites. Chem Commun 2012;48:7741–3.
[120] Müller-Pfeiffer S, Van Kranenburg H, Lodder JC. A two-dimensional Monte Carlo model for thin film growth by oblique evaporation: simulation of two component systems for the example Co–Cr. Thin Solid Films 1992;213:143–53.
[121] He YP, Fu JX, Zhang Y, Zhao YP, Zhang LJ, Xia AL, et al. Multilayered Si/Ni nanosprings and their magnetic properties. Small 2007;3:153–60.
[122] He YP, Wu JS, Zhao YP. Designing catalytic nanomotors by dynamic shadowing growth. Nano Lett 2007;7:1369–75.
[123] Blackwell B, Zhao YP. Metal nanoparticle embedded porous thin films prepared by oblique angle evaporation. J Vac Sci Technol B 2008;26:1344–9.
[124] Larsen GK, Fitzmorris BC, Longo C, Zhang JZ, Zhao Y. Nanostructured homogeneous CdSe–TiO_2 composite visible light photoanodes fabricated by oblique angle deposition. J Mater Chem 2012;22:14205–18.
[125] He Y, Brown C, Lundgren CA, Zhao Y. The growth of CuSi composite nanorod arrays by oblique angle co-deposition and their structural, electrical and optical properties. Nanotechnology 2012;23:365703–13.
[126] Berglund SP, Flaherty DW, Hahn NT, Bard AJ, Mullins CB. Photoelectrochemical oxidation of water using nanostructured $BiVO_4$ films. J Phys Chem C 2012;115:3794–802.
[127] Karinki NN, Khudhayer WG, Karabacak T, Myers DJ. Glancing angle deposited Pt–Ni alloy nanorods for oxygen reduction reaction. ACS Catal 2013;3:3123–32.
[128] Keitoku S, Kamimori T, Goto M. Inhomogeneous concentration distribution in obliquely evaporated Fe–Cu films. Jpn J Appl Phys 1986;25:1668–71.
[129] Suzuki M, Taga Y. Anisotropy in the optical-absorption of Ag–SiO_2 thin-films with oblique columnar structures. J Appl Phys 1992;71:2848–54.
[130] Alvarez R, Garcia-Martin JM, Lopez-Santos MC, Rico V, Ferrer FJ, Cotrino J, et al. On the deposition rate of magnetron sputtered thin films at oblique angles. Plasma Proc Polym 2014;11:571–6.
[131] Wagner R, Ellis W. Vapor–liquid–solid mechanism of single crystal growth. Appl Phys Lett 1964;4:89–90.
[132] Suzuki M, Hamachi K, Hara H, Nakajima K, Kimura K, Hsu CW, et al. Vapor–liquid–solid growth of Ge nanowhiskers enhanced by high-temperature glancing angle deposition. Appl Phys Lett 2011;99:223107.
[133] Beaudry AL, Tucker RT, LaForge JM, Taschuk MT, Brett MJ. Indium tin oxide nanowhisker morphology control by vapour–liquid–solid glancing angle deposition. Nanotechnology 2012;23:105608.
[134] Tucker RT, Beaudry AL, LaForge JM, Taschuk MT, Brett MJ. A little ribbing: flux starvation engineering for rippled indium tin oxide nanotree branches. Appl Phys Lett 2012;101:193101.
[135] Taschuk MT, Tucker RT, LaForge JM, Beaudry AL, Kupsta MR, Brett MJ. Towards engineered branch placement: unreal match between vapour–liquid–solid glancing angle deposition nanowire growth and simulation. J Appl Phys 2013;114:244304.
[136] Beaudry AL, LaForge JM, Tucker RT, Li P, Taschuk MT, Brett MJ. Flux engineering for indium tin oxide nanotree crystal alignment and height-dependent branch orientation. Cryst Growth Des 2013;13:212–9.
[137] Beaudry AL, LaForge JM, Tucker RT, Sorge JB, Adamski NL, Li P, et al. Directed branch growth in aligned nanowire arrays. Nano Lett 2014;14:1797–803.
[138] Kelly PJ, Arnell RD. Magnetron sputtering: a review of recent developments and applications. Vacuum 2000;56:159–72.
[139] Ehsani MH, Dizaji HR, Azizi S, Ghavami Mirmahalle SF, Hosseini Siyanaki F. Optical and structural properties of cadmium telluride films grown by glancing angle deposition. Phys Scr 2013;88:025602.
[140] Snow P, Gaire C, Lu TM, Wang GC. Temperature dependent biaxial texture evolution in Ge films under oblique angle vapor deposition. Thin Solid Films 2011;519:5413–8.
[141] Schmidt D, Kjerstad AC, Hofmann T, Skomski R, Schubert E, Schubert M. Optical, structural and magnetic properties of cobalt nanostructured thin films. J Appl Phys 2009;105:113508.
[142] Mukherjee S, Gall D. Structure zone model for extreme shadowing conditions. Thin Solid Films 2013;527:158–63.
[143] Stagon SP, Huang H, Baldwin JK, Misra M. Anomaly of film porosity dependence on deposition rate. Appl Phys Lett 2012;100:061601.
[144] Alouach H, Mankey GJ. Texture orientation of glancing angle deposited copper nanowire arrays. J Vac Sci Technol A 2004;22:1379–82.
[145] Brown T, Robbie K. Observations of self-assembled microscale triangular-shaped spikes in copper and silver thin films. Thin Solid Films 2013;531:103–12.
[146] LaForge JM, Ingram GL, Taschuk MT, Brett MJ. Flux engineering to control in-plane crystal and morphological orientation. Cryst Growth Des 2012;12:3661–7.
[147] Wang S, Xia G, He H, Yi K, Shao J, Fan Z. Structural and optical properties of nanostructured TiO_2 thin films fabricated by glancing angle deposition. J Alloys Compd 2007;431:287–91.
[148] Teki R, Parker TC, Li H, Koratkar N, Lu TM, Lee S. Low temperature synthesis of single crystalline ZnO nanorods by oblique angle deposition. Thin Solid Films 2008;516:4993–6.
[149] Basnet P, Larsen GK, Jadeja RP, Hung YC, Zhao Y. α-Fe_2O_3 nanocolumns and nanorods fabricated by electron beam evaporation for visible light photocatalytic and antimicrobial applications. ACS Appl Mater Interfaces 2013;5:2085–95.
[150] Yang B, Duan H, Zhou C, Gao Y, Yang J. Ordered nanocolumn-array organic semiconductor thin films with controllable molecular orientation. Appl Surf Sci 2013;286:104–8.
[151] Chen L, Lu TM, Wang GC. Incident flux angle induced crystal texture transformation in nanostructured molybdenum films. J Appl Phys 2012;112:024303.
[152] Krishnan R, Parker T, Lee S, Lu TM. The formation of vertically aligned biaxial tungsten nanorods using a novel shadowing growth technique. Nanotechnology 2009;20:465609.

[153] Chen L, Lu TM, Wang GC. Creation of biaxial body center cubic tungsten nanorods under dynamic shadowing effect. Thin Solid Films 2013;539:65–9.
[154] Shetty AR, Karimi A, Cantoni M. Effect of deposition angle on the structure and properties of pulsed-DC magnetron sputtered TiAlN thin films. Thin Solid Films 2011;519:4262–70.
[155] Shetty AR, Karimi A. Texture mechanisms and microstructure of biaxial thin films grown by oblique angle deposition. Phys Status Solidi B 2012;249:1531–40.
[156] Morrow P, Tang F, Karabacak T, Wang PI, Ye DX, Wang GC, et al. Texture of Ru columns grown by oblique angle sputter deposition. J Vac Sci Technol A 2006;24:235–44.
[157] Mahieu S, Buyle G, Ghekiere P, Heirwegh S, De Gryse R, Depla D. Mechanism of biaxial alignment in thin films deposited by magnetron sputtering. Thin Solid Films 2006;515:416–20.
[158] Mahieu S, Ghekiere P, De Winter G, Depla D, De Gryse R, Lebedev OI, et al. Influence of the Ar/O_2 ratio on the growth and biaxial alignment of yttria stabilized zirconia layers during reactive unbalanced magnetron sputtering. Thin Solid Films 2005;484:18–25.
[159] Mahieu S, Ghekiere P, De Winter G, De Gryse R, Depla D, Van Tendeloo G, et al. Biaxially aligned titanium nitride thin films deposited by reactive unbalanced magnetron sputtering. Surf Coat Technol 2006;200:2764–8.
[160] Mahieu S, De Winter G, Depla D, De Gryse R, Denul J. A model for the development of biaxial alignment in yttria stabilized zirconia layers deposited by unbalanced magnetron sputtering. Surf Coat Technol 2004;187:122–30.
[161] MahieuS, Ghekiere P, Depla D, De Gryse R. Biaxial alignment in sputter deposited thin films. Thin Solid Films 2006;515:1229–49.
[162] Mahieu S, Buyle G, Depla D, Heirwegh S, Ghekiere P, De Gryse R. Monte Carlo simulation of the transport of atoms in DC magnetron sputtering. Nucl Instrum Methods Phys Rev B 2006;243:313–9.
[163] Mahieu S, Ghekiere P, Depla D, De Gryse R, Lebedev OI, Van Tendeloo G. Mechanism of in-plane alignment in magnetron sputtered biaxially aligned yttria-stabilized zirconia. J Cryst Growth 2006;290:272–9.
[164] Lintymer J, Gavoille J, Martin N, Takadoum J. Glancing angle deposition to modify microstructure and properties of sputter deposited chromium thin films. Surf Coat Technol 2003;174(175):316–23.
[165] Jang HW, Kang HC, Noh DY, Yi MS. Crossover of the preferred growth orientation of AlN/Si(001) films during off-axis radiofrequency sputter growth. J Appl Phys 2003;94:2957–61.
[166] Ghekiere P, Mahieu S, De Gryse R, Depla D. Structure evolution of the biaxial alignment in sputter-deposited MgO and Cr. Thin Solid Films 2006;515:485–8.
[167] Ghekiere P, Mahieu S, De Winter G, De Gryse R, Depla D. Scanning electron microscopy study of the growth mechanism of biaxially aligned magnesium oxide layers grown by unbalanced magnetron sputtering. Thin Solid Films 2005;493:129–34.
[168] Flickyngerová S, Netrvalová M, Šutta P, Novotný I, Tvarožek V, Gašpierik P, et al. Effects of sputtering power and pressure on properties of ZnO:Ga thin films prepared by oblique-angle deposition. Thin Solid Films 2011;520:1233–7.
[169] Ye L, Kim SG, Kim YJ, Kim HJ. Effect of oblique sputtering on microstructural modification of ZnO thin films. J Vac Sci Technol A 1997;15:1194–9.
[170] Sit JC, Vick D, Robbie K, Brett MJ. Thin film microstructure control using glancing angle deposition by sputtering. J Mater Res 1999;14:1197–9.
[171] Deniz D, Karabacak T, Harper JME. Competitive growth mechanisms of AlN thin films deposited by off-normal reactive magnetron sputtering. J Appl Phys 2008;103:083553.
[172] Alvarez R, Garcia-Martin JM, Macias-Montero M, Gonzalez-Garcia L, Gonzalez JC, Rico V, et al. Growth regimes of porous gold thin films deposited by magnetron sputtering at oblique incidence: from compact to columnar microstructures. Nanotechnology 2013;24:045604.
[173] Janmohamed R, Steele JJ, Scurtescu C, Tsui YY. Study of porous carbon thin films produced by pulsed laser deposition. Appl Surf Sci 2007;253:7964–8.
[174] Vick D, Tsui YY, Brett MJ, Fedosejevs R. Production of porous carbon thin films by pulsed laser deposition. Thin Solid Films 1999;339:88–94.
[175] Sun YW, Gospodyn J, Kursa P, Sit J, DeCorby RG, Tsui YY. Dense and porous ZnO thin films produced by pulsed laser deposition. Appl Surf Sci 2005;248:392–6.
[176] Sun YW, Tsui YY. Production of porous nanostructured zinc oxide thin films by pulsed laser deposition. Opt Mater 2007;29:1111–4.
[177] Mukherjee D, Hordagoda M, Hyde R, Bingham N, Srikanth H, Witanachchi S, et al. Nanocolumnar interfaces and enhanced magnetic coercivity in preferentially oriented cobalt ferrite thin films grown using oblique-angle pulsed laser deposition. ACS Appl Mater Interfaces 2013;5:7450–7.
[178] Lu L, Xiao DQ, Sun Y, Zhang YB, Zhu JG. Preparation and characteristics of $0.95(K_{0.48}Na_{0.52}NbO_3)$–$0.05(LiSbO_3)$ films by pulsed laser deposition technique. Ferroelectrics 2009;385:8–14.
[179] Wang H, Zhao YP. Nanostructure evolution of $YBa_2Cu_3O_x$ thin films grown by pulsed-laser glancing-angle deposition. J Vac Sci Technol B 2006;24:1230–3.
[180] Chen A, Bi Z, Tsai CF, Chen L, Su Q, Zhang X, et al. Tilted aligned epitaxial $La_{0.7}Sr_{0.3}MnO_3$ nanocolumnar films with enhanced low-field magnetoresistance by pulsed laser oblique-angle deposition. Cryst Growth Des 2011;11:5405–9.
[181] Martinu L, Zabeida O, Klemberg-Sapieha JE. Plasma enhanced chemical vapor deposition of functional coatings. In: Martin PE, editor. Handbook of deposition technologies for films and coatings. Elsevier; 2009. p. 392–465.
[182] Sato H, Hata K. Growth of carbon nanotubes by plasma-enhanced chemical vapor deposition. New Diamond Front Carbon Technol 2006;16:163–76.
[183] Lim SH, Luo ZQ, Shen ZX, Lin JY. Plasma-assisted synthesis of carbon nanotubes. Nanosc Res Lett 2010;5:1377–86.
[184] Bo Z, Yang Y, Chen JH, Yu KH, Yan JH, Cen KF. Plasma-enhanced chemical vapor deposition synthesis of vertically oriented graphene nanosheets. Nanoscale 2013;5:5180–204.
[185] Hsu CM, Lin CH, Chang HL, Kuo CT. Growth of the large area horizontally-aligned carbon nanotubes by ECR-CVD. Thin Solid Films 2002;420(421):225–9.

[186] Macias-Montero M, Borras A, Saghi Z, Romero-Gomez P, Sanchez-Valencia JR, Gonzalez JC, et al. Superhydrophobic supported AgNPs@ZnO-nanorods with photoactivity in the visible. J Mater Chem 2012;22:1341–6.
[187] Macias-Montero M, Borras A, Saghi Z, Espinos JP, Barranco A, Cotrino J, et al. Vertical and tilted Ag-NPs@ZnO nanorods by plasma-enhanced chemical vapour deposition. Nanotechnology 2012;23:255303.
[188] Macias-Montero M, Borras A, Romero-Gomez P, Cotrino J, Frutos F, Gonzalez-Elipe AR. Plasma deposition of superhydrophobic Ag@TiO_2 core@shell nanorods on processable substrates. Plasma Process Polym 2014;11:164–74.
[189] Borras A, Cotrino J, Gonzalez-Elipe AR. Type of plasmas and microstructure of TiO_2 thin films prepared by PECVD. J Electrochem Soc 2007;154:152–7.
[190] Choukourov A, Solar P, Polonskyi O, Hanus J, Drabik M, Kylian O, et al. Structured Ti/Hydrocarbon plasma polymer nanocomposites produced by magnetron sputtering with glancing angle deposition. Plasma Process Polym 2010;7:25–32.
[191] Ostrikov K. Control of energy and matter at nanoscales: challenges and opportunities for plasma nanoscience in a sustainability age. J Phys D: Appl Phys 2011;44:174003.
[192] Manova D, Gerlach JW, Mandl S. Thin film deposition using energetic ions. Materials 2010;3:4109–41.
[193] Ensinger W. Ion bombardment effects during deposition of nitride and metal films. Surf Coat Technol 1998;99:1–13.
[194] Alami J, Persson POA, Music D, Gudmundsson JT, Bohlmark J, Helmersson U. Ion-assisted physical vapor deposition for enhanced film properties on non-flat surfaces. J Vac Sci Technol A 2005;23:278–80.
[195] Alami J, Eklund P, Emmerlich J, Wilhelmsson O, Jansson U, Högberg H. High-power impulse magnetron sputtering of Ti–Si–C thin films from a Ti_3SiC_2 compound target. Thin Solid Films 2006;515:1731–6.
[196] Barsoum MW. The M(N+1)AX(N) phases: a new class of solids: thermodynamically stable nanolaminates. Prog Solid State Chem 2000;28:201–81.
[197] Elofsson V, Magnfält D, Samuelsson M, Sarakinos K. Tilt of the columnar microstructure in off-normally deposited thin films using highly ionized vapor fluxes. J Appl Phys 2013;113:174906.
[198] Johansson V. Off-normal film growth by high power impulse magnetron sputtering. Master thesis. Linkoping Univ., Sweden; October 2011.
[199] Zeng F, Gao Y, Fan Y, Pan F. Skew ion-bombardment-induced microstructure and magnetic anisotropy evolutions in the immiscible Co–Cu system during deposition process. Jpn J Appl Phys 2003;42:6869–74.
[200] Feng T, Jiang B, Zhuo S, Wang X, Liu X. Study on the orientation of silver films by ion-beam assisted deposition. Appl Surf Sci 2008;254:1565–8.
[201] Sorge JB, Taschuk MT, Wakefield NG, Sit JC, Brett MJ. Metal oxide morphology in argon-assisted glancing angle deposition. J Vac Sci Technol A 2012;30:021507.
[202] Taschuk MT, Sorge JB, Steele JJ, Brett MJ. Ion-beam assisted glancing angle deposition for relative humidity sensors. IEEE Sens J 2008;8:1521–2.
[203] Enders B, Chayahara A, Fujii K. Ion beam assisted deposition under off-normal ion incidence: an experimental and analytical study of re-sputtering effects. Surf Coat Technol 2000;128:303–7.
[204] Jiang B, Ren C, Zheng Z, Liu X, Fan H, Yao L, et al. Preferred crystal orientation of hafnium films prepared by ion beam assisted deposition. Nucl Instrum Methods Phys Res B 2004;215:413–8.
[205] Abrasonis G, Kovacs GJ, Mucklich A, Zhou S, Babonneau D, Martinavicius A, et al. Substrate effects on the morphology of carbon encapsulated nickel nanoparticles grown by surface diffusion assisted phase separation. J Phys Chem C 2009;113:8645–51.
[206] Abrasonis G, Oates TWH, Kovács GJ, Grenzer J, Persson POA, Heinig KHH, et al. Nanoscale precipitation patterns in carbon–nickel nanocomposite thin films: period and tilt control via ion energy and deposition angle. J Appl Phys 2010;108:043503.
[207] Hodgkinson I, Wu Q. Ion-beam control of thin-film microstructural columnar angle. Mod Phys Lett B 2001;15:1328–31.
[208] Kitagawa T, Miyauchi K, Toyoda N, Tsubakino T, Yamada I. Optimum incident angle of Ar cluster ion beam for super hard carbon film deposition. Jpn J Appl Phys 2004;43:3955–8.
[209] Fleischauer MD, Sorge JB, Joseph RA, Brett MJ. Enhanced control of porous thin film morphology via Ion bombardment. Mater Res Soc Symp Proc 2007;960:N01–3.
[210] Chan WL, Chason E. Making waves: kinetic processes controlling surface evolution during low energy ion sputtering. J Appl Phys 2007;101:121301.
[211] Müller-Buschbaum P. A basic introduction to grazing incidence small-angle X-ray scattering. Lect notes phys, vol. 77. Berlin: Springer; 2009. p. 61–89.
[212] Dalla Torre J, Gilmer GH, Windt DL, Kalyanaraman R, Baumann FH, O'Sullivan PL, et al. Microstructure of thin tantalum films sputtered onto inclined substrates: experiments and atomistic simulations. J Appl Phys 2003;94:263–71.
[213] Rico V, Borras A, Yubero F, Espinos JP, Frutos F, Gonzalez-Elipe AR. Wetting angles on illuminated Ta_2O_5 thin films with controlled nanostructure. J Phys Chem C 2009;113:3775–84.
[214] Barabási AL, Stanley HE. Fractal concepts in surface growth. Cambridge: University Press; 1995.
[215] Pelliccione M, Lu T-M. Evolution of thin film morphology: modeling and simulations. Heidelberg: Springer Series in Materials Science, Springer Verlag; 2007.
[216] Backholm M, Foss M, Nordlund K. Roughness of glancing angle deposited titanium thin films: an experimental and computational study. Nanotechnology 2012;23:385708.
[217] Karabacak T, Wang GC, Lu TM. Quasi-periodic nanostructures grown by oblique angle deposition. J Appl Phys 2003;94:7723–8.
[218] Karabacak T, Mallikarjunan A, Singh JP, Ye D, Wang GC, Lu TM. β-phase tungsten nanorod formation by oblique-angle sputter deposition. Appl Phys Lett 2003;83:3096–8.
[219] Buzea C, Beydaghyan G, Elliott C, Robbie K. Control of power law scaling in the growth of silicon nanocolumns pseudo-regular arrays deposited by glancing angle deposition. Nanotechnology 2005;16:1986–92.
[220] Mukherjee S, Gall D. Power law scaling during physical vapor deposition under extreme shadowing conditions. J Appl Phys 2010;107:084301.

[221] Tang F, Karabacak T, Li L, Pelliccione M, Wang GC, Lu TM. Power-law scaling during shadowing growth of nanocolumns by oblique angle deposition. J Vac Sci Technol A 2007;25:160–6.
[222] Krause KM, Thommes M, Brett MJ. Pore analysis of obliquely deposited nanostructures by krypton gas adsorption at 87 K. Microporous Mesoporous Mater 2011;143:166–73.
[223] Itoh K, Ichikawa F, Takahashi Y, Tsutsumi K, Noguchi Y, Okamoto K. Columnar grain structure in cobalt films evaporated obliquely at low substrate temperatures. Jpn J Appl Phys 2006;45:2534–8.
[224] Okamoto K, Itoh K. Incidence angle dependences of columnar grain structure and texture in obliquely deposited iron films. Jpn J Appl Phys 2005;44:1382–8.
[225] Sanchez-Valencia JR, Toudert J, Borras A, Barranco A, Lahoz R, de la Fuente GF, et al. Selective dichroic patterning by nanosecond laser treatment of Ag nanostripes. Adv Mater 2011;23:848–53.
[226] Gonzalez-Garcia L, Parra-Barranco J, Sanchez-Valencia JR, Ferrer J, Garcia-Gutierrez MC, Barranco A, et al. Tuning dichroic plasmon resonance modes of gold nanoparticles in optical thin films. Adv Funct Mater 2013;23:1655–63.
[227] Aspnes DE. Optical properties of thin films. Thin Solid Films 1982;89:249–62.
[228] Poxson DJ, Mont FW, Schubert MF, Kim JK, Schubert EF. Quantification of porosity and deposition rate of nanoporous films grown by oblique-angle deposition. Appl Phys Lett 2008;93:101914.
[229] Cano M, Castillero P, Roales J, Pedrosa JM, Brittle S, Richardson T, et al. A transparent TMPyP/TiO_2 composite thin film as an HCl sensitive optochemical gas sensor. Sens Actuat B 2010;150:764–9.
[230] Sanchez-Valencia JR, Toudert J, Gonzalez-Garcıa L, Gonzalez-Elipe AR, Barranco A. Excitation transfer mechanism along the visible to the near-IR in rhodamine J-heteroaggregates. Chem Commun 2010;46:4372.
[231] Flaherty DW, Hahn NT, May RA, Berglund SP, Lin YM, Stevenson KJ, et al. Reactive ballistic deposition of nanostructured model materials for electrochemical energy conversion and storage. Acc Chem Res 2012;45:434–43.
[232] Brunauer S, Emmett PH, Teller E. Adsorption of gases in multimolecular layers. J Am Chem Soc 1938;60:309–19.
[233] Gregg SJ, Sing KSW. Adsorption, surface area and porosity. London: Academic Press; 1982.
[234] Borras A, Barranco A, Gonzalez-Elipe AR. Design and control of porosity in oxide thin films grown by PECVD. J Mater Sci 2006;41:5220–6.
[235] Borras A, Sanchez-Valencia JR, Garrido-Molinero J, Barranco A, Gonzalez-Elipe AR. Porosity and microstructure of plasma deposited TiO_2 thin films. Microporous Mesoporous Mater 2009;118:118314–24.
[236] Poxson DJ, Kuo ML, Mont FW, Kim YS, Yan X, Welser RE, et al. High performance antireflection coatings utilizing nanoporous layers. Mater Res Soc Bull 2011;36:434–8.
[237] Xi JQ, Schubert MF, Kim JK, Schubert EF, Chen M, Lin Sh-Y, et al. Optical thin-film materials with low refractive index for broad band elimination of Fresnel reflection. Nat Photon 2007;1:176–9.
[238] Chattopadhyay S, Huang YF, Jen YJ, Ganguly A, Chen KH, Chen LC. Anti-reflecting and photonic nanostructures. Mater Sci Eng R 2010;69:1–35.
[239] Dohnálek Z, Kimmel GA, McCready DE, Young JS, Dohnálková A, Smith RS, et al. Structural and chemical characterization of aligned crystalline nanoporous MgO films grown via reactive ballistic deposition. J Phys Chem B 2002;106:3526–9.
[240] Falconer JL, Schwarz JA. Temperature-programmed desorption and reaction: applications to supported catalysts. Catal Rev Sci Eng 1983;25:141–227.
[241] Weiss W, Ranke W. Surface chemistry and catalysis on well-defined epitaxial iron-oxide layers. Prog Surf Sci 2002;70:1–151.
[242] Sanchez-Valencia JR, Borras A, Barranco A, Rico VJ, Espinos JP, Gonzalez-Elipe AR. Preillumination of TiO_2 and Ta_2O_5 photoactive thin films as a tool to tailor the synthesis of composite materials. Langmuir 2008;24:9460–9.
[243] Sanchez-Valencia JR, Blaszczyk-Lezak I, Espinos JP, Hamad S, Gonzalez-Elipe AR, Barranco A. Incorporation and thermal evolution of Rhodamine 6G dye molecules adsorbed in porous columnar optical SiO_2 thin films. Langmuir 2009;25:9140–8.
[244] Castillero P, Sanchez-Valencia JR, Cano M, Pedrosa JM, Roales J, Barranco A, et al. Active and optically transparent tetracationic porphyrin/TiO_2 composite thin films. ACS Appl Mater Interfaces 2010;2:712–21.
[245] Sanchez-Valencia JR, Aparicio FJ, Espinos JP, Gonzalez-Elipe AR, Barranco A. Rhodamine 6G and 800 J-heteroaggregates with enhanced acceptor luminescence (HEAL) adsorbed in transparent SiO_2 GLAD thin films. Phys Chem Chem Phys 2011;13:7071–82.
[246] Oliveros M, Gonzalez-Garcia L, Mugnaini V, Yubero F, Roques N, Veciana J, et al. Novel guests for porous columnar thin films: the switchable perchlorinatedtrityl radical derivatives. Langmuir 2011;27:5098–106.
[247] Roales J, Pedrosa JM, Castillero P, Cano M, Richardson TH, Barranco A, et al. Selective detection of volatile organic compounds by spectral 2 imaging of porphyrin derivatives bound to TiO_2 porous films. ACS Appl Mater Interfaces 2012;4:5147–54.
[248] Roales J, Pedrosa JM, Cano M, Guillen MG, Lopes-Costa T, Castillero P, et al. Anchoring effect on (tetra)carboxyphenylporphyrin/TiO_2 composite films for VOC optical detection. RSC Adv 2014;4:1974–81.
[249] Kosmulski M. Chemical properties of material surfaces. New York: Marcel Dekker Inc.; 2001.
[250] Sharma SK, Kim MS, Kim DY, Yu JS. Al nanorod thin films as anode electrode for Li-ion rechargeable batteries. Electrochim Acta 2013;87:872–9.
[251] Tang T, Gaire C, Ye DX, Karabacak T, Lu TM, Wang GC. AFM, SEM and in situ RHEED study of Cu texture evolution on amorphous carbon by oblique angle vapor deposition. Phys Rev B 2005;72:035430.
[252] Balu R, Raju AR, Lakshminarayanan V, Mohan S. Investigations on the influence of process parameters on the structural evolution of ion beam sputter deposited chromium thin films. Mater Sci Eng B 2005;123:7–12.
[253] Chi ChS, Wang BY, Pong WF, Ho TY, Tsai ChJ, Lo FY, et al. Uniaxial magnetic anisotropy in Pd/Fe bilayers on $Al_2O_3(0001)$ induced by oblique deposition. J Appl Phys 2012;111:123918.
[254] Yu M, Qiu H, Chen X, Wu P, Tian Y. Comparative study of the characteristics of Ni films deposited on SiO_2/Si(100) by oblique-angle sputtering and conventional sputtering. Thin Solid Films 2008;516:7903–9.
[255] Morrow P, Tang F, Karabacak T, Wang PI, Ye DX, Wang GC, et al. Texture of Ru columns grown by oblique angle sputter deposition. J Vac Sci Technol A 2006;24:235–45.

[256] Tang F, Wang GC, Lu TM. Surface pole figures by reflection high-energy electron diffraction. Appl Phys Lett 2006;89:241903.
[257] Hagemeyer A, Richter AJ, Hibst H, Maier V, Marosi L. Crystallographic texture and morphology of obliquely deposited Co–Cr magnetic thin films on flexible polymeric substrates. Thin Solid Films 1993;230:199–202.
[258] Frederick JR, D'Arcy-Gall J, Gall G. Growth of epitaxial CrN on MgO(001): role of deposition angle on surface morphological evolution. Thin Solid Films 2006;494:330–5.
[259] Dimos D, Chaudhari P, Mannhart J. Superconducting transport-properties of grain-boundaries in $YBa_2Cu_3O_7$ bicrystals. Phys Rev B 1990;41:4038–49.
[260] Hannemann U, Melcher S, Neu V, Fähler S, Holzapfel B, Schultz L. Microstructure and coercivity mechanism of highly textured Nd–Fe–B films. IEEE Trans Magn 2003;39:2726–8.
[261] Messing GL, Trolier-McKinstry S, Sabolsky EM, Duran C, Kwon S, Brahmaroutu B, et al. Templated grain growth of textured piezoelectric ceramics. Crit Rev Solid State Mater Sci 2004;29:45–96.
[262] Wolter SD, Borca-Tasciucc D, Chend G, Praterb JT, Sitar Z. Processing and thermal properties of highly oriented diamond thin films. Thin Solid Films 2004;469(470):105–11.
[263] Tang T, Lu TM, Wang GC. Reflection high energy electron diffraction (RHEED) study of nanostructures: from diffraction patterns to surface pole figures. Mater Res Soc Symp Proc 2009;1184:85–90.
[264] Plawsky JL, Kim JK, Schubert EF. Engineered nanoporous and nanostructured films. Mater Today 2009;12:36–45.
[265] Messier R. The nano-world of thin films. J Nanophoton 2008;2:021995.
[266] Bindell JB, Tisone TC. Step coverage from an extended sputtering source. Thin Solid Films 1974;23:31–47.
[267] Bales GS, Zangwill A. Macroscopic model for columnar growth of amorphous films by sputter deposition. J Vac Sci Technol A 1991;9:145–9.
[268] Cho J, Terry SG, LeSar R, Levi CK. A kinetic Monte Carlo simulation of film growth by physical vapor deposition on rotating substrates. Mater Sci Eng A 2005;391:390–401.
[269] Voter AF. A method for accelerating the molecular dynamics simulation of infrequent events. J Chem Phys 1997;106:4665–77.
[270] Dong L, Smith RW, Srolovitz DJ. A two-dimensional molecular dynamics simulation of thin film growth by oblique deposition. J Appl Phys 1996;80:5682–90.
[271] Alvarez R, Palmero A, Prieto-Lopez LO, Yubero F, Cotrino J, de la Cruz W, et al. Morphological evolution of pulsed laser deposited ZrO_2 thin films. J Appl Phys 2010;107:054311.
[272] Huang H, Gilmer GH, de la Rubia TM. An atomistic simulator for thin film deposition in three dimensions. J Appl Phys 1998;84:3636–49.
[273] Yang YG, Johnson RA, Wadley HNG. A Monte Carlo simulation of the physical vapor deposition of nickel. Acta Mater 1997;45:1455–68.
[274] Wang L, Clancy P. Kinetic Monte Carlo simulation of the growth of polycrystalline Cu films. Surf Sci 2001;473:25–38.
[275] Lao C, Cotrino J, Palmero A, Gamero A, Gonzalez-Elipe AR. Electron temperature measurement in a surface-wave-produced argon plasma at intermediate pressures. Eur Phys J D 2001;14:361–6.
[276] Cotrino J, Palmero A, Rico V, Barranco A, Espinos JP, Gonzalez-Elipe AR. Electron temperature measurement in a slot antenna 2.45 GHz microwave plasma source. J Vac Sci Technol B 2001;19:410–4.
[277] Amassian A, Kaminska K, Suzuki M, Martinu L, Robbie L. Onset of shadowing-dominated growth in glancing angle deposition. Appl Phys Lett 2007;91:173114.
[278] van der Drift A. Evolutionary selection, a principle governing growth orientation in vapour-deposited layers. Philips Res Pep 1967;22:267–88.
[279] Meakin P, Krug J. Three-dimensional ballistic deposition at oblique incidence. Phys Rev A 1992;46:3390–9.
[280] Alvarez R, Lopez-Santos C, Parra-Barranco J, Rico V, Barranco A, Cotrino J, et al. Nanocolumnar growth of thin films deposited at oblique angles: beyond the tangent rule. J Vac Sci Technol B 2014;32:041802.
[281] The software STRONG can be freely downloaded from the webpage. <http://nanoscops.icmse.csic.es>.
[282] Alvarez R, Gonzalez-Garcia L, Romero-Gomez P, Rico V, Cotrino J, Gonzalez-Elipe AR, et al. Theoretical and experimental characterization of TiO_2 thin films deposited at oblique angles. J Phys D: Appl Phys 2011;44:385302.
[283] Krause KM, Taschuk MT, Harris KD, Rider DA, Wakefield NG, Sit JC, et al. Surface area characterization of obliquely deposited metal oxide nanostructured thin films. Langmuir 2010;26:4368–76.
[284] Gonzalez-Garcia L, Idigoras J, Gonzalez-Elipe AR, Barranco A, Anta JA. Charge collection properties of dye-sensitized solar cells based on 1-dimensional TiO_2 porous nanostructures and ionic-liquid electrolytes. J Photochem Photobiol A: Chem 2012;241:58–66.
[285] Oliva-Ramirez M, Gonzalez-Garcia L, Parra-Barranco J, Yubero F, Barranco A, Gonzalez-Elipe AR. Liquids analysis with optofluidic Bragg microcavities. ACS Appl Mater Interfaces 2013;5:6743–50.
[286] Backholm M, Fossa M, Nordlundb K. Roughness scaling in titanium thin films: a three-dimensional molecular dynamics study of rotational and static glancing angle deposition. Appl Surf Sci 2013;268:270–3.
[287] Pillai PP, Paclawski K, Kim J, Grzybowski BA. Nanostructural anisotropy underlies anisotropic electrical bistability. Adv Mater 2013;25:1623–8.
[288] Lau WF, Bai F, Huang Z. Ballistic glancing angle deposition of inclined Ag nanorods limited by adatom diffusion. Nanotechnology 2013;24:465707.
[289] Palmero A, van Hattum ED, Arnoldbik WM, Vredenberg AM, Habraken FHP. Characterization of the plasma in a radio-frequency magnetron sputtering system. J Appl Phys 2004;95:7611–8.
[290] Palmero A, Tomozeiu N, Vredenberg AM, Arnoldbik WM, Habraken FHPM. On the deposition process of silicon suboxides by a RF magnetron reactive sputtering in $Ar–O_2$ mixtures: theoretical and experimental approach. Surf Coat Technol 2004;177(178):215–21.
[291] van Hattum ED, Palmero A, Arnoldbik WM, Habraken FHPM. Experimental characterization of the deposition of silicon suboxide films in a radiofrequency magnetron reactive sputtering system. Surf Coat Technol 2004;188–189:399–403.
[292] Palmero A, Rudolph H, Habraken FHPM. Study of the gas rarefaction phenomenon in a magnetron sputtering system. Thin Solid Films 2006;515:631–5.

[293] van Hattum ED, Palmero A, Arnoldbik WM, Rudolph H, Habraken FHPM. On the ion and neutral atom bombardment of the growth surface in magnetron sputter deposition. Appl Phys Lett 2007;91:171501.
[294] Palmero A, van Hattum ED, Rudolph H, Habraken FHPM. Characterization of a low-pressure argon plasma using optical emission spectroscopy and a global model. J Appl Phys 2007;101:053306.
[295] van Hattum ED, Palmero A, Arnoldbik WM, Rudolph H, Habraken FHPM. Distinct processes in radio-frequency reactive magnetron plasma sputter deposition of silicon suboxide films. J Appl Phys 2007;102:124505.
[296] Macias-Montero M, Garcia-Garcia FJ, Alvarez R, Gil-Rostra J, Gonzalez JC, Cotrino J, et al. Influence of plasma-generated negative oxygen ion impingement on magnetron sputtered amorphous SiO_2 thin films during growth at low temperatures. J Appl Phys 2012;111:054312.
[297] Alvarez R, Vazquez L, Gago R, Redondo-Cubero A, Cotrino J, Palmero A. Atomistic model of ultra-smooth amorphous thin film growth by low-energy ion-assisted physical vapour deposition. J Phys D: Appl Phys 2013;46:395303.
[298] Musil J, Baroch P, Vlcek J, Nam KH, Han JG. Reactive magnetron sputtering of thin films: present status and trends. Thin Solid Films 2005;475:208–18.
[299] Bradley JW, Welzel T. Physics and phenomena in pulsed magnetrons: an overview. J Phys D: Appl Phys 2009;42:093001.
[300] Palmero A, Rudolph H, Habraken FHPM. Gas heating in plasma-assisted sputter deposition. Appl Phys Lett 2005;87:071501.
[301] Palmero A, Rudolph H, Habraken FHPM. Generalized Keller–Simmons formula for nonisothermal plasma-assisted sputtering depositions. Appl Phys Lett 2006;89:211501.
[302] Mahieu S, van Aeken K, Depla D. Quantification of the ion and momentum fluxes toward the substrate during reactive magnetron sputtering. J Appl Phys 2008;104:113301.
[303] Kools JCS. Suppression of nanoscopic shadowing during physical vapor deposition by biased diffusion. J Vac Sci Technol A 2005;23(1):85–9.
[304] Zhou XW, Wadley HNG. Hyperthermal vapor deposition of copper: athermal and biased diffusion. Surf Sci 1999;431:42–57.
[305] Zhou XW, Wadley HNG. Hyperthermal vapor deposition of copper: reflection and resputtering effects. Surf Sci 1999;431:58–73.
[306] Gras-Marti A, Valles-Abarca JA. Slowing down and thermalization of sputtered particle fluxes: energy distributions. J Appl Phys 1983;54:1071.
[307] Garcia-Martin JM, Alvarez R, Romero-Gomez P, Cebollada A, Palmero A. Tilt angle control of nanocolumns grown by glancing angle sputtering at variable argon pressures. Appl Phys Lett 2010;97:173103.
[308] Alvarez R, Romero-Gomez P, Gil-Rostra J, Cotrino J, Yubero F, Palmero A, et al. On the microstructure of thin films grown by an isotropically directed deposition flux. J Appl Phys 2010;108:064316.
[309] Depla D, Mahieu S, editors. Reactive sputter deposition. Berlin: Springer Series in Materials Science, Springer-Verlag; 2008.
[310] Westwood WD. Calculation of deposition rates in diode sputtering systems. J Vac Sci Technol 1978;15:1–9.
[311] Gil-Rostra J, Cano M, Pedrosa JM, Ferrer FJ, Garcia-Garcia F, Yubero F, et al. Electrochromic behavior of $W_xSi_yO_z$ thin films prepared by reactive magnetron sputtering at normal and glancing angles. ACS Appl Mater Interfaces 2012;22:628–38.
[312] Alvarez R, Romero-Gomez P, Gil-Rostra J, Cotrino J, Yubero F, Gonzalez-Elipe AR, et al. Growth of SiO_2 and TiO_2 thin films deposited by reactive magnetron sputtering and PECVD by the incorporation of non-directional deposition fluxes. Phys Status Solidi A 2013;210:796–801.
[313] Alvarez R, Lopez-Santos C, Ferrer FJ, Rico V, Cotrino J, Gonzalez-Elipe AR, et al. Modulating low energy ion plasma fluxes for the growth of nanoporous thin films. Plasma Process Polym 2015;12:719–24.
[314] Granqvist CG. Transparent conductors as solar energy materials: a panoramic review. Sol Energy Mater Sol Cells 2007;91:1529–98.
[315] Yamada N, Hitosugi T, Hoang N, Furubayashi Y, Hirose Y, Konuma S, et al. Structural, electrical and optical properties of sputter-deposited Nb-doped TiO_2 (TNO) polycrystalline films. Thin Solid Films 2008;516:5754–7.
[316] Schubert MF, Kim JK, Chhajed S, Schubert EF. Conductive distributed Bragg reflector fabricated by oblique angle deposition from a single material. In: Ellison MJ, editor. Thin-film coatings for optical applications IV. Proc of SPIE, 6674; 2007. p. 667403.
[317] Harris KD, van Popta AC, Sit JC, Broer DJ, Brett MJ. A birefringent and transparent electrical conductor. Adv Funct Mater 2008;18:2147–53.
[318] Zhong Y, Shin YC, Kim CM, Lee BG, Kim EH, Park YJ, et al. Optical and electrical properties of indium tin oxide thin films with tilted and spiral microstructures prepared by oblique angle deposition. J Mater Res 2008;23:2500–5.
[319] Rider DA, Tucker RT, Worfolk BJ, Krause KM, Lalany A, Brett MJ, et al. Indium tin oxide nanopillar electrodes in polymer/fullerene solar cells. Nanotechnology 2011;22:085706.
[320] Renault C, Harris KD, Brett MJ, Balland V, Limoges L. Time-resolved UV–visible spectroelectrochemistry using transparent 3D-mesoporous nanocrystalline ITO electrodes. Chem Commun 2011;47:1863–5.
[321] Lalany A, Tucker RT, Taschuk MT, Fleischauer MD, Brett MJ. Axial resistivity measurement of a nanopillar ensemble using a cross-bridge Kelvin architecture. J Vac Sci Technol A 2013;31:031502.
[322] Leem JW, Yu JS. Glancing angle deposited ITO films for efficiency enhancement of a-Si:H/μc-Si:H tandem thin film solar cells. Opt Exp 2011;19:A258–68.
[323] Leem JW, Yu JS. Influence of oblique-angle sputtered transparent conducting oxides on performance of Si-based thin film solar cells. Phys Status Solidi A 2011;208:2220–5.
[324] Sood AW, Poxson DJ, Mont FW, Chajed S, Cho J, Schubert EF, et al. Experimental and theoretical study of the optical and electrical properties of nanostructured indium tin oxide fabricated by oblique-angle deposition. J Nanosci Nanotechnol 2012;12:3950–3.
[325] Yang CS, Chang CH, Lin MH, Yu P, Wada O, Pan CL. THz conductivities of indium-tin-oxide nanowhiskers as a graded-refractive-index structure. Opt Exp 2012;20:A441–51.
[326] Yao YC, Tsai MT, Hsu HC, She LW, Cheng CM, Chen YC, et al. Use of two-dimensional nanorod arrays with slanted ITO film to enhance optical absorption for photovoltaic applications. Opt Exp 2012;20:3479–89.

[327] Lee YJ, Yao YC, Yang CH. Direct electrical contact of slanted ITO film on axial p-n junction silicon nanowire solar cells. Opt Exp 2013;21:A7–A14.
[328] Yang CS, Chang CM, Chen PH, Yu P, Pan CL. Broadband terahertz conductivity and optical transmission of indium-tin-oxide (ITO) nanomaterials. Opt Exp 2013;21:16670–82.
[329] Yu P, Chang CH, Chiu CH, Yang CS, Yu JC, Kuo HC, et al. Efficiency enhancement of GaAs photovoltaics employing antireflective indium tin oxide nanocolumns. Adv Mater 2009;21:1618–21.
[330] Schubert MF, Xi JQ, Kim JK, Schubert EF. Distributed Bragg reflector consisting of high-and low-refractive-index thin film layers made of the same material. Appl Phys Lett 2007;90:141115.
[331] Chang CH, Yu P, Yang CS. Broadband and omnidirectional antireflection from conductive indium-tin-oxide nanocolumns prepared by glancing-angle deposition with nitrogen. Appl Phys Lett 2009;94:051114.
[332] Kim JK, Chhajed S, Schubert MF, Schubert EF, Fischer AJ, Crawford MH, et al. Light-extraction enhancement of GaInN light-emitting diodes by graded-refractive-index indium tin oxide anti-reflection contact. Adv Mater 2008;20:801–4.
[333] Chiu CH, Yu PC, Chang CH, Yang CS, Hsu MH, Kuo HC, et al. Oblique electron-beam evaporation of distinctive indium-tin-oxide nanorods for enhanced light extraction from InGaN/GaN light emitting diodes. Opt Exp 2009;17:21250–6.
[334] Fung MK, Sun YC, Ng A, Ng AMC, Djurisic AB, Chan HT, et al. Indium tin oxide nanorod electrodes for polymer photovoltaics. ACS Appl Mater Interfaces 2011;3:522–7.
[335] Poxson DJ, Kuo ML, Mont FW, Kim YS, Yan X, Welser RE, et al. High-performance antireflection coatings utilizing nanoporous layers. MRS Bull 2011;36:434–8.
[336] Kwon H, Ham J, Kim DY, Oh SJ, Lee S, Oh SH, et al. Three-dimensional nanostructured indium-tin-oxide electrodes for enhanced performance of bulk heterojunction organic solar cells. Adv Energy Mater 2014;4:1301566.
[337] Renault C, Andrieux CP, Tucker RT, Brett MJ, Balland V, Limoges B. Unraveling the mechanism of catalytic reduction of O_2 by microperoxidase-11 adsorbed within a transparent 3d-nanoporous ITO film. J Am Chem Soc 2012;134:6834–45.
[338] Byu KM, Kim NH, Leem JW, Yu JS. Enhanced surface plasmon resonance detection using porous ITO-gold hybrid substrates. Appl Phys B 2012;107:803–8.
[339] Yao K, Toole R, Basnet P, Zhao Y. Highly sensitive double-layered nanorod array gas sensors prepared by oblique angle deposition. Appl Phys Lett 2014;104:073110.
[340] Park H, Iftiquar SM, Thuy TT, Jang J, Ahn S, Kim S, et al. Effects of target angle on the properties of aluminum doped zinc oxide films prepared by DC magnetron sputtering for thin film solar cell applications. J Nanosci Nanotechnol 2014;14:7710–7.
[341] Sato Y, Yanagisawa K, Oka N, Nakamura SI, Shigesato Y. Sputter deposition of Al-doped ZnO films with various incident angles. J Vac Sci Technol A 2009;27:1166–71.
[342] Cao SP, Ye F, Hou B, Xu AY. Aluminum-doped zinc oxide film with gradient property deposited at oblique angle. Thin Solid Films 2013;545:205–9.
[343] Leem JW, Yu JS. Structural, optical, and electrical properties of AZO films by tilted angle sputtering method. Thin Solid Films 2010;518:6285–8.
[344] Yang W, Joo J. Electrical resistivity change in Al:ZnO thin films dynamically deposited by bipolar pulsed direct-current sputtering and a remote plasma source. J Vac Sci Technol A 2010;28:856–60.
[345] Tucker RT, Beckers NA, Fleischauer MD, Brett MJ. Electron beam deposited Nb-doped TiO_2 toward nanostructured transparent conductive thin films. Thin Solid Films 2012;525:28–34.
[346] Lee HK, Kim MS, Yu JS. Improved device performance of AlGaInP-based vertical light-emitting diodes with low-n ATO antireflective coating layer. Microelectr Eng 2013;104:29–32.
[347] Flickyngerova S, Netrvalova M, Novotny I, Bruncko J, Gaspierik P, Sutta P, et al. Ion sputter etching of ZnO:Ga thin film surfaces. Vacuum 2012;86:703–6.
[348] Netrvalova M, Novotny I, Prusakova L, Tvarozek V, Sutta P. Influence of deposition regime on physical properties of gallium doped zinc oxide films. Vacuum 2012;86:707–10.
[349] Lee CC, Li MC, Chen SH, Kuo CC. Transparent conductive distributed Bragg reflectors composed of high and low refractive index transparent conductive films. Jpn J Appl Phys 2012;51:052602.
[350] Schubert MF, Poxson DJ, Mont FW, Kim JK, Schubert EF. Performance of antireflection coatings consisting of multiple discrete layers and comparison with continuously graded antireflection coatings. Appl Phys Exp 2010;3:082502.
[351] Poxson DJ, Schubert MF, Mont FW, Schubert EF, Kim JK. Broadband omnidirectional antireflection coatings optimized by genetic algorithm. Opt Lett 2009;34:728–30.
[352] Oh SJ, Chhajed S, Poxson DJ, Cho J, Schubert EF, Tark SJ, et al. Enhanced broadband and omni-directional performance of polycrystalline Si solar cells by using discrete multilayer antireflection coatings. Opt Exp 2013;21:A157–66.
[353] Kuo ML, Poxson DJ, Kim YS, Mont FW, Kim JK, Schubert EF, et al. Realization of a near-perfect antireflection coating for silicon solar energy utilization. Opt Lett 2008;33:2527–9.
[354] Schubert MF, Mont FW, Chhajed S, Poxson DJ, Kim JK, Schubert EF. Design of multilayer antireflection coatings made from co-sputtered and low-refractive-index materials by genetic algorithm. Opt Exp 2008;16:5290–8.
[355] Yan X, Poxson DJ, Cho J, Welser RE, Sood AK, Kim JK, et al. Enhanced omnidirectional photovoltaic performance of solar cells using multiple-discrete-layer tailored-and low-refractive index anti-reflection coatings. Adv Funct Mater 2013;23:583–90.
[356] Sood AK, Pethuraja G, Sood AW, Welser RE, Puri YR, Haldar P, et al. Development of large area nanostructured ar coatings for eo/ir sensor applications. In: Proc SPIE 8868, infrared sensors, devices, and applications III, 88680P; 2013. http://dx.doi.org/10.1117/12.2032206.
[357] Poxson DJ, Mont FW, Cho J, Schubert EF, Siegel RW. Tailored nanoporous coatings fabricated on conformable polymer substrates. ACS Appl Mater Interfaces 2012;4:6295–301.
[358] Woo SH, Park YJ, Chang DH, Sobahan KMA, Hwangbo CK. Wideband antireflection coatings of porous MgF2 films by using glancing angle deposition. J Kor Phys Soc 2007;51:1501–6.
[359] Kong WJ, Shen ZC, Wang SH, Shao JD, Fan ZX, Lu CJ. Graded index broadband antireflection coating prepared by glancing angle deposition for a high-power laser system. Chin Phys B 2010;19:044210.

[360] Jun-Chao Z, Li-Min X, Ming F, Hong-Bo H. Wide-angle and broadband graded-refractive-index antireflection coatings. Chin Phys B 2013;22:044201.
[361] Sobahan KMA, Park YJ, Kim JJ, Hwangbo CK. Nanostructured porous SiO_2 films for antireflection coatings. Opt Commun 2011;284:873–6.
[362] Zhao B, Zhou J, Chen Y, Peng Y. Structure and optical properties of TiO_2 thin films prepared by glancing angle deposition. Optoelectr Adv Mater Rapid Commun 2010;4:1990–3.
[363] Yan X, Shatalov M, Saxena T, Shur MS. Deep-ultraviolet tailored-and low-refractive index antireflection coatings for light-extraction enhancement of light emitting diodes. J Appl Phys 2013;113:163105.
[364] Leem JW, Jun DH, Jonggon H, Park WK, Park JH, Cho WJ, et al. Single-material zinc sulfide bi-layer antireflection coatings for GaAs solar cells. Opt Exp 2013;21:A821–8.
[365] Huang JH, Chen CY, Lai YF, Shih YI, Lin YC, He JH, et al. Large-area oblique-aligned ZnO nanowires through a continuously bent columnar buffer: growth, microstructure, and antireflection. Cryst Growth Des 2010;10:3297–301.
[366] Leem JW, Yu JS, Heo J, Park WK, Park JH, Cho WJ, et al. Nanostructured encapsulation coverglasses with wide-angle broadband antireflection and self-cleaning properties for III-V multi-junction solar cell applications. Sol Energy Mater Sol Cells 2014;120:555–60.
[367] Chen S, Li Z, Zhang Z. Anisotropic $Ti_xSn_{1-x}O_2$ nanostructures prepared by magnetron sputter deposition. Nanoscale Res Lett 2011;6:326.
[368] Chen S, Li Z, Zhang Z. Fabrication and optical property of periodic $Sn_{1-x}Ti_xO_2$ nanostructures patterned by the polystyrene microsphere templates. J Nanomater 2011:510237.
[369] Ni J, Zhu Y, Wang S, Li Z, Zhang Z, Wei B. Nanostructuring HfO_2 thin films as antireflection coatings. J Am Ceram Soc 2009;92:3077–80.
[370] Godinho V, Caballero-Hernandez J, Jamon D, Rojas TC, Schierholz R, Garcia-Lopez J, et al. Nanotechnology 2013;24:275604.
[371] Hung KH, Chiou GD, Wong MS, Wang YC, Chung IS. Transparent sculptured titania films for enhanced light absorption in thin-film Si solar cells. Thin Solid Films 2011;520:1385–9.
[372] Gratzel M. Photoelectrochemical cells. Nature 2001;414:338–44.
[373] Mor GK, Varghese OK, Paulose M, Shankar K, Grimes CA. A review on highly ordered, vertically oriented TiO_2 nanotube arrays: fabrication, material properties, and solar energy applications. Sol Energy Mater Sol Cells 2006;90:2011–75.
[374] Mor GK, Shankar K, Paulose M, Varghese OK, Grimes CA. Use of highly-ordered TiO_2 nanotube arrays in dye-sensitized solar cells. Nano Lett 2006;6:215–8.
[375] Gratzel M. Recent advances in sensitized mesoscopic solar cells. Acc Chem Res 2009;42:1788–98.
[376] Kiema GK, Colgan MJ, Brett MJ. Dye sensitized solar cells incorporating obliquely deposited titanium oxide layers. Sol Energy Mater Sol Cells 2005;85:321–31.
[377] Yang HY, Lee MF, Huang CH, Lo YS, Chen YJ, Wong MS. Glancing angle deposited titania films for dye-sensitized solar cells. Thin Solid Films 2009;518:1590–4.
[378] Turkevych I, Hara K, Kondo M. Nanostructured TiO_2 photoelectrodes for dye sensitized solar cells. ECS Trans 2010;25:123–8.
[379] Kamat PV. Quantum dot solar cells. Semiconductor nanocrystals as light harvesters. J Phys Chem C 2008;112:18737–53.
[380] Xu J, Chen Z, Zapien JA, Lee CS, Zhang W. Surface engineering of ZnO nanostructures for semiconductor-sensitized solar cells. Adv Mater 2014;26:5337–67.
[381] Fitzmorris BC, Larsen GK, Wheeler DA, Zhao Y, Zhang JZ. Ultrafast charge transfer dynamics in polycrystalline CdSe/TiO_2 nanorods prepared by oblique angle codeposition. J Phys Chem C 2012;116:5033–41.
[382] Lee SH, Jin H, Kim DY, Song K, Oh SH, Kim S, et al. Enhanced power conversion efficiency of quantum dot sensitized solar cells with near single-crystalline TiO_2 nanohelixes used as photoanodes. Opt Exp 2014;22:A867–79.
[383] Gerein NJ, Fleischauer MD, Brett MJ. Nanostructured titanium dioxide/polythiophene photovoltaic devices. In: 33rd IEEE photovoltaic specialists conference [0160-8371]; 2008. p. 1116–21.
[384] Gerein NJ, Fleischauer MD, Brett MJ. Effect of TiO_2 film porosity and thermal processing on TiO_2-P3HT hybrid materials and photovoltaic device performance. Sol Energy Mater Sol Cells 2010;94:2343–50.
[385] Xie Z, Henry BM, Kirov KR, Smith HE, Barkhouse A, Grovenor CRM, et al. Study of the effect of changing the microstructure of titania layers on composite solar cell performance. Thin Solid Films 2006;511(512):523–8.
[386] Chen CC, Chen CL. Fabrication and characteristics of ZnO/OAD-InN/PbPc hybrid solar cells prepared by oblique-angle deposition. Molecules 2012;17:9496–505.
[387] Ma Y, Liu F, Zhu M, Liu J, Yang Y, Li Y, et al. Silicon nanorods/P3HT hybrid solar cells. In: 34th IEEE photovoltaic specialists conference; 2009, 1/3. p. 811–3.
[388] Demiroglu D, Tatar B, Kazmanli K, Urgen M. Structural and photovoltaic properties of a-Si (SNc)/c-Si heterojunction fabricated by EBPVD technique. AIP Conf Proc 2013;1569:154–7.
[389] Hong L, Rusli, Wang X, Zheng H, Wang H, Yu HY. Design guidelines for slanting silicon nanowire arrays for solar cell application. J Appl Phys 2013;114:084303.
[390] Weickert J, Dunbar RB, Hesse HC, Wiedemann W, Schmidt-Mende L. Nanostructured organic and hybrid solar cells. Adv Mater 2011;23:1810–28.
[391] Zheng J, Xue J. Organic photovoltaic cells based on molecular donor-acceptor heterojunctions. Polym Rev 2010;50:420–53.
[392] Chen JT, Hsu CS. Conjugated polymer nanostructures for organic solar cell applications. Polym Chem 2011;2:2707–22.
[393] Zhang J, Salzmann I, Rogaschewski S, Rabe JP, Koch N, Zhang F, et al. Arrays of crystalline C60 and pentacene nanocolumns. Appl Phys Lett 2007;90:193117.
[394] Li N, Forrest SR. Tilted bulk heterojunction organic photovoltaic cells grown by oblique angle deposition. App Phys Lett 2009;95:123309.
[395] Thomas M, Worfolk BJ, Rider DA, Taschuk MT, Buriak JM, Brett MJ. Controlling C60 fullerene nanocolumn morphology for organic photovoltaic applications. IEEE Conf Publ 2011:744–7. http://dx.doi.org/10.1109/PVSC.2011.6186060.

[396] van Dijken JG, Fleischauer MD, Brett MJ. Solvent effects on ZnPc thin films and their role in fabrication of nanostructured organic solar cells. Org Electron 2011;12:2111–9.
[397] Zhou Y, Taima T, Miyadera T, Yamanari T, Kitamura M, Nakatsu K, et al. Glancing angle deposition of copper iodide nanocrystals for efficient organic photovoltaics. Nano Lett 2012;12:4146–52.
[398] Liu Y, Zhang F, Wang J. Organic photovoltaic cells based on PbPc nanocolumns prepared by glancing angle deposition. Int J Photoenergy 2013:346818.
[399] Taima T, Zhou Y, Kuwabara T, Takahashi K. Efficient small-molecule photovoltaic cells using nanostructured template. Proc SPIE 2014;8983:898310.
[400] Kim H, Lee S, Han D, Yoo S. High-density organic photovoltaic modules: mask-free fabrication using nozzle jet printing and oblique deposition. Sol Energy Mater Sol Cells 2014;120:561–5.
[401] Thomas M, Worfolk BJ, Rider DA, Taschuk MT, Buriak JM, Brett MJ. C60 fullerene nanocolumns polythiophene heterojunctions for inverted organic photovoltaic cells. ACS Appl Mater Interfaces 2011;3:1887–94.
[402] Yang Y, Aryal M, Mielczarek K, Hu W, Zakhidov A. Nanoimprinted P3HT/C60 solar cells optimized by oblique deposition of C60. J Vac Sci Technol B 2010;28. C6M104-7.
[403] van Dijken JG, Brett MJ. Dry etching of copper phthalocyanine thin films: effects on morphology and surface stoichiometry. Molecules 2012;17:10119–30.
[404] Fuyishima A, Honda K. Electrochemical photolysis of water at a semiconductor electrode. Nature 1972;238:37–8.
[405] Chen X, Li C, Gratzel M, Kostecki R, Mao SS. Nanomaterials for renewable energy production and storage. Chem Soc Rev 2012;41:7909–37.
[406] Hahn NT, Ye H, Flaherty DW, Bard AJ, Mullins CB. Thin films for photoelectrochemical water oxidation. ACS Nano 2010;4:1977–86.
[407] Hahn NT, Mullins CB. Photoelectrochemical performance of nanostructured Ti- and Sn-doped alpha-Fe_2O_3 photoanodes. Chem Mater 2010;22:6474–82.
[408] Chemelewski WD, Hahn NT, Mullins CB. Effect of Si doping and porosity on hematite's (α-Fe_2O_3) photoelectrochemical water oxidation performance. J Phys Chem C 2012;116:5255–61.
[409] Kronawitter CX, Mao SS, Antoun BR. Doped, porous iron oxide films and their optical functions and anodic photocurrents for solar water splitting. Appl Phys Lett 2011;98:092108.
[410] Berglund SP, He H, Chemelewski WD, Celio H, Dolocan A, Mullins CB. p-Si/W_2C and p-Si/W_2C/Pt photocathodes for the hydrogen evolution reaction. J Am Chem Soc 2014;136:1535–44.
[411] Khare C, Sliozberg K, Meyer R, Savan A, Schuhmann W, Ludwig A. Layered WO_3/TiO_2 nanostructures with enhanced photocurrent densities. Int J Hydrogen Energy 2013;38:15954–64.
[412] Smith W, Wolcott A, Fitzmorris RC, Zhang JZ, Zhao Y. Quasi-core-shell TiO_2/WO_3 and WO_3/TiO_2 nanorod arrays fabricated by glancing angle deposition for solar water splitting. J Mater Chem 2011;21:10792–800.
[413] He YP, Zhang ZY, Zhao YP. Optical and photocatalytic properties of oblique angle deposited nanorod array. J Vac Sci Technol B 2008;26:1350–8.
[414] Wolcott A, Smith WA, Kuykendall TR, Zhao YP, Zhang JZ. Photoelectrochemical water splitting using dense and aligned TiO_2 nanorod arrays. Small 2009;5:104–11.
[415] Wolcott A, Smith WA, Kuykendall TR, Zhao Y, Zhang JZ. Photoelectrochemical study of nanostructured ZnO thin films for hydrogen generation from water splitting. Adv Funct Mater 2009;19:1849–56.
[416] Liu Y, Chen L, Lu TM, Wang GC. Low-temperature cycling of hydrogenation-dehydrogenation of Pd-decorated Mg nanoblades. Int J Hydrogen Energy 2011;36:11752–9.
[417] Babita D, Vashistha M, Jain IP. Hydrogen in obliquely deposited LaNi5 thin films. Int J Hydrogen Energy 2001;26:1189–92.
[418] He Y, Zhao YP. Hydrogen storage and cycling properties of a vanadium decorated Mg nanoblade array on a Ti coated Si substrate. Nanotechnology 2009;20:204008.
[419] He Y, Zhao YP. Mg nanostructures tailored by glancing angle deposition. Cryst Growth Des 2010;10:440–8.
[420] He Y, Fan J, Zhao YP. The role of differently distributed vanadium nanocatalyst in the hydrogen storage of magnesium nanostructures. Int J Hydrogen Energy 2010;35:4162–70.
[421] Liu Y, Wang GC. Air stability of low-temperature dehydrogenation of Pd-decorated Mg blades. Nanotechnology 2012;23:025401.
[422] Liu Y, Rzhevskii A, Rigos S, Xie WY, Zhang SB, Lu TM, et al. A study of parylene coated Pd/Mg nanoblabes for reversible hydrogen storage. Int J Hydrogen Energy 2013;38:5019–29.
[423] Bayca SU, Cansizoglu MF, Biris AS, Watanabe F, Karabacak T. Enhanced oxidation resistance of magnesium nanorods grown by glancing angle deposition. Int J Hydrogen Energy 2011;36:5998–6004.
[424] Herring AM, Zawedrinski TA, Hamrock SJ. Fuel cell chemistry and operation. Oxford Univ. Press; 2010.
[425] Gasda MD, Teki R, Lu TM, Koratkar N, Eisman GA, Gall D. Sputter-deposited Pt PEM fuel cell electrodes: particles vs layers. J Electrochem Soc 2009;156:B614–9.
[426] Gasda MD, Eisman GA, Gall D. Nanorod PEM fuel cell cathodes with controlled porosity. J Electrochem Soc 2010;157:B437–40.
[427] Gasda MD, Eisman GA, Gall D. Pore formation by in situ etching of nanorod PEM fuel cell electrodes. J Electrochem Soc 2010;157:B113–7.
[428] Gasda MD, Eisman GA, Gall D. Sputter-deposited Pt/CrN nanoparticle PEM fuel cell cathodes: limited proton conductivity through electrode dewetting. J Electrochem Soc 2010;157:B71–6.
[429] Khudhayer WJ, Kariuki NN, Wang X, Myers DJ, Shaikh AU, Karabacak T. Oxygen reduction reaction electrocatalytic activity of glancing angle deposited platinum nanorod arrays. J Electrochem Soc 2011;158:B1029–41.
[430] Khudhayer WJ, Shaikh AU, Karabacak T. Platinum nanorod arrays with preferred morphological and crystal properties for oxygen reduction reaction. Adv Sci Lett 2011;4:3551–9.
[431] Khudhayer WJ, Shaikh AU, Karabacak T. Periodic Pt nanorod arrays with controlled porosity for oxygen reduction reaction. Nanosci Nanotechnol Lett 2012;4:999–1007.
[432] Bonakdarpour A, Fleischauer MD, Brett MJ, Dahn JR. Columnar support structures for oxygen reduction electrocatalysts prepared by glancing angle deposition. Appl Catal A: Gen 2008;349:110–5.

[433] Bonakdarpour A, Tucker RT, Fleischauer MD, Beckers NA, Brett MJ, Wilkinson DP. Nanopillar niobium oxides as support structures for oxygen reduction electrocatalysts. Electrochim Acta 2012;85:492–500.
[434] Francis SA, Tucker RT, Brett MJ, Bergens SH. Structural and activity comparison of self-limiting versus traditional Pt electro-depositions on nanopillar Ni films. J Power Sources 2013;222:533–41.
[435] Matolin V, Matolinova I, Vaclavu M, Khalakhan I, Vorokhta M, Fiala R, et al. Platinum-doped CeO_2 thin film catalysts prepared by magnetron sputtering. Langmuir 2010;26:12824–31.
[436] Yoo SJ, Jeon TY, Kim KS, Lima TH, Sung YE. Multilayered Pt/Ru nanorods with controllable bimetallic sites as methanol oxidation catalysts. Phys Chem Chem Phys 2010;12:15240–6.
[437] Saraf L, Matson DW, Shutthanandan V, Wang CM, Marina O, Thevuthasan S. Ceria incorporation into YSZ columnar nanostructures. Electrochem Solid-State Lett 2005;8:A525–7.
[438] Wu MH, Huang JL, Fung KZ, Lii DF. Conductivity study of porous yttria-doped zirconia and strontia-doped lanthanum manganite bilayer film by glancing angle deposition. Surf Coat Technol 2010;205:30–4.
[439] Wu MH, Huang JL, Fung KZ, Lii DF. Application of samaria doped sculptured ceria/$La_{1-x}Sr_xCo_{1-y}Fe_yO_{3-\delta}$ in cathode of SOFCs at intermediate temperature. Vacuum 2014;101:57–62.
[440] Teki R, Datta MD, Krishnan R, Parker TC, Lu TM, Kumta PN, et al. Nanostructured silicon anodes for lithium ion rechargeable batteries. Small 2009;5:2236–42.
[441] Su X, Wu Q, Li J, Xiao X, Lott A, Lu W, et al. Silicon-based nanomaterials for lithium-ion batteries: a review. Adv Energy Mater 2014;4:1300882.
[442] Parkinson MF, Ko JK, Halajko A, Sanghvi S, Amatucci GG. Effect of vertically structured porosity on electrochemical performance of FeF_2 films for lithium batteries. Electrochim Acta 2014;125:71–82.
[443] Fleischauer MD, Li J, Brett MJ. Columnar thin films for three-dimensional microbatteries. J Electrochem Soc 2009;156:A33–6.
[444] He Y, Fan J, Zhao YP. Engineering a well-aligned composition-graded CuSi nanorod array by an oblique angle codeposition technique. Cryst Growth Des 2010;10:4954–8.
[445] Krishnan R, Lu M, Koratkar N. Functionally strain-graded nanoscoops for high power Li-ion battery anodes. Nano Lett 2011;11:377–84.
[446] Abel PR, Chockla AM, Lin YM, Holmberg VC, Harris JT, Korgel BA, et al. Nanostructured $Si_{(1-x)}Ge_x$ for tunable thin film lithium-ion battery anodes. ACS Nano 2013;7:2249–57.
[447] Sharma SK, Kim MS, Kim DY, Yu JS. Al nanorod thin films as anode electrode for Li ion rechargeable batteries. Electrochim Acta 2013;87:872–9.
[448] Sun J, Tang K, Yu X, Li H, Huang X. Needle-like $LiFePO_4$ thin films prepared by an off-axis pulsed laser deposition technique. Thin Solid Films 2009;517:2618–22.
[449] Legrand C, Dupont L, Tang K, Li H, Huang XJ, Baudrin E. Structural and textural characterization of $LiFePO_4$ thin films prepared by pulsed laser deposition on Si substrates. Thin Solid Films 2010;518:5447–51.
[450] Lin YM, Abel PR, Flaherty DW, Wu J, Stevenson KJ, Heller A, et al. Morphology dependence of the lithium storage capability and rate performance of amorphous TiO_2 electrodes. J Phys Chem C 2011;115:2585–91.
[451] Liu DL, Ye DX, Khan F, Tang F, Lim BK, Picu RC, et al. Mechanics of patterned helical Si springs on Si substrate. J Nanosci Nanotechnol 2003;3:492–5.
[452] Sharma SK, Kim DY. Abnormal residual stress in nanostructured Al thin films grown on Ti/glass substrates. Current Appl Phys 2013;13:1874–9.
[453] Abel PR, Lin YM, Celio H, Heller A, Mullins CB. Improving the stability of nanostructured silicon thin film lithium-ion battery anodes through their controlled oxidation. ACS Nano 2012;6:2506–16.
[454] Abel PR, Lin YM, Souza T, Chou CY, Gupta A, Goodenough JB, et al. Nanocolumnar germanium thin films as a high-rate sodium-ion battery anode material. J Phys Chem C 2013;117:18885–90.
[455] Granqvist CG. Solar energy materials. Adv Mater 2003;15:1789–803.
[456] Le Bellac D, Azens A, Granqvist CG. Angular selective transmittance through electrochromic tungsten-oxide films made by oblique angle sputtering. Appl Phys Lett 1995;66:1715–6.
[457] Garcia-Garcia FJ, Gil-Rostra J, Yubero F, Gonzalez-Elipe AR. Electrochromism in WO_x and $W_xSi_yO_z$ thin films prepared by magnetron sputtering at glancing angles. Nanosci Nanotechnol Lett 2013;5:89–93.
[458] Gil-Rostra J, Garcia-Garcia F, Yubero F, Gonzalez-Elipe AR. Tuning the transmittance and the electrochromic behavior of $Co_xSi_yO_z$ thin films prepared by magnetron sputtering at glancing angle. Sol Energy Mater Sol Cells 2014;123:130–8.
[459] Wang ZL. Towards self-powered nanosystems: from nanogenerators to nanopiezotronics. Adv Funct Mater 2008;18:3553–67.
[460] Qin Y, Wang X, Wang ZL. Microfibre-nanowire hybrid structure for energy scavenging. Nature 2008;451:809–13.
[461] Ku NJ, Huang JH, Wang CH, Fang HC, Liu CP. Crystal face-dependent nanopiezotronics of an obliquely aligned InN nanorod array. Nano Lett 2012;12:562–8.
[462] Chen CY, Huang JH, Song J, Zhou Y, Lin L, Huang PC, et al. Anisotropic outputs of a nanogenerator from oblique-aligned ZnO nanowire arrays. ACS Nano 2011;5:6707–13.
[463] Chun J, Lee KY, Kang CY, Kim W, Kim SW, Baik JM. Embossed hollow hemisphere-based piezoelectric nanogenerator and highly responsive pressure sensor. Adv Funct Mater 2014;24:2038–43.
[464] Steele JJ, Fitzpatrick GA, Brett MJ. Capacitive humidity sensors with high sensitivity and subsecond response times. IEEE Sens J 2007;7:955–6.
[465] Kupsta MR, Taschuk MT, Brett MJ, Sit JC. Reactive ion etching of columnar nanostructured TiO_2 thin films for modified relative humidity sensor response time. IEEE Sens J 2009;9:1979–86.
[466] Taschuk MT, Steele JJ, van Popta AC, Brett MJ. Photocatalytic regeneration of interdigitated capacitor relative humidity sensors fabricated by glancing angle deposition. Sens Actuat B 2008;134:666–71.
[467] Steele JJ, Taschuk MT, Brett MJ. Nanostructured metal oxide thin films for humidity sensors. IEEE Sens J 2008;8:1422–8.
[468] Beckers NA, Taschuk MT, Brett MJ. Selective room temperature nanostructured thin film alcohol sensor as a virtual sensor array. Sens Actuat B 2013;176:1096–102.

[469] Kanamori Y, Itoh E, Miyairi K. Improvement of sensitivity and response speed of capacitive type humidity sensor using partially fluorinated polyimide thin film. Mol Cryst Liquid Cryst 2007;472:717–25.
[470] Chu J, Peng X, Sajjad M, Yang B, Feng PX. Nanostructures and sensing properties of ZnO prepared using normal and oblique angle deposition techniques. Thin Solid Films 2012;520:3493–8.
[471] Moon HG, Choi YR, Shim YS, Choi KI, Lee JH, Kim JS, et al. Extremely sensitive and selective no probe based on villi-like WO_3 nanostructures for application to exhaled breath analyzers. ACS Appl Mater Interfaces 2013;5:10591–6.
[472] Ahmad MZ, Wisitsoraat A, Zoolfakar AS, Ab Kadir A, Wlodarski W. Investigation of RF sputtered tungsten trioxide nanorod thin film gas sensors prepared with a glancing angle deposition method toward reductive and oxidative analytes. Sens Actuat B 2013;183:364–71.
[473] Wongchoosuk C, Wisitsoraat A, Phokharatkul D, Horprathum M, Tuantranont A, Kerdcharoend T. Carbon doped tungsten oxide nanorods NO_2 sensor prepared by glancing angle RF sputtering. Sens Actuat B 2013;181:388–94.
[474] Manera MG, Montagna G, Ferreiro-Vila E, Gonzalez-Garcia L, Sanchez-Valencia JR, Gonzalez-Elipe AR, et al. Enhanced gas sensing performance of TiO_2 functionalized magneto-optical SPR sensors. J Mater Chem 2011;21:16049–56.
[475] Hwang S, Kwon H, Chhajed S, Byon JW, Baik JM, Im J, et al. A near single crystalline TiO_2 nanohelix array: enhanced gas sensing performance and its application as a monolithically integrated electronic nose. Analyst 2013;138:443–50.
[476] Kwan JK, Sit JC. High sensitivity Love-wave humidity sensors using glancing angle deposited thin films. Sens Actuat B 2012;173:164–8.
[477] Kwan JK, Sit JC. Acoustic wave liquid sensors enhanced with glancing angle-deposited thin films. Sens Actuat B 2013;181:715–9.
[478] Wu TT, Chen YY, Huang GT, Chang PZ. Evaluation of elastic properties of submicrometer thin films using slanted finger interdigital transducers. J Appl Phys 2005;97:073510.
[479] Hirakata H, Ajioka Y, Yonezu A, Minoshima K. Fabrication and mechanical properties of column-particle nanocomposites by multiscale shape-assisted self-assembly. J Phys D: Appl Phys 2012;45:025302.
[480] Hirakata H, Nishihira T, Yonezu A, Minoshima K. Frictional anisotropy of oblique nanocolumn arrays grown by glancing angle deposition. Tribol Lett 2011;44:259–68.
[481] Madurga V, Vergara J, Favieres C. Generating and measuring the anisotropic elastic behaviour of Co thin films with oriented surface nano-strings on micro-cantilevers. Nanoscale Res Lett 2011;6:325.
[482] Jimenez-Pique E, Gonzalez-Garcia L, Rico VJ, Gonzalez-Elipe AR. Nanoindentation of nanocolumnar TiO_2 thin films with single and stacked zig-zag layers. Thin Solid Films 2014;550:444–9.
[483] Singh JP, Chu HY, Abell J, Trippa RA, Zhao YP. Flexible and mechanical strain resistant large area SERS active substrates. Nanoscale 2012;4:3410–4.
[484] Stempfle P, Besnard A, Martin N, Domatti A, Takadoum J. Accurate control of friction with nanosculptured thin coatings: application to gripping in microscale assembly. Tribol Int 2013;59:67–78.
[485] Tawfick S, Hart AJ, de Volder M. Capillary bending of Janus carbon nanotube micropillars. Nanoscale 2012;4:3852–6.
[486] Yamaguchi M, Liu J, Ye D, Lu TM. Coherent acoustic vibrations in silicon submicron spiral arrays. J Appl Phys 2009;106:033517.
[487] Kesapragada SV, Victor P, Nalamasu O, Gall D. Nanospring pressure sensors grown by glancing angle deposition. Nano Lett 2006;6:854–7.
[488] Li W, Huang G, Wang J, Yu Y, Wu X, Cui X, et al. Superelastic metal microsprings as fluidic sensors and actuators. Lab Chip 2012;12:2322–8.
[489] Chun J, Lee KY, Kang CY, Kim MW, Kim SW, Baik JM. Embossed hollow hemisphere-based piezoelectric nanogenerator and highly responsive pressure sensor. Adv Funct Mater 2014;24:2038–43.
[490] Lakhtakia A, McCall W, Sherwin JA, Wu Q, Hodgkinson IJ. Sculptured-thin-film spectral holes for optical sensing of fluids. Opt Commun 2001;194:33–46.
[491] Motohiro Y, Taga Y. Thin film retardation plate by oblique deposition. Appl Opt 1989;28:2466–82.
[492] Hodgkinson I, Wu QH. Serial bideposition of anisotropic thin films with enhanced linear birefringence. Appl Opt 1999;38:3621–5.
[493] van Popta AC, Sit JC, Brett MJ. Optical properties of porous helical thin films. Appl Opt 2004;43:3632–9.
[494] van Popta AC, van Popta KR, Sit JC, Brett MJ. Sidelobe suppression in chiral optical filters by apodization of the local form birefringence. J Opt Soc Am A 2007;24:3140–9.
[495] Hodgkinson I, Wu QH, Silva LD, Arnold M, Lakhtakia MA, et al. Structurally perturbed chiral Bragg reflectors for elliptically polarized light. Opt Lett 2005;30:2629–31.
[496] Kennedy SR, Brett MJ. Porous broadband antireflection coating by glancing angle deposition. Appl Opt 2003;42:4573–9.
[497] Xi JQ, Schubert MF, Kim JK, Schubert EF, Chen M, Lin SY, et al. Optical thin-film materials with low refractive index for broadband elimination of Fresnel reflection. Nat Photon 2007;1:176–9.
[498] Lu Z. Multiple narrow bandpass optical filters based on one-dimensional rugate photonic structures of two periodicities. Opt Lett 2011;36:573–5.
[499] Zhu Y, Jiao H. Rugate filter with multi-channel grown by glancing angle deposition. Optik 2012;123:1501–3.
[500] Hawkeye MM, Brett MJ. Photonic bandgap properties of nanostructured materials fabricated with glancing angle deposit. Proc SPIE 2007:683204.
[501] Gospodyn J, Taschuk MT, Hrudey PCP, Tsui YY, Fedosejevs R, Brett MJ, et al. Photoluminescence emission profiles of Y_2O_3:Eu films composed of high-low density stacks produced by glancing angle deposition. Appl Opt 2008;47:2798–805.
[502] Gonzalez-Garcia L, Lozano G, Barranco A, Miguez H, Gonzalez-Elipe AR. TiO_2–SiO_2 one-dimensional photonic crystals of controlled porosity by glancing angle physical vapour deposition. J Mater Chem 2010;20:6408–12.
[503] Kaminska K, Robbie K. Birefringent omnidirectional reflector. Appl Opt 2004;43:1570–6.
[504] Kennedy SR, Brett MJ, Toader O, John S. Fabrication of tetragonal square spiral photonic crystals. Nano Lett 2002;2:59–62.
[505] Ye DX, Yang ZP, Chang ASP, Bur J, Lin SY, Lu TM, et al. Experimental realization of a well-controlled 3D silicon spiral photonic crystal. J Phys D: Appl Phys 2007;40:2624–8.
[506] Jensen OE, Brett MJ. Square spiral 3D photonic crystals at telecommunications frequencies. Opt Exp 2005;13:3348–54.

[507] Parra-Barranco J, Oliva-Ramirez M, Gonzalez-Garcia L, Alcaire M, Macias-Montero M, Borras A, et al. Bending induced self-organized switchable gratings on polymeric substrates. ACS Appl Mater Interfaces 2014;6:11924–31.
[508] Yang PD, Wirnsberger G, Huang HC, Cordero SR, McGehee MD, Scott B, et al. Mirrorless lasing from mesostructured waveguides patterned by soft lithography. Science 2000;287:465–7.
[509] Vogel R, Meredith P, Kartini I, Harvey M, Riches JD, Bishop A, et al. Mesostructured dye-doped titanium dioxide for micro-optoelectronic applications. ChemPhysChem 2003;4:595–603.
[510] Sanchez C, Belleville P, Popall M, Nicole L. Applications of advanced hybrid organic–inorganic nanomaterials: from laboratory to market. Chem Soc Rev 2011;40:696–753.
[511] Czimerova A, Jankovic L, Bujdak J. Spectral properties of rhodamine 6G in smectite dispersions: effect of the monovalent cations. J Colloid Interface Sci 2011;357:322–30.
[512] Hamad S, Sanchez-Valencia JR, Barranco A, Mejias JA, Gonzalez-Elipe AR. Molecular dynamics simulation of the effect of pH on the adsorption of rhodamine laser dyes on TiO_2 hydroxylated surfaces. Mol Simul 2009;35:1140–51.
[513] Sanchez-Valencia JR, Toudert J, Gonzalez-Garcia L, Gonzalez-Elipe AR, Barranco A. Excitation transfer mechanism along the visible to the near-IR in rhodamine J-heteroaggregates. Chem Commun 2010;46:4372–4.
[514] Khelchand N, Choudhuri B, Mondal A, Dhar JC, Goswami T, Saha S, et al. 2D Like photonic crystal using In_2O_3-SiO_x heterostructure nanocolumn arrays and humidity sensing. Electr Mat Let 2014;10:975–80.
[515] Steele JJ, van Popta AC, Hawkeye MM, Sit JC, Brett MJ. Nanostructured gradient index optical filter for high-speed humidity sensing. Sens Actuat B – Chem 2006;120:213–9.
[516] Hawkeye MM, Brett MJ. Optimized colorimetric photonic-crystal humidity sensor fabricated using glancing angle deposition. Adv Funct Mater 2011;21:3652–8.
[517] Wisitsoorat A, Ahmad MZ, Yaacob MH, Horpratum M, Phakaratkul D, Lomas T, et al. Optical H_2 sensing properties of vertically aligned Pd/WO_3 nanorods thin films deposited via glancing angle RF magnetron sputtering. Sens Actuat B – Chem 2013;182:795–801.
[518] Li L, Sasaki T, Shimizu Y, Koshizaki N. Controlled cobalt oxide from two-dimensional films to one-dimensional nanorods and zero-dimensional nanoparticles: morphology-dependent optical carbon monoxide gas-sensing properties. J Phys Chem C 2009;113:15948–54.
[519] van Popta AC, Steele JJ, Tsoi S, Veinot JG, Brett MJ, Sit JC. Porous nanostructured optical filters rendered insensitive to humidity by vapor-phase functionalization. Adv Funct Mater 2006;16:1331–6.
[520] He Y, Fu J, Zhao Y. Oblique angle deposition and its applications in plasmonics. Front Phys 2014;9:47–59.
[521] Abdulhalim I. Plasmonic sensing using metallic nano-sculptured thin films. Small 2014;10:3499–514.
[522] Filippin AN, Borras A, Rico VJ, Frutos F, Gonzalez-Elipe AR. Laser induced enhancement of dichroism in supported silver nanoparticles deposited by evaporation at glancing angles. Nanotechnology 2013;24:045301.
[523] Sanchez-Valencia JR, Toudert J, Borras A, Lopez-Santos C, Barranco A, Feliu IO, et al. Tunable in-plane optical anisotropy of Ag nanoparticles deposited by dc sputtering onto SiO_2 nanocolumnar films. Plasmonics 2010;5:241–50.
[524] Suzuki M, Maekita W, Kishimoto K, Teramura S, Nakajima K, Kimura K, et al. Direct formation of arrays of prolate Ag nanoparticles by dynamic oblique deposition. Jpn J Appl Phys 2005;44:193–5.
[525] Suzuki M, Maekita W, Wada Y, Nakajima K, Kimura K, Fukuoka T, et al. In-line aligned and bottom-up Ag nanorods for surface-enhanced Raman spectroscopy. Appl Phys Lett 2006;88:203121.
[526] Suzuki M, Maekita W, Wada Y, Nagai K, Nakajima K, Kimura K, et al. Ag nanorod arrays tailored for surface-enhanced Raman imaging in the near-infrared region. Nanotechnology 2008;19:265304.
[527] Fu JX, Zhao YP. Au nanoparticle based localized surface plasmon resonance substrates fabricated by dynamic shadowing growth. Nanotechnology 2010;21:175303.
[528] Gish DA, Nsiah F, McDermott MT, Brett MJ. Localized surface plasmon resonance biosensor using silver nanostructures fabricated by glancing angle deposition. Anal Chem 2007;79:4228–32.
[529] Shalabney A, Abdulhalim I. Sensitivity-enhancement methods for surface plasmon sensors. Laser Photon Rev 2011;5:571–606.
[530] Fu JX, Collins A, Zhao YP. Optical properties and biosensor application of ultrathin silver films prepared by oblique angle deposition. J Phys Chem C 2008;112:16784.
[531] Zhang N, Su X, Free P, Zhou X, Neoh KG, Teng J, et al. Plasmonic metal nanostructure array by glancing angle deposition for biosensing application. Sens Actuat B – Chem 2013;183:310–8.
[532] Wachter EA, Moore AK, Haas JW. Fabrication of tailored needle substrates for surface-enhanced Raman scattering. Vib Spectrosc 1992;3:73–8.
[533] Martinez JL, Gao Y, Lopez-Rios T, Wirgin A. Anisotropic surface-enhanced Raman scattering at obliquely evaporated Ag films. Phys Rev B 1987;35:9481–8.
[534] Martinez JL, Gao Y, Lopez-Rios T. Surface-enhanced Raman scattering of obliquely evaporated Ag films. Phys Rev B 1986;33:5917–9.
[535] Liao PF, Bergman JG, Chemla DS, Wokaun A, Melngailis J, Hawryluk AM, et al. Surface-enhanced Raman scattering from microlithographic silver particle surfaces. Chem Phys Lett 1981;82:355–9.
[536] Ruan CM, Eres G, Wang W, Zhang ZY, Gu BH. Controlled fabrication of nanopillar arrays as active substrates for surface-enhanced Raman spectroscopy. Langmuir 2007;23:5757–60.
[537] De Jesus MA, Giesfeldt KS, Oran JM, Abu-Hatab NA, Lavrik NV, Sepaniak MJ. Nanofabrication of densely packed metal-polymer arrays for surface-enhanced Raman spectrometry. Appl Spectrosc 2005;59:1501–8.
[538] Liu YJ, Chu HY, Zhao YP. Silver nanorod array substrates fabricated by oblique angle deposition: morphological, optical, and SERS characterizations. J Phys Chem C 2010;114:8176–83.
[539] Driskell JD, Shanmukh S, Liu Y, Chaney SB, Tang XJ, Zhao YP, et al. The use of aligned silver nanorod arrays prepared by oblique angle deposition as surface enhanced Raman scattering substrates. J Phys Chem C 2008;112:895–901.
[540] Singh JP, Lanier TE, Zhu H, Dennis WM, Tripp RA, Zhao YP. Highly sensitive and transparent surface enhanced Raman scattering substrates made by active coldly condensed Ag nanorod arrays. J Phys Chem C 2012;116:20550–7.
[541] Zhou Q, He Y, Abell J, Zhang ZJ, Zhao YP. Optical properties and surface enhanced Raman scattering of L-shaped silver nanorod arrays. J Phys Chem C 2011;115:14131–40.

[542] Zhou Q, Li ZC, Yang Y, Zhang ZJ. Arrays of aligned, single crystalline silver nanorods for trace amount detection. J Phys D: Appl Phys 2007;41:152007.
[543] Zhou Q, He Y, Abell J, Zhang ZJ, Zhao Y. Surface-enhanced Raman scattering from helical silver nanorod arrays. Chem Commun 2011;47:4466–8.
[544] Abdulhalim I, Karabchevsky A, Patzig C, Rauschenbach B, Fuhrmann B, Eltzov E, et al. Surface-enhanced fluorescence from metal sculptured thin films with application to biosensing in water. Appl Phys Lett 2009;94:063106.
[545] Karabchevsky A, Khare C, Rauschenbach B, Abdulhalim I. Microspot sensing based on surface-enhanced fluorescence from nanosculptured thin films. J Nanophoton 2012;6:061508.
[546] Karabchevsky A, Tsapovsky L, Marks RS, Abdulhalim I. Optical immunosensor for endocrine disruptor nanolayer detection by surface plasmon resonance imaging. Proc SPIE 2011;8099:809918.
[547] Karabchevsky A, Patzig C, Rauschenbach B, Abdulhalim I. Microspot surface enhanced fluorescence from sculptured thin films for control of antibody immobilization. Proc SPIE 2011;8104:81040L.
[548] Feng X, Jiang L. Design and creation of superwetting/antiwetting surfaces. Adv Mater 2006;18:3063–78.
[549] Tawfick S, De Volder M, Copic D, Park SJ, Oliver CR, Polsen ES, et al. Engineering of micro-and nanostructured surfaces with anisotropic geometries and properties. Adv Mater 2012;24:1628–74.
[550] Tuteja A, Choi W, Ma M, Mabry JM, Mazzella SA, Rutledge GC, et al. Designing superoleophobic surfaces. Science 2007;318:1618–22.
[551] Chu Z, Seeger S. Superamphiphobic surfaces. Chem Soc Rev 2014;43:2784–98.
[552] Blossey R. Self-cleaning surfaces-virtual realities. Nat Mater 2003;2:301–6.
[553] Wenzel RN. Resistance of solid surfaces to wetting by water. Ind Eng Chem 1936;28:988–94.
[554] Cassie ABD, Baxter S. Wettability of porous surfaces. Trans Faraday Soc 1944;40:0546–550.
[555] Rahmawan Y, Yoon H, Moon MW, Jeong HG, Suh KY. Janus-faced micro and nanopillars for geometry and surface chemistry controllable bioinspired dry adhesives. J Adhes Sci Technol 2014;28:367–86.
[556] Khudhayer WJ, Sharma R, Karabacak T. Hydrophobic metallic nanorods with Teflon nanopatches. Nanotechnology 2009;20:275302.
[557] Kannarpady GK, Khedir KR, Ishihara H, Woo J, Oshin OD, Trigwell S, et al. Nanorods using template-assisted glancing angle deposition for superhydrophobic applications. ACS Appl Mater Interfaces 2011;3:2332–40.
[558] Khedir KR, Kannarpady GK, Ishihara H, Woo J, Ryerson C, Biris AS. Design and fabrication of teflon-coated tungsten nanorods for tunable hydrophobicity. Langmuir 2011;27:4661–8.
[559] Bayat A, Ebrahimi M, Moshfegh AZ. Correlation between surface roughness and hydrophobicity of GLAD RF sputtered PTFE/W/glass nanorod thin films. Vacuum 2014;101:279–82.
[560] Tsoi S, Fok E, Sit JC, Veinot JGC. Superhydrophobic, high surface area, 3-D SiO_2 nanostructures through siloxane-based surface functionalization. Langmuir 2004;20:10771–4.
[561] Dawood MK, Zheng H, Liew TH, Leong KC, Foo YL, Rajagopalan R, et al. Mimicking both petal and lotus effects on a single silicon substrate by tuning the wettability of nanostructured surfaces. Langmuir 2011;27:4126–33.
[562] Dawood MK, Zheng H, Kurniawan NA, Leong KC, Foo YL, Rajagopalan R, et al. Modulation of surface wettability of superhydrophobic substrates using Si nanowire arrays and capillary-force-induced nanocohesion. Soft Matter 2012;8:3549–57.
[563] Macias-Montero A, Borras A, Alvarez R, Gonzalez-Elipe AR. Following the wetting of one-dimensional photoactive surfaces. Langmuir 2012;28:15047–55.
[564] Fujii T, Aoki Y, Habazak H. Fabrication of super-oil-repellent dual pillar surfaces with optimized pillar intervals. Langmuir 2011;27:11752–6.
[565] Fujii T, Sato H, Tsuji E, Aoki Y, Habazaki H. Important role of nanopore morphology in superoleophobic hierarchical surfaces. J Phys Chem C 2012;116:23308–14.
[566] Tsoi S, Fok E, Sit JC, Veinot JGC. Surface functionalization of porous nanostructured metal oxide thin films fabricated by glancing angle deposition. Chem Mater 2006;18:5260–6.
[567] Uchida K, Nishikawa N, Izumi N, Yamazoe S, Mayama H, Kojima Y, et al. Phototunable diarylethene microcrystalline surfaces: lotus and petal effects upon wetting. Angew Chem Int Ed 2010;49:5942–4.
[568] Borras A, Gonzalez-Elipe AR. Wetting properties of polycrystalline TiO_2 surfaces: a scaling approach to the roughness factors. Langmuir 2010;26:15875–82.
[569] Borras A, Groning P, Sanchez-Valencia JR, Barranco A, Espinos JP, Gonzalez-Elipe AR. Air- and light-stable superhydrophobic colored surfaces based on supported organic nanowires. Langmuir 2010;26:1487–92.
[570] Macias-Montero M, Filippin AN, Saghi Z, Aparicio FJ, Barranco A, Espinos JP, et al. Vertically aligned hybrid core/shell semiconductor nanowires for photonics applications. Adv Funct Mater 2013;23:5981–9.
[571] Nguyen CV, Delzeit L, Cassell AM, Li J, Han J, Meyyappan M. Preparation of nucleic acid functionalized carbon nanotube arrays. Nano Lett 2002;2:1079–81.
[572] Fan JG, Dyer D, Zhang G, Zhao YP. Nanocarpet effect: pattern formation during the wetting of vertically aligned nanorod arrays. Nano Lett 2004;4:2133–8.
[573] Fan JG, Zhao YP. Characterization of watermarks formed in nano-carpet effect. Langmuir 2006;22:3662–71.
[574] Fan JG, Fu JX, Zhao YP. The effect of the shape of nanorod arrays on the nanocarpet effect. Nanotechnology 2008;19:045713.
[575] Fan J, Zhao YP. Nanocarpet effect induced superhydrophobicity. Langmuir 2010;26:8245–50.
[576] Ojha M, Chatterjee A, Mont F, Schubert EF, Wayner Jr PC, Plawsky JL. The role of solid surface structure on dropwise phase change processes. Int J Heat Mass Transfer 2013;53:910–22.
[577] Shah PJ, Wu Z, Sarangan AM. Effects of CO_2 critical point drying on nanostructured SiO_2 thin films after liquid exposure. Thin Solid Films 2013;527:344–8.
[578] Ye DX, Lu TM, Karabacak T. Influence of nanotips on the hydrophilicity of metallic nanorod surfaces. Phys Rev Lett 2008;100:256102.
[579] Fan JG, Zhao YP. Freezing a water droplet on an aligned Si nanorod array substrate. Nanotechnology 2008;19:155707.

[580] Malvadkar NA, Hancock MH, Sekeroglu K, Dressick WJ, Demirel MC. An engineered anisotropic nanofilm with unidirectional wetting properties. Nat Mater 2010;9:1023–8.
[581] Christophis C, Sekeroglu K, Demirel G, Thome I, Grunze M, Demirel MC, et al. Fibroblast adhesion on unidirectional polymeric nanofilms. Biointerphases 2011;6:158–63.
[582] Kubus L, Erdogan H, Piskin E, Demirel G. Controlling uni-directional wetting via surface chemistry and morphology. Soft Matter 2012;8:11704–7.
[583] Cetinkaya M, Boduroglu S, Demirel MC. Growth of nanostructured thin films of poly(p-xylylene) derivatives by vapor deposition. Polymer 2007;48:4130–4.
[584] Demirel MC. Emergent properties of spatially organized poly(p-xylylene) films fabricated by vapor deposition. Colloid Surf A: Physicochem Eng Aspects 2008;321:121–4.
[585] Malvadkar N, Park S, Urquidi-MacDonald M, Wang H, Demirel MC. Catalytic activity of cobalt deposited on nanostructured poly(p-xylylene) films. J Power Sources 2008;182:323–8.
[586] He M, Wang PI, Lu TM. Mechanism for the formation of isolated poly(p-xylylene) fibrous structures under shadowing growth. Langmuir 2011;27:5107–11.
[587] Wei L, Parhi P, Vogler EA, Ritty TR, Lakhtakia A. Thickness-controlled hydrophobicity of fibrous parylene-C films. Mater Lett 2010;64:1063–5.
[588] Wei L, Lakhtakia A, Roopnariane AP, Ritty TM. Human fibroblast attachment on fibrous parylene-C thin-film substrates. Mater Sci Eng C 2010;30:1252–9.
[589] Bezuidenhout LW, Nazemifard N, Jemere AB, Harrison DJ, Brett MJ. Microchannels filled with diverse micro-and nanostructures fabricated by glancing angle deposition. Lab Chip 2011;11:1671–8.
[590] Xiao C, Cao Z, Deng J, Huang Z, Xu Z, Fu J, et al. Microfluidic-based metal enhanced fluorescence for capillary electrophoresis by Ag nanorods arrays. Nanotechnology 2014;25:225502.
[591] Basnet P, Larsen GK, Jadeja RP, Hung YC, Zhao Y. α-Fe_2O_3 nanocolumns and nanorods fabricated by electron beam evaporation for visible light photocatalytic and antimicrobial applications. ACS Appl Mater Interfaces 2013;5:2085–95.
[592] Lopian M, Motemani Y, Borgmann A, Khare C, Buenconsejo PJS, Schildhauer TA, et al. Structure-related antibacterial activity of a titanium nanostructured surface fabricated by glancing angle sputter deposition. Nanotechnology 2014;25:195101.
[593] Izquierdo-Barba I, Garcia-Martin JM, Alvarez R, Palmero A, Esteban J, Perez-Jorge C, et al. Nanocolumnar coatings with selective behavior towards osteoblast and *Staphylococcus aureus* proliferation. Acta BioMater 2015, in press. http://dx.doi.org/10.1016/j.actbio.2014.12.023.
[594] Tyagi M, Tomar M, Gupta V. Glad assisted synthesis of NiO nanorods for realization of enzymatic reagent less urea biosensor. Biosens Bioelectr 2014;52:196–201.
[595] Xie Z, Liu X, Wang W, Liu C, Li Z, Zhang Z. Fabrication of TiN nanostructure as a hydrogen peroxide sensor by oblique angle deposition. Nanoscale Res Lett 2014;9:105.
[596] Schaming D, Renault C, Tucker RT, Lau-Truong S, Aubard J, Brett MJ, et al. Spectroelectrochemical characterization of small hemoproteins adsorbed within nanostructured mesoporous ITO electrodes. Langmuir 2012;28:14065–72.
[597] Zhang W, Ganesh N, Block ID, Cunningham BT. High sensitivity photonic crystal biosensor incorporating nanorod structures for enhanced surface area. Sens Actuat B 2008;131:279–84.
[598] Zhang N, Su X, Free P, Zhou X, Neoh KG, Teng J, et al. Plasmonic metal nanostructure array by glancing angle deposition for biosensing application. Sens Actuat B – Chem 2013;183:310–8.
[599] Gibbs JB, Zhao YP. Design and characterization of rotational multicomponent catalytic nanomotors. Small 2009;5:2304–8.
[600] Jensen UB, Ferapontova EE, Sutherland DS. Quantifying protein adsorption and function at nanostructured materials: enzymatic activity of glucose oxidase at glad structured electrodes. Langmuir 2012;28:11106–14.
[601] Granqvist CG. Preparation of thin films and nanostructured coatings for clean tech applications: a primer. Sol Energy Mater Sol Cells 2012;99:166–75.
[602] Motohiro T, Yamadera H, Taga Y. Angular-resolved ion-beam sputtering for large-area deposition. Rev Sci Instrum 1989;60:2657–65.
[603] Sugita R, Nambu T, Sakamoto Y. Magnetic properties of vacuum deposited Co–Cr perpendicular media and their recording performances. IEEE Trans Magn 1987;23:2449–54.
[604] Hibst H. In: Buschow KHJ, Long GJ, Grandjean F, editors. High density digital recording. Kluwer Academic Press; 1993 [chapter 5].
[605] Hagemeyer A, Richter HJ, Hibst H, Maier V, Marosi L. Crystallographic texture and morphology of obliquely deposited Co–Cr magnetic thin films on flexible polymeric substrates. Thin Solid Films 1993;230:199–202.
[606] Chiba K, Sato K, Ebine Y, Sasaki T. Metal evaporated tape for high band 8 mm video system. IEEE Trans Cons Electr 1989;35:421–8.
[607] Dee RH. Magnetic tape far data storage: an enduring technology. Proc IEEE 2008;96:1775–8.
[608] Krause KM, Taschuk MT, Brett MJ. Glancing angle deposition on a roll: toward high throughput nanostructured thin films. J Vac Sci Technol A 2013;31:031507.

Glossary

ADAFC: Alkaline direct alcohol fuel cell
AFM: Atomic force microscopy
AR: Antireflection coating
AZO: Aluminum-doped zinc oxide
BET method: Brunauer, Emmett and Teller method
CNT: Carbon nanotubes
DMFC: Direct methanol fuel cell

D-SSC: Dye sensitized solar cells
ETC theory: Effective thermalizing collision theory
FTO: Fluorinated tin oxide
GISAXS: Grazing incidence small-angle X-ray scattering
GLAD: Glancing angle deposition
GLADCO: Glancing angle co-deposition
GLADOX: Glancing angle deposition with anodization
HAADF-STEM: High-angle annular dark-field scanning transmission electron microscopy
HIPIMS: High-power impulse magnetron sputtering
HPV: Hybrid photovoltaic solar cell
IA-OAD: Ion-assisted oblique angle deposition
IB-OAD: Ion beam oblique angle deposition
IBAD: Ion-beam-assisted deposition
IT-SOFC: Intermediate temperature solid oxide fuel cell
ITO: Indium tin oxide
IUPAC: International Union of Pure Applied Chemistry
LCD: Liquid crystal display
LSCF: $La_{1x}Sr_xCo_{1y}Fe_yO_{3d}$
LSMO: Strontium-doped lanthanum manganite
LED: Light emitting displays
K–S formula: Keller–Simmons formula
MC: Monte Carlo
MD: Molecular dynamics
MEF: Metal-enhanced fluorescence
MS: Magnetron sputtering
MS-OAD: Magnetron sputtering oblique angle deposition
MPc: Metal phthalocyanines
OA: Oblique angle
OAD: Oblique angle deposition
OAP: Oblique angle polymerization
OER: Oxygen evolution reaction
OPV: Organic photovoltaic solar cells
P3HT: Poly(3-hexylthiophene)
PDMS: Polydimethylsiloxane
PEC: Photo-electrochemical cell
PECVD: Plasma-enhanced chemical vapor deposition
PEDOT:PSS: Poly(3,4-ethylenedioxythiophene):poly(p-styrenesulfonate))
PEMFC: Proton exchange membrane fuel cell
PLD: Pulsed laser deposition/ablation
PL-OAD: Pulsed laser at oblique angle deposition
PVD: Physical vapor deposition
QCM: Quartz crystal microbalance
QD: Quantum dots
QD-SSC: Quantum dot sensitized solar cell
RF: Radiofrequency
RHEED: Reflection high-energy electron diffraction
RMS: Root mean square
SAD: Small angle deposition
SAW: Surface acoustic wave
SDC: Samarium-doped ceria
SEM: Scanning electron microscopy
SOFC: Solid-oxide fuel cell
SPR: Surface plasmon resonance
SZM: Structure zone model
TCO: Transparent conductive oxides
TNO: Niobium-doped titanium oxide
THz-TDS: Terahertz time-domain spectroscopy
TPD: Temperature programmed desorption
UV: Ultraviolet
VLS: Vacuum liquid–solid deposition
VLS-OAD: Vacuum liquid–solid oblique angle deposition
VOC: Volatile organic compound
WCA: Wetting contact angle
YSZ: Yttria-stabilized zirconia
ZPC: Zero point of charge